Characterising & classifying the local population of ultracool dwarfs with *Gaia* DR2 and EDR3.

Richard C. Laithwaite

Department of Physics
Imperial College London

Thesis submitted for the degree of Doctor of Philosophy to Imperial College London
March 2022

Dedication

I would like to dedicate this thesis to my wonderful wife Melanie for her support and understanding on this challenging and fascinating journey to fulfil a lifelong ambition throughout the last 3.5 years. I would like to thank my bright and talented girls, Amelia and Sophie, for not finding it at all odd that their middle-aged dad opted to study the stars rather than get a 'normal' job. I would also like to thank the faculty staff and my fellow students of the Astrophysics group at Imperial College for giving me this incredible opportunity and for embracing me as one of their own. In particular I would like to thank my supervisor, Professor Steve Warren as well as Professor Alan Heavens and Dr Daniel Mortlock for their support and patience with me through this journey. A PhD is an experience and a gift as much as a qualification. There is no greater gift than the opportunity to spend some time trying to figure out the universe, discover new knowledge and seeing your own existence through different eyes.

Declaration & Copyright

This thesis is my own work, except where explicitly indicated in the text.

Acknowledgements

This work has made use of data from the European Space Agency (ESA) mission *Gaia* (`https://www.cosmos.esa.int/gaia`), processed by the *Gaia* Data Processing and Analysis Consortium (DPAC, `https://www.cosmos.esa.int/web/gaia/dpac/consortium`).
Funding for the DPAC has been provided by national institutions, in particular the institutions participating in the *Gaia* Multilateral Agreement.

Contents

List of Tables

List of Figures

Published work

Laithwaite, R. C. & Warren, S. J. (2020), 'The absolute magnitudes M_J, the binary fraction, and the binary mass ratios of M7-M9.5 dwarfs', *MNRAS* 499(2), 2587–2597

Warren, S. J., Ahmed, S. & **Laithwaite, R. C.** (2021), 'The local vertical density distribution of ultracool dwarfs M7 to L2.5 and their luminosity function', *The Open Journal of Astrophysics* 4(1), 4.

Laithwaite, R. C. & Warren, S. J. (2022), 'The field luminosity function and binary fraction at the end of the main sequence with Gaia EDR3 and 2MASS' (in prep)

Laithwaite, R. C. & Warren, S. J. (2022), 'The vertical density profile close to the galactic plane' (in prep)

Chapter 1

Abstract

Ultracool dwarfs (UCDs) are the lowest mass products of star formation and span the end of the stellar main sequence from very-low mass, hydrogen-burning M stars to the coolest brown dwarfs.

In this thesis we characterise and classify the ultracool dwarf population in the solar neighbourhood using the accuracy and precision of data from the *Gaia* space observatory. Combining astrometric (in particular parallax) and photometric data from *Gaia* DR2 and EDR3 with photometry from UKIDSS, SDSS and 2MASS, we prepare some of the largest and most accurate, near-100% complete volume-limited populations of nearby, field late-M, L and T dwarfs. From these samples we derive key population characteristics such as colour-absolute magnitude relationships, the stellar luminosity function, the binary fraction and the binary mass ratio. Our statistical-based approach differs from much of the UCD literature to date which seeks to prepare meta-catalogues from disparate surveys and individual spectroscopic observations with distance determined by indirect methods. Our approach offers improvements in scale, completeness, and distance accuracy. In particular we use *Gaia* to update the colour-magnitude relations and derive the stellar luminosity functions in M_J and M_G of the UCDs. We calculate the binary fraction of the late-M and early-L dwarfs as a function of spectral type by carefully modelling the over-luminous unresolved binary population and show that late-M dwarf binaries reside almost exclusively in equal-mass pairs or twins.

Given the complex spectral features of UCDs, consistent and accurate classification is challenging. We investigate the current traditional methods of classification and evaluate a range of alternative techniques including supervised and unsupervised machine learning.

In a separate study we use *Gaia* data to prepare a large, cylindrical sample of FGK main sequence dwarf stars to calculate the structure of the vertical density distribution close to the galactic plane, in fine detail, as a function of colour. Using our derived colour-dependent thin disk scale height we directly determine the star formation history of the solar neighbourhood by modelling the evolution of stellar populations using state-of-the-art PARSEC isochrones.

Chapter 2

Introduction

2.1 Ultracool dwarfs

The ultracool dwarfs (UCDs) describe objects ranging from the very lowest mass (< 0.1 $M_{\odot}$), and coldest ($T_{eff} < 2700$K) stars ($>$ M7) to the coolest brown dwarfs through spectral types L, T and Y (Kirkpatrick 2005). They are the lowest mass products of star formation. Very low mass stars, spectral types from $\sim$ M7 to L2.5, are characterised by extremely long lives as they slowly fuse hydrogen reserves in their convective envelopes. Brown dwarfs on the other hand do not generate sufficient energy from fusion in their core and therefore lack the thermal pressure to balance gravitational collapse. Instead they are supported by electron degeneracy pressure. Young brown dwarfs emit thermal energy from their formation and slowly cool and dim over their lifetime, this leads to a degeneracy in age, mass and luminosity. Objects $\geq$L3 are unequivocally brown dwarfs however spectral types M7.0 to $\sim$L2.5 include both very low mass hydrogen-burning stars as well as young brown dwarfs. The coolest, lowest mass brown dwarfs share many characteristics with extrasolar giant planets (EGPs).

Late M-type stars have masses in the range $\sim$ 0.090 to 0.075 M_{sun} with T_{eff} in the range $\sim$ 2700K to 2300K respectively. Models of stellar structure indicate that stars with M$<$0.3$M_{\odot}$ are fully convective (Baraffe et al. 1998). As a result He produced through H fusion does not build up in the core but circulates throughout the star's interior. As a result M-type stars are characterised by constant luminosity, extremely long lives and ubiquity; they account for around 75-80% of all stars. Proxima Centauri our nearest stellar neighbour is an M5 dwarf star. Two of our closest neighbours are Luhman 16 (WISE 1049-5319) at 2.0 pc, a brown dwarf binary system comprising a primary L7.5 and secondary T0.5 (Burgasser et al. 2013), and WISE 0855-0714 a Y4 sub-brown dwarf at 2.28 pc (Luhman 2014).

Brown dwarfs are substellar objects defined as those with mass $< 75M_J$ where core conditions do not allow for hydrogen fusion[1] and therefore such objects cannot be classified a stars. Since their discovery just over 25 years ago (Rebolo et al. 1995, Nakajima et al. 1995) there

[1] this does not negate the possibility of limited deuterium fusion in early years of objects life

has been great interest in their discovery, identification, classification as well as understanding their formation, evolution and complex, dynamic atmospheres through observation and modelling. As more substellar objects are discovered, sufficiently large samples are enabling us to determine their population characteristics and constrain their space density, mass and luminosity functions, and multiplicity. To date around 2513 L, T and Y dwarfs have been discovered and spectroscopically confirmed (Kirkpatrick et al. 2021) while many more have been identified photometrically.

Much like stars, brown dwarfs are characterised by their effective temperature, mass, age, radii, surface gravity and atmospheric composition. Due to their relatively low T_{eff}, brown dwarfs have rich, molecular atmospheres observable in their spectra. Their atmospheres include neutral metals, molecules and solid/liquid condensates forming a complex thermo-chemical environment. Variability in luminosity and magnetic activity suggests active and dynamic internal and atmospheric processes with likely surface features and 'weather'.

Brown dwarfs have extremely low luminosity due to both their low T_{eff} (< 2400K) and small size ($R \sim R_J$) making observation difficult, yet they may be some of the most ubiquitous objects in the Universe. The majority of their emitted radiation is in the near-infrared (NIR) from $\sim$1.0 to 2.5μm. Large scale sky surveys and successive generations of NIR telescopes and instruments have added to the number of identified and confirmed brown dwarfs such that a sufficiently large sample now exists to constrain population parameters. That said, unlike main sequence stars, additional complexity arises from the fact that brown dwarfs continuous evolve throughout their life as they cool and contract changing their spectral type and characteristics. As a result both age and mass are required to characterise a brown dwarf.

While the hotter brown dwarfs (early to mid-L dwarfs) share many of the properties and characteristics of their cousins the M-dwarfs; the cooler L and T dwarfs increasingly share characteristics of hot extrasolar giant planets (EGPs) with their complex, molecular-rich, highly dynamic atmospheres and surface features such as bands and spots. As we proceed into the even cooler Y-dwarf regime, such objects are barely distinguishable from large gaseous planets and their low photospheric temperatures may even support molecular water, ammonia or simple carbon-based liquids and ice.

The distinction between low mass brown dwarfs and EGPs is unclear. Estimates from Kirkpatrick et al. (2021) suggest that some brown dwarfs can have mass $< 5M_J$. Other authors suggest that objects $< 13M_J$ (i.e. below the deuterium burning limit) and not bound to a host star should be classified as 'free floating planets' (FFPs). These are defined as objects with masses 4-13 M_J (Miret-Roig et al. 2021).

Brown dwarfs might be the most populous object in the Universe. Mužić et al (2017) estimates a lower limit[2] for the number of brown dwarfs in the Milky Way between 25 and 100

[2]Only objects with mass $> 0.03M_\odot$ are included in the analysis so many fainter, less massive objects likely omitted

billion, and the rate of brown dwarf formation seen in nearby clusters suggests approximately one brown dwarf for every two stars formed. Given these estimates and a very low mass limit, it is likely that many of our closest neighbours are faint, low mass, as-yet-undetected brown dwarfs.

Cool brown dwarfs are also of particular interest to exoplanetary scientists due to the many similarities between the coolest brown dwarfs and extrasolar giant planets (EGPs). From the current catalogue of 4890 confirmed exoplanets[3], there are currently 491 confirmed Jupiter-like gas giant exoplanets with minimum mass[4] in the range $1M_J$ to $20\mathrm{M}_J$. Of these 341 have minimum mass $>5\mathrm{M}_J$ and therefore overlap in mass with the coolest brown dwarfs. These objects share many of the characteristics and observational features of the cooler brown dwarfs. In particular both types of object have fully convective interiors and slowly radiate energy through gravitational contraction and cooling, as well as supporting rich molecular atmospheres.

Using Jupiter and Saturn as analogues for the coolest brown dwarfs and EGPs we anticipate surface features such as bright and dark zones and bands created by upward and downward convection cells, and strong zonal winds. Colourful features created by inorganic compounds and semi-stable cyclonic storms such as Jupiter's great red spot may also be common.

It is becoming increasingly clear that such substellar objects significantly overlap in mass, or form a mass continuum, from the coolest brown dwarfs and free floating planets into the large gas planetary regime where the only apparent difference relates to their formation. Brown dwarf formation is not well understood and a number of different formation mechanisms have been proposed. Possible formation mechanisms range from molecular cloud collapse to disc accretion, migration and ejection which may ultimately result in similar end points.

This thesis is organised as follows. Chapters 3 and 4 comprise a literature review of relevant material. Chapter 3 discusses the main observational characteristics of UCDs and the current theoretical models used to explain the observations. We discuss the current state of the UCD field luminosity function and our understanding of UCD multiplicity. Chapter 4 takes a slight detour and discusses models of galactic structure, in particular the vertical structure of the Milky Way in the solar neighbourhood in relation to main sequence dwarf stars. This relates to research performed in Chapter 7.

Each of the following four Chapters 5 through to 8 discusses a research topic covered by this work. In Chapter 5 we prepare a volume-complete samples of late-M and early-L dwarfs in order to prepare colour-magnitude relations and derive the binary characteristics for the M7 - L3 dwarfs. In Chapter 6 we estimate the field luminosity function and binary fraction relation for the largest, most complete sample of UCDs to date. Chapter 7 is in some sense standalone and uses *Gaia* EDR3 data to investigate the fine structure of the vertical density distribution of

[3]http://exoplanet.eu/catalog/ retrieved on 8 December 2021

[4]Msin(i) i.e. the minimum mass of the planet due to inclination (i) uncertainty.

main sequence FGK stars in the solar neighbourhood. We use these data along with PARSEC[5] isochrones to directly determine the star formation history of the thin disk. Finally, Chapter 8 investigates and evaluates a number of machine learning classification and anomaly detection methods for UCDs using large photometric and spectroscopic datasets. Each of our four research chapters contain their own results, discussion and conclusion section therefore no overall conclusion chapter is required.

[5]Padova-Trieste Stellar Evolution Code (PARSEC)

Chapter 3

Ultracool dwarfs: theory & observations

In this section we describe the main observational characteristics and theory of ultracool dwarfs, in particular their evolution, classification, internal structure and atmospheric properties.

3.1 The first brown dwarfs

The first confirmed brown dwarf, Gilese 229B, was discovered in 1995 as a companion to a cool, main sequence M1 dwarf star Gilese 229 located around 18.8 light years away in Lepus (Nakajima et al. 1995). In the same year the first isolated brown dwarf, Teide 1, was discovered (Rebolo et al. 1995). Since then thousands more have been discovered by a sequence of large scale optical and near-infrared surveys including SDSS, 2MASS, WISE, DENIS, and UKIDSS[1].

Unlike a star, whose position on the main sequence is determined primarily by its mass and its temperature with largely constant luminosity for much of its life, a brown dwarf's effective temperature and luminosity is a function of both mass and age. During their pre-main sequence contraction, gravitational collapse is not opposed by thermal pressure as the core does not reach sufficient temperature and density for hydrogen fusion to occur. Instead the brown dwarf continues to collapse under gravity until it is opposed by electron degeneracy pressure once sufficient core density is reached. As a result once formed, brown dwarfs continue to slowly contract and cool over their lifetime as their initial thermal energy is radiated away.

As more brown dwarfs were discovered a spectral sequence began to emerge. These were subsequently given the classifications L, T and Y getting progressively cooler.

[1]SDSS: Sloan Digital Sky Survey; 2MASS:Two Micron All-Sky Survey; WISE: Wide-field Infrared Survey Explorer; DENIS: Deep Near Infrared Survey of the Southern Sky; UKIDSS: UKIRT Infrared Deep Sky Survey

3.2 Classification

The earliest attempts to classify these objects built on the MK system of classification which utilises a purely qualitative approach based on visual pattern recognition. The rationale was to avoid incorporating theory into the scheme while our understanding of these objects was incomplete and in its infancy. The MK system of spectral classification uses specific actual objects as 'anchors' to define a specific class to which other objects may be compared.

Kirkpatrick et al. (1999) applied a 'movie frame consistency' approach using optical spectra for the L-dwarfs. The optical range (0.68 μm to 0.87μm) includes many useful atomic and molecular absorption lines and bands but suffers from the limitation that only a small proportion of the emitted flux from these objects falls into the visible range.

Reid, Burgasser, Cruz, Kirkpatrick & Gizis (2001) focused on the near infrared ('NIR') range from 1.0μm to 2.5μm where the majority of the flux is emitted. In this range the main photometric passbands are Y (1.02μm), J (1.22μm), H (1.63μm) and K (2.19μm)[2].

Other approaches used indices based on spectral features or ranges. Martín et al. (1999) applied this approach to the L-dwarfs in the optical followed by Geballe et al. (2002) for the L-dwarfs in the NIR. The T-dwarfs were classified using a similar approach in the NIR (Burgasser et al. 2002). As more T-dwarfs were discovered, these approaches were unified by Burgasser, Geballe, Leggett, Kirkpatrick & Golimowski (2006).

Flux emitted in the mid-IR at $> 2.5\mu$m includes important features such as the fundamental methane band at 3.3μm. This is the strongest methane band and would indicate the onset of methane in the atmosphere (Geballe et al. 2001) however high levels of methane and water absorbs most of the flux in the range 3.1-4.0μm reducing its value for classification purposes.

The classification scheme that emerged was initially based on a relatively small sample of L dwarf spectra in the optical which was then extended to infrared. As more brown dwarfs were discovered of cooler types, an infrared only sequence was prepared. These optical and infrared classifications differ. As a result, many published brown dwarf spectral classifications are inconsistent or inhomogeneous. A number of authors (e.g. Schneider et al. 2014) have reclassified large samples of brown dwarf spectra on a consistent basis as part of their research. The current spectral standard objects for M7 to T8 is show in Figure 3.1.

3.3 Observational features of L-dwarfs

The transition from late M-stars to L-dwarfs occurs around 2200-2300K although as discussed T_{eff} alone is an insufficient determinant of spectral type. The L-dwarf sequence continues

[2]See appendix A.2 for a discussion on photometric systems and bands

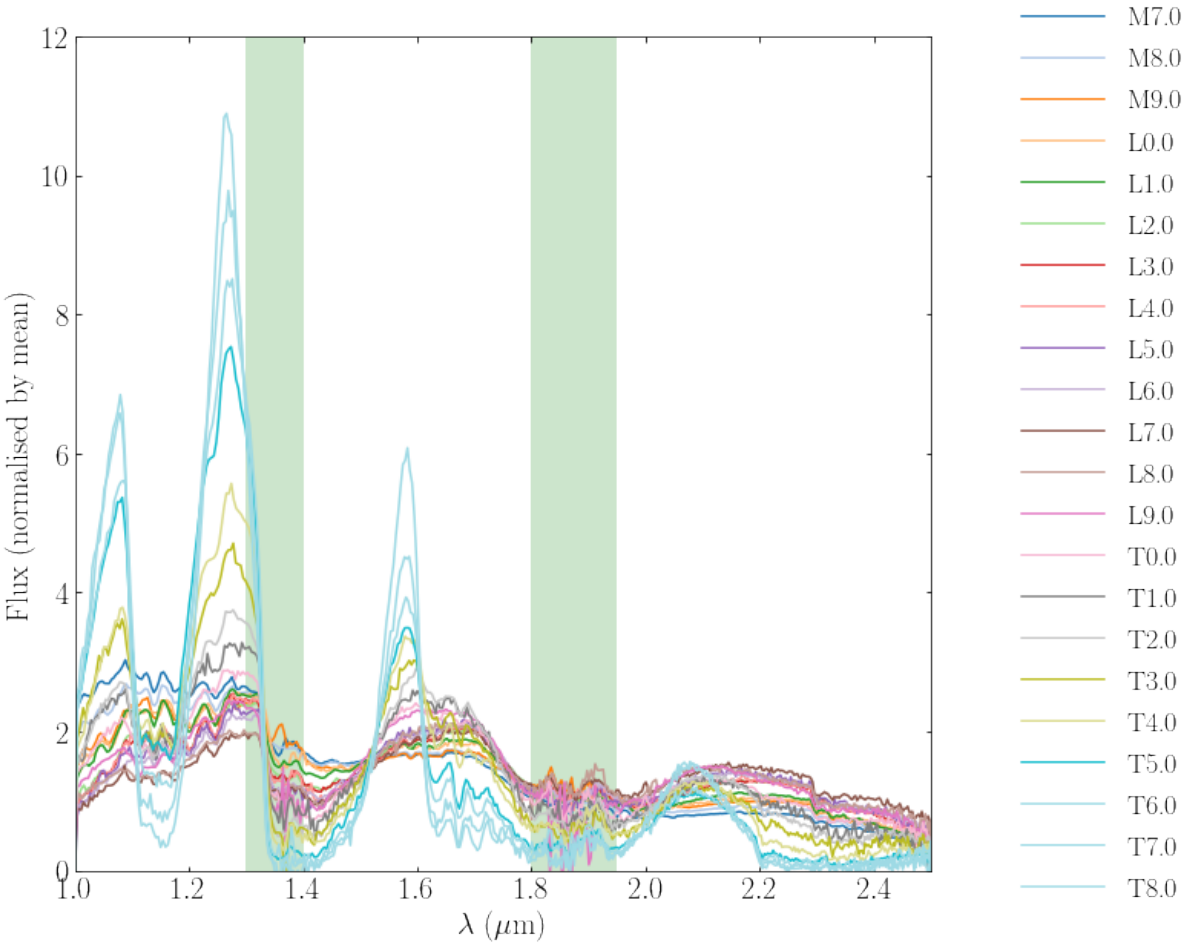

Figure 3.1: Current spectral standard objects M7 to T8 from 1.0 to 2.5 μm. Flux is normalised by dividing by the mean flux across this wavelength range. Telluric regions are shown in light green. Spectra sourced from SpeX Prism Library.

to ∼1400K. Although early L-dwarf spectra are shaped by molecular absorption, condensates and clouds they retain relatively little of a blackbody-shaped energy distribution associated with main sequence stars. As we progress further through the sequence, the spectral energy distribution no longer retains a broadly blackbody profile as molecular absorption carves deep grooves and bands. Similar the evolution of colour differs significantly from that expected by a blackbody over the temperature range of L- and T-dwarfs as illustrated in the colour-magnitude diagram in Figure 3.2 by Morley et al. (2012). A blackbody would show gradual reddening (increasing) in colour through the sequence.

While M-dwarf spectra show clear optical absorption features from VO and TiO, these bands disappear from early L-dwarf spectra as these molecules condensate into VO_2 and TiO_2 (Lodders & Fegley 2002). Dominant features in the optical range include neutral Na and K lines as well as hydride molecules such as FeH and CrH appearing in the optical and NIR. FeH absorption is particularly dominant in late M- and L-dwarfs with the Wing-Ford band at 0.985–1.020 μm being a strong function of T_{eff}, surface gravity and metallicity (Schiavon et al. 1997*a*).

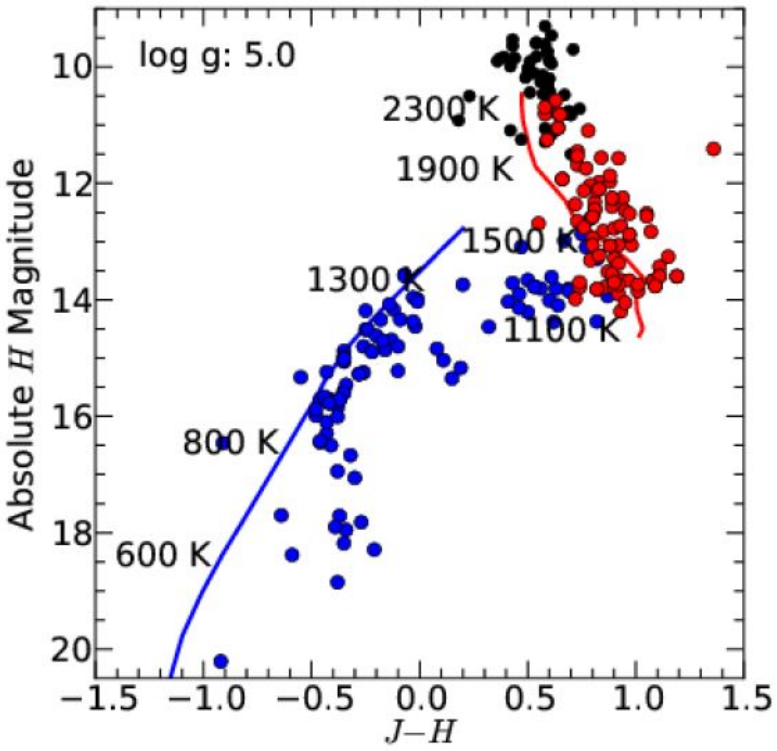

Figure 3.2: J-H vs M_H with known parallaxes. M-dwarfs (black), L-dwarfs (red) and T-dwarfs (blue). Figure from Morley et al. (2012).

Over 100 FeH absorption features appear in the z, J & H bands with the bandhead of the Wing-Ford band at 0.99μm being the most prominent (Cushing et al. 2003). Solid, dusty condensates in the form of clouds are used to explain the spectral shape of late L-dwarfs. The vertical distribution, density and mean particle size of these dusty condensates play a crucial role in determining the emergent flux through scattering and absorption.

Also for late L-dwarfs methane bands begin to appear in the mid-IR at 3.3μm and 7.7μm and H_2O lines strengthen. The dominant form of carbon begins to shift from carbon monoxide to methane through the reaction $CO + 3\,H_2 \longrightarrow CH_4 + H_2O$ marking the start of the T-dwarfs also known as the "methane" dwarfs.

3.4 Observational features of T-dwarfs

T-dwarf spectra are significantly impacted by deep absorption bands and lines. As a result maximum flux occurs in the J-band, around 1.2μm compared to maximum flux for an equivalent blackbody with T_{eff} ~1000K beyond 3 μm. T dwarfs are characterised by strengthening

methane (CH_4) absorption and decreasing CO absorption along with strengthening H_2O but also the rapid disappearance of the dusty condensates that played a major role in shaping the L-dwarf spectra. As pointed out in Geballe et al. (2001), the appearance of detectable CH_4 in the spectra of early T-dwarfs is not a particularly good spectral type boundary as CH_4 can be detected in spectra >L5 at 3.3μm. The start of the T-dwarf sequence is defined by the appearance of CH_4 at 1.6μm.

The classic explanation for the sudden clearing of the atmosphere is that at a certain critical temperature the dust particles grow too large to remain suspended in the upper atmosphere and 'rain out' sinking to deeper, optically thick regions of the atmosphere allowing flux from hotter, deeper layers to emerge. This picture helps explain the re-emergence and strengthening of FeH bands throughout the early to mid T-dwarf spectra. Condensate rain out and other potential mechanisms to explain these features are discussed in greater detail in the section on the L/T transition.

In addition to key sources of opacity from CH_4, H_2O and dusty condensates, other molecules being to appear including NH_3, collision-induced H_2 and CO. In the cooler upper layers of the T-dwarfs much of the CO should be converted into CH_4 so the presence of unexpectedly high levels of CO suggests that some form of vertical transport or convection from the warmer lower levels up to the cooler upper levels is occurring at a timescale faster than the reaction time. This hints at some disequilibrium processes occurring in the atmospheres of T-dwarfs.

3.5 Observational features of Y-dwarfs

With $T_{eff} < 500$K, Y-dwarfs are characterised by deep H_2O and CH_4 bands in their NIR spectra with water clouds. Increasing levels of ammonia (NH_3) are an important source of opacity (Canty et al. 2015*a*). At only 2.3 pc, WISE J0855-0714 is the fourth nearest neighbour to the sun. This is the coolest Y-dwarf discovered to date with $T_{eff} \sim 220$ to 260K and mass $\sim$ 3 to 10 M_J (Cushing et al. 2011, Luhman 2014). It is the only object in the 150-300K range and represents an important link between the Y-dwarfs and giant planets. Y-dwarfs are extremely faint with only $\sim$ 29 objects confirmed to date (Leggett et al. 2017, Kirkpatrick et al. 2021). In 2020, Bardalez Gagliuffi et al. (2020) announced the discovery of four late-T dwarfs and one Y-dwarf, WISEA J0830+2837. This object was determined to have an effective temperature of 350K at a distance of 11.1pc and adds to the small population of Y-dwarfs. The WISE space telescope (Wright et al. 2010) was specifically designed to detect Y-dwarfs with its $W2$ band which peaks at 4.6μm. A citizen science project 'Backyards Worlds: Planet 9' launched in 2017 (Kuchner et al. 2017), helped identify potential candidate objects. Citizen scientists were asked to review stacked unWISE images in $W1$ and $W2$ bands over a 5.5 year timeline and highlight moving objects. These objects were characterised as fast-moving objects ('movers'), or slower-moving objects ('dipoles'). Interesting candidates were then followed up with observations using

Spitzer and the Hubble Space Telescope. Using the time between observations to calculate the proper motion, and Spitzer $ch1$ and $ch2$ photometry, the spectral type, effective temperature and parallax was estimated. Meisner et al. (2020) reported 95 extremely cool brown dwarf candidates discovered through the Backyards World project and subsequently followed up with Spitzer observations. Four of these objects are likely Y-dwarfs further adding to this extremely small pool.

Y-dwarfs are good analogues for EGPs as they share many of the same characteristics as giant gas planets with very similiar atmospheric properties and composition without the emission and reflected radiation from the host star. Both atmospheres are rich in molecules such as CH_4, H_20 and NH_3 with ice water clouds. Characterising the structure and composition of their atmospheres will require larger samples and higher resolution instruments in the near-IR which will be provided by the James Webb Space Telescope (JWST) in the future.

3.6 Evolution of brown dwarfs

Burrows et al. (1997), Chabrier et al. (2000) and Baraffe et al. (2003) prepared evolutionary models spanning spectral types M, L, T and Y. These models use estimates for the mass limit for hydrogen burning between $\sim$ 72M$_J$ and $\sim$ 78M$_J$. The current theoretical estimate for the minimum mass for Hydrogen burning is 78.5 M_J (Baraffe et al. 2015). Since brown dwarfs lack a consistent source of thermonuclear energy they cool throughout their lives. Higher mass brown dwarfs ($\gtrsim$ 20 M_J) evolve from M through L and T spectral types, while lower mass brown dwarfs ($\lesssim$ 20 M_J) start as a L or T type before rapidly cooling and evolving through later spectral types. Brown dwarfs exhibit age-mass degeneracy meaning that for an observed luminosity the object could have a range of masses dependent on its age. To characterise a brown dwarf it is necessary to consider its mass, metallicity and age. See Figure 3.3 for cooling curves based on Burrows et al. (1997). For example a young 100 Myr 20 M$_J$ object would have the same T$_{eff}$ $\sim$ 2300K and classification, say L0, as a 1 Gyr old 60 M$_J$ object.

Below the hydrogen burning limit, L-dwarfs with mass $\gtrapprox$ 63M$_J$ (Nelson et al. 1993) can burn lithium through a process of proton capture until it is rapidly depleted as shown in equations 3.1 and 3.2.

$$p + {}^{7}Li \rightarrow 2\ {}^{4}He \tag{3.1}$$

$$p + {}^{6}Li \rightarrow {}^{4}He + {}^{3}He \tag{3.2}$$

All stars and brown dwarfs start with a baseline abundance of Li from Big Bang nucleosynthesis. Testing for lithium in the spectra of brown dwarf candidates is known as the "lithium test". This is most commonly observed using a lithium I resonance doublet feature at 670.8nm. The internal temperature needed to sustain hydrogen burning (3×10^6K) is slightly higher than that required to burn lithium (2×10^6K). Given that all objects in this mass range have fully convective interiors and are well mixed, depleted levels of lithium in the spectra of early L-dwarfs is an indicator of mass. Objects with detected lithium are brown dwarfs below this minimum mass limit.

Using 15 low mass components in 9 binary systems, Martín et al. (2021) measured pseudo equivalent widths for the Li I feature in the optical spectra and showed observationally that there is a sharp mass boundary for lithium burning at $51.46^{+0.22}_{-4.00}$ M_J. This is lower than current theoretical estimates. Binary systems were selected as these provide accurate determinations of dynamic mass.

Similarly all brown dwarfs with mass greater than $\sim$ 12M$_J$ (Saumon et al. 1996) will burn deuterium for a short period early in their life <100Myr as shown in equation 3.3. This is rapidly depleted and provides a very short term source of fusion energy.

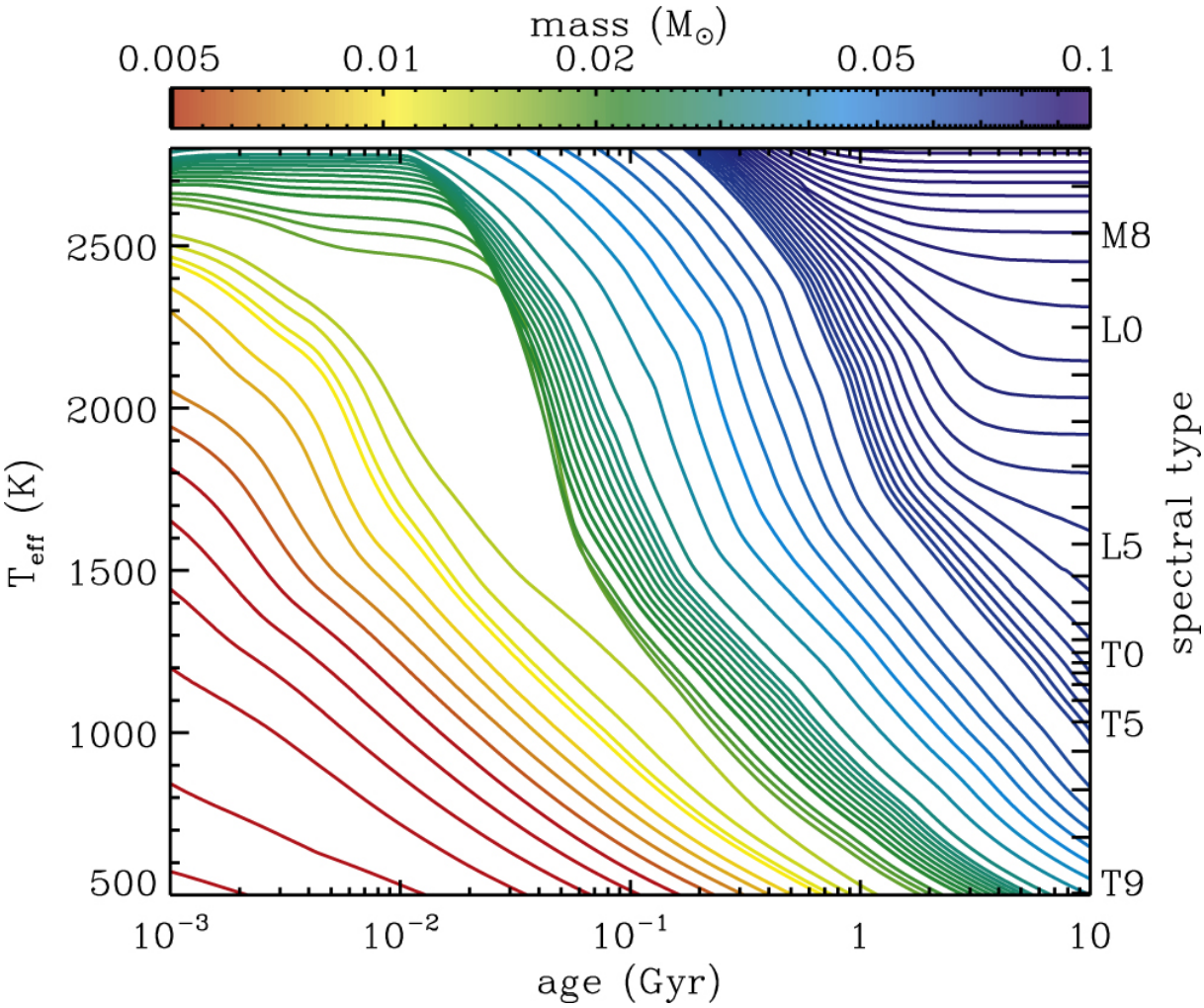

Figure 3.3: Cooling curves for UCDs based on Burrows et al. (1997). The lines represent the evolution of temperature and spectral type as a function of mass and age. Figure from Ryan et al. (2017).

$$p + {}^2H \rightarrow \gamma + {}^3He \tag{3.3}$$

As we have seen, brown dwarfs emit most of their energy in the near infrared (NIR). Using Wien's displacement law for a blackbody, an early L dwarf with $T_{eff} \sim 2000$K would emit maximum flux at 1.45μm well into the NIR range. Approaching the end the L-dwarf sequence with $T_{eff} \sim 1400$K, maximum flux would be emitted at 2.07 μm. By the end of the T-dwarfs where T_{eff} has fallen to $\sim$ 600K, maximum flux is emitted at 4.83 μm however it should be noted that throughout most of the late-L and T-dwarf sequence, molecular absorption has significantly eaten into the flux > 2.5 μm so relatively little flux remains as seen in Figure 3.1.

3.7 Atmospheric models

Much research has been performed to understand and model the cool and dusty (Allard et al. 1997, Tsuji et al. 1999; Burrows et al. 2000; Ackerman & Marley 2001*a*; Allard et al. 2001; Allard et al. 2012; Phillips et al. 2020; Marley et al. 2021) atmospheres of UCDs where the effective temperature ranges from ∼250K to 2700K.

One-dimensional equilibrium models of substellar atmospheres typically make initial assumptions for mass, radius, gravity, chemical composition and metallicity and then solve for an emergent spectrum by applying the following equilibrium conditions in the atmosphere:

- Hydrostatic equilibrium: This determines pressure as a function of radius or altitude
- Radiative-convective equilibrium: This determines the pressure-temperature profile assuming a given flux from the interior and any energy redistribution mechanisms
- Chemical equilibrium: This determines atomic and molecular abundances and sources of opacity
- Local thermodynamic equilibrium (LTE): changes in temperature and transport of heat energy occurs slowly

The limitation of such models is that they assume that atmospheric dynamics and non-equilibrium processes occur on a timescale such that LTE is maintained and an equilibrium P-T profile and chemical composition is maintained. As we shall see there is ample evidence to suggest that various non-equilibrium mechanisms are occurring and atmospheric models need to include these effects in order to explain the observed spectra and variability.

While these equilibrium models explain many observed features of brown dwarf spectra, they do not, for example, explain the transition that takes place over a narrow 200K temperature range at ∼ 1400K where the colours turn bluer, the J-band suddenly brightens, and variability increases. This is known as the L/T transition.

The appearance of condensates and clouds in the atmospheres of late-M dwarfs and cooler was first observed with the appearance of Al_2O_3 by Jones & Tsuji (1997) and how it shapes the observed near-infrared properties of L-dwarfs (Tsuji et al. 1999). Late L dwarfs are more accurately modelled by dusty atmospheric models; while the T dwarf, or methane dwarfs, are better reproduced with clear atmospheric models where the effect of dusty condensates is largely removed. Observational evidence (Burgasser et al. 2002) suggests that complex atmospheric changes are occurring in this transition region resulting in the rapid removal of dusty condensates from the atmosphere.

Many cool stars support thick chromospheres, an inhomogeneous region above the photosphere of hot, ionised, magnetically-coupled plasma that gives rise to prominences, filaments and flares. In general, M-dwarfs > M2, the point at which their interiors become fully convective, are very strong H_α emitters, an indicator of significant chromospheric activity (Mohanty

& Basri 2003). However chromospheric activity falls rapidly for > M9 and Mohanty & Basri (2003) found no persistent chromospheric activity in late-L or T objects studied despite the generation of strong magnetic fields in the interior. This is explained by the rapid drop in electrical conductivity of the increasing cooler and neutral atmospheres of these objects (Mohanty et al. 2002).

3.8 Atmospheric chemistry

Carbon, nitrogen and oxygen are the most abundant elements found in low mass stars, brown dwarfs and EGPs after hydrogen and helium. The main atmospheric molecular species are CH_4, CO, NH_3, N_2 and H_2O (Lodders & Fegley 2002). Assuming thermochemical equilibrium, the composition and abundance of the molecular species present in the atmosphere at any given point is a unique function of pressure, temperature and metallicity. As such, certain species can be used to probe temperature (CO_2, C_2H_6, CH_3OH and NH) and pressure (HCN, HCNO, CH_2O). Lodders & Fegley (2002) calculated expected chemical abundances in P-T space based on solar metallicity. As well as molecular species, solid and liquid condensates can form directly from constituent gas molecules (primary) or from reactions between solid primary condensates and surrounding gas (secondary). Condensates suspended in the atmosphere form clouds which are a major source of atmospheric opacity.

Carbon exists in a number of forms at the pressures and temperatures present in substellar atmospheres. CH_4 is dominant in the cooler, denser regions while CO dominates in hotter, less dense regions. CO_2 only forms in much cooler, lower pressure regions. At equilibrium the following reaction occurs:

$$CO + 3H_2 \rightleftharpoons CH_4 + H_2O \tag{3.4}$$

Water vapour is another important source of opacity in the atmosphere. Oxygen is around twice as abundant as carbon so even when the majority of C is locked up in CO the remaining O exists in H_2O. Faherty et al. (2014) found evidence for sulphide and water ice clouds in the atmosphere of the WISE 0855-07144 (Luhman 2014), one of the coldest brown dwarfs discovered to date with $T_{eff} \sim$ 225 - 260K.

3.9 Dusty models

The importance of dust in the upper atmospheres of cool stars and L-dwarfs was first shown by Tsuji et al. (1996). Dusty condensates are clearly evident in late M and L-dwarf spectra while T-dwarfs show evidence of much clearer atmospheres. Iron and silicate solids condense in the cooler upper atmosphere of L and T dwarfs while CO converts to CH_4 and oxygen binds to hydrogen forming gaseous H_2O. The thick clouds form from the condensation of $MgSiO_3$, Mg_2SiO_4 and Fe which, along with H_2O are the major sources of opacity (Marley et al. 1999;

Lodders 1999). Marley et al. (1999) also showed that particle size has a significant effect on the efficiency of Mie scattering and extinction with larger particles having greater absorption and scattering efficiency. In hotter objects where clouds are formed near the top of the atmosphere, the emission from optically thick clouds more closely resembles blackbody radiation with relatively less molecular opacity.

Models of dust formation and clouds (Helling et al. 2001; Woitke & Helling 2004; Helling et al. 2004; Helling & Woitke 2006; Helling et al. 2008) are used to explain the appearance of dust and the progressive J-K reddening of the spectra as the column mass of condensates thicken. Given that condensate species always form at same temperature, once the cloud layer is sufficiently optically thick the J-K colours saturate. With further cooling the clouds sink further into the atmosphere exposing clearer upper levels and the opacity of CH_4 and H_2 reduces the K-band emissions resulting in increasingly blue J-K colours.

3.10 Quenching

One source of disequilibrium in the chemical composition of brown dwarfs and EGPs is quenching. Bulk transport in the atmosphere strongly influences the abundance of molecular species in the upper, observable layers of the atmosphere. This occurs when the timescale required to reach chemical equilibrium (τ_{chem}) is much greater than the timescale for mixing or transport (τ_{mix}). The molecular abundance at the quench point in the atmosphere occurs when $\tau_{chem} = \tau_{mix}$ and that abundance is then transported higher into the atmosphere at that level. Beneath this level thermo-chemical equilibrium is maintained.

This mechanism was used by Visscher & Moses (2011) to explain the overabundance of CH_4 (compared to expected equilibrium levels) in L dwarf and hot Jupiter giant planets when CO is the expected dominant carbon molecule. Similarly the reverse is true for cooler T dwarfs and cold Jupiter-like planets (including Jupiter itself) where an overabundance of CO is observed in the spectra transported up from deeper, hotter layers of the atmosphere.

3.11 Cloud-free models

Tremblin et al. (2015) proposed an alternative explanation for the observed spectra of L, T and Y dwarfs using cloudless models. This model uses vertical advective transport, NH_3 and CH_4 quenching, as well as the onset of turbulent mixing called fingering convection to explain the disequilibrium chemical composition and enhanced cooling of deep layers. For a given pressure-temperature (P-T) structure in the atmosphere, a static chemical equilibrium is reached; however the gradient of mean molecular weight between the main carbon molecules (CO/CH_4) and the main nitrogen molecules (N_2/NH_3) can result in chemical instabilities between atmospheric layers.

At high temperature and pressure, deeper in the atmosphere, carbon prefers CO; while at lower temperature and pressure, carbon prefers the CH_4 form. Similarly for nitrogen, its preferred form at higher temperature and pressure is N_2 but ammonia (NH_3) at lower temperature and pressure. The higher mean molecular weight molecules (CH_4, and NH_3) sink into the warmer, lower layers and since the timescale for chemical equilibrium is relatively slow, the instability persists changing the adiabatic index and P-T structure of the atmosphere and explaining the reddening of brown dwarf spectra (Tremblin et al. 2019).

The spectral features of the L-dwarfs can be modelled by this thermo-chemical instability at the chemical CO/CH_4 interface reducing the temperature gradient. This heating of the atmosphere results from dissipation of turbulence energy into thermal energy. Kinetic energy contained in large scale eddies cascades to smaller and smaller scales before dissipating fully into thermal energy of the fluid. Around the transition between late L-dwarfs and early T-dwarfs the instability is said to vanish, increasing the temperature gradient again and explaining the reappearance of FeH and brightening in the J-band.

As with the CO/CH_4 instability discussed above, Tremblin et al. (2015) also showed that a reduced temperature gradient is created by the same effect due to NH_3 quenching at the N_2/NH_3 boundary without needing to invoke clouds. Spectral observations of Y dwarfs were successfully recreated using vertical mixing. Evidence for vertical mixing was shown by low levels of ammonia compared to its expected chemical equilibrium abundance (Saumon et al. 2006; Saumon et al. 2012; Cushing et al. 2011) identified by the lack of an absorption feature around 1μm. With vertical mixing the abundance of NH_3 (as well as H_2O, CH_4, CO and CO_2) is quenched deep in the atmosphere (below 10 bar) and transported to the upper atmosphere.

3.12 The L/T transition

As discussed earlier the transition between $\sim$ L7 and T3 shows a rapid change in spectral energy distribution (SED) over a very limited range in effective temperature $1200 < T_{\rm eff} < 1400$K and luminosity (Golimowski et al. 2004) known as the L/T transition.

The following specific features are observed across the L/T transition (Dupuy & Liu 2012):

- Unusual brightening of J-band at $\sim 1\mu$m known as the "J-band jump" (see Figure 3.4)
- Reappearance of FeH and alkali metals absorption lines
- An increase in photometric variability
- Methane bands gradually strength (1.6-1.8μm and 2.2-2.5μm)
- H_2O band at 1.15μm gradually strengthens and absorbs all flux by mid-T
- CH_4 bands appear at 1.6-1.7μm as well as$>$2.2μm but these are difficult to isolate in the K band due to it being heavily contaminated with CO and collision-induced-absorption from H_2
- Spectral energy distribution getting gradually bluer from $J - K \sim$ 1.5-2.5 to $J - K \leq 1$ across the transition (see Figure 3.2)

A physical understanding of what brings about this transition is not available (Vos et al. 2019). The traditional explanation is that thick, dusty condensate clouds sink below the photosphere letting deeper, hotter layers emerge and allowing the photosphere to clear. However 1D models predict a slower decline in condensate opacity as a function of T_{eff} than observations suggest (Ackerman & Marley 2001*a*, Marley et al. 2002). Other explanations include:

1. Patches or holes in the clouds allowing deeper, hotter flux to emerge. This explanation is supported by variability in the SED as such features rotate in and out of view (Apai et al. 2013, Crossfield et al. 2014*a*).
2. Rapid change in cloud thickness or opacity driven by atmospheric perturbations and/or convection (Knapp et al. 2004, Saumon & Marley 2008)

Clouds of condensate in the photosphere weaken absorption bands reddening the spectra. By the end of the L/T transition the atmosphere appears to have cleared of condensates and a much larger optically thin region is exposed. Possible triggers for this rapid condensate depletion or "rainout" have been suggested as follows:

- Temperature: the transition occurs over a range of only $\sim$200K in T_{eff} (Faherty et al. 2012)
- Change in opacity due to condensate grain size (Marley et al. 2003)

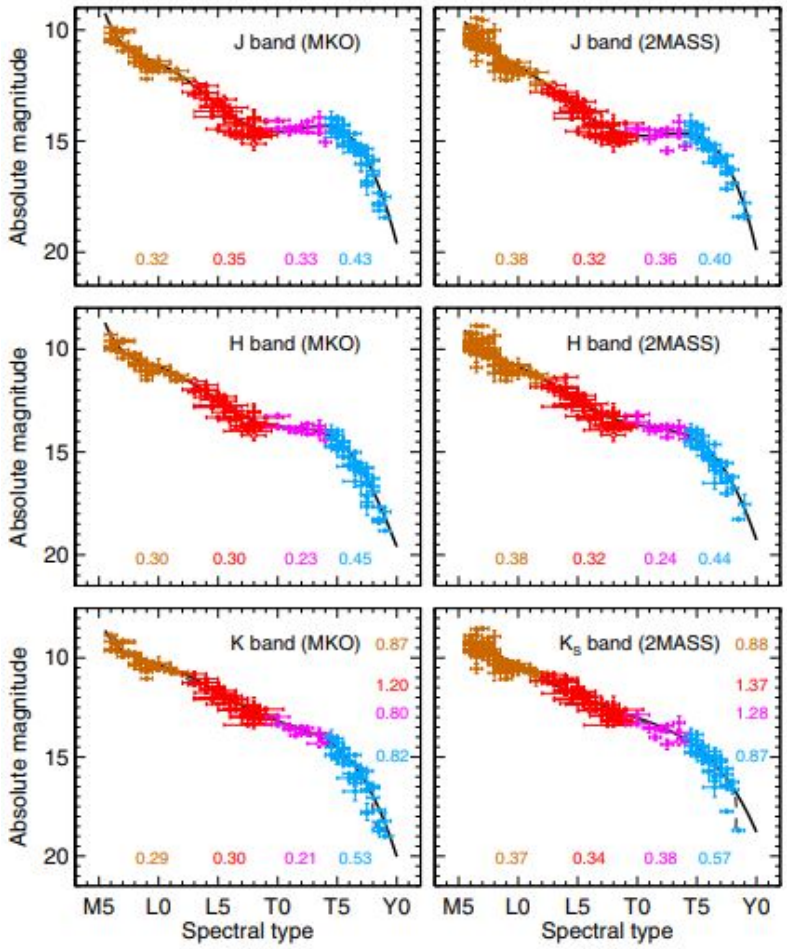

Figure 3.4: Absolute magnitude evolution by spectral type. Solid lines are polynomial fits. Values shown are rms of fit within the coloured spectral range bands. Figure from Dupuy & Liu (2012).

- Surface gravity: It has been shown that young, low gravity objects retain their clouds to lower T_{eff} (Faherty et al. 2016)
- Metallicity: Clouds appear suppressed in low metallicity objects (Gizis & Harvin 2006; Zhang et al. 2017)
- Rotational effects: Cloud layers differentially affected by substellar rotation (Zhou et al. 2018)

Sinking clouds and condensate rainout are not the only explanations for the changes occurring over transition. Tremblin et al. (2019) have presented a radically different model that is cloud free, which models these changes as a non-equilibrium thermochemical mixing via advective transport. Tan & Showman (2017) and Tan & Showman (2019) have presented a model that may explain both cloud breaking at the L/T transition and the observed variability of transition objects using radiative cloud heating/cooling and the periodic formation and dissipation of clouds.

3.13 Dynamics

In addition to their thermo-chemical properties, atmospheric models also predict important dynamical features (e.g. Zhang & Showman 2014, Tan & Showman 2019, Tan & Showman 2021) such as: (i) stable zonal band pattern driven by planetary rotational dynamics; (ii) random, less structured circulatory features driven by heat transport. To date 78 L, T and Y dwarf rotational periods have been measured (Tannock et al. 2021) with periods ranging from ~ 1 to > 20 hours. There is a limit to the speed of rotation before the object would break up. (Tannock et al. 2021) identified three rapid rotating brown dwarfs with spectral types T7, L3.5, L8 with photometric periods ~ 1 hour implying equatorial rotational velocities in excess of 100 km s^{-1}. Heterogeneous cloud coverage is predicted for the majority of brown dwarfs and they exhibit rapid change in the intensity of light emitted over short timescales, often a few rotations (Apai et al. 2013). This study also found strong evidence of banded zonal atmospheric circulation driven by high zonal winds. Such structures are observed in both the gas and ice giant planets within our own solar system. Stable zonal features on Neptune and Uranus are understood to be alternative warm and cold bands driven by rising adiabatic cooling zones at the mid-latitudes and descending warmer, dryer adiabatic warming zones at the equator and poles (de Pater et al. 2014).

3.14 Internal structure

Stellar models indicate that objects with $M<0.35M_{\odot}$ at solar metallicity have fully convective interiors (Chabrier & Baraffe 1997). This means that their internal composition is well-mixed and low mass M-stars do not accumulate He in their cores accounting for their extremely long lifetimes $>10^{12}$years. This is much greater than the age of the Universe suggesting that all the low-mass and brown dwarfs ever formed should still exist[3].

Brown dwarfs have core densities reaching 1000 g cm^{-3} and pressures upto 10^{17} Pa with a central core temperature below the threshold for hydrogen fusion ($\sim 10^{6}$K). In such extreme conditions gravity is opposed by electron degeneracy pressure. The state of matter in the core is believed to be liquid metallic hydrogen and helium. Dynamo currents in the electrically conductive core are the most likely source of magnetic fields which drive the observed correlation between x-ray emission and rotation.

3.15 Radii of brown dwarfs

Even after their initial rapid post-formation contraction, brown dwarfs continue to contract as they cool and age. Their radii are determined by degeneracy pressure rather than thermal pressure opposing gravitational collapse. Burrows et al. (1997) was the first to show with

[3]Except for those destroyed by catastrophic or collisional events

evolutionary models that most brown dwarfs cool and collapse to approximate constant R $\sim$ 0.9$\pm$0.15R$_J$ before this equilibrium is reached (see Figure 3.5). Note that unlike main sequence stars but in common with white dwarfs, higher mass brown dwarfs have smaller radii due to gravitational collapse being supported by electron degeneracy pressure. The density of an object ρ supported by electron degeneracy pressure is proportional to its mass, M^2, and given that $\rho \propto M/R^3$, then the radius, $R \propto M^{-\frac{1}{3}}$ i.e. R decreases as M increases.

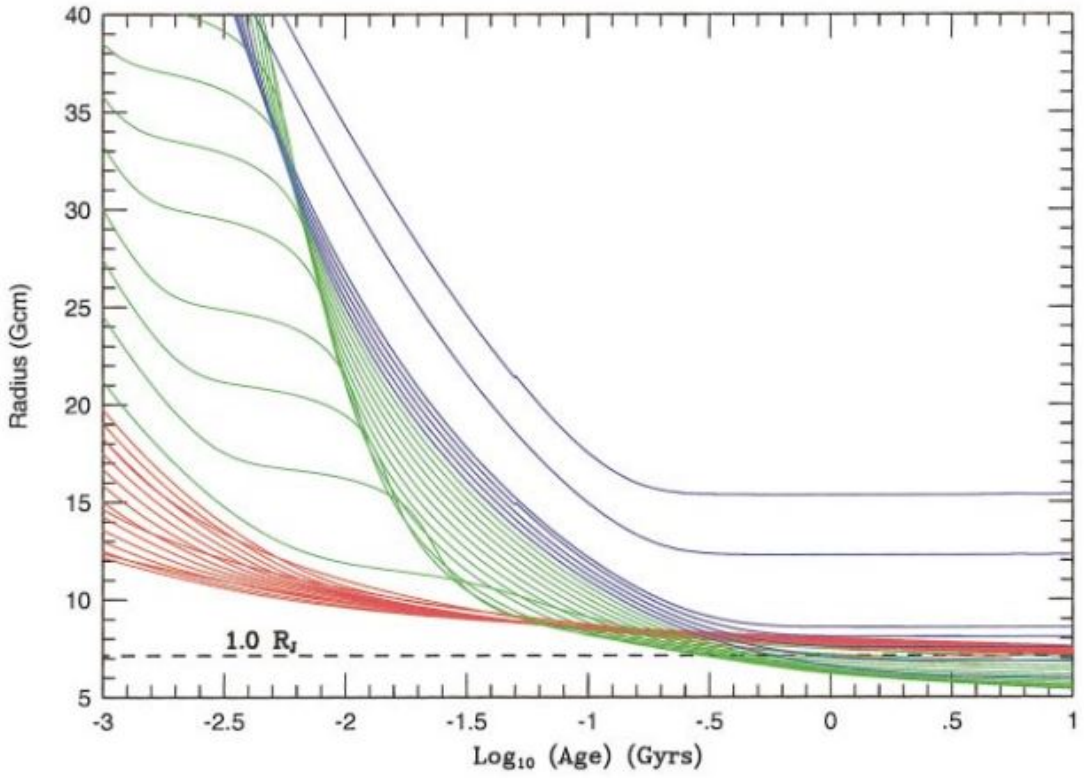

Figure 3.5: Evolutionary models for radius vs. Log$_{10}$(age) across a range of stellar-substellar of masses as indicated. Stars (blue),brown dwarfs (green), low mass brown dwarfs/EGPs (red). Figure from Burrows et al. (2001).

3.16 Surface gravity

The surface gravity of brown dwarfs increases with age as these objects cool and contract. Hot, young brown dwarfs have log g $\sim$3 in cgs units of cm s^{-2} due to their large radii for their given mass. This is similar to the surface gravity of the Earth of log g = 2.992. As they cool and contract their surface gravity increases to log g $\sim$5. In addition to spectral type, brown dwarfs are often given a gravity classification (Kirkpatrick 2005) as follows which also acts as a proxy for age:

- α: normal or field gravity (age >200Myr)
- β: intermediate gravity (age $\sim$30-200Myr)

- γ: low gravity or δ: very low gravity (age <30Myr)

Low gravity objects exhibit specific features in the optical and NIR range (Helling & Casewell 2014) including: (i) Weaker KI/NaI lines; (ii) Weaker FeH absorption; (iii) Stronger VO absorption; and (iv) A triangular-shaped peaked H-band. Low gravity, and therefore young, objects are unusually red due to the presence of more dust in the upper atmosphere. Scatter observed in the H-K colour for cooler T-dwarfs and the shape of the H-band is a result of collision-induced absorption (CIA) of H_2. Increasing surface gravity drives a corresponding increase in pressure-driven CIA absorption features.

Gravity-dependent features can be used as a indicator of age. Allers & Liu (2013) first used NIR spectral indices and equivalent widths of absorption lines sensitive to gravity to determine surface gravity. Martin et al. (2017*a*) updated this approach with a series of spectral indices for classifying surface gravity in M7 to L7 dwarfs as a determinant of their age. This study found a linear relationship between log(age) and the equivalent width of KI absorption lines as 1.1692, 1.1778, 1.2529μm. Determining both the age and T_{eff} are required for estimating mass.

3.17 Magnetic fields

Measuring the strength and topology of a stars magnetic field can yield valuable insight into its atmospheric and internal structure. A stars magnetic field strength and direction is often measured with Zeeman splitting and the polarisation of certain transition lines in the spectra. For cool stars and planets, the magnetic field strength can vary over three orders of magnitude. Christensen et al. (2009) proposed a scaling law derived from geodynamic models based on the principle that energy flux available for generating the magnetic field sets the field strength. This law fits the observed magnetic field strength of the solar system planets and rapidly rotating low mass stars. As a result they predicted that the magnetic fields of rapidly rotating giant exoplanets, brown dwarfs and low mass stars should be observable via radio emissions of their cyclotron radiation.

X-ray emissions are one indicator of magnetic activity. X-rays typically arise from highly energetic processes or hot plasma driving rapidly changing magnetic fields. As previously discussed, mid- to late-M dwarfs are the only main sequence stars to have fully convective interiors. Many M-dwarfs are magnetically active with powerful x-ray, UV and radio emissions from the chromosphere and corona. In more massive main sequence stars, magnetic activity is believed to originate from a dynamo process linked to shearing at the tachocline, the boundary between the radiative and convective zone. Mid- to late-M dwarfs do not have such a boundary so alternative dynamo mechanisms are needed. Uniquely to M dwarfs, the magnetic field strength drives physical changes in the star. In particular, the observed radii of magnetically active M dwarfs is inflated compared to theoretical evolutionary predictions (Ribas 2006; Torres 2013). Strong magnetic fields are believe to alter the convective energy transport in the stellar interior

(Chabrier et al. 2007). X-ray emissions decline rapidly for spectral types > M7 (e.g. Mohanty & Basri 2003) which is explained by a decreasing fraction of ionisation in the photosphere and atmosphere of UCDs. Internally generated magnetic fields become decoupled from the neutral atmosphere reducing its ability to release magnetic energy. through plasma heating.

Despite being generally less magnetically active than M-dwarfs, brown dwarfs have been observed to emit strong X-rays and flares. Evidence of persistent X-ray flares from young (≤ 10 Myr) brown dwarfs have been detected due to their active accretion and collapse (Grosso et al. 2007). However older brown dwarfs are not expected to emit significant X-rays due to their cooler, increasingly electrically neutral photosphere and chromosphere and their lack of a hot corona typically found in main sequence stars. Rutledge et al. (2000*a*) detected a bright X-ray flare lasting around 1-2 hours using the *Chandra* X-ray Observatory from a older, isolated brown dwarf LP 944-20. The flare's peak luminosity of $L_X = 1.0^{+0.5}_{-0.3} \times 10^{26}$ erg s^{-1} is comparable to a small solar flare, but this is still an order of magnitude weaker than X-ray flares detected by late-M main sequence stars with similar bolometric luminosity. Rutledge et al. (2000*a*) suggest that a potential source of these flares is twisted magnetic fields sourced from hot, magnetised material deep within the object, heating and electrifying the atmosphere in a short burst of energy. Subsequent observational studies on LP944-20 by (Martín & Bouy 2002*a*) set an upper limit for quiescent X-ray emission at $L_X = 3.1 \times 10^{23}$ erg s^{-1} or $\log(L_X/L_{bol}) \leq$ -6.28. Older brown dwarfs like LP 944-20 are surprisingly inactive in X-ray emission given their magnetic field strength and rapid rotation.

In 2020, De Luca et al. (2020) announced the first detection of an X-ray flare from an L-dwarf, J0331-27. The flare's peak luminosity was 6.3×10^{29} erg s^{-1} and lasted around 2400 seconds. No quiescent emission was detected. De Luca et al. (2020) suggest that these flares are the result of strong magnetic reconnection and plasma heating in the photospheres of the relatively cool L-dwarfs and that magnetic energy in such objects is more often released in such superflares.

Brown dwarfs can emit radio waves in a process similar to Jupiter and Saturn. Their strong magnetic fields accelerate charged particles (primarily electrons) and emit cyclotron radiation at radio frequencies. This mechanism is also responsible for the bright aurora observed on the gas giants (Hallinan et al. 2008; Hallinan et al. 2015; Nichols et al. 2012). Hallinan et al. (2008) showed evidence that the periodic and highly circular polarised radio emissions observed from some UCDs suggest that the electron cyclotron maser instability is the dominant mechanism for radio emissions as is the case for Jupiter and Saturn. Nichols et al. (2012) showed that intense auroral emissions could be generated by powerful electric currents arising from the angular velocity shear in magnetic field and plasma in fast-rotating UCDs. Radio emissions have recently been used to provide the first detection of a cool, methane T-dwarf BDR J1750+3809 (Vedantham et al. 2020). This object was found to have a planetary-scale magnetic field $B \gtrapprox 25$ G. For comparison, Jupiter has the strongest magnetic field in the solar systems with an equatorial magnetic field strength of 4.17 G. This radio source detection at 144Mhz or 2.1m has only recently become achievable with low frequency metre-length detectors such as the Low-Frequency

Array (LOFAR) based mainly in the Netherlands. This detection was subsequently followed up with NIR photometry and spectroscopy to classify the object as T6.5±1 at a distance of 65^{+9}_{-8} pc. This object with quasi-quiescent radio luminosity of $\simeq 5\times\ 10^{15}$ ergs s^{-1} Hz^{-1} is greater than two orders of magnitude louder than comparable T-dwarfs. Based on our understanding of the Jovian magnetosphere and its mechanisms for electron acceleration and radio emission, Vedantham et al. (2020) propose two explanations for this: (i) special viewing geometry related to the breakdown of co-rotation between the plasma and the magnetic field particularly at high magnetic latitudes, or (ii) interaction with a close and/or large companion. In the second case, emission strength would be a function of orbital dynamics of the brown dwarf and its companion. An analogous effect is seen between Jupter and Io as well as Saturn and Enceladus. Given that the low frequency magnetic field measured by Vedantham et al. (2020) is within the known planetary magnetic fields of extrasolar giant gas planets, this method of detection has potentially interesting applications for radio detections of both cool brown dwarfs and giant exoplanets.

3.18 Young, low-gravity brown dwarfs

Most brown dwarfs are older than 1 Gyr, so young objects are of particular interest as they exhibit unique spectral features. At $<$ 200 Myr old, young brown dwarfs have high T_{eff} for their given mass, large radii and low surface gravity. WISE J1741-4642 is one such example (Schneider et al. 2014) of a young L7±2 dwarf with $T_{eff} \sim$ 1450±100K and mass $\sim$ 4 to 21 M_J. Its low surface gravity leads to enhanced VO bands, narrow/weak neutral alkali metal lines and a distinctive triangular shaped H-band.

Using a sample of 73 young field dwarfs with spectral types M5-L7, Allers & Liu (2013) established a method of spectral typing independent of gravity in the NIR. In addition they defined a set of gravity-dependent spectral indices using FeH, VO, KI features and the H-band continuum to create a gravity classification method for very young ($\lesssim$ 10 Myr) ultra cool dwarfs. The K-band continuum shape can also be used to identify very young brown dwarfs from a field population. Canty et al. (2013*a*) created a H_2 index in the K-band to quantify the continuum slope defined as,

$$H_2(K) = \frac{F(\lambda = 2.17\mu m)}{F(\lambda = 2.24\mu m)} \tag{3.5}$$

where F($\lambda = 2.17\mu$m) and F($\lambda = 2.24\mu$m) are the median fluxes over a range of 0.02μm centred at the given wavelengths. Figure 3.6 shows how this index identifies young or very red objects from a sample of L-dwarfs (Schneider et al. 2014).

Young objects' spectra exhibit extreme red colours for a given magnitude and are not well represented by the evolutionary models. The colours are typically $>$ 0.5 magnitude greater in $J - K$ than field objects. Their low gravity makes these objects useful analogs of EGP atmospheres.

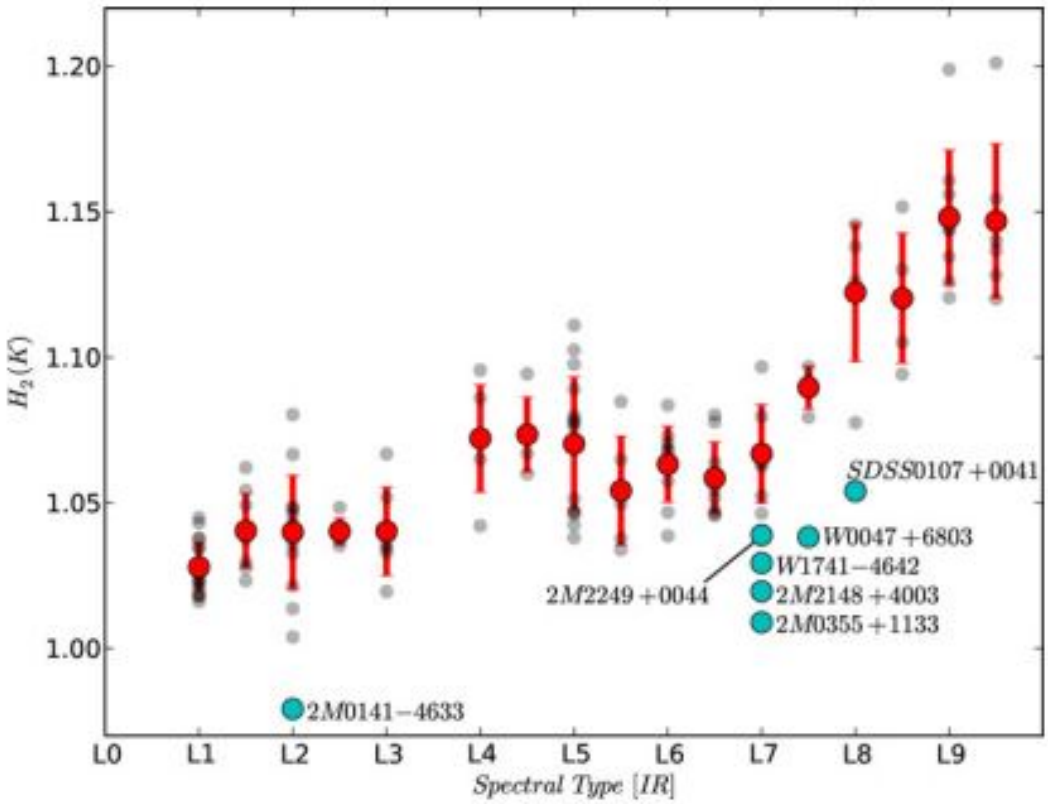

Figure 3.6: H_2(K) index as a function of spectral type for L dwarfs for a sample of L-dwarf spectra from the SpeX Prism Spectral Library. Average H_2(K) index (red points) and standard deviation binned by 0.5 subtype. Young or particular red L dwarfs individually identified. Figure from Schneider et al. (2014).

3.19 Low metallicity brown dwarfs

There exists a sub-category of brown dwarfs that are both cool and very old. Their low metallicity implies that they were formed in the early universe and have cooled and contracted over a long lifetime. Helling & Casewell (2014) identified 30 such objects, mainly early L-dwarfs. These objects known as 'subdwarfs' are identified by appearing overluminous in M_J and underluminous in M_K (Burgasser 2008*a*). This is explained by reduced cloud opacity combined with strong Ti, FeH, Ca lines. The K-band flux is suppressed through higher pressure induced absorption of H_2 as a result of higher surface gravity (Ackerman & Marley 2001*a*). Subsequently many more L subdwarfs have been identified e.g. Zhang et al. (2018). Dozens of low-metallicity T subdwarfs have also been identified (Pinfield et al. 2014; Zhang et al. 2019; Schneider et al. 2020; Meisner et al. 2021). The most extreme of these subdwarfs with $T_{eff} < 1400$ K and [Fe/H] $\leq$ -1 show unusual and distinctive NIR colours. Given their age many are expected to reside in the Galactic thick disk or halo.

3.20 Brown dwarf variability

Periodic variability in near-IR and mid-IR bands is a common feature observed in field L and T dwarfs as well as low gravity objects such as young brown dwarfs and giant exoplanets (Artigau 2018). Metchev et al. (2016*a*) observed variability in 80% of a sample of L3-L9.5 dwarfs and 36% of T0-T8 dwarfs. They concluded that spots and surface features are common on most if not all brown dwarfs. Inhomogeneous surface features may be responsible for some of the observed variability as lighter or darker patches or regions pass into and out of the line of sight. Greatest variability occurs around the L/T transition suggesting that surface inhomogeneties are at maximum over the transition and that clouds dissipate unevenly over the surface (Radigan et al. 2014). Variations in brown dwarf brightness is not well understood. Observational evidence continues to grow of active weather systems on brown dwarfs leading to variability on timescales shorter than the rotational period.

Current instruments are not able to directly image the lowest mass objects however large libraries of ultracool dwarf spectra and photometry exist. These measurements are time-averaged and spatially unresolved. Detecting and measuring variability offers an alternative method to probe the atmospheres of these objects.

It is important to distinguish between periodic and non-periodic variability. Non-periodic variability is observed in young, hot brown dwarfs and is likely driven by accretion disks, planetary disks or irregularly magnetically driven phenomena such as flares.

Periodic variability is driven by inhomogeneous surface features such as sun spots, longitudinal bands or patchy cloud coverage rotating into and out of view (Apai et al. 2017*a*). The frequency of variability is on the timescale of the period of rotation.

The amplitude of periodic variability appears to reach a maximum around the L/T transition. Three of the highest amplitude variable brown dwarfs observed are: SIMP J013656.5+093347, 2MASS J21392676+0220226 and Luhman 16B[4] with spectral types T2.5, T1.5 and T0.5 respectively (Biller 2017*a*).

Metchev et al. (2015) investigated photometric variability for 44 L and T dwarfs and found 61% or 14 of 23 of their L dwarfs, and 31% or 5 of 16 of their T dwarfs, exhibited variability. One third of their L dwarfs shows irregularities which suggest multiple spots or patchy cloud features. Taking account of sensitivity, they conclude that spots are ubiquitous for L3 to T8 objects. There are only a few confirmed variable objects in the cooler late T and Y spectral types e.g. Cushing et al. (2016), Leggett et al. (2016). Multi-band studies of variability have enabled greater exploration of variability at different depths, or pressures, within the atmosphere. While some observations show clear correlation in variability across multiple bands, others show phase lags. This allows us to probe atmospheric conditions at different altitudes: higher altitudes with mid-IR and lower altitudes with the near-IR.

One argument for the idea of deep holes opening up in the thick cloud cover across the

[4]Note that Luhman 16AB is a brown dwarf binary at a distance of $\sim$ 2 pc. It has L7.5 and T0.5 components and as such both objects fall within the L/T transition region.

L/T transition was the reemergence of FeH. The 0.99 μm FeH feature is clearly observed in the spectra of early to mid-L dwarfs but subsequently disappears as the Fe clouds sink below the photosphere. The reappearance of this feature in early to mid-T dwarf spectra was explained by deep holes appearing in the thick cloud cover exposing the deep layers of FeH gas. Unfortunately the expected variability in FeH as these holes pass across the observed face of the object has not been observed.

Cloud-free models proposed by Tremblin et al. (2015) to explain the observed spectral energy distribution based on thermochemical instabilities in the CO/CH_4 transition at the L/T boundary and N_2/NH_3 at the T/Y boundary, do not make a strong case for variability.

3.21 The substellar mass and luminosity functions

The stellar luminosity function is a fundamental property of the general population of stars. It measures the number of stars in an interval of luminosity or, more often, absolute magnitude. Measuring the field luminosity function of ultracool dwarf populations has proved difficult (Cruz et al. 2007, Reylé et al. 2010, Bardalez Gagliuffi et al. 2019, Kirkpatrick et al. 2021) for three primary reasons: first obtaining an accurate measurement of distance for each source in order to determine its absolute magnitude as well as its accurate location within a volume; second an accurate determination of multiplicity; and thirdly ensuring a high degree of completeness within a given volume given Malmquist and other observational biases.

Recent data releases from the *Gaia* spacecraft have created an opportunity to measure the stellar luminosity function and binary fraction in a different way. Previously the limiting factor was the time involved in spectroscopic identification of candidates, distance determination, and resolution of multiple systems. While the broad *Gaia* G-band is not well suited for faint ultracool sources, there are in fact large numbers of ultracool dwarfs detected by *Gaia*, at high S/N, for $G < 20$.

The current state of the art for measurement of the luminosity function, for the spectral range from M7 to L5, is the study by Bardalez Gagliuffi et al. (2019) who used a volume-limited sample of 410 dwarfs within 25 pc of the Sun. This sample is still quite moderate in size and used spectral classifications and resolved binaries drawn from the literature. Figure 3.7 summarises the results of various studies to prepare the luminosity function in M_J for the UCDs (Bardalez Gagliuffi et al. 2019). We discuss each of these studies including the size of the sample and its volume, distance determination, and binarity assumptions below. As can be seen from the discrepancies between these surveys and their respective errors, the luminosity function is not particularly well-constrained for the UCDs. In Chapter 6, we use *Gaia* data to construct a luminosity function using the largest, most homogeneous sample to date.

Bochanski et al. (2010) created a luminosity function for the low mass M dwarfs ($0.1 < M/M_{\odot} < 0.8$) using SDSS DR6 photometry. Distances were estimated using photometric parallax relations based on nearby stars with known trigonometric parallax. The unresolved binary fraction is found using an assumed mass-dependent binary fraction relation and an iterative Monte Carlo method was used to fit to the *system* luminosity function (i.e. one that ignores the unresolved binaries).

Cruz et al. (2007) estimated the luminosity function for a 20pc, volume-limited sample of 99 M7-L8 dwarfs in 91 systems using data from the 2MASS catalogue. Distances were estimated using a combination of trignometric parallaxes (where available) and spectrophotometric methods. This sample was determined to be complete for $M_J < 14$ for 36% of the sky. Given the close proximty of these objects, 55 systems were observed using high-resolution ground based

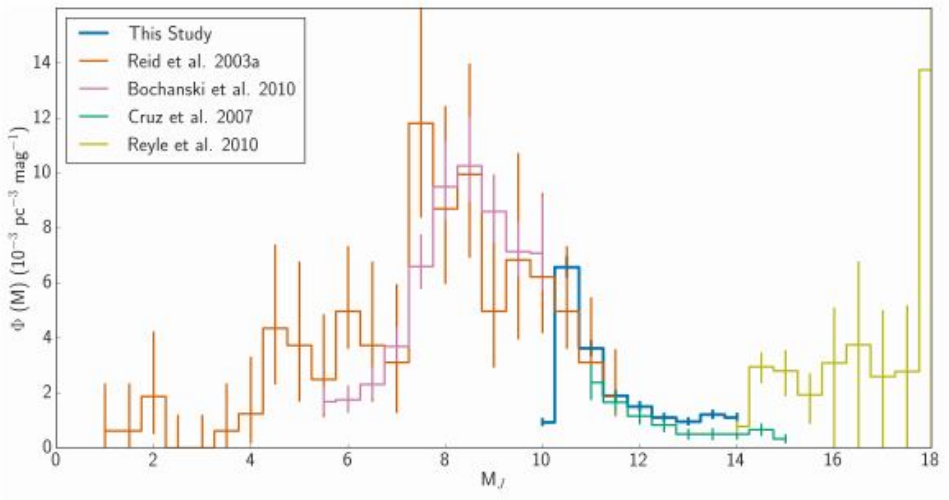

Figure 3.7: Summary of various studies for luminosity function for ultra-cool dwarfs. Orange (Reid et al. 2002); Pink (Bochanski et al. 2010); Green (Cruz et al. 2007); Yellow (Reylé et al. 2010). Blue is Bardalez Gagliuffi et al. (2019). Figure from Bardalez Gagliuffi et al. (2019).

observations and nine resolved binaries found. This observed binary fraction of 17% was extended to the full sample.

Reid et al. (2002) created a 25 pc volume-limited sample of 764 main sequence systems spanning a large magnitude range from solar-type stars to low mass M dwarfs (-1 $< M_V <$ 17) using *Hipparcos* distances and with an observed average multiplicity fraction of 30.1%±2.4%. It was recognised that this likely understates the binary fraction and an assumed upper limit of 60% was applied to construct a stellar luminosity function.

Reylé et al. (2010) used data from the Canada-France Brown Dwarf Survey to measure the system luminosity function for the L5 to T8 dwarfs (13.5 $< M_J <$ 18.0). Their sample comprised 97 field brown dwarfs drawn from 16 patches covering a total area of 444 deg^2. No adjustment for binaries was considered.

The initial mass function (IMF) is an empirical relation that describes the distribution of masses at birth and is commonly described by a power law of the form $N(M) \propto M^{-\alpha}$ where $N(M)$ is the number of stars formed in the mass interval M to $M + dM$ in $M_\odot$ units. The exponent, α, was initially estimated at 2.35 (Salpeter 1955) for masses $\sim$ 1M$\odot$ however subsequent studies by Miller & Scalo (1979), Kroupa (2001) and Chabrier (2003) have refined this relationship over a wider range of initial mass. Kroupa (2001) introduced a broken power law with three indices (α = 2.3, 1.3 and 0.3) and two breaks at 0.5 M$\odot$ and 0.08 M$\odot$. The IMF for the very-low mass and substellar mass range $<$ 0.1M$\odot$ remains poorly constrained.

The most recent study to estimate the substellar mass function by Kirkpatrick et al. (2021)

is based on a full-sky 20 pc census comprising 525 L, T and Y dwarfs. Despite the small sample size, this survey provided an initial constraint on the space density and substellar mass function of the coolest brown dwarfs.

Various forms of the substellar mass function were considered and the best fit was determined to be a single power law distribution with an $\alpha = 0.6 \pm 0.1$ (see Figure 3.8). Assuming a power law mass function with index 0.6, the space density for late-T and Y dwarfs could be as high as 3 to 5 $\times$ 10^{-3} pc^{-3} 150K^{-1}.

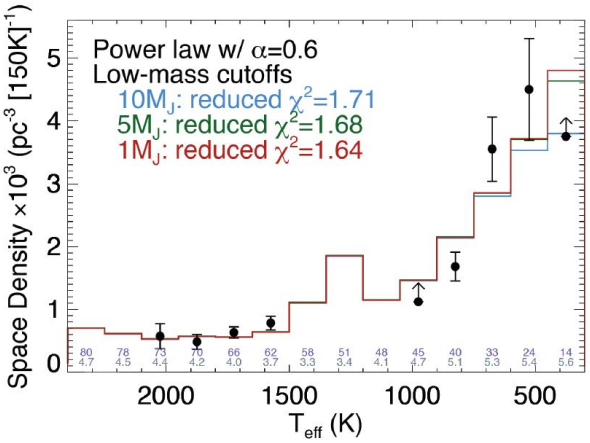

Figure 3.8: Number density distribution of objects in solar neighbourhood with power law best fit with index $\alpha = 0.6$ at various minimum mass cutoffs. Figure from Kirkpatrick et al. (2021).

3.22 Multiplicity

Binary star systems are an important laboratory for directly determining stellar parameters, in particular mass and radii. In addition the study of stellar (and brown dwarf) multiplicity statistics are important for characterising stellar populations and useful for star formation theories.

Binaries and multiple star systems are systems of two or more stars (or brown dwarfs) gravitationally bound to each other and orbiting around a common centre of mass or barycentre. The majority of stars are members of a binary or multiple system (Binney & Merrifield 1998). Binary systems are considered close if they are close enough to interact and transfer matter. Close binary systems have usually evolved together. They are difficult to resolve visually and, depending on the resolution of the instrument and distance to the object, will often appear as a single 'blended' source so other methods must be used to resolve the components. Wide binaries are generally considered to have > 10 AU separation (Bate 2012). Such objects evolve separately with relatively little influence on each other. It is accepted that some unknown proportion of all sources are unresolved binaries or multiple systems. In UCD population surveys this is often a major source of uncertainty.

It is estimated that around one third of all star systems are binary or higher order and that the majority of all stars are in multiple systems. That said, it has been shown empirically that the fraction of multiple star systems, as measured by the multiplicity fraction, increases with primary mass (see Figure 3.9). Extending this trend into the very low mass and substellar range suggests that UCDs would have among the lowest multiplicity fraction.

The generally accepted model for star formation is that stars form from collapsing dense molecular cores. Fragmentation results in multiple objects within each core. Goodwin & Kroupa (2005) placed a limit on the this of between 2 and 3 stars per core setting a limit on primordial multiplicity. Young multiple systems typically decay within 0.1 Myr through the ejection of single stars reducing the multiplicity fraction and hardening the resulting system. Ejections of sub-stellar embryos during the accretion phase of young sources before they reach stellar masses has been proposed as a formation mechanism for brown dwarfs. Bate et al. (2002) showed that the frequency of close binary systems can also be produced through dynamical interactions in unstable multiple systems and the orbital decay of initially wider binaries rather than fragmentation. Formation mechanisms for very low mass binaries are poorly understood.

Binaries can be identified optically (visual binaries), spectroscopically (spectroscopic binaries), astrometrically (astrometric binaries) or photometrically (photometric or eclipsing binaries[5]). Resolving substellar binaries and constraining the multiplicity fraction would help inform brown dwarf formation mechanisms.

[5]i.e. stellar components happen to orbit in a plane along our line of sight

Key multiplicity parameters of a given stellar population include the following:

1. Multiplicity Fraction (MF): the fraction of binary (or higher order) systems to the total number of systems

2. Companion Frequency (CF): Average number of companions per system which is always greater than or equal to the MF and can be greater than one. This is primarily a function of how common higher order (i.e. above binary) systems are for a given primary mass.

3. Mass ratio (q): $q = \frac{M_{sec}}{M_{prim}} \leq 1$ however q is most commonly parameterised by γ where $f(q) \propto q^{\gamma}$ i.e. The distribution of companion masses is a power law with index γ.

4. Orbital period (p), average orbital distance ($\bar{a}$) and eccentricity (e)

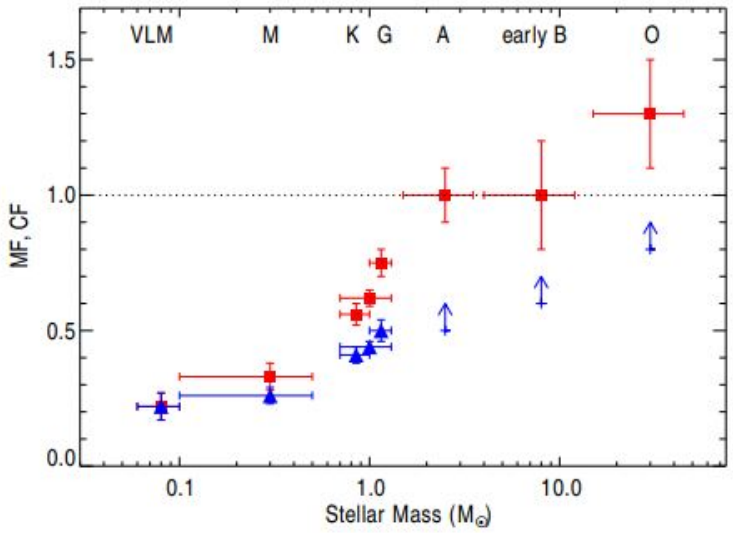

Figure 3.9: Multiplicity Fraction, MF (blue triangles) and Companion Frequency, CF (red squares) as a function of primary mass. Figure from Duchêne & Kraus (2013*a*).

Initial studies show that very low mass systems were heavily skewed towards equal mass systems (Burgasser et al. 2007) and that such distributions were best described by a power law relationship with a high index (Allen 2007; Burgasser, Geballe, Leggett, Kirkpatrick & Golimowski 2006; Liu et al. 2010). In particular, based on a sample of 30 brown dwarfs, Burgasser, Geballe, Leggett, Kirkpatrick & Golimowski (2006) estimated γ=4.2±1.0. Current estimates of multiplciity parameters for very low mass stars and brown dwarfs with mass < 0.1 $M_{\odot}$ and low mass M-dwarfs with mass between $0.5M_{\odot}$ and $0.1M_{\odot}$ are shown in Table 3.1.

A mass ratio index (γ) of 4.2 for brown dwarfs implies that nearly equal mass binaries are highly favoured although why this appears to be the case is not known. These estimates should be considered in the light of various studies of multiplicity in the substellar mass range (Burgasser et al. 2007; Luhman 2012) that show a wide range of results based on different completeness limits. It is particularly challenging to correct such studies for Malmquist bias i.e. selection

Mass	< 0.1 M$\odot$	0.1M$_\odot$ to 0.5M$\odot$
MF	22^{+6}_{-4}%	26^{+3}_{-3}%
CF	22^{+6}_{-4}%	33^{+5}_{-5}%
γ	4.2±1.0	0.4±0.2
$\bar{a}$	4.5 AU	5.3 AU
σ_{logp}	0.5	1.3

Table 3.1: Multiplicity parameters from Duchêne & Kraus (2013*a*)

effects from preferential detection of bright objects. Allen (2007) undertook a Bayesian analysis of various surveys and calculated a multiplicity fraction in the range 20 to 25% consistent with the review by Duchêne & Kraus (2013*a*).

Relatively few substellar triple systems have been confirmed (Bouy et al. 2005; Burgasser et al. 2012*a*; Radigan et al. 2013; Guirado et al. 2018). An 8pc sample of 118 field M dwarfs by Reid & Hawley (2005) found a ratio of triples to binaries of 1:4 and a triple fraction of $\sim$ 4%. Faherty et al. (2010) searched for wide companion substellar systems and found a surprisingly high triple to binary fraction of 3:5 in this population.
A large, all-sky, volume-limited survey of 1120 M-dwarfs within 25 pc (Winters et al. 2019*a*) searched for both wide and close companions with up to a maximum 300" separation. These objects ranged in mass from 0.075M$_\odot$ to 0.6M$_\odot$. Multiple systems with $>$ 5" separation were identified from image archives. The most challenging companions to identify were very close companions at <2" separation. Astrometric and photometric methods were used to identify overluminious stars (i.e. those objects elevated from the main sequence in a colour-absolute magnitude plot) as well as those with a photometric and trigonometric distance mismatch. This study found a stellar MF of 26.8±1.4% and a CF of 32.4±1.4% (see Figure 3.10). The ratio of singles : binaries : triples : higher-order systems after adjusting for known brown dwarf companions was found to be 75 : 21 : 4 : 0.3%. In addition, as shown in Figure 3.10, this survey showed that the greatest contributor to the MF was from close ($<$ 2" separation) binaries hinting at possible insights into formation mechanisms.

Winters et al. (2019*a*) stratified their results into three mass ranges (0.3 to 0.6 M$_\odot$, 0.15 to 0.30 M$_\odot$, and 0.075 to 0.15 M$_\odot$). Figure 3.11 shows the cumulative MF as a function of distance for each mass range. The lowest mass range, just above the brown dwarf limit, has the lowest multiplicity fraction of $\sim$ 16% and a clearly declining MF with lower mass.

Figure 3.12 shows the distribution of mass ratio q, and log(separation) for the same mass ranges. The lowest mass range has bias towards a q of 1 i.e. near equal-mass components, and a smaller peak separation of $\sim$ 7 AU although the sample size for the lowest mass range is fairly small.

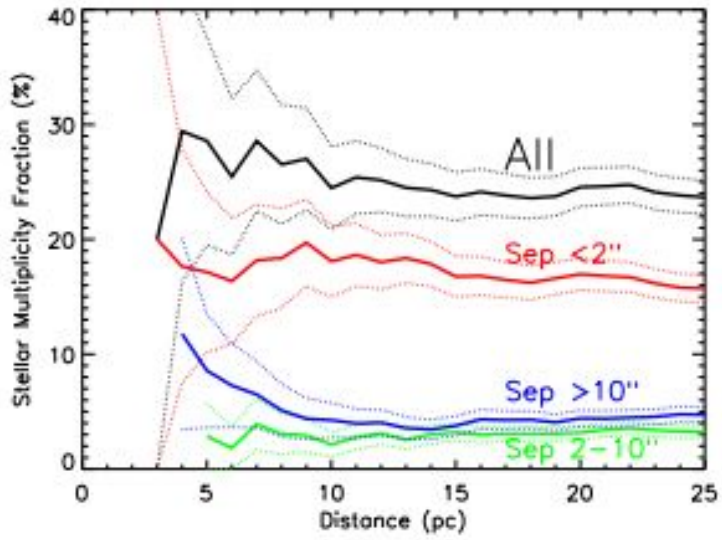

Figure 3.10: Multiplicity fraction showing contribution by angular separation bins as a function of distance. The greatest contribution is from multiple systems with close separations (<2"). Figure from Winters et al. (2019)

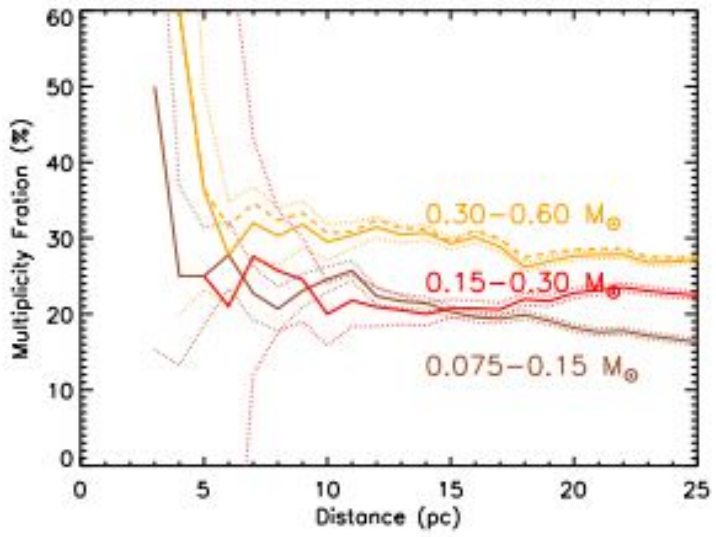

Figure 3.11: Cumulative multiplicity fraction by distance and binned by primary mass range. The declining profile with distance is likely to be the result of unidentified/unresolved multiple systems at the larger distances. The scatter and large errors at short distances are due to small sample sizes at these Figure from Winters et al. (2019*a*)

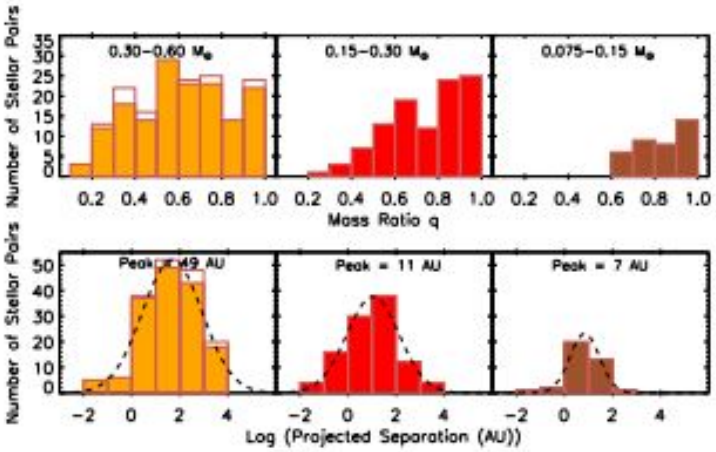

Figure 3.12: Distributions of multiple systems by mass ratio (q) and $\log_{10}$ separation (AU) by mass range bin. This would indicate a stronger preference for equal mass companions for the lower mass stars. Peak separation appears to decline with primary mass also. Figure from Winters et al. (2019*a*)

3.23 The brown dwarf desert

Star systems are thought to form by giant molecular cloud collapse and fragmentation; while giant planets are assumed to form in protoplanetary disks via disk instability or core accretion. Disk instability occurs when massive fragments of a circumstellar disk form self-gravitating clumps which form giant planets. In core accretion solid dust particles in the disk coalesce and grow to such a size that they eventually attracting a gaseous envelope. Binary systems can also result from both these processes. Turbulence within a core leads to multiple stars forming independently but gravitationally bound to each other. Alternatively instabilities in an accretion disk can lead to fragmentation with multiple large objects forming each with own secondary disk. The net result of these distinct processes is a binary system differing only in the relative masses of the constituent components. The formation and subsequent migration of brown dwarfs may involve elements of both processes. From a formation perspective, the onset of hydrogen burning (or deuterium/lithium burning) has little influence on the distribution of masses arising from fragmentation, collapse and accretion since these energetic processes only commence once gravitation collapse is significantly underway. That said, a deficit of brown dwarf companions is observed to FGK stars relative to both giant planetary companions as well as to stellar companions (Lineweaver & Grether 2005, Grether & Lineweaver 2006, Kraus et al. 2008, Evans et al. 2012, Metchev & Hillenbrand 2009) as shown in Figure 3.13.

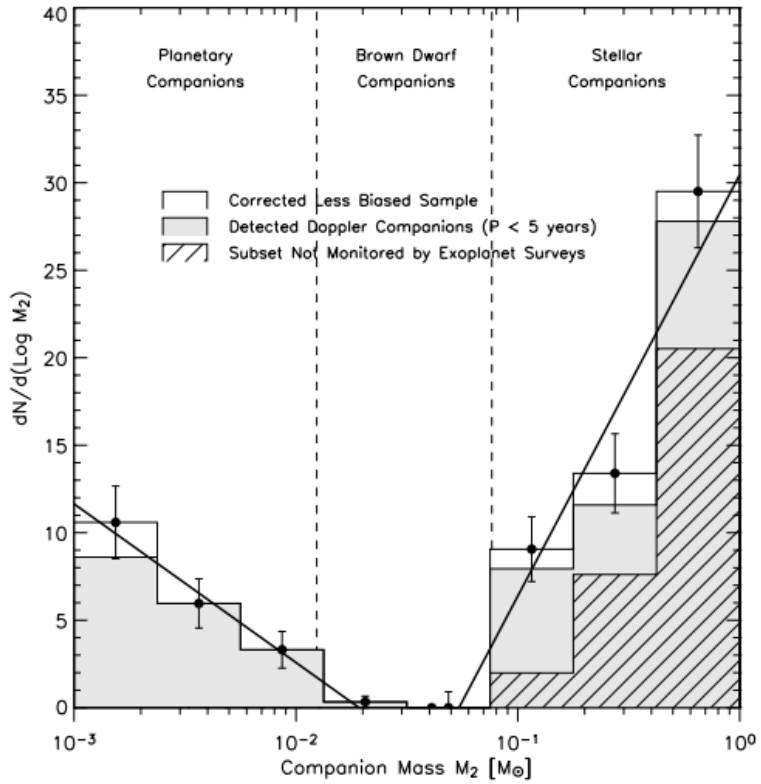

Figure 3.13: Number density of close (separation < 3 AU) companions to sun-like stars as a function of companion mass based on a 50pc sample. Figure by Grether & Lineweaver (2006)

This deficit compared to relative abundance of brown dwarfs and their initial mass function suggests unknown processes are occurring in fragmentation or subsequent migratory processes that are ejecting brown dwarfs from close orbits. Ma & Ge (2014) suggest that the gap is the result of two distinct brown dwarf populations resulting from two different formation mechanisms. Identifying brown dwarf companions is challenging due to the significantly higher luminosity of the primary star so it is difficult to rule out observational bias and selection effects. However transiting brown dwarfs offer the opportunity to study these systems in detail of which ~ 30 are currently known (Carmichael et al. 2019; Carmichael et al. 2021).

Other studies (e.g. Hogg et al. 2020, Steele et al. 2011) searched for such binaries systems in their evolved state i.e. white dwarf - brown dwarf systems. Small stars and brown dwarfs can survive the atmospheric expansion of a more massive stellar companion as it evolves off the main sequence. The friction generated as the companion passes through the thin outer layers of the primary star provides a drag reducing the orbital separation distance. As a result of this process most identified systems white dwarf - brown dwarf systems are very close and tidally locked with extremely short orbital periods. The dayside of the brown dwarf is perpetually exposed to the white dwarf ($> 10{,}000$K) and irradiated by intense UV radiation. The temperature and incident UV radiation difference between the day and night side of the brown dwarf causes orbital period variability in J, H and K_S bands (Casewell et al. 2015). However the variability increases from J to K_s suggesting these emissions are arising from different depths in the brown dwarf atmosphere. Despite their rarity (Casewell et al. 2018) such systems provide excellent probes of brown dwarf atmospheric structure and composition (Longstaff et al. 2017).

3.24 Exoplanetary systems

Mid to late-M dwarfs are known to host planetary systems. Examples include the Kepler-186 (Quintana et al. 2014), LHS 1140 (Dittmann et al. 2017) and the TRAPPIST-1 (Gillon et al. 2016) systems. M dwarfs in particular are found to be favourable host stars for small, rocky exoplanetary systems and are therefore of interest to exoplanetary scientists and astrobiologists. Due to their low luminosity relative to other stars, their habitable zones are much closer to their host star. The relative compactness of these exoplanets and the low mass of the host star mean shorter orbital periods and greater radial velocities. Both these factors are advantageous to radial velocity and transit methods of exoplanetary detection around M dwarfs (Bonfils et al. 2013, Dressing & Charbonneau 2015). Radial velocity surveys are responsible for around 19% of all confirmed exoplanet detections using ground-based instruments such as the HARPS (High Accuracy Radial Velocity Planet Searcher) spectrometer at the ESO 3.6 meter telescope in La Silla Observatory, Chile, and the HIRES spectrometer at the Keck telescopes. The transit method utilises the periodic dimming of light as a planet passes in front of its host star. This method is responsible for around 76% of all confirmed detections using instruments such as the Kepler Space Telescope and TESS (Transiting Exoplanet Survey Satellite).

Despite the apparent abundance of small, close exoplanetary systems around these stars, the high levels of magnetic activity, and resulting UV/X-ray radiation, stellar wind, flares and coronal mass ejections, towards late spectral types (Reiners & Mohanty 2012) would likely have significant impact on the atmospheres of these planets and their potential habitability.

3.25 Atmospheric habitability

While most attention in the search for life in the universe is focused on the surface of rocky planets or subsurface oceans, an interesting and speculative idea is to consider the atmospheres of the coolest (T_{eff} <500K) brown dwarfs as a potentially intriguing site to search for life in the form of aerial biospheres (Lingam & Loeb 2019*b*,*a*). This study estimates an upper bound on the habitable volume of brown dwarfs is around two orders of magnitude larger than rocky, Earth-like exoplanets in the habitable zone. Volume is interpreted as both spatial extent and temporal duration.

Chapter 4

Galactic structure

This literature review primarily relates to the research performed in Chapter 7.

4.1 Galactic Structure

The structure and evolution of the Milky Way has been a continuous area of research for many decades. Our modern view is largely formed from spatial and kinematic observations of the most luminous stars, main sequence and red giants, given their luminosity. Large scale astrometric surveys such as *Gaia* and the Sloan Digital Sky Survey (SDSS) provide accurate six-dimensional position and velocity data, and combined with photometric and spectroscopic surveys we can build up a detailed picture of our own galaxy.

As well as star counts and astrometry, we look to photometry to distinguish between different types and temperatures of stars. That said, large scale photometry of the Milky Way is hindered by dust. The Milky Way is awash with large amount of dust which obscures our view particularly in the visible part of the spectrum. Dust is less opaque in the near-infrared region (2-4 μm) which happily coincides with the wavelength emitted by the many of the most common M dwarf stars and brown dwarfs. Much of the interstellar dust itself emits in the mid- and far-infrared as it is warmed by nearby hot stars. Given near-infrared absorption due to molecules in the Earth's atmosphere, galactic structure is best observed from space.

The current accepted view is that the Milky Way is a large, barred spiral galaxy with around 250±150 billion stars and total mass (including dark matter) of 0.8 - 1.5 $\times$ 10^{12} $M_{\odot}$. Estimates of baryonic mass vary as this is an open problem[1] however many estimates converge around $\sim$ 6 $\times$ 10^{10} M$\odot$ (e.g. Flynn et al. 2006; Gerhard 2002). The Milky way is generally assumed to consist of three stellar populations: the thin disk; the thick disk; and the halo[2]. As is believed to be the case with all galaxies, the galactic centre comprises an intense radio source and supermassive black hole, Sagittarius A*. The sun is located around 7.5 kpc from the galactic centre and $\sim$ 20 pc above the galactic plane.

[1]The "missing baryonic mass problem"
[2]Baryonic mass only

4.2 Models of galactic structure

Galactic structure models allow us to calculate the stellar density profile along a given line of sight. Stellar positions and densities are typically described in cylindrical coordinates (R,θ, z) where $R_\odot$ is $\sim$ 8.5 kpc. In addition azimuthal symmetry is applied in the solar neighbourhood such that $\rho = \rho(R, z)$.

An example of a simple multi-component (thin disk, thick disk and halo), 8-parameter model for the Galaxy is shown in equation 4.1. In this case both the radial and vertical density distributions are described by a simple exponential (Covey et al. 2008). This model describes the stellar density profile along a given line of sight in the solar neighbourhood.

$$\rho_{thin} = e^{-\frac{|z|}{z_{thin}}} e^{-\frac{|R|}{R_{thin}}} \tag{4.1}$$

$$\rho_{thick} = e^{-\frac{|z|}{z_{thick}}} e^{-\frac{|R|}{R_{thick}}} \tag{4.2}$$

$$\rho_{halo} = \left(\sqrt{R^2 + (z\frac{a}{c})^2}\right)^{\gamma_{halo}} \tag{4.3}$$

$$\rho_{total} = f_{thin}\left(\frac{\rho_{thin}}{\rho_{thin,z=0}}\right) + f_{thick}\left(\frac{\rho_{thick}}{\rho_{thick,z=0}}\right) + f_{halo}\left(\frac{\rho_{halo}}{\rho_{halo,z=0}}\right) \tag{4.4}$$

Illustrative parameters estimated by Covey et al. (2008) are shown in Table 4.1.

Parameter	Description	Estimated value
f_{thin}	Thin disk stellar density	1 - f_{thick} - f_{halo}
f_{thick}	Thick disk stellar density	5%
f_{halo}	Halo stellar density	0.15%
z_{thin}	Thin disk scale height vertical direction	280 pc
R_{thin}	Thin disk scale length radial direction	2500 pc
z_{thick}	Thick disk scale height vertical direction	900 pc
R_{thick}	Thick disk scale height radial direction	3500 pc
$\frac{c}{a}$	Halo flattening parameter	0.7
γ_{halo}	Halo power law density gradient	-2.75

Table 4.1: Best fit values of galactic structure parameters from Covey et al. (2008).

Methods of counting stars to determine the structure of our galaxy have been used since the early days of modern astronomy. Early models included a disk of Population I stars surrounded by a spheroid of Population II stars. While a reasonable first approximation, more sophisticated models are now used. Lack of data, poor photometric accuracy, small samples and difficulties adjusting for extinction led to unreliable results (Bahcall 1986). However with the advent of modern powerful computers and deeper, more accurate star surveys (e.g. SDSS, *Hipparcos*, *Gaia*), as well as detailed observations of other galaxies, these approaches have been revived. Such approaches (e.g. Bahcall & Soneira 1984) assume a galactic structure model (based on

observing the geometrical structure of other galaxies), determine what the model implies we would observe in terms of number density per magnitude and/or colour interval, and infer the structure parameters using iterative methods.

4.3 The thick disk

The thick disk was first proposed by Gilmore & Reid (1983) where they found that the vertical stellar density for $M_V > 4$ followed an exponential density law with a thin disk component with $z_h \sim 300$pc which dominated for z between 100-1000pc and a thick disk component with $z_h \sim 1450$pc for z > 1000pc.

The current view is that the thick disk is kinematically and chemically distinct from the thin disk and consists of old, low metallicity stars slowly rotating around the galactic centre. It dominates the stellar number density in the range 1 to 5 kpc above and below the galactic plane however the origin and formation of the thick disk remains unknown. Various theories include:

- The result of a merger between the Milky Way and a large dwarf galaxy (Helmi et al. 2018; Myeong et al. 2019)
- Migration of kinetically active stars out of the galactic plane (Loebman et al. 2011; Schönrich & Binney 2009)
- Part of the early formation of the Milky Way (Jones & Wyse 1983; Brook et al. 2004)
- Heating of the thin disk (Lacey 1984; Quinn et al. 1993; Villalobos & Helmi 2008)

Recently data from *Gaia* in combination with large scale spectroscopic data has found evidence of historical large-scale merger events that may have led to the formation of the thick disk and halo. These are the Gaia-Enceladus / Gaia-Sausage event (e.g. Belokurov et al. 2018, Myeong et al. 2018, Helmi et al. 2018) and Sequoia events (Myeong et al. 2019).

The Gaia-Enceladus event was a head-on collision between a Magellanic-sized dwarf galaxy and the early Milky Way with mass ratio of around one to four. This major merger (or mergers) occurred around 8 to 11 billion years ago and heavily shaped the structure of the Milky Way we observe today by giving rise to the thick disk and inner halo. This collision was identified due to its elongated shape in velocity space using *Gaia* data (the 'Gaia-sausage)' as well as the excess of eccentric and retrograde stars in the inner halo (Helmi et al. 2018).

The Sequoia event early in the life of the Milky Way is believed to be distinct from Gaia-Enceladus. It was identified from a number of large retrograde globular clusters that may be from a dwarf galaxy renmant. They have a distinct track in age-metallicity when compared to other Milky Way globular clusters as well as objects associated with Gaia-Enceladus (Myeong et al. 2019).

4.4 Vertical structure of the Milky Way

It is well established that M-dwarfs with masses 0.69 to 0.075 $M_{\odot}$ are the single largest contributor to stellar mass in the Milky Way and therefore excellent probes of number density.

Modern parameterisations of vertical stellar density distribution (e.g. Dobbie & Warren 2020) often include a sech^{α} functional form rather than an exponential to reflect a softening or flattening in the central plane as follows:

$$n(z) = N_0 \left(sech^{\alpha} \frac{|z + z_0|}{z_{thin}} + f sech^{\alpha} \frac{|z + z_0|}{z_{thick}} \right) \tag{4.5}$$

where:
f = proportion of thick disk stars to total number of stars
$N_0(1 + f)$ = mid-plane density
z_0 = height of sun above mid-place[3]

There is ongoing work to refine these models and parameters and determine whether the thin and thick disk represent distinct physical populations (Bovy, Rix, Hogg 2012b).

4.5 Velocity dispersion

In addition to understanding the structure of the Galaxy in terms of number density by colour, luminosity, mass etc, we also would like to understand structural features in terms of velocities, metallicity and age. Stellar kinematics (the movement of stars in the Milky Way) is a major source of information on galactic structure. Velocities are usually measured relative to the Local standard of rest (LSR). This is the mean motion of a hypothetical group of stars rotating in the plane of the Milky Way in the vicinity of the sun. The distance from the centre of the galaxy (R_0) is often assumed to be $\sim$ 8 kpc and the mean rotational velocity of the LSR (V_0) $\sim$ 220 km/s (Sofue 2017).

In order to measure stellar velocities it is also necessary to know the solar peculiar motion, or motion of the sun relative to the LSR. The solar peculiar motion is described by the three velocity components: $U_{\odot}$, the velocity in the direction of the Galactic Center; $V_{\odot}$ the velocity in the direction of Galactic rotation; and $W_{\odot}$, the velocity in the direction of the North Galactic Pole. A recent measurement of the solar pecular motion by Ding et al. (2019) using *Gaia* DR2 found $U_{\odot}$ of 8.63±0.64km/s, $V_{\odot}$ of 4.76±0.49km/s, and $W_{\odot}$ of 7.26±0.36km/s.

Such characteristics are required to form an understanding of the formation and evolution of the Milky Way. It has been known for a long time that the velocity dispersion of stars in the solar neighbourhood increases on average with age. The velocity dispersion of a given stellar type is defined as:

$$\sigma_i \equiv \langle (v_i - \langle v_i \rangle)^2 \rangle^{1/2}$$

[3]Median of published estimates 17.4±1.9pc (Karim & Mamajek 2017)

Due to the difficulty in obtaining accurate ages for stars, the observational age-velocity dispersion relation remains poorly constrained and often suffers from an age-bias towards brighter and younger stars. The age-velocity dispersion relation is often described using a simple power law as follows:

$$\sigma(\tau) \propto \tau^{\beta}$$

or in the vertical direction,

$$\sigma_W(\tau) \propto \tau^{\beta_W}$$

where τ is age and β or β_W the exponent of the velocity component in the vertical z-direction. Hänninen & Flynn (2002) include a summary of empirically derived values for β in the range 0.25 and 0.6. Recent observational values for α include 0.35 (Aumer & Binney 2009), 0.33 (Binney et al. 2000) and 0.34 (Nordström et al. 2004). Velocity dispersion in the vertical direction σ_W is generally found to be higher than σ_U, σ_V, and σ_{tot}. Recent estimates range from 0.375 to 0.47 (e.g. Aumer & Binney 2009, Binney et al. 2000, Just & Jahreiss 2007). This relation between age and velocity dispersion suggests a heating mechanism by which velocity dispersion increases over time.

Theoretical models predict a range of values for β dependent on the underlying assumptions: $\beta_z \sim \frac{1}{4}$ (Lacey 1984, Hänninen & Flynn 2002), $\beta \sim \frac{1}{3}$ (Spitzer & Schwarzschild 1953), and $\beta \sim \frac{1}{2}$ (Wielen 1977, Fujimoto 1980). The age-velocity relation is explained using disk heating caused by gravitational perturbations of non-axisymmetric galactic structures, such as the spiral arms and central bar, giant molecular clouds (Spitzer & Schwarzschild 1951, Spitzer & Schwarzschild 1953) as well as satellite galaxies (Aumer et al. 2016, Hänninen & Flynn 2002) although this is far from being fully understood.

Binney & Merrifield (1998), Aumer & Binney (2009) and Binney et al. (2000) showed that the velocity dispersion in each principal direction[4] centred on the sun is a function of $B-V$ for main sequence stars. They found that velocity dispersion as a function of $B-V$ increases to a maximum around $B-V=0.6$ and then decreases slightly to an approximately constant for redder colours. This is explained in terms of the age profile of the stars. The bluest stars are relatively young since many of the older stars will have evolved off the main sequence. As a result the average age of stars in the bluest colour bins will be relatively low. On the other hand stars redder than $B-V \sim 0.6$ will contain stars of all ages as even the oldest star will still be on the main sequence.

4.6 Age of the solar neighbourhood

The universe is around 13.8 Gyr old. This estimate is based on the latest Λ-CDM cosmological models and data from the *Planck* and WMAP spacecraft. The first stars in the Milky Way

[4] x towards the Galactic Centre, y in the direction of Galactic rotations, z towards North Galactic Pole

began to form around 500 Myr after the Big Bang. How do we determine the age of our Galaxy and the stars in the solar neighbourhood? Various approaches have been adopted to estimate this age.

1. Isotope ratios predicted by nucleosyntheis and decay rates imply a lower limit to the age of the solar neighbourhood of $\sim$ 9Gyr (e.g. Morell et al. (1992) used thorium abundances in 20 solar-like stars)

2. Comparing the white dwarf luminosity function to theoretical cooling models sets a lower limit on age (e.g. Leggett et al. 1998; Kilic et al. 2019).

3. The lifetime of G and F stars are comparable to the age of the solar neighbourhood. Measuring the luminosity and colour of a sample of individual F stars, metallicity can be accurately measured and then the age determined with an age-metallicity relation (Ng & Bertelli 1998).

4. Fitting an open cluster (of approximately fixed age) to theoretical isochrones on a colour-magnitude diagram can determine the age of the cluster and set a lower bound to the age of the solar neighbourhood. A study by Carraro et al. (1999) found this age to be at least 10Gyr.

5. Fitting isochrones to a sequence of subgiant stars in a colour-magnitude diagram. Using this approach (Jimenez et al. 1998) estimated the minimum age of solar neighbourhood to be 8Gyr.

6. Using the relation that velocity dispersion increases with age, kinematic data provided by *Hipparcos* and, more recently *Gaia*, allow the analysis of velocity dispersion as a function of colour to be used to accurately model the star formation history and estimate age (Aumer et al. 2016). A study (Binney et al. 2000) using 12,000 main sequence stars and subgiants from *Hipparcos* estimates the age of the solar neigbourhood to be 11.2 $\pm$ 0.75Gyr.

The coolest main sequence stars, ultracool dwarfs and brown dwarfs comprise a significant proportion ($>>$ 50%) of the stellar population by number in the solar neighbourhood and as such provide an interesting and alternative population of objects to study galactic structure and evolution. In addition to their ubiquity, their long lifetimes (much longer than the lifetime of the Universe) means that every ultracool dwarf ever formed is still around today. Unfortunately their relatively low luminosity means that observing these objects at the distances required for galactic studies of the Milky Way is not achievable with current instrumentation. For this reason we use low-mass FGK dwarf stars for our research on galactic structure.

In section 7, we use the latest *Gaia* EDR3 data to prepare volume-complete, colour-dependent cylindrical volumes of stars to determine the vertical density distribution close to the galactic plane. Using our structural parameters such as the thin disk scale height as a function of colour and PARSEC isochrones, we model the evolution of a population of stars by colour bin and directly determine the star formation history of the solar neighbourhood.

Chapter 5

Late-M and early-L field dwarf characteristics

This chapter has appeared as a published paper: Laithwaite & Warren (2020). Section 5.8 then extends this analysis to the early-L dwarfs and this was used in Warren et al. (2021).

5.1 Introduction

The luminosity function is a fundamental property of the population of stars. The measurement of the field luminosity function of ultracool dwarfs, spectral type M7 and later, has proved difficult (Cruz et al. 2007, Reylé et al. 2010, Bardalez Gagliuffi et al. 2020). The main bottleneck in this work used to be the measurement of distances, but with the release of *Gaia* DR2 (Gaia Collaboration et al. 2018*b*) this is no longer the case. Instead the limiting factor is the time involved in spectroscopic identification of candidates. The situation for hotter stars is completely different. For these more luminous stars large samples of dwarfs with accurate $G_{BP} - G_{RP}$ colours, which may be transformed to luminosities, may be selected from the *Gaia* database. While there are in fact large numbers of ultracool dwarfs detected by *Gaia*, at high S/N, very few have accurate *Gaia* colours: at $G = 20$ typical uncertainties are $\sigma_G = 0.01$, but for G_{BP} and G_{RP} the uncertainties are 20 times greater (Gaia Collaboration et al. 2018*b*). This means that for measuring the luminosity function, selecting samples using *Gaia* data alone is not effective, since the spectral types (equivalent to luminosity) cannot be determined accurately.

The current state of the art for measurement of the luminosity function, for the spectral range from M7 to L5, is the study by Bardalez Gagliuffi et al. (2020) who used a volume-limited sample of 410 dwarfs within 25 pc of the Sun. This sample is still quite moderate in size, but increasing the size by an order of magnitude is not feasible using the conventional route of measuring spectral types using spectroscopy. An alternative approach is to determine spectral types using accurate multiband photometry. Skrzypek et al. (2015) developed the *phototype* method, which employs 8-band $izYJHKW1W2$ photometry, to measure accurate spectral types without spectroscopy. They applied the method to produce a sample of 1361 L and T dwarfs brighter than $J = 17.5$ (Skrzypek et al. 2016). Ahmed & Warren (2019) extended

this work to earlier spectral types and produced a sample of 33 665 M7 to M9.5 dwarfs, to the same magnitude limit. The accuracy of the spectral typing is better than one spectral sub-type, and is competitive with spectroscopy.

The *phototype* method has increased the size of samples of ultracool dwarfs with accurate spectral types by an order of magnitude. These samples can be matched to *Gaia* to produce larger volume-limited samples than existing. The *phototype* samples cited above reach larger distances than *Gaia* for ultracool dwarfs, primarily because they are selected in the near-infrared. The volume of the *phototype* samples can therefore be maximised by using a calibration between spectral type and luminosity, rather than employing the *Gaia* distances directly. This will be useful, for example, in investigating the local vertical structure of the disk of the Milky Way.

The best existing calibration of the relation between absolute magnitude and spectral type for ultracool dwarfs comes from the study of Dupuy & Liu (2012), who used pre-*Gaia* ground-based parallaxes, covering the spectral range M6 to T9. They derived polynomial relations between absolute magnitude and spectral type, for several photometric bands, but the number of sources remains relatively small, ~ 10 per subtype. The principal goal of this chapter is to use *Gaia* parallaxes to determine an improved calibration between spectral type and absolute magnitude for spectral types M7 to M9.5. This measurement involves identifying unresolved binaries within the sample, since they will appear as apparently overluminous sources. We therefore have expanded the analysis to include a measurement of the multiplicty of M7 to M9.5 dwarfs. To quantify the multiplicity requires a careful consideration of selection biases involved in matching a magnitude-limited sample to *Gaia*.

Two key parameters used to describe multiplicity are the frequency of multiple systems (MF) and the companion frequency (CF). The MF is the frequency of multiple systems as a proportion of the total number of systems. The CF is the average number of companions per system and can exceed 100%. There is a well-known trend of decreasing MF and CF with primary mass (Duchêne & Kraus 2013*b*). This trend continues towards the lowest masses, from early M down to the ultracool dwarfs, types ≥M7. An additional important property is the distribution of mass ratios. Defining q as the mass ratio $\frac{M_{\rm sec}}{M_{\rm prim}} \leq 1$, it is common to characterise the distribution of mass ratios as a power law (Duchêne & Kraus 2013*b*)

$$f(q) \propto q^{\gamma}\,, \tag{5.1}$$

which applies over the range $0 < q < 1$. A large value of γ, a "steep" index, e.g. $\gamma > 5$, implies that the components of most binaries are of approximately equal mass.

We now summarise some of the main recent surveys for multiplicity for cool and ultracool primaries. A survey by Close et al. (2003) of 39 M8.0 to L0.5 stars found a MF of $15 \pm 7\%$ for separations greater than 2.6AU. Gizis et al. (2003) analysed 82 nearby field late M and L dwarfs using the Hubble Space Telescope and estimated a MF of $15 \pm 5\%$ for separations in the range 1.6 to 16 AU. **?** undertook an extensive Bayesian investigation of ultracool dwarfs finding a best fit CF (approximately equal to MF, because dominated by binaries) of ∼20-22%, for types M6 and later, with a wide binary frequency, defined as separation distance>20AU, contributing no

more than 1-2%. Law et al. (2008) found a MF of 13.6 $^{+6.5}_{-4}$ from a sample of 77 field M dwarfs from M4.5 to M6.0. Dieterich et al. (2012) calculated a MF for M0-M9 dwarfs of $10.3^{+3.4}_{-2.1}$%, for separations of $5 - 70$AU, based on 126 systems within ~ 10 pc of the sun. A similar survey by Ward-Duong et al. (2015) found a binary fraction of 23.5 ± 3.2% for a sample of 245 K7-M6 dwarfs within 15pc over separations from 3AU to 10,000AU. Some of these surveys provide only lower limits to the total MF, as they are not sensitive over some separation ranges. Many of these results also depend on complex corrections for incompleteness.

The largest recent study of the multiplicity of M dwarfs is the analysis of a volume-limited survey of 1120 M dwarf primaries within 25 pc by Winters et al. (2019*a*). They estimated a MF of 26.8 ± 1.4% (23.7% before correction for incompleteness), nearly all in singles or binaries, with only 0.3% being in triples or higher order systems. The MF declines with mass, and the measured MF for M dwarfs of mass $0.075 - 0.15 M_{\odot}$, uncorrected for incompleteness, is 19.8 ± 3.6%. This corresponds to the spectral range M4 to M9. Applying the same correction factor implies a true MF of 22.4 ± 4.1% for this mass range, in agreement with the measurement of **?** of $20 - 22$%, cited above. The survey is limited to stellar companions of M dwarf primaries i.e. companions down to L2. There is a trend towards higher average mass ratios for lower mass primaries. This could be in part because brown dwarf companions are excluded, but they argue that including brown dwarfs would make little change to this trend. This trend towards equal mass ratios at the bottom of the main sequence agrees with the conclusion of Duchêne & Kraus (2013*b*) who argued that the flatter value of the power-law index of the distribution of mass ratios, $\gamma = 1.8^{+0.4}_{-0.6}$, measured by **?**, implies too many binaries with $q \leq 0.7$, and that the very steep value $\gamma = 4.2 \pm 1.0$ measured by Burgasser, Kirkpatrick, Cruz, Reid, Leggett, Liebert, Burrows & Brown (2006) is more likely to be appropriate for very low-mass stars.

In this chapter we match the large *phototype* sample of M7 to M9.5 stars of Ahmed & Warren (2019) to *Gaia* DR2, to determine the relation between absolute magnitude and spectral type, as well as the MF, over this spectral range. Almost all multiple systems in the sample are observed as unresolved, and are identified by virtue of being overluminous. To obtain an unbiased estimate of the MF requires selecting a volume-complete sample. For a given spectral type, the selection of appropriate upper and lower distance limits to define a sample that is unbiased with respect to multiplicity requires a careful consideration of: the flux limits of the sample of Ahmed & Warren (2019); the flux limits of the *Gaia* sample of sources with parallaxes; and the fact that unresolved multiple systems are brighter than single sources. Furthermore because luminosity is a strong function of spectral type, the optimal upper and lower distance limits that maximise sample size vary strongly with spectral type. We solve this problem by using the colour $G - J$ as a proxy for spectral type (or luminosity), defining upper and lower distances limits as a function of $G - J$. As we show later the $G - J$ colours are very accurate for this sample. The long baseline from G to J means that the colour range from M7 to M9.5 is large $\Delta(G - J) \sim 1$.

The layout of this chapter is as follows. In section 5.2 we describe the sample of Ahmed & Warren (2019) and the matching to *Gaia*. In section 5.3 we explain the principles of selecting a volume-complete sample as a function of $G - J$ from the *Gaia* matched sample. In section 5.4 we provide the details of applying this procedure to the *Gaia* matched sample, and in section

5.5 we use a maximum-likelihood method to determine the MF, as well as the relation between M_J and $G - J$, and convert this to a relation between M_J and spectral type. In section 5.6 we compare our results on M_J as a function of spectral type, and the measured MF, against previous determinations, and we analyse the mass ratios of the stars in the unresolved binary systems. We summarise in section 5.7.

5.2 Parent sample of M7 - M9.5 dwarfs

This study uses the homogeneous sample of M7 - M9.5 dwarfs presented by Ahmed & Warren (2019). The sample comprises 33 665 sources over an effective area of 3 070 deg^2, with magnitude limits $13.0 < J(Vega) < 17.5$, on the MKO system. The sample was shown to be effectively complete except for a bias in the classification of rare peculiar blue or red objects that it is estimated affects $\sim 1\%$ of sources. The sample is classified to the nearest half spectral subtype using the *phototype* method applied to *iz* SDSS photometry and *YJHK* UKIDSS photometry. This classification was shown to be accurately calibrated to the BOSS Ultracool Dwarf (BUD) spectroscopic sample (Schmidt et al. 2015*a*), with precision better than 0.5 subtypes rms (Ahmed & Warren 2019). From this sample we eliminated the 108 sources identified as peculiar, where the best template fit has $\chi^2 > 20$, which removes many of the subdwarfs in the sample. The sample is characterised by high S/N. For example the median and 90% quantile photometric uncertainties in the J band are 0.016 and 0.028 respectively.

We matched this sample to the *Gaia DR2* database selecting the nearest source within a $3''$ matching radius, and after adjusting for the average parallax zero-point shift of 0.029 mas (Lindegren et al. 2018), we calculated distances by a simple inversion of parallax i.e. $d\ (pc) = 1000/\varpi_{adj}$. We note the concern of Bailer-Jones (2015) that a simple inversion of *Gaia* parallaxes can introduce distance inaccuracies for parallax errors $\gtrsim 20\%$. Below we show (Figure 5.4) that our final sample has parallax errors $< 10\%$ (i.e. parallax over error > 10) and therefore this approach is justified. At this point we limited the sample to sources with positive parallaxes, and distances < 1 kpc. Sources at larger distances are obvious mismatches, based on the absolute magnitudes of Dupuy & Liu (2012), given the sample magnitude limit[1]. This initial sample contains 14 434 sources ('the matched parallax sample').

5.3 Method

In the section we explain the principles of selecting a large sample of ultracool M dwarfs with accurate distances, that is fully representative of the multiplicity of the population. This turns out to be a difficult problem. Our solution is to select using distance limits that are a function of $G - J$ colour. The principal difficulty is to do with the sharp decrease in luminosity in the *Gaia* G band with spectral type, meaning that the *Gaia* distance limit falls sharply from M7 to

[1]Mismatches can occur, for example, when the M star is blended with a close neighbour of earlier spectral type. This can be a problem in *Gaia* because of the shorter effective wavelength of the G filter, compared to the $izYJHK$ filters used in the original selection.

M9.5. We will show later that the absolute magnitude in the G band of a M9.5 dwarf is 2.2 mag. larger than for a M7 dwarf. This means that the volume surveyed by *Gaia* for M9.5 dwarfs is smaller than for M7 dwarfs by a factor of 20. Therefore if we took the same distance limit for M7 dwarfs as for M9.5 dwarfs the resultant sample would be unnecessarily small. To obtain a large sample we need a distance limit that varies with spectral type.

Over the bands used *izYJHK* the colours are all approximately linearly related (e.g. Fig. 1 in Ahmed & Warren (2019)). This means that the accuracy of the spectral classifications from colours is maximised by maximising the wavelength range and minimising the photometric errors. Because of the accuracy of the *Gaia* G-band photometry and the UKIDSS J-band photometry, and the large wavelength range, the $G-J$ colour provides an excellent approximation to spectral type, or luminosity. We now explain how we use upper and lower distance limits that are a function of $G-J$ to select a volume-complete sample of ultra-cool M stars that is representative of the multiplicity of the population. The selection relies on knowing the relation between M_J as a function of $G-J$, but since this is something we want to measure from the sample, the process is iterative. We start with an approximate measure of the relation, define the sample using it, refine the estimate, and iterate. The process converged after only one iteration.

The selection is explained by reference to Fig. 5.1. The $G-J$ range plotted is the colour range for M7 to M9.5 stars. In this discussion we assume that the distances, from *Gaia*, are accurate. We discuss the effect of the parallax errors when considering the actual sample in §5.4. Based on Winters et al. (2019*a*) we neglect triple and higher systems. Therefore point sources will comprise single sources, and unresolved binaries. For binaries the maximum luminosity will correspond to equal masses for the primary and secondary. We want to ask the question over what region of this plot are all sources on the sky (single or binary) included in the matched parallax sample. Initially assume that at any particular $G-J$ colour there is negligible spread in M_J. Then, using the relation between M_J and $G-J$, we can plot the lower and upper distance cuts for single sources at the sample magnitude limits $J=13$ and $J=17.5$ (solid blue lines). Similarly we can plot the same limits for equal mass binaries (dashed blue lines) i.e. a binary of the same apparent magnitude as a single is in fact located at a distance $\sqrt{2}$ greater. This says that the original sample of Ahmed & Warren (2019) is only complete within the volume defined by the lower dashed blue line and the upper solid blue line. Equal-mass binaries will be missing below the lower limit because brighter than $J=13$, and single stars will be absent above the upper limit because fainter than $J=17.5$.

We show in section 5.4.1 that the *Gaia* DR2 sample of sources with parallaxes is highly complete down to $G=20$ i.e. essentially all sources brighter than $G=20$ will appear in the *Gaia* database, but the database becomes progressively incomplete fainter than $G=20$. If we know M_J as a function of $G-J$, we also know M_G as a function of $G-J$. In this way we can plot the distance completeness limits for single and binary sources corresponding to $G=20$. These are plotted as solid and dashed yellow lines respectively. The bright limit of *Gaia* is so bright that it is not relevant to defining a volume-complete sample.

The result of this analysis shows that the matched parallax sample is complete for all singles and binaries only between the lower blue dashed line (the distance of an unresolved equal-mass

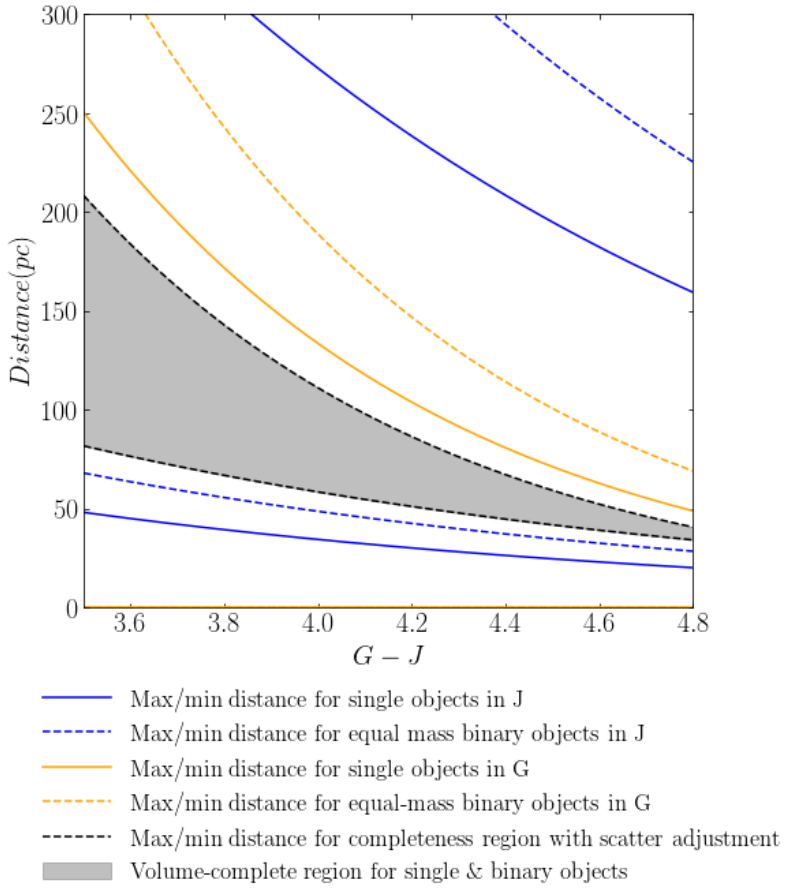

Figure 5.1: Illustration of method to select a volume complete sample as a function of $G - J$ colour, that includes singles and binaries, and accounts for intrinsic spread in M_J at any colour.

binary of $J = 13$) and the solid yellow line (the distance of a single source of $G = 20$). Outside these distance limits some stars of types M7 to M9.5 would have been missed either by the UKIDSS selection or by the *Gaia* selection. Note that the Eddington bias (the bias due to objects scattered across the magnitude limit because of photometric errors) in this sample is negligible, because of the accuracy of the G and J photometry. The random uncertainty for $G - J$ is less than 0.02 mag. for every source in the final sample.

The above summary is still not quite correct because there is an intrinsic scatter in M_J, at any $G - J$, of approximately 0.2 mag. For example an intrinsically underluminous single source at the upper distance limit described above will be fainter than $G = 20$, and so may be missing from *Gaia*. Our final selection squeezes both the lower and upper distance limits by 0.4 mag. With an upper distance limit $d_S(G = 19.6)$ corresponding to singles at $G = 19.6$ and a lower distance limit $d_B(J = 13.4)$ corresponding to equal mass binaries at $J = 13.4$, sources of every type will be included in the matched parallax sample within this volume, regardless of absolute magnitude spread, and whether single or binary. These distance limits (they are not photometric cuts) therefore define a volume-complete sample. A sample selected within these limits will be representative of the population in terms of multiplicity, assuming the multiplicity characteristics do not vary strongly within this spectral range.

5.4 Creation of the volume-complete sample

5.4.1 The *Gaia* G magnitude limit

The *Gaia* G-band limit down to which essentially all sources have a parallax in the DR2 database is a crucial quantity for establishing the upper distance limit for a volume-complete sample (as explained in section 5.3). The source counts for sources with parallaxes in DR2 peaks a little fainter than $G = 20$ (Fig. 2, Gaia Collaboration et al. 2018*b*), but this is only an approximation to the completeness limit. What is needed is to measure the recovery fraction as a function of G, for a sample with accurate G photometry, and a distribution in G extending, say, to $G = 21$. While this may appear difficult because the G band is unique to *Gaia*, we can in fact create such a sample using the sample of Ahmed & Warren (2019) itself, even though many of the sources are not detected in DR2. This is because the sample is homogeneous, and has high S/N, so we can predict the G magnitudes from their other colours. The method to achieve this is illustrated in Fig. 5.2 which plots $G - J$ against $i - K$ for sources in the matched parallax sample. We fit a cubic polynomial to this relation, and the best fit curve is as follows:

$$G - J = 1.151 + 0.462\ (i - K) + 0.142\ (i - K)^2 - 0.019\ (i - K)^3\ .$$

We have then used this relation to predict the G magnitudes of the full sample of Ahmed & Warren (2019) from the $i - K$ colours. The accuracy of the predicted G magnitudes is set by the accuracy of the $i - K$ colours, the intrinsic scatter in the relation, and the gradient of the relation (the J uncertainties are very small in comparison). We find that the accuracy of the $i - K$ colours dominates over the intrinsic scatter in the relation. By this means we can

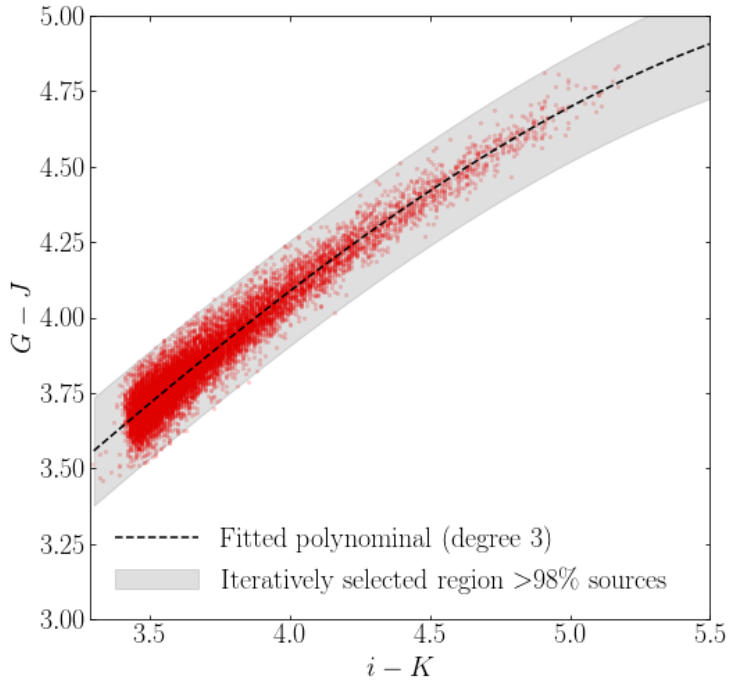

Figure 5.2: Colour-colour relation $G-J$ against $i-K$ for the matched sources in the sample. An iteratively derived polynomial relation of order 3 (black dotted line) is shown with rms = 0.053. Outliers, dominated by mismatches, representing $< 2\%$ of the sample are iteratively removed.

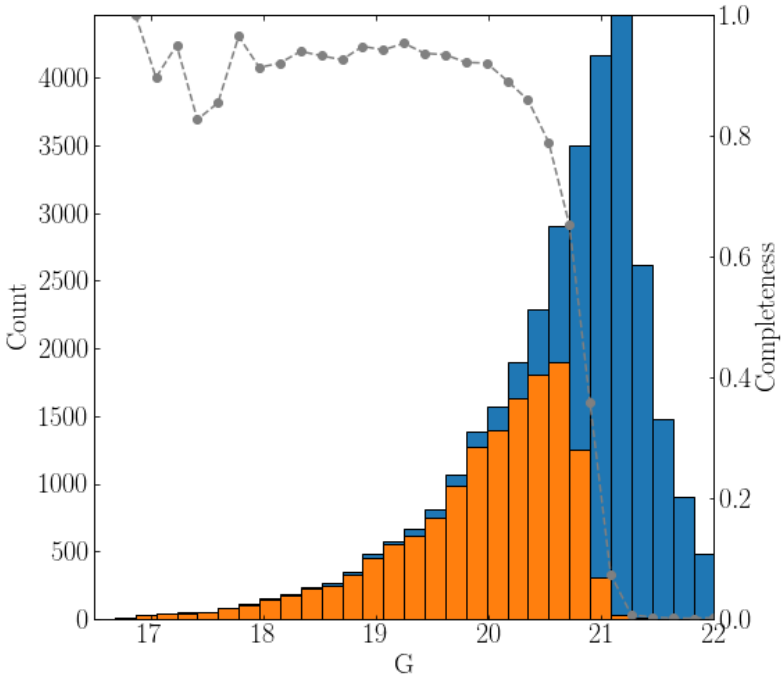

Figure 5.3: Histogram of sources by G for the full sample of Ahmed & Warren (2019) (blue) and the subsample matched with *Gaia* (orange). The dotted line shows the ratio, which is the completeness as a function of G.

establish that the predicted G magnitudes are accurate to substantially better than 0.1 mag. *r.m.s.*, brighter than $G = 21$, which is easily sufficient for our purposes.

With these results we then measure the fraction of sources that matched to *Gaia* DR2 as a function of (predicted) G magnitude. The results are plotted in Fig. 5.3. The blue histogram is the distribution of (predicted) G magnitudes of the full Ahmed & Warren (2019) sample, while the orange histogram represents the matched parallax sample. The completeness is given by the ratio orange/blue and is plotted as the dashed line. The completeness is very high down to $G = 20$, average 94%, then starts to roll over and falls rapidly beyond $G = 20.3$. We therefore treat $G = 20$ as the completeness limit. The small proportion of sources missing brighter than $G = 20$ is associated with issues such as blending mentioned previously, flaws or diffraction spikes, and does not show a clear dependence on G magnitude. Therefore this does not affect the calculation of M_J as a function of $G - J$ or the calculation of the MF. It would only affect the calculation of the space density, which we do not address here, and which could be accounted for by an adjustment to the effective area of the survey.

In Fig. 5.4 we plot the matched parallax sample as green points. For the sake of clarity we show only sources brighter than $G = 20$. The volume-complete subset, within the distance limits $d_S(G = 19.6)$ and $d_B(J = 13.4)$ is plotted as red points, and comprises 2706 sources. As already explained the curves, computed from the relation between M_J and $G - J$, were determined in

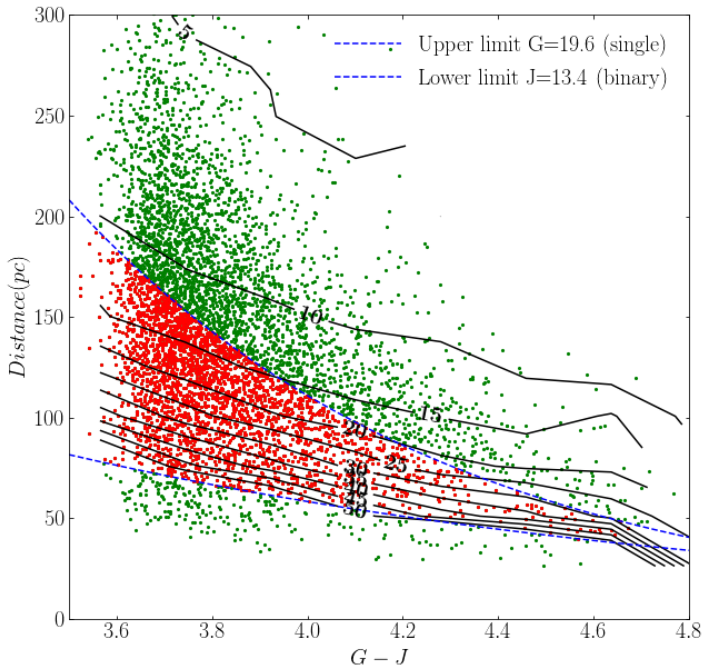

Figure 5.4: Plot of distance against $G - J$ for the matched parallax sample (green points) and the volume-complete subset (red points). The upper and lower distance limits, $d_S(G = 19.6)$ and $d_B(J = 13.4)$, are plotted as blue dashed lines. Black lines are contours of average parallax over error.

an iterative fashion from the sample itself. The derivation of the curve is explained in Section 5.5.

We now briefly consider the possibility that any of the 2706 sources could be matched to the wrong object in *Gaia*, considering that the target may have moved, due to proper motion, and there may then be another nearer source within the 3 arcsec search radius. This secondary source cannot be within 1 arcsec of the target position as it would be blended in the original survey, and therefore the target would not have been selected. To measure the relevant surface density of *Gaia* sources within the survey region, we shifted the source positions by 1 deg. in RA, and rematched to *Gaia*, finding only 23 matches within the annulus from 1 to 3 arcsec radius. This quantifies the number of potential mismatches, provided the proper motion of the target is sufficiently large. But in the original matching of the 2706 sources, 68% match within 1 arcsec i.e. have small proper motion. This suggests that there could be at most about seven mismatches. Of these, some would be excluded by the distances cuts. So we may conclude that the number of potential mismatches is negligibly small and can therefore be ignored.

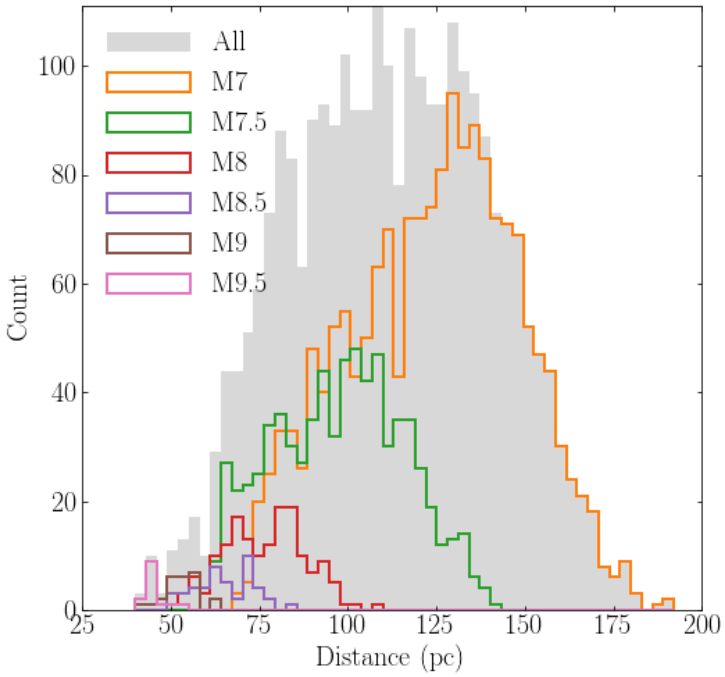

Figure 5.5: Histogram of volume-complete sample by distance (pc) and spectral type.

5.4.2 Properties of the volume-complete sample

The numbers of sources of each spectral type in the volume-complete sample of 2706 sources are provided in Table 5.1. The sample is dominated by types M7 and M7.5 because the volumes sampled are much greater for these types. The distribution of distances, separated by spectral type, and for the whole sample, is plotted in Fig. 5.5. A similar plot showing the distribution of $G - J$ colours is provided in Fig. 5.6. This plot illustrates the fact that there is very little overlap in $G - J$ colour between the different spectral types. While this is not surprising it confirms that $G - J$ is a good proxy for luminosity, for this sample.

The distance limit cuts applied to the sample have eliminated Malmquist bias in the sample. There may be a residual bias in the sample, the Lutz-Kelker bias, depending on the accuracy of the parallaxes. In the DR2 sample the accuracy of the parallaxes depends both on the distances and the S/N, which in turn depends on the G magnitude. The typical accuracy of the parallaxes is illustrated in Fig. 5.4 where we plot contours of parallax-over-error for the sources in the matched parallax sample. For the volume-complete sample the 10, 50 and 90% quantiles of parallax over error are 11, 21, and 47. In the context of Lutz-Kelker bias these values are large, and according to Binney & Merrifield (1998) Lutz-Kelker bias is negligible for such large values.

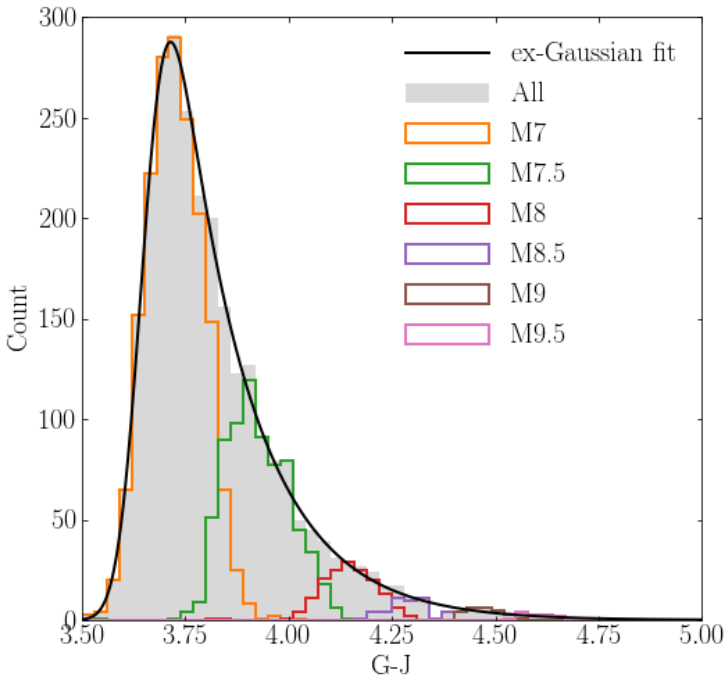

Figure 5.6: Histogram of volume-complete sample by $G-J$ and spectral type. The ex-Gaussian fit is explained in Section 5.5.1.

SpT	N	$G-J$ median	M_J	$M_J(DL)$ mean	$M_J(DL)$ poly
M7	1737	3.72	9.92	10.31	10.65
M7.5	725	3.92	10.21	10.82	10.88
M8	159	4.15	10.56	10.99	11.06
M8.5	46	4.29	10.78	11.40	11.19
M9	25	4.47	11.05	11.80	11.31
M9.5	14	4.69	11.25	11.50	11.41

Table 5.1: Properties of the volume-complete sample as a function of spectral type, listing: number of objects, median $G-J$ colour, absolute magnitude M_J inferred from the median colour and the fitted linear relation. The final two columns list the mean M_J from Dupuy & Liu (2012), and the M_J computed from their polynomial relation.

5.5 Results

5.5.1 Model fitting

The volume-complete sample is shown in Fig. 5.7, plotting M_J against $G-J$. The distribution is dominated by a band sloping down to the right, which comprises the single sources, and for which the relation between colour and absolute magnitude appears linear. Above this sequence there is a sense of a parallel sequence of overluminous sources, which are presumed to be binaries.

To model the distribution of points in this 2D space we assume a linear variation of $G-J=v$ against $M_J=u$, for the singles, parameterised by $v=au+b$. We fit a binary sequence, offset to brighter absolute magnitudes by ΔM, which is a free parameter. The measured value of ΔM should then give an indication of the characteristic luminosity ratio of secondaries to primaries L_s/L_p. Both the singles and binaries are characterised by a Gaussian spread in absolute magnitude, of the same standard deviation σ_M. This simplification is discussed at the end of this section. The fraction of sources that are singles is given by n_1, so the fraction of binaries is $1-n_1$. The variation of the number as a function of $G-J$, plotted in Fig. 5.6, is parameterised by the ex-Gaussian distribution, which is the convolution of an exponential with a Gaussian, and has three parameters: mean μ_{col}, standard deviation σ_{col}, and $K_{col}=\frac{1}{\sigma_{col}\lambda}$, where λ is the exponential rate parameter.

The model therefore has 8 parameters, $a, b, \Delta M, n_1, \sigma_M, \mu_{col}, \sigma_{col}, K_{col}$, plus a normalisation. The number of objects in an area element $dudv$ is $p(u,v)dudv$ where the function $p(u,v)$ is given by:

$$p(u,v)=p(v)\left(\frac{n_1}{\sqrt{2\pi}\sigma_M}e^{-\frac{\left(u-\frac{(v-b)}{a}\right)^2}{2\sigma_M^2}}+\frac{(1-n_1)}{\sqrt{2\pi}\sigma_M}e^{-\frac{\left(u+\Delta M-\frac{(v-b)}{a}\right)^2}{2\sigma_M^2}}\right), \tag{5.2}$$

and $p(v)=\text{ex-Gaussian}(v|\mu_{col},\sigma_{col},K_{col})$.

We adopt broad uniform priors for all the parameters, so the best fit corresponds to the maximum-likelihood solution. The likelihood assumes a Poisson point process (e.g. Marshall et al. 1983). To avoid sensitivity to outliers, after obtaining the best fit, points more than 3σ from the nearest population (i.e. binaries at high luminosities and singles at faint luminosities) were clipped, before iterating. The results of the fit are provided in Table 6.1. In Fig. 5.6 we plot the ex-Gaussian curve as the dashed black line. The linear relation between colour and absolute magnitude for the singles, and offset by ΔM for the binaries, is plotted in Fig. 5.7.

To illustrate the two populations, in Fig. 5.8 we plot the histogram of the horizontal distance from the linear fit, the M_J offset, for all the points. Also plotted are the two Gaussians, for singles and binaries, and the sum of these, which provides a good fit to the histogram. The Gaussian fit to the binaries had no particular physical motivation, and was used simply as a tool in order to extract the colour-magnitude relation for single stars, unbiased by the presence of binaries. Nevertheless the fitted value $\Delta M=-0.73$ is striking. This has a small formal uncertainty of 0.02 and therefore is consistent with the value for binaries of equal mass of $\Delta M=-0.75$. This implies a steep distribution of mass ratios $f(q)\propto q^{\gamma}$ i.e. a large value of γ, and in turn provides

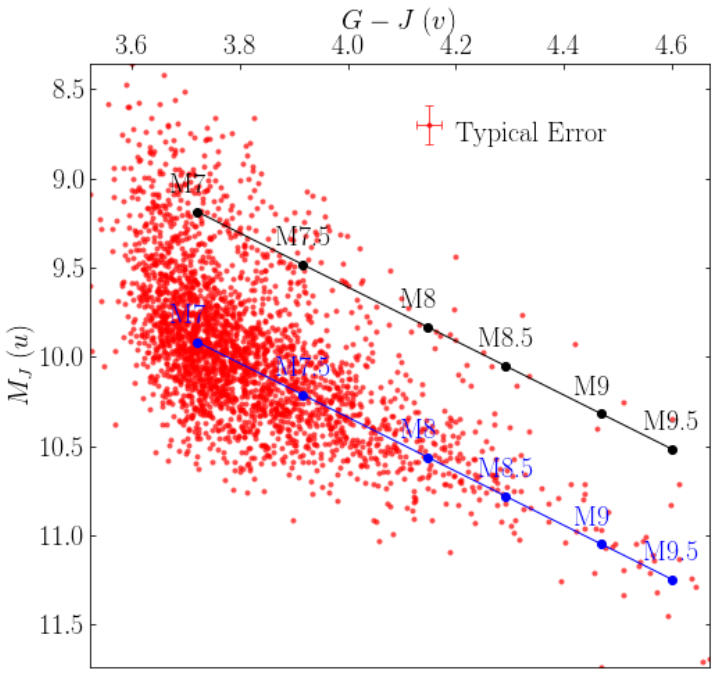

Figure 5.7: Colour-magnitude relation for the volume-complete sample. The blue line is the colour-magnitude relation for single stars, and the black line is the corresponding relation for binaries, as determined by the double Gaussian fit. The points on each line are plotted at the median $G - J$ colour for each spectral type.

2D model parameter	Best fit values
a	0.661
b	−2.832
ΔM	−0.730
n_1	0.855
σ_M	0.246
μ_{col}	3.652
σ_{col}	0.048
K_{col}	3.585

Table 5.2: Best fit values of model parameters from equation 5.2.

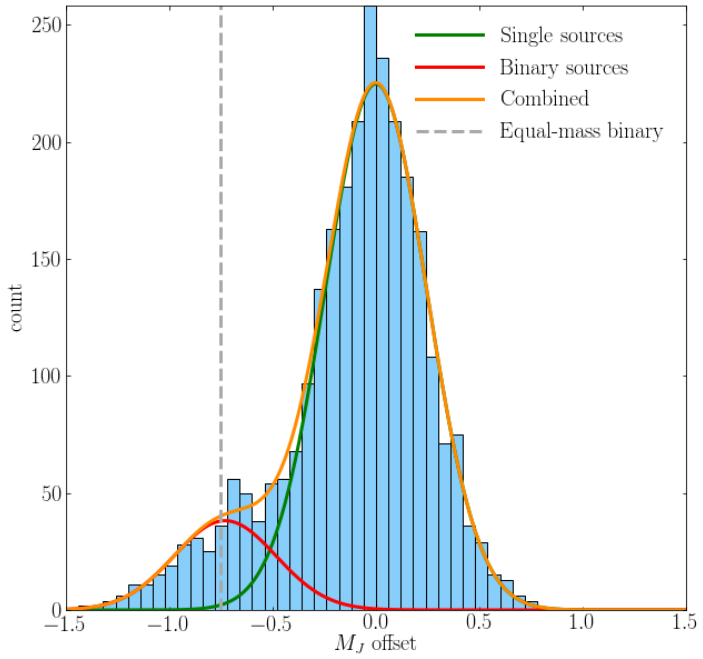

Figure 5.8: Histogram of the absolute magnitude offset from the linear relation for all points. The curves are the Gaussian fit for the population of singles (green) and binaries (red), as well as the sum (orange). The vertical line represents the absolute magnitude offset for a equal-mass binary (grey, dashed)

some justification (after the event) for adopting the same value of σ_M for the singles and the binaries. As a check we reran the fit, with separate values of σ_M, measuring $\sigma_M = 0.276 \pm 0.024$ for the binaries. This is slightly larger but not significantly so. The derived colour-magnitude relation was essentially identical, confirming that the fit is insensitive to the exact details of how the binaries are fit. This discussion nevertheless motivates a careful analysis of constraints on the distribution of mass ratios, which we present in section 5.6.2.

5.5.2 Absolute magnitudes M_J for M7 to M9.5 dwarfs

We compute the absolute magnitudes as a function of spectral type by finding the median colour of each spectral type in the final sample, and computing M_J from the linear relation $M_J = (G - J - b)/a$. The colours and absolute magnitudes are provided in Table 5.1. The best fit quadratic relation between M_J and spectral type (SpT, where e.g. 7 represents M7) is

$$M_J = 2.249 + 1.5061 \times SpT - 0.05882 \times SpT^2 \,. \tag{5.3}$$

Also listed in Table 5.1 are the mean values measured by Dupuy & Liu (2012) as well as the values computed from their polynomial relation. These numbers are very different to our measured

values. In Section 5.6 we investigate the reasons for the differences.

The scatter in M_J, at any particular $G - J$, is $\sigma_M = 0.246$ (Table 6.1). This includes a contribution from the parallax uncertainties as well as a small contribution from the uncertainties in J. Summing the variances of these individual uncertainties results in an average measurement error in M_J of 0.13. Subtracting in quadrature we calculate that the average intrinsic spread in absolute magnitude M_J is 0.21 mag. at any particular $G - J$.

5.6 Discussion

The model fit produced two interesting results. First, the derived absolute magnitudes are quite different to those provided by Dupuy & Liu (2012). Second the offset of the binary population $\Delta M = -0.73$ implies that the binary population is dominated by approximately equal mass pairs. We discuss both of these points in detail in this section. We also provide a value for the total MF for the population, by adding an estimate of the number of resolved binaries to the measured number of unresolved binaries.

5.6.1 Absolute magnitudes M_J compared to Dupuy & Liu (2012)

The discrepancy between the two measurements of absolute magnitudes is illustrated in Fig. 5.9. The red points are our measured values and the dashed red curve is the quadratic fit, eqn 5.3. The green points are the mean values (suspected binaries removed) of the measurements of Dupuy & Liu (2012) and the green curve is their polynomial, of degree five, which is a fit applicable over the range M6 to T9. The larger scatter of the green points compared to the red points is explained by the smaller size of the sample of Dupuy & Liu (2012). There are only 25 sources M7 to M9.5 in their sample with $J(MKO)$ photometry (there are 48 with 2MASS photometry). The average offset is 0.51 mag.

We have confirmed that the discrepancy is not due to systematic errors in the parallaxes of Dupuy & Liu (2012). We matched their sample of M7 to M9.5 dwarfs to *Gaia*. In Fig. 5.10 we plot their distance modulus against the distance modulus from *Gaia* for the 41 objects with good matches, and fit a straight line to the data, assuming that the *Gaia* uncertainties may be neglected in comparison. We increased the parallax uncertainties quoted by (Dupuy & Liu 2012) by a factor 1.8, to achieve $\chi^2_\nu \sim 1$. The linear fit has a slope almost exactly unity, with small offset, indicating that any systematic errors in the parallaxes of (Dupuy & Liu 2012) are at the level of < 0.1 mag. in the distance modulus and therefore cannot explain the discrepancy between our results and theirs, which are at the level of 0.5 mag.

An alternative explanation is that the discrepancy originates in the spectral types assigned to the objects. This corresponds to a horizontal shift in Fig. 5.9. The average slope of the red curve over the spectral range is close to -0.5, meaning that there would need to be a systematic difference of one spectral type between the classifications on average to explain the differences. That is to say, for example, that a star classified M8 in the sample of Dupuy & Liu (2012) would be classified M9 in Ahmed & Warren (2019). This is a surprisingly large difference, but we have

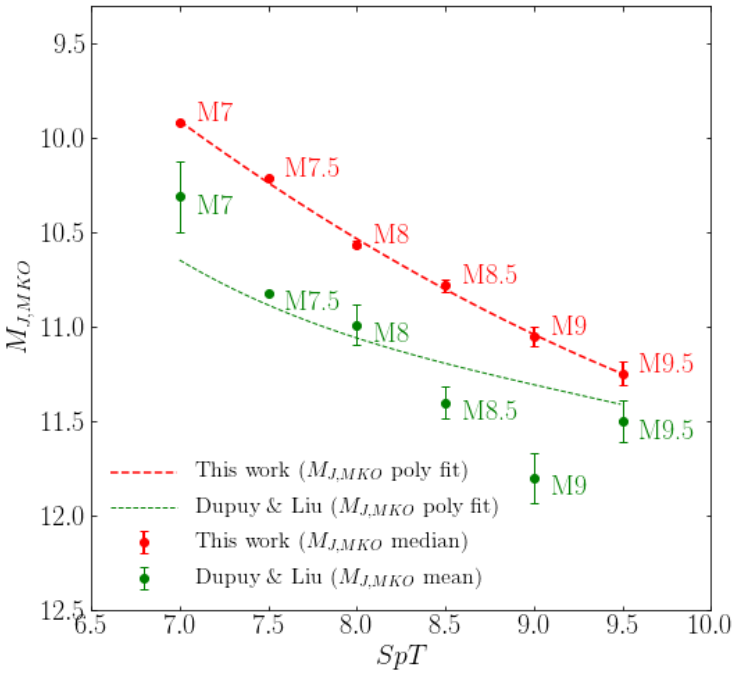

Figure 5.9: Absolute magnitude as a function of spectral type from this work (in red, upper) and from (Dupuy & Liu 2012) (in green, lower). The points are the median (red) or mean (green) value of $M_J(MKO)$ for that spectral type, and the curves are the polynomial relations. The mean (green) values are taken from Table 15 of (Dupuy & Liu 2012) and the uncertainties are the *r.m.s.* values divided by $\sqrt{N}$. No error bar is plotted for M7.5 as there is only one star of this type. The formal uncertainties on the red points are mostly too small to be visible.

not found any obvious explanation.

The spectral types in the sample of Ahmed & Warren (2019), derived from $izYJHK$ colours, are very accurately calibrated to the BOSS ultracool dwarf spectroscopic sample (Schmidt et al. 2015*a*). The BOSS ultracool dwarf sample contains high quality photometric data for 11820 M7 to L8 dwarfs from SDSS DR7, 2MASS and WISE. Schmidt et al. (2015*a*) presented median colours for $i-z$, $i-J$, $J-H$, $H-K_S$, K_S-W1, $W1-W2$ and $W2-W3$ as a function of optical spectral type which was shown to be in good agreement with West et al. (2011). Comparing classifications of objects in common between the two samples, the average difference is 0.05 spectral subtypes, with a dispersion of only 0.6 subtypes (Ahmed & Warren 2019). Our volume-complete sample of 2706 stars includes 449 stars with BOSS classifications. These are classified to one spectral subtype. The median values of M_J for single stars are 10.07, 10.53, and 11.02 for spectral types M7 (310 sources), M8 (120 sources), M9 (19 sources), after eliminating bias from the binary fraction i.e. we took the appropriate quantile assuming a binary fraction of 0.15. These values agree closely with the values in Table 5.1.[2] Therefore the apparent difference in spectral typing is a difference between the BOSS classifications and the classifications used by Dupuy & Liu (2012). Unfortunately there are only a few stars in common between these two samples. Of stars with classifications M6.5 to M9 in Dupuy & Liu (2012), we found 10 matches in the BOSS sample. The average type difference is 0.7 subtypes, in the sense that the BOSS classifications are later. Therefore this small sample provides some support for the idea that spectral typing is the origin of the differences found in absolute magnitude.

The classifications of Dupuy & Liu (2012) come from a variety of sources and some date to a time when the classification of ultracool M dwarfs was in its infancy. The BOSS classifications are homogeneous and use spectra that are subject to uniform quality control, with good sensitivity at long wavelengths. They benefitted also from the existence of standards of L dwarfs, so the calibration is smooth through the end of the M sequence. The BOSS methods for classification are described in West et al. (2011) and Schmidt et al. (2015*a*). Spectra were classified by eye, by a team, with extensive cross checks for systematics. The reason for using visual classification, despite the subjectivity, and the time involved, is that the automated classifications were judged unreliable.

While it appears that the difference between our values of M_J are those of Dupuy & Liu (2012) relate to differences in spectral typing it is not possible to be certain on this without going back to the original spectra used for their classifications. It is sufficient to say that our classifications are on the BOSS system, which has become the *de facto* standard because the sample is homogeneous and has been subject to careful checks for systematics.

5.6.2 The binary mass ratio distribution

The offset $\Delta M = -0.73$ implies that most of the unresolved binaries comprise stars of nearly equal mass, $M_s/M_p = q \sim 1$. This in turn implies a large value of the exponent γ of the

[2]The value of 10.07 for M7 is actually biased to a larger numerical value than the true value, because stars classified M7 by BOSS, but M6.5 by Ahmed and Warren, are not included here, meaning the actual agreement for M7 would be even better. This bias does not affect the M8 and M9 classifications.

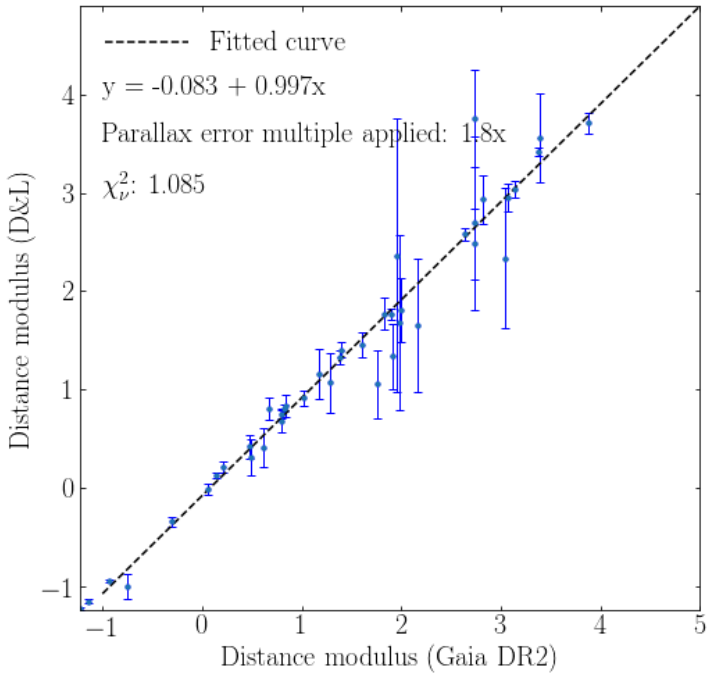

Figure 5.10: Distance modulus (Dupuy & Liu 2012) vs. distance modulus (*Gaia*).

distribution of mass ratios, $f(q) \propto q^\gamma$. This is exacerbated by the steep relation between luminosity and mass for late M dwarfs (Baraffe & Chabrier 1996). To see this, consider a power law relation between luminosity and mass:

$$\frac{L}{L_\odot} \propto \left(\frac{M}{M_\odot}\right)^\beta . \tag{5.4}$$

Then the relation between luminosity ratio and mass ratio of secondary to primary is

$$l = \frac{L_s}{L_p} = \left(\frac{M_s}{M_p}\right)^\beta = q^\beta \tag{5.5}$$

The pdf for l is given by

$$m(l) = \left(\frac{\gamma+1}{\beta}\right) l^{\frac{\gamma-\beta+1}{\beta}} . \tag{5.6}$$

By integrating over the pdf the average value of l is

$$\langle l \rangle = \frac{1+\gamma}{1+\gamma+\beta} . \tag{5.7}$$

We now consider the consequences for γ of the measured offset $\Delta M = -0.73$. We define the parameter $d = \Delta M_J$ which is the horizontal distance of a binary from the linear colour-absolute magnitude relation for primaries plotted as the blue line in Fig. 5.7. Compared to the location

of the primary in this Figure, addition of a secondary shifts the system in both M_J and colour, such that the dependence of d on l is given by

$$d(l) = -2.5 \log_{10} \left(\frac{(1+l)^{1+\frac{1}{a}}}{(1+l^{1+a})^{\frac{1}{a}}} \right) , \tag{5.8}$$

where a, the slope of the colour-absolute magnitude relation, is listed in Table 5.2. As an example an M7-M7.5 binary would have colour $G-J$ of 3.802 and M_J of 9.302, and d of -0.737. The binary combinations of any given primary star in Fig. 5.7 trace an arc running from the position of the single star to the equal-mass binary of the same colour. This relation means that d is relatively insensitive to changes in l for values of d approaching the equal-mass limit.

The mass-luminosity relation becomes very steep for ultracool dwarfs. Using the values of $L/L_\odot$ and $M/M_\odot$ provided in Table 1 of Baraffe & Chabrier (1996), we estimate $\beta = 8$ for the spectral range M7.0 to M9.5. Here L is the bolometric luminosity. The relation for luminosity measured in the J band will be slightly steeper (this may be verified by using M_K, again from Table 1 of Baraffe & Chabrier (1996), and the $J-K$ colours from Skrzypek et al. (2015, 2016)). The significance of the large value of β may be seen by inserting $\beta = 8$ and $\gamma = 8$ into eqn 5.7, which yields $\langle l \rangle = 0.53$. Then the characteristic offset of the binary sequence would be 0.67 mag., from equation 5.8. The measured offset of 0.73 ± 0.02 mag. therefore implies a large value of γ.

It is possible to actually measure γ by fitting to the distribution of offsets in absolute magnitude i.e. the data plotted as a histogram in Fig. 5.8, as follows. Suppose firstly that there is no intrinsic spread in absolute magnitude of stars of a particular mass. Then the pdf of the distribution of stars in the parameter d is

$$p(d) = (1-n_1)g(d) + n_1\delta(d) , \tag{5.9}$$

where $\delta(d)$ is the Dirac delta function, n_1 is the fraction of systems that are single stars (as before), and $g(d)$ is given by

$$g(d(l)) = \frac{m(l)}{\frac{dd}{dl}} . \tag{5.10}$$

Differentiating equation 5.8 gives

$$\frac{dd}{dl} = -\frac{2.5}{\ln(10)} \left(\frac{(1+\frac{1}{a})}{(1+l)} - \frac{(1+a)l^a}{a(1+l^{1+a})} \right) . \tag{5.11}$$

The function $g(d)$ is the pdf for the distribution of binaries over the parameter d, as a function of γ and β, and is defined within the range $-2.5\log_{10}(2) < d < 0$, equivalent to $1 > l > 0$. Examples of $g(d)$ for different combinations of γ and β are plotted in Figure 5.12.

To allow for an intrinsic dispersion in absolute magnitude we convolve $p(d)$ with a Gaussian of standard deviation σ_M, then multiply by a normalisation N and fit to the data, computing the likelihood in the same manner as before. Fixing β, the free parameters are γ, n_1, N, σ_M.

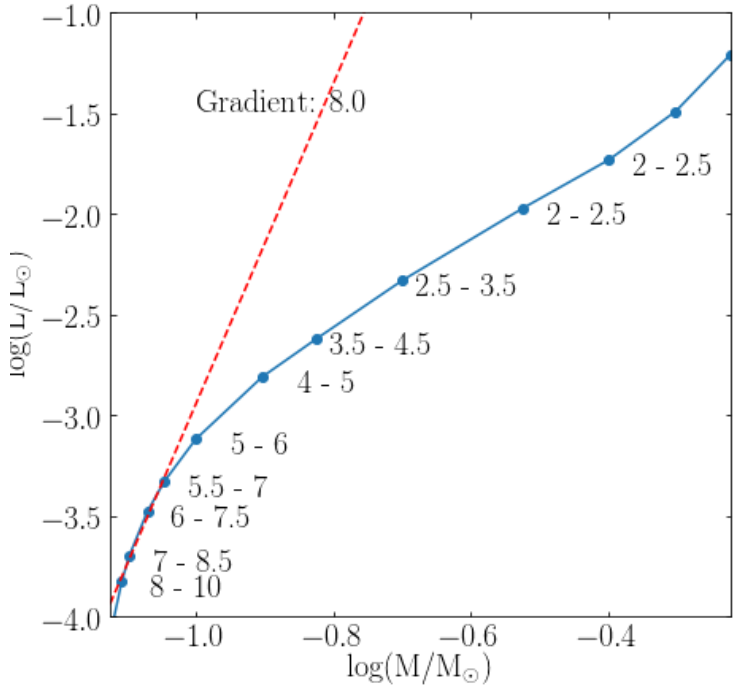

Figure 5.11: Log-log plot of the mass-luminosity relation for M-dwarfs (Baraffe & Chabrier 1996). Note that the data labels refer to the classification range i.e. M1 = 1, M7.5 = 7.5. The gradient of the curve for M≥7.5 is calculated as a linear fit through the relevant data.

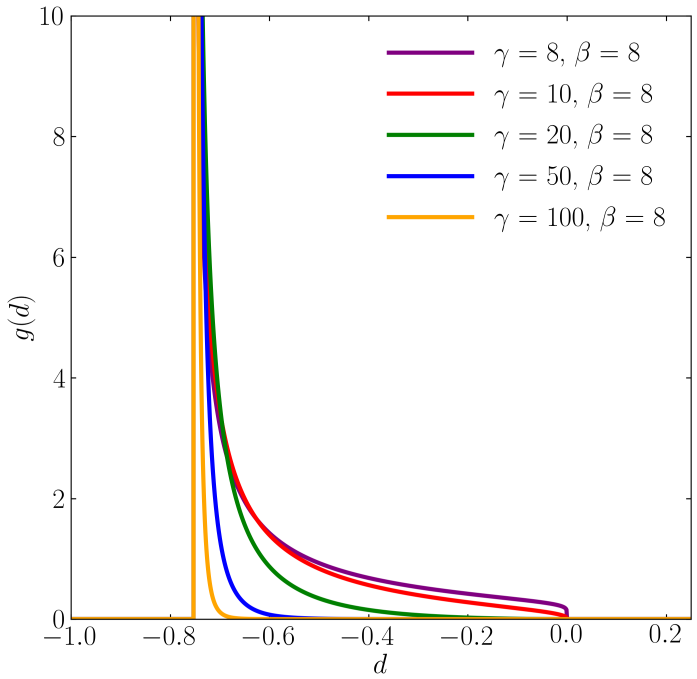

Figure 5.12: The pdf $g(d)$ giving the distribution of magnitude offsets for the binaries plotted for $\beta = 8$ and various values of γ.

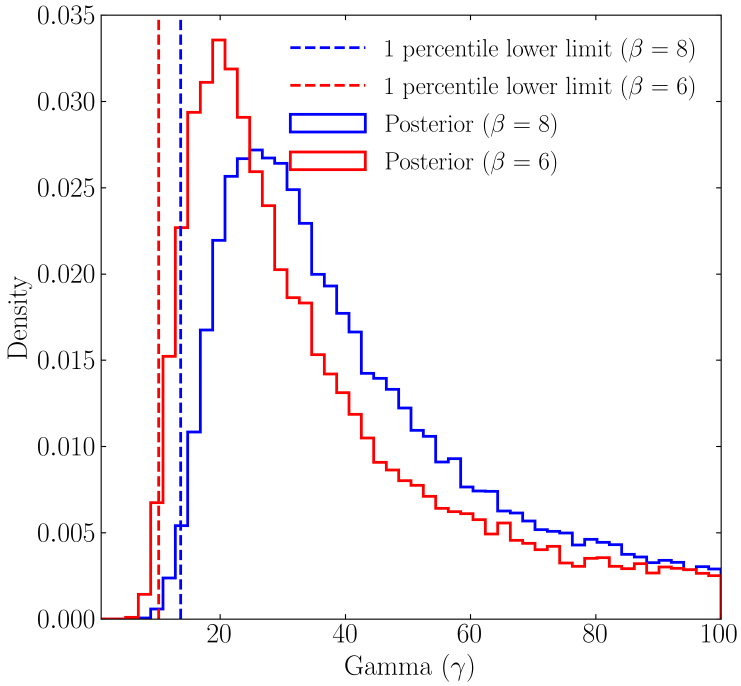

Figure 5.13: The posterior probability for γ for a prior $\propto \gamma^{-2}$, and assuming $\beta = 6$ and $\beta = 8$.

Note that as γ becomes very large $p(d) \rightarrow (1 - n_1)\delta(d + 0.75) + n_1\delta(d)$ and the model becomes a double Gaussian, with the binaries offset by 0.75 mag.

The choice of prior for γ is not straightforward. Because we already know that a double Gaussian with the binaries offset by 0.75 mag. provides a satisfactory fit, this implies that $\gamma = \infty$ is consistent with the data, and all large values of γ will be nearly equally preferred. This is problematic because adopting a uniform prior on γ then leads to a meaningless posterior. Under this condition all that can usefully be achieved is to place a lower limit on γ. A pragmatic approach to this is to think in terms of an alternative parameter $\alpha = 1/\gamma$, and to adopt a uniform prior in this parameter. This is in fact identical to adopting a prior on γ of the form $\propto \gamma^{-2}$. This is the form we have chosen to adopt, with the range $\beta - 1 < \gamma < 100$. We impose a lower limit for γ of $\beta - 1$ because $m(l)$ is undefined at $l = 0$ for lower values of γ. In fact this lower limit does not come into play because the likelihood drops off so steeply as a function of γ well before the limit. The upper limit for γ is arbitrary, and we discuss this point below. For the mass-luminosity relation we conservatively select $\beta = 6$. This is conservative compared to $\beta = 8$ in the sense that it leads to lower values of γ. [3]

The results for the posterior on γ, determined by MCMC sampling, are plotted in Fig. 5.13. The median value for $\beta = 6$ is $\gamma = 29$ and for $\beta = 8$ is $\gamma = 36$. The best-fit value of n_1 is slightly lower at 0.84 than from the double Gaussian fit, while σ_M is almost identical.

[3]Concerning the chosen prior, an alternative might have been to adopt a uniform prior for a parameter $\alpha' = \log(\gamma)$. This is the same as a prior on γ of the form $\propto \gamma^{-1}$, which is less conservative.

Plotting the function it is essentially identical to the double Gaussian plotted in Fig. 5.8. This is as expected, and the median value of γ itself is not particularly interesting or meaningful – it suffices to say that it is very large. More interestingly we find that 99% of the posterior probability lies at $\gamma > 10$ for the more conservative $\beta = 6$ case. Similarly large values for the lower limit on γ were obtained even when we changed substantially the upper limit of the prior and the functional form of the prior. We conclude that $\gamma > 10$ for unresolved binaries in the spectral range M7 to M9.5, and this is the important result from this analysis. Since M_J falls by 0.5 mag. per spectral type, the typical difference in spectral type between primary and secondary is calculated to be less than half a spectral type. In effect unresolved binaries of ultracool M dwarfs are identical twins.

Could the steep measured value of γ be because of a bias arising from how the sample of Ahmed & Warren (2019) was selected? If the secondary were of a different spectral type to the primary would the unresolved binary still be selected, or would it be rejected because of the peculiar colours? It is easy to see that there would be no bias from this effect, because the colours from M7 to L0 lie along a linear sequence over the bands $izYJHK$ used in the selection (Skrzypek et al. 2015, 2016). This means that any binaries with combinations from within this sequence would have colours that lie on the colour sequence, and so would be selected. So there is no bias against unresolved binaries with small values of ΔM.

Although this analysis provides a strong lower limit on γ, it only applies over a limited mass range. This is because of the steep mass-luminosity relation, meaning that this survey is not sensitive to the detection of brown dwarf companions. A small number of unresolved late-M + brown dwarf binaries have been found (e.g. Blake et al. 2008, Biller et al. 2006, Burgasser et al. 2012*a*, Burgasser et al. 2015). In principle the true mass ratio distribution could be bimodal, with an additional peak due to secondaries in the brown dwarf mass range.

5.6.3 The binary fraction

Using the maximum-likelihood solution for n1 based on the $p(d)$ in section 5.6.2, the fraction of binaries is $n_2 = 1 - n_1 = 16.2\%$. This is the MF for unresolved systems, assuming triples and higher do not contribute significantly, as found by Winters et al. (2019*a*). This corresponds to 438 systems. However this neglects resolved binaries. The proportion of resolved binaries is expected to be very small (**?**Winters et al. 2019*a*). Winters et al. (2019*a*) find a lognormal distribution of separations for their lowest mass bin ($0.075 - 0.15 M_{\odot}$) with a mean 7 AU. Given the distribution of distances of objects in our sample, we can compute the expected distribution of angular separations. The median seeing in the UKIDSS LAS data is 0.8 arcsec (e.g. Warren et al. 2007), while in the SDSS data it is 1.3 arcsec. Binaries with separations less than 0.8 arcsec will have been counted in our volume-complete sample. We would expect to detect binaries with separations larger than 1.3 arcsec as resolved. In the range 0.8 arcsec to 1.3 arcsec objects would be missed since the photometry (two single objects in UKIDSS, one merged object in SDSS) would be inconsistent. The predicted number of binaries with separations between 0.8 and 1.3 arcsec is five. We will neglect this minor source of incompleteness. The predicted number

with separations greater than 1.3 arcsec is just two.

To identify secondaries with separation greater than 1.3 arcsec we have made a search around every object in our volume complete sample (which all have accurate distances) for objects within a projected separation of 1000 AU in the parent sample of Ahmed & Warren (2019). Because the distance limits of the parent sample are much greater than for the volume-complete sample, any stars in the spectral range M7 to M9.5 that are companions will be found, as can be seen by reference to the distance limits plotted in Fig. 5.1. We also searched in the sample of L and T dwarfs of Skrzypek et al. (2016), which extends the search to later types, with the same magnitude limits $13 < J < 17.5$. However the upper distance limit falls rapidly with spectral type so this search would not find all companions to primaries in the volume-complete sample. When a potential match was found within the specified angular separation limit, we then checked that the distances matched, using the *Gaia* parallax if available, otherwise the distance computed from the absolute magnitudes in Table 5.1. A further visual confirmation was performed with SDSS DR13 images. Using this method we identified four candidate wide binary pairs where both stars are in the volume complete sample. This increases the number of binaries by four, and at the same time reduces the total number of systems by four, to 2702. We additionally found five candidate wide binaries where the secondary is not in the volume complete sample.

Combining the number of unresolved binaries with our candidate wide binaries, we measure 447 binary systems with an uncertainty of 21 (assuming Poisson statistics) from a total number of 2702 systems, yielding a total binary fraction, equal to the MF, of 16.5±0.8%. This value is similar to but a little smaller than the values $20 - 22\%$ measured by **?** and Winters et al. (2019*a*). Their samples are for spectral types M6 and later and M4 and later, respectively. The small difference is consistent with the trend of decreasing binary fraction with spectral type. Interestingly our binary fraction of 16.5% is close to the value found for L-dwarfs by Reid et al. (2008), suggesting that the M7-M9.5 dwarfs have more similar formation mechanisms to the L-dwarfs than to the higher mass, early M-dwarfs (Whitworth et al. 2007).

5.7 Summary

We have derived a volume-complete sample of 2706 M7.0-M9.5 dwarf systems, where the distance limits vary with $G - J$ colour, a proxy for luminosity. The sample benefits from accurate distances, and is unbiased with respect to multiplicity. We have determined the relation between M_J and spectral type over this spectral range, measured the unresolved binary fraction, and determined the distribution of mass ratios of the stars in the unresolved binary systems. We have also measured the small fraction of resolved binaries where both the primary and the secondary are in this spectral range. The main results of our analysis of this sample are:

1. We present a revised absolute magnitude - spectral type relation for the ultracool M-dwarfs. This revised relation relative to the determination of Dupuy & Liu (2012) is on average 0.5 mag. brighter. We present evidence that the differences are due to differences

in the measured spectral types between the uniform BOSS sample of Schmidt et al. (2015*a*) and the stars in the sample of Dupuy & Liu (2012), with an average offset of close to one spectral subtype.

2. We find that the distribution of mass ratios in unresolved binaries in this spectral range $f(q) \propto q^{\gamma}$ is very steep, with $\gamma > 10$ (99% probability). In effect unresolved binaries of ultracool M dwarfs are identical twins.

3. We provide an estimate for the multiplicity fraction for M7 to M9.5 dwarfs of 16.5±0.8%, consistent with previous estimates. Of these 98% are unresolved.

4. The spread in absolute magnitude for ultracool M dwarfs is $\sigma = 0.21$ mag. at fixed colour.

5.8 Extending the analysis to the early-L dwarfs

5.8.1 Introduction

In this section we extend the work of Laithwaite & Warren (2020) to the early-L dwarfs. Starting with the homogeneous magnitude-limited (J < 17.5) catalogue of L and T dwarfs prepared by (Skrzypek et al. 2015, 2016) we use *Gaia* DR2 parallax and their associated errors to calculate the colour-magnitude relation, the absolute magnitude relation, and binary fraction for the early L-dwarfs. We apply many of the same ideas, sample preparation techniques and distribution models that were used for the late-M dwarf analysis (Laithwaite & Warren 2020).

This catalogue of 1361 L and T dwarfs (see Figure 5.14) is prepared using 8 band photometry in izYJHKW1W2, ranging from 0.75 to 4.6 μm, covering an area of 3344 deg^2, by combining SDSS, UKIDSS LAS, and ALLWISE data (see Figure 5.15). As discussed previously the *phototype* method developed by Skrzypek et al. (2015) is used to accurately classify each source by spectral type in the catalogue using photometry rather than spectroscopy.

The objectives of this section are as follows:

1. Prepare a high quality, volume-limited sample of L-dwarfs using *Gaia* parallax;
2. Determine the L-dwarf colour-magnitude relation;
3. Determine the L-dwarf absolute magnitude vs spectral type relation; and,
4. Estimate the L-dwarf binary fraction.

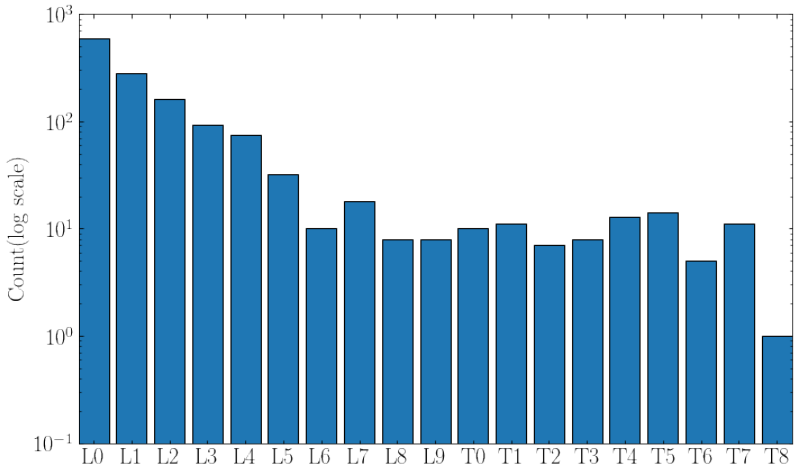

Figure 5.14: The magnitude-limited sample of 1362 L and T dwarfs by spectral subtype (Skrzypek et al. 2015, Skrzypek et al. 2016).

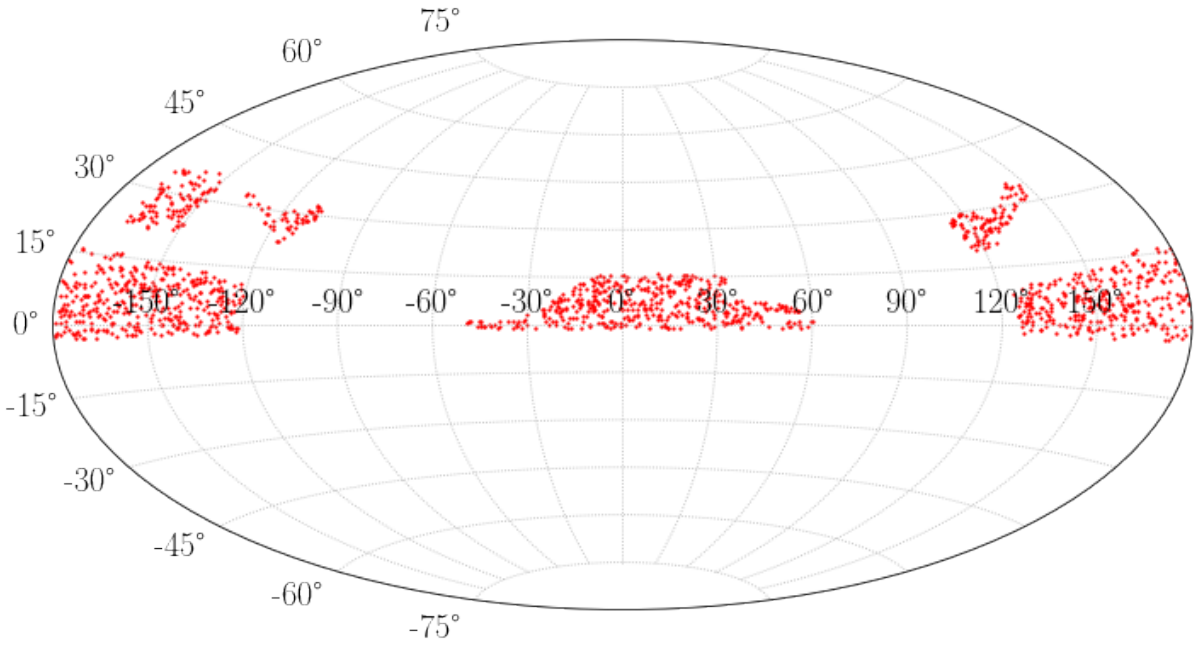

Figure 5.15: Sky map in Galactic coordinates of the magnitude-limited sample of 1362 L and T dwarfs covering an area of 3344 deg^2 (Skrzypek et al. 2015, Skrzypek et al. 2016).

5.8.2 Preparing the sample with *Gaia* DR2

Starting with the Skrzypek et al. (2016) catalogue we matched the position to the *Gaia* catalogue using a 5 arcsec matching radius with the TOPCAT software tool (Taylor 2005). We found 281 matches and used *Gaia* parallax and parallax error to calculate distance, distance error, and the absolute magnitudes M_J, M_H and M_K.

We applied the following quality cuts to the matched sample: (i) parallax-over-error > 10 (ii) G-J > 3 (iii) we remove 13 objects marked as p (peculiar) or : (reddened) and a single L6.5 object (iv) Ahmed & Warren (2019) noted two small regions of excessive reddening which has been cut out removing one further source.

After these quality cuts our remaining sample comprises 93 L dwarfs with high parallax-over-error. Not surprisingly given the magnitude limit in the *Gaia* G-band, these sources are close to the sun (<100pc) and biased towards the brighter, early L-type objects as shown in Figure 5.16. Our sample includes spectral subtypes from L0 to L4 only.

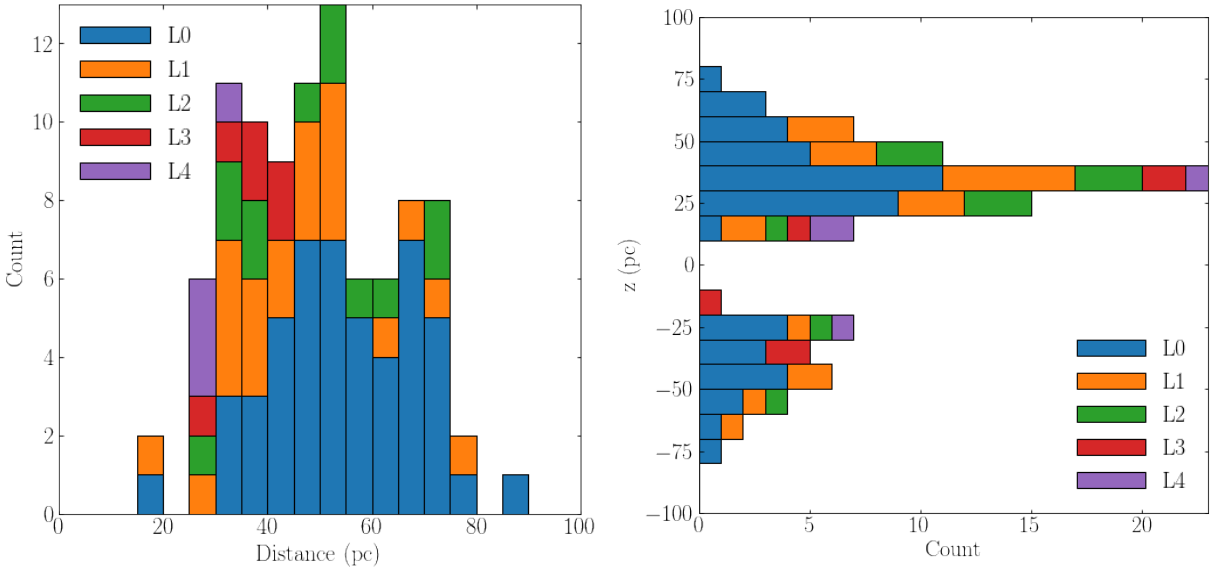

Figure 5.16: Our sample of 96 high quality L dwarfs with *Gaia* parallax. The left plot shows this sample by absolute distance in parsec by spectral subtype. The right plot shows the sample by vertical distance, z, from the sun. There are relatively few sources close to the sun due to the small conical volume.

5.8.3 Determining the L-dwarf colour-magnitude relation

The colour-magnitude plot of our sample of 93 L dwarfs is shown in Figure 5.17 with corresponding $M - J$ and $G - J$ errors. Similar to our equivalent plot for the late-M dwarfs there appears to be two populations of sources, sloping down and to the right, separated by a sparse region of few objects.

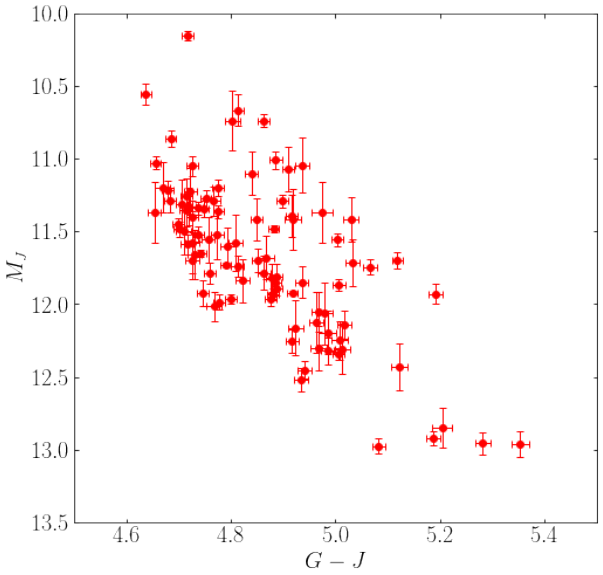

Figure 5.17: A sample of 93 L dwarfs in a colour-magnitude diagram with errors.

As with the late-M dwarfs, our distribution model assumes two populations of sources: a population of single stars described by a colour-absolute magnitude relation in $G - J$ and M_J with variance σ^2, and a second binary population centred around the same relation shifted by ΔM in absolute magnitude space with the same variance. Extending our findings for the late-M dwarf we anticipate that the second binary population will be found close to the equal-mass binary magnitude i.e. offset by -2.5log_{10}2.
Previously we showed that the binary mass ratio $q = M_s/M_p$ of ultracool dwarfs M7 to M9.5 is very close to 1.0[4] and that very-low mass M dwarf binaries reside almost exclusively in equal-mass pairs, or twins. We assume a constant binary fraction over the relatively narrow range of spectral subtypes in this sample We model the G-J colour distribution as we did for the late-M dwarfs using a normalised exponential-Gaussian function. Note that the distribution of G-J is not in itself of particular interest as it is primarily a function of the selection criteria used in preparing the sample.

[4]based on a binary mass distribution $p(q) \propto q^{\gamma}$ where γ >10

$$x = G - J \tag{5.12}$$

$$y = M_J \tag{5.13}$$

$$f(x,y) = A\ g(x)\ \left(\frac{n_1}{\sqrt{2\pi\sigma^2}} e^{\frac{-(y-y_0(x)}{2\sigma^2}} + \frac{1-n_1}{\sqrt{2\pi\sigma^2}} e^{\frac{-(y-y_0(x)+\Delta M)^2)}{2\sigma^2}} \right) \tag{5.14}$$

where:

- A is a normalisation constant over the range $G - J_{min}$ to $G - J_{max}$;
- $g(x; k, \mu, s)$ is an exponential-Gaussian distribution which describes the distribution of objects in $G - J$;
- $y_0(x; a_0, a_1) = a_0 x + a_1$
- n_1 is the proportion of single systems to total systems;
- σ is the standard deviation of the spread in M_J; and,
- ΔM is the offset in M_J between the single and binary colour-magnitude relation.

The likelihood based on the two-dimensional density model in equation 6.4 assumes a Poisson point process (see appendix B.3). We minimise the negative log likelihood to determine the best fit parameters as shown in Table 6.1. For completeness we include the exponential-Gaussian parameters however these are nuisance parameters with no physical meaning.

Table 5.3: Best fit model parameters for colour-magnitude relation.

Parameter	Value
A	96.52
k	6.159
μ	4.683
s	0.032
a_0	2.973
a_1	-2.618
n_1	0.786
σ	0.218
ΔM	0.810

The resulting contour plot based on the fitted parameters is shown in Figure 5.18. We find that the median colour-magnitudes by spectral subtype broadly fall along our single star colour-magnitude relation and that the binary population is offset in line with the theoretical equal-mass binary population. However the median objects for L2, L2.5, L3 and L3.5 appear brighter than the single star relation would suggest. This is due to the small number of objects in each of these later half spectral types skewing the median position (i.e. L2=7, L2.5=5, L3.0=3, L3.5=3, L4.0=4). Our colour-magnitude relation for single L dwarfs is given

by $M_J = 2.973(G-J) - 2.618$ with intrinsic scatter 0.218.

A histogram of M_J offset from the single star colour-magnitude relation shows how our distributions compare to the two Gaussian populations assumed in our model. The parameter n_1 shows the proportion of single stars to total system i.e. $1 -$ binary fraction. This is shown in Figure 5.19. We find a binary fraction of 21.4% for our sample of L-dwarfs.

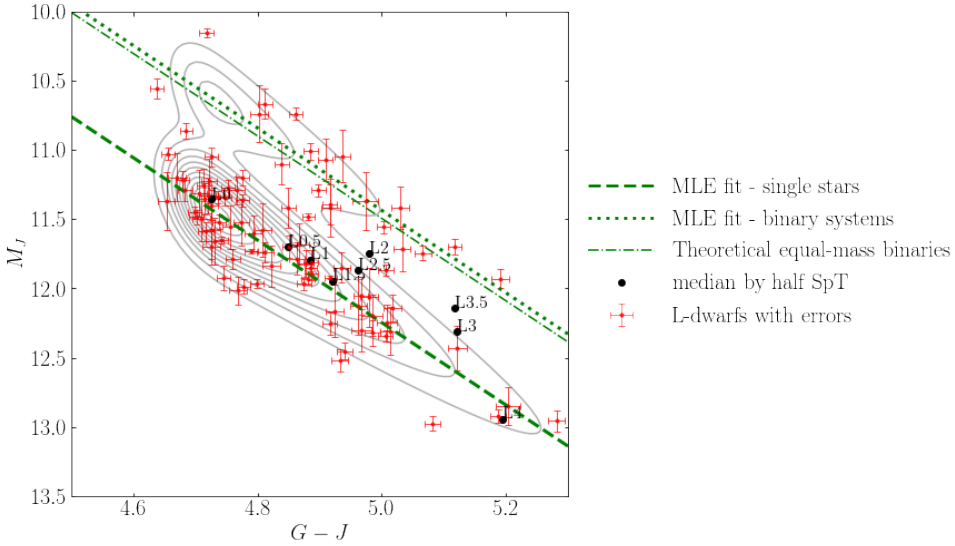

Figure 5.18: Maximum likelihood fit for colour-magnitude ($G-J-M_J$) relation for the L-dwarf sample assuming distribution model described by equation 6.4. The ΔM parameter is close to the equal-mass binary relation. The median colour-magnitude positions by half spectral subtype (e.g. L3.5) are shown.

5.8.4 Determining the M_J vs. spectral type relation

We determine the relationship between spectral subtype and M_J using a two-dimensional double-Gaussian density model for the L-dwarf sample as described in equation 5.17. The spectral subtype is encoded such that L0 = 10 and L4 = 14. We do not model a functional form for the density distribution by spectral subtype (as we did for colour $G-J$ above) given the discrete nature of the spectral subtype encoding. Note that the distribution by spectral subtype has no physical meaning; it is a sample selection effect only.

$$x = SpT \tag{5.15}$$

$$y = M_J \tag{5.16}$$

$$f(x,y) = A\left(\frac{n_1}{\sqrt{2\pi\sigma^2}}e^{\frac{-(y-y_0(x)}{2\sigma^2}} + \frac{1-n_1}{\sqrt{2\pi\sigma^2}}e^{\frac{-(y-y_0(x)+\Delta M)^2)}{2\sigma^2}}\right) \tag{5.17}$$

where:

- A is a normalisation constant over the range $G-J_{min}$ to $G-J_{max}$;

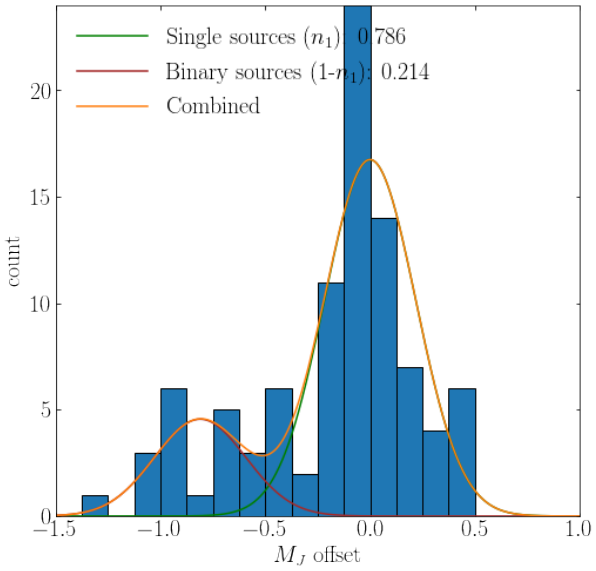

Figure 5.19: Histogram of M_J offset based on fitting the distribution model to $(G-J)-M_J$. The bi-Gaussian fitted distributions are overlaid scaled by the binary fraction (n2) and single fraction (n1).

- $y_0(x; a_0, a_1) = a_0 x + a_1$
- n_1 is the proportion of single systems to total systems;
- σ is the standard deviation of the spread in M_J; and,
- ΔM is the offset in M_J between the single and binary colour-SpT relation.

The likelihood function, based on the two-dimensional density model in equation 6.4, assumes a Poisson point process (see appendix B.3). We minimise the negative log likelihood to determine the best fit parameters as shown in Table 6.1.

Table 5.4: Best fit model parameters for M_J as a function of spectral subtype.

Parameter	Value
A	18.64
a_0	0.359
a_1	7.882
n_1	0.777
σ	0.236
ΔM	0.783

The resulting contour plot based on the fitted parameters is shown in Figure 5.20. We see that the single star population closed agrees with the colour-magnitude relation of (Dupuy & Liu 2012) and that the binary star population closely agrees with the theoretical equal-mass binary offset. Our M_J vs spectral type relation for single L dwarfs is $M_J = 0.359SpT + 7.882$ with intrinsic scatter 0.236.

A histogram of M_J offset from the single star colour-SpT relation shows how our distributions compare to the two Gaussian populations assumed in our model. The parameter n_1 shows the proportion of single stars to total system i.e. $1 -$ binary fraction. This is shown in Figure 5.21. We find a binary fraction of 22.3% for our sample of L-dwarfs.

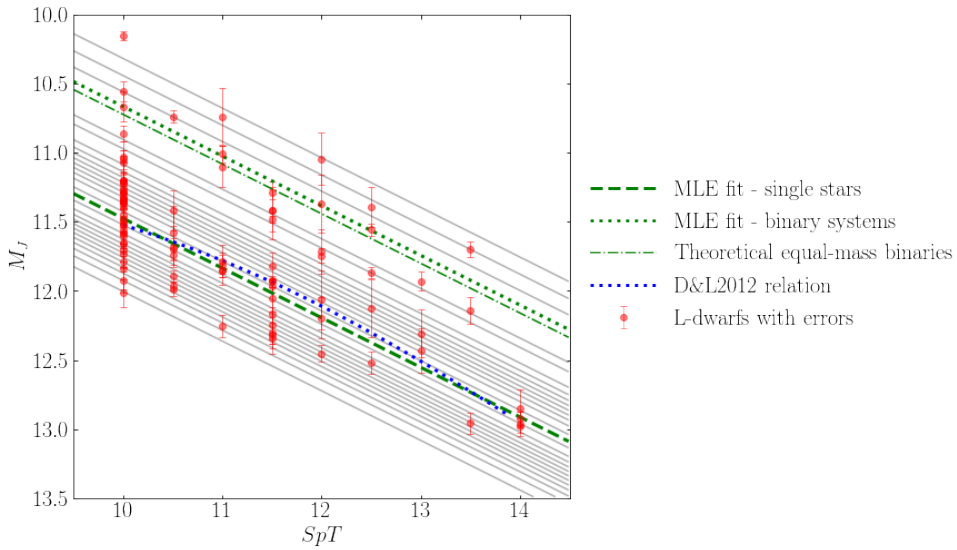

Figure 5.20: Maximum likelihood fit for M_J-spectral type relation assuming distribution model described by equation 5.17. The ΔM parameter is close to the equal-mass binary relation. Here we show the polynomial relation derived by Dupuy & Liu (2012) as blue dotted line. This closely matches our single source fitted relation.

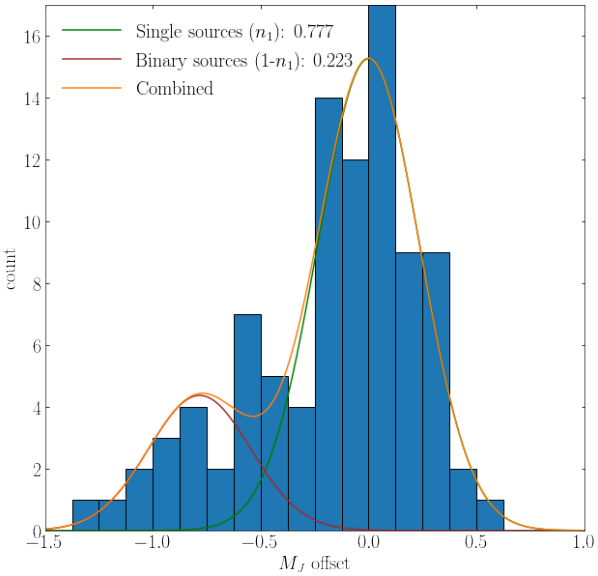

Figure 5.21: Histogram of M_J based on fitting to the M_J-spectral type relation. The fitted Gaussian distributions for the single star population (green line), binary star population (red line) and combined population (orange line) are shown scaled by the single star fraction (n_1) and binary star fraction (1-n_1).

5.8.5 The combined absolute magnitude M_J relation

Combining our absolute magnitude relations for the late-M dwarfs and the early-L dwarfs, and comparing to the canonical relation from Dupuy & Liu (2012), we can generate a revised M_J-SpT relation over the range M7 to T8 as shown in Figure 5.22. The best fit combined UCD polynomial relation is given by equation 5.18 with an rms of 0.230.

$$M_J = a_0 + a_1 SpT + a_2 SpT^2 + a_3 SpT^3 + a_4 SpT^4 + a_5 SpT^5 \tag{5.18}$$

where:
a_0 = +1.831 × 10^{-5}
a_1 = -1.330 × 10^{-3}
a_2 = +3.606 × 10^{-2}
a_3 = -4.688 × 10^{-1}
a_4 = +3.416
a_5 = -4.275 × 10^{-1}

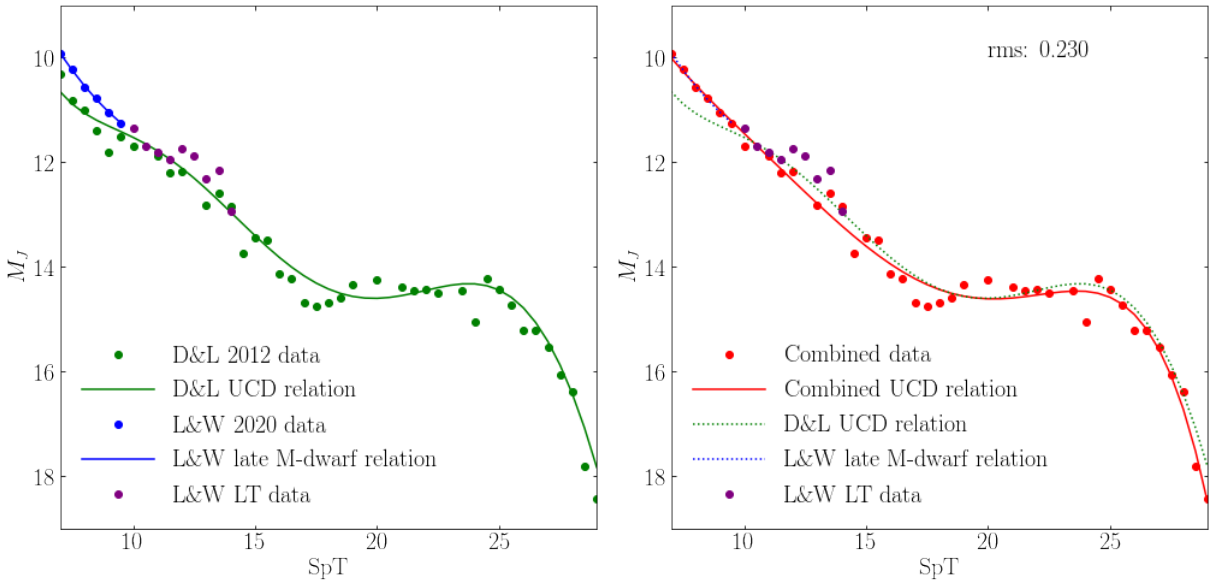

Figure 5.22: The left plot shows M_J as a function of spectral type for M7 (SpT = 7) to T8 (SpT=28). The green dots and line show the often used data and polynomial fit from Dupuy & Liu (2012). The blue dots and line are the data and polynomial fit from Laithwaite & Warren (2020) for the late-M dwarfs. The purple dots are the data from this work. The right plot combines the late-M data from Laithwaite & Warren (2020) with the Dupuy & Liu (2012) data from L0 onward and the data from this work to fit a revised polynomial M_J-SpT relation (red line) used in Warren et al. (2021).

Chapter 6

UCD field luminosity function & binary fraction

In this chapter we seek to use *Gaia* EDR3 to determine the field luminosity function in M_J and M_G at the end of the main sequence and the evolution of the binary fraction over this range of absolute magnitudes.

6.1 Introduction

We use Gaia EDR3 measured parallaxes to create a large volume-limited sample of sources spectral types M7 to L2.5. While the unparallelled accuracy of *Gaia* parallax has enabled highly accurate luminosity functions to be prepared for objects across the main sequence, the *Gaia* G-band is not well suited to observing these objects which emit primarily in the near infrared. The near infrared J-band is the most suitable filter for deriving the luminosity function for these very low mass stars. By combining 2MASS photometry in the J-band with *Gaia* parallax and G-band photometry, we are able to obtain highly accurately $G - J$ colour and absolute J magnitudes for a large volume-complete sample from which to derive the luminosity function. In order to prepare the luminosity function a careful consideration of binarity is needed. We estimate the binary fraction over this range of magnitude using a statistical model based on Laithwaite & Warren (2020) for a population of single and unresolved binaries within the *Gaia* data set and derive a binary fraction in each luminosity interval in our analysis. We define the binary fraction as per Lada (2006) and Duchêne & Kraus (2013*a*) as the fraction of binary systems in a population of systems.

Despite the fact that the luminosity function at the end of the main sequence has been estimated numerous times in recent years (see section 3.21) and discussed most recently by Bardalez Gagliuffi et al. (2019), it remains ill-defined. For the first time, *Gaia* EDR3 affords us the opportunity to prepare a large and complete sample without the need for spectroscopy of individual sources and confirmed resolved binaries.

This chapter is organised as follows. In section 6.2 we describe how we prepare our sample of objects starting with a catalogue of nearby stars (Gaia Collaboration et al. 2020) derived from the

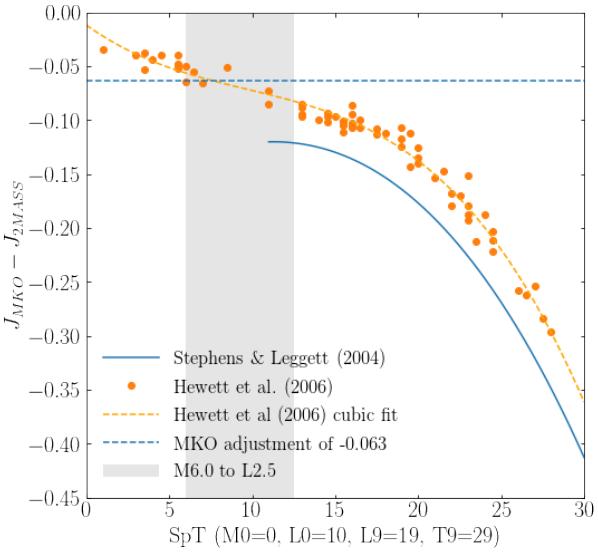

Figure 6.1: Difference in magnitude between J_{MKO} and J_{2MASS} based on Hewett et al. (2006) and Stephens & Leggett (2004).

latest *Gaia* release EDR3, along with the quality cuts applied. Given that our sources of interest are approaching the limit of completeness for the *Gaia* G-band we describe in section 6.2.2 how we estimate completeness as a function of G magnitude and the corresponding magnitude limits we apply. In section 6.2.3 we also discuss our procedure for removing outliers from the selected region in colour-magnitude space. In section 6.3 we describe our statistical model for describing the population of single and binary sources and the method of fitting to the data. This method allows us to statistically separate single and binary objects and count objects in absolute magnitude bins in J and G as well as calculate the binary fraction in each bin. The uncertainties in our model parameters are estimated using a Markov Chain Monte Carlo approach. Section 6.4 provides the detailed results of our work including the luminosity function and binary fraction in intervals of M_J and M_G. In Section 6.5 we discuss the impact of resolvable wide binaries in our sample; we compare our binary fraction estimate to other work; and compare our luminosity function in M_J to other studies. We summarise our results and conclusions in section 6.6.

Our results are presented using J_{2MASS}. Where comparisons to other results are made in J_{MKO} we apply adjustments as shown in Figure 6.1. In this Figure we show the difference between J_{MKO} and J_{2MASS} as measured by Stephens & Leggett (2004) and Hewett et al. (2006) for the M, L and T dwarfs. The grey region shows the spectral types within our sample M6.0 to L2.5 and the blue dotted line is the average difference over this region. Given that $\langle J_{MKO} - J_{2MASS} \rangle = -0.063$, We apply an adjustment of $+0.063$ to J_{MKO} to convert to J_{2MASS} throughout.

6.2 Sample preparation

Our starting catalogue is the *Gaia* Catalogue of Nearby Stars (GCNS) prepared by the Gaia Collaboration et al. (2020). This is a census of stars in a spherical volume of 100pc radius of

the Sun as measured by the *Gaia* spacecraft. This is volume complete for sources to M8 at a G magnitude of 20.7. Completeness decreases rapidly with distance for sources > M8.

GCNS has been compiled from *Gaia* EDR3 by applying the following selection criteria and quality indicators. Initially all objects with measured parallax > 8mas i.e. a crude initial selection of objects with distance $\lesssim$ 125pc were selected. Then sources with spurious astronomical solutions were removed using a random forest classifier based on a set of astronomical features of which, perhaps not surprisingly, the most important features were parallax_error and parallax_over_error. These spurious sources are generally due to very close pairs which can only be resolved in some *Gaia* transits and directions. They are generally found in regions of high surface density or for close binary systems (Gaia Collaboration et al. 2021). The training set was constructed from a set of 291,030 sources in low density regions of the sky crossmatched to 2MASS. A representative colour magnitude diagram was calculated based on $G - J$ and M_G, M_{RP}, M_H and M_K and models constructed for white dwarfs, red clump, giant branch and the main sequence. Photometric features were not used in the classifier directly. Good and poor astrometric sources are well separated by this technique and a probability p, representing the probability of reliable astrometry, is assigned. The true distance to each good source from above is inferred using a simple Bayesian distance estimation method. The posterior for each source is reported as the following percentiles: dist_1, dist_16, dist_50, dist_84 and dist_99.

Criteria for inclusion in the GCNS is p>=0.38 (determined as the optimal probability threshold) and dist_1<100pc i.e. retaining all sources with > 1% probability of being within 100pc.

The GCNS has been enriched with optical magnitudes g, r, z, i from the Sloan Digital Sky Survey (SDSS) and other surveys; near-infrared magnitudes J, H, K from 2MASS; and mid-infrared magnitudes $W1$, $W2$ from CATWISE2020 and $W3$, $W4$ from ALLWISE. Sources are matched using existing *Gaia* cross-match tables except for CATWISE2020 where a 5as nearest-neighbour search was performed.

The resulting GCNS includes 331,312 sources.

6.2.1 Sample selection

Starting with the GCNS we applied the following selection criteria as explained below:

- Select distance limits: 10pc < dist_50 < 30pc
- Remove white dwarfs: WD_PROB < 0.5
- Remove sources close to the galactic plan: $|b| > 20$

The spherical maximum distance of 30 pc is based on the completeness magnitude limits of the 2MASS J-band J<16, and *Gaia* G-band G<20 as shown in Figure 6.2. At these limiting magnitudes we found that we could prepare a large sample of objects in our region of interest in colour-absolute magnitude space between $3.2 < G - J < 5.0$ and $7.5 < M_J < 12.5$. We will demonstrate later that this allows us to determine the luminosity function and binary fraction for the UCDs with $9.5 < M_J < 12.5$. These bounds are based on determining the faintest spectral

type observable at J=16 and G=20 using the M_J-SpT relation from Dupuy & Liu (2012) and Laithwaite & Warren (2020) as shown in Figure 6.3. The upper M_J limit of 7.5 is well above the absolute magnitude limit for a single M7.0 source in order to ensure we do not artificially remove the bright M7.0 multiple systems.

A number of corrections to the GCNS catalogue have been identified subsequent to its publication however only two of these corrections fall within 30pc: the very close binary Luhman 16A/B. However Gaia Collaboration et al. (2020) identified a potential issue with nearby (< 10 pc) spectroscopic or close binary systems giving large residuals for single star solutions and therefore failing the five-parameter astrometric quality checks. As a result we chose to set a minimum distance of 10pc which has a minimal impact on the number of sources and volume of our sample.

We found that at low latitudes our sample was crowded and therefore to minimise the risk of contamination from overlapping or background sources we removes sources with $|b| > 20$. Although white dwarfs are removed with the GCNS flag (PROB_WD) there is no contamination in our region of interest.

Even after applying these cuts we are sampling a volume of 71.6 $\times$ 10^3 pc^3 representing 63.4% of the volume of a complete 30pc sphere centred on the sun. We enhance the sample by calculating absolute magnitudes M_J, M_H, M_K and M_G using the magnitudes provided in the GCNS catalogue and the median distance (dist_50) as well as colours $G - J$ and $J - K$. Galactic longitude and latitude coordinates are also added with distance uncertainty calculated as $\frac{\sigma_\varpi}{\varpi^2}$.

6.2.2 Determining completeness

We estimate and confirm the completeness of our sample in a number of ways. First we compare our sample of sources to other ultracool dwarf studies. In each case we performed an initial best match in TOPCAT (Taylor 2005) using a 1 arcmin search radius followed by a individual item-by-item check. We compare to the 20pc census of LTY sources by Kirkpatrick et al. (2021), the 25pc volume-limited sample of M7 to L5 objects by Bardalez Gagliuffi et al. (2019), and the 20 pc volume-limited sample of M7 to L8 sources by Cruz et al. (2007).

Of the 525 sources in the Kirkpatrick et al. (2021) census, 50 sources are classified as <=L3 of which we match 48 to GCNS. Of the 410 sources in 394 systems compiled by Bardalez Gagliuffi et al. (2019), 334 are classified as <= $L3$. Of these 317 are matched to GCNS. For the Bardalez Gagliuffi et al. (2019) comparison we use the 410 main catalogue objects only and not the 'additional' 60 objects. These objects were flagged as having a larger uncertainty in distance and therefore may or may not fall within the distance limit of this study. These objects have a large effective volume as they are disproportionately not using *Gaia* parallax measurements and the associated smaller uncertainty for distance.

The Cruz et al. (2007) sample contains 73 sources classified $\leq$ L3 of which 71 are matched to GCNS. Many of the sources in these catalogues overlapped and therefore it was necessary to

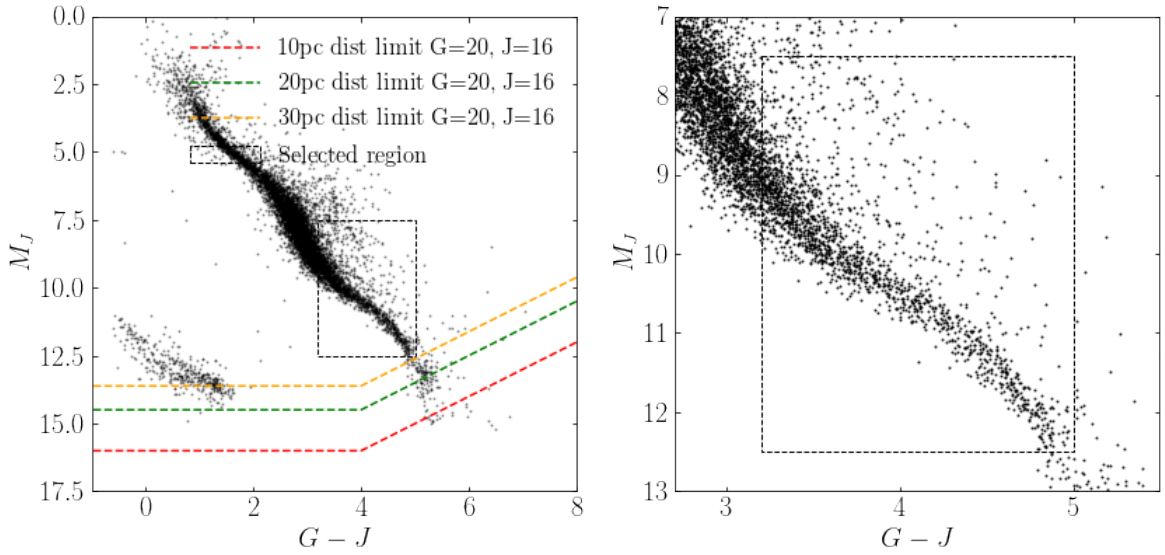

Figure 6.2: Left hand side shows colour $(G-J)$ absolute magnitude (MJ) plot for all source in GCNS from 5 to 30 pc. Completeness distance limits at 10, 20 and 30 pc based on Gaia EDR G magnitude of 20 and 2MASS J magnitude of 16. Selected region highlighted (dotted box) is bounded by $G-J$ of 3.2 to 5.0, and M_J of 7.5 to 12.5. Note that this region is larger in M_J than the luminosity range of interest in this study but is necessary to avoid missing over-luminous multiple sources. Right hand side shows an enlargement of the selected $G-J$ $M-J$ region.

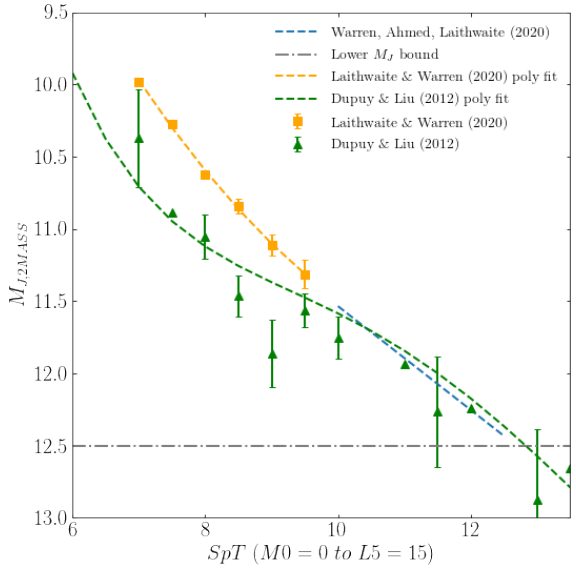

Figure 6.3: Absolute magnitude M_J as a function of spectral type using Dupuy & Liu (2012) and Laithwaite & Warren (2020) relations. Note that error bars are not shown for those points in the Dupuy & Liu (2012) data comprising only one data point.

match between samples to estimate a true completeness. We estimate a total combined number of sources of 353 with 18 non-matches giving a completeness in GCNS of 95%.

In addition to this we compared *Gaia* EDR3 to a large, homogeneous photometric sample of late-M, L and T dwarfs prepared by Ahmed & Warren (2019) and Skrzypek et al. (2016). These catalogues are highly complete over 3070 deg^2 for all objects brighter than J(Vega) of 17 and therefore present an excellent comparative sample for the faint end of the *Gaia* EDR3 catalogue. The photometric sample is much deeper than *Gaia* where the number of sources falls steeply from G$\gtrapprox$ 20.5. We select sources with spectral types from M7 to L3 from the photometric sample for comparison. Using a 3as radius we match these catalogues and calculated a G magnitude for each item in the photometric sample using the G-J vs. i-k colour-colour relation from Laithwaite & Warren (2020). 92% of matches have angular matching distance $<$ 1as. We tested our calculated G magnitudes against the actual G magnitudes to ensure our relation was valid. We count the number of sources in G-magnitude bins for both catalogues and compare bin counts to estimate completeness as a function of G as shown in Figure 6.4. Completeness falls sharply for G $>$ 20 however the number of sources with G $\leq$ 20 in our M7-L3 photometric sample is 7070 and the number of matched sources in our sample with G $\leq$ 20 is 6906 implying a completeness of 97.7$\pm$1.7%. Combining our methods above we adopt a completeness of 95% for our analysis.

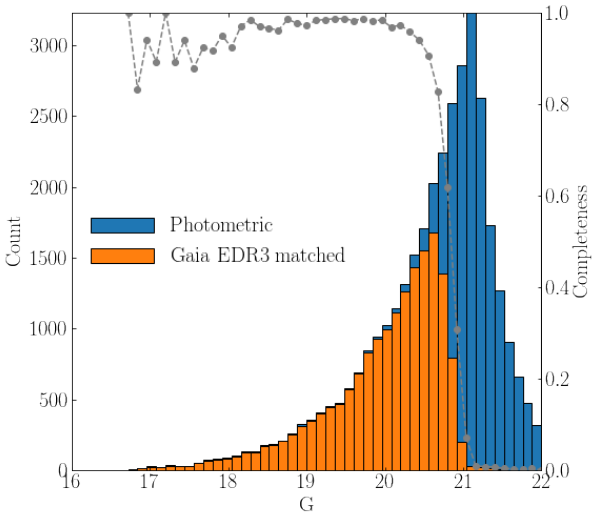

Figure 6.4: Estimating the completeness of late-M, early-L dwarfs in Gaia EDR3 by comparing to a highly-complete independent photometric catalogue over 3070 deg^2. The blue bins are the counts of the photometric catalogue and the orange bins are Gaia EDR3. Completeness in Gaia falls rapidly for G fainter than $\sim$ 20.5.

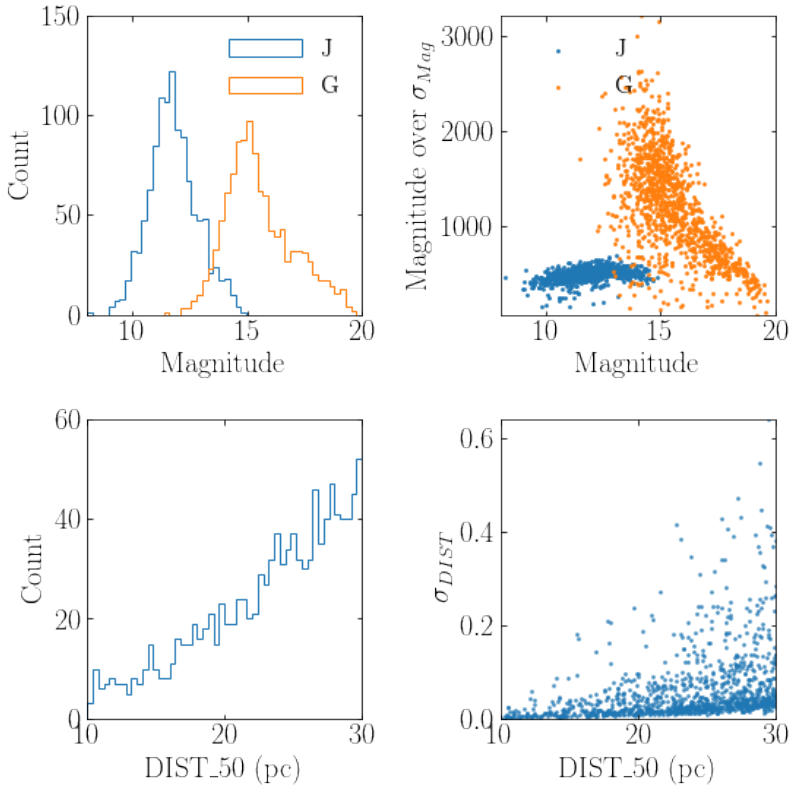

Figure 6.5: Analysis of final sample: Distribution of G, J; G, J magnitude over error; median distance; and uncertainty in median distance (dist_50)

6.2.3 Outlier removal

In order to remove spurious bright sources from our sample we iteratively performed a Maximum Likelihood model fit (see 6.3) on our sample and removed all objects $> 3\sigma$ from the fitted polynomial as shown in Figure 6.6. 63 outliers were removed ($\sim$5% of the sample) as shown in Figure 6.6. All these outliers are brighter than a unresolved equal-mass triple for a given colour. In order to understand what these objects might be we compared the outliers against the remaining sample for angular matching distance between *Gaia* EDR3 and 2MASS, and for multiple matches flagged in *Gaia*. We found that the median angular matching distance for the outliers was significantly larger than the remaining sample and that the proportion of *Gaia* multiple matches was 28.6% in the outliers and only 1.6% in the remaining sample. We therefore conclude that the outliers are likely mismatched or contaminated sources.

After removing outliers, our sample contains 1122 sources. Histograms of G-magnitude, J-magnitude, associated magnitude over error scatter plots as well as distance and distance uncertainty are shown in Figure 6.5. Over 98% of this sample has a distance uncertainty of less than 0.3pc.

6.3 Method

Our overall aim is to statistically separate the overluminous binaries from the single sources in the sample in order to count the single sources and binary systems within magnitude bins for the derivation of the luminosity function.

Our sample is sufficiently large that we are able to directly calculate the binary fraction in each magnitude bin with a reasonable uncertainty without resorting to relying on literature resolved binaries which is expected to be highly incomplete (Bardalez Gagliuffi et al. 2019) for these objects.

Laithwaite & Warren (2020) showed that the binary mass ratio $q = M_s/M_p$ of ultracool dwarfs M7 to M9.5 is extremely close to 1.0[1] and that very-low mass M dwarf binaries reside almost exclusively in equal-mass pairs, or twins. Given that we see no reason why this relation would not extend into the Hydrogen-burning early L-dwarfs, we extend this assumption over the range of objects in our sample. We utilise this result in designing our statistical model.

Our primary motivation in fitting our model to the data is to determine the colour-absolute magnitude relations for the single sources and a corresponding overluminous relation for the equal-mass binaries as well as an indication of how the binary fraction varies with $G - J$.

Our model assumes two populations of sources: a larger sequence of single stars centred around a quartic polynomial colour-absolute magnitude relation in $G-J$ and M_J with variance σ^2, and a second equal-mass binary population centred around the same polynomial relation shifted by -2.5log_{10}2 in absolute magnitude space with the same variance. We do not however assume a constant binary fraction over the range of colour and magnitude of our sample. We represent the binary fraction as a simple linear relation of $G - J$ i.e. $b_f = a + b(G - J)$. The G-J colour distribution is most accurately modelled with a normalised exponential plus constant relation. Other than ensuring an accurate fit this relation has no particular physical interest and is simply a function of our sample selections.

$$x \;=\; G - J \tag{6.1}$$

$$y \;=\; M_J \tag{6.2}$$

$$\begin{aligned} &f(x, y; \mu, c, a_0, a_1, a_2, a_3, a_4, \sigma, A, a, b) = \\ &A\ g(x) \left(\frac{(1 - b_f)}{\sqrt{2\pi\sigma^2}} e^{\frac{-(y-q(x))^2}{2\sigma^2}} + \frac{b_f}{\sqrt{2\pi\sigma^2}} e^{\frac{-(y-q(x)+2.5log_{10}2)^2}{2\sigma^2}} \right) \end{aligned} \tag{6.3}$$

where:

1. $g(x;\ \mu,\ c)$ is a normalised exponential plus constant over the range $(G - J_{min},\ G - J_{max})$

2. $q(x; a_0, a_1, a_2, a_3) = a_0x^4 + a_1x^3 + a_2x^2 + a_3x + a_4$;

[1] based on a binary mass distribution $p(q) \propto q^\gamma$ where $\gamma > 10$

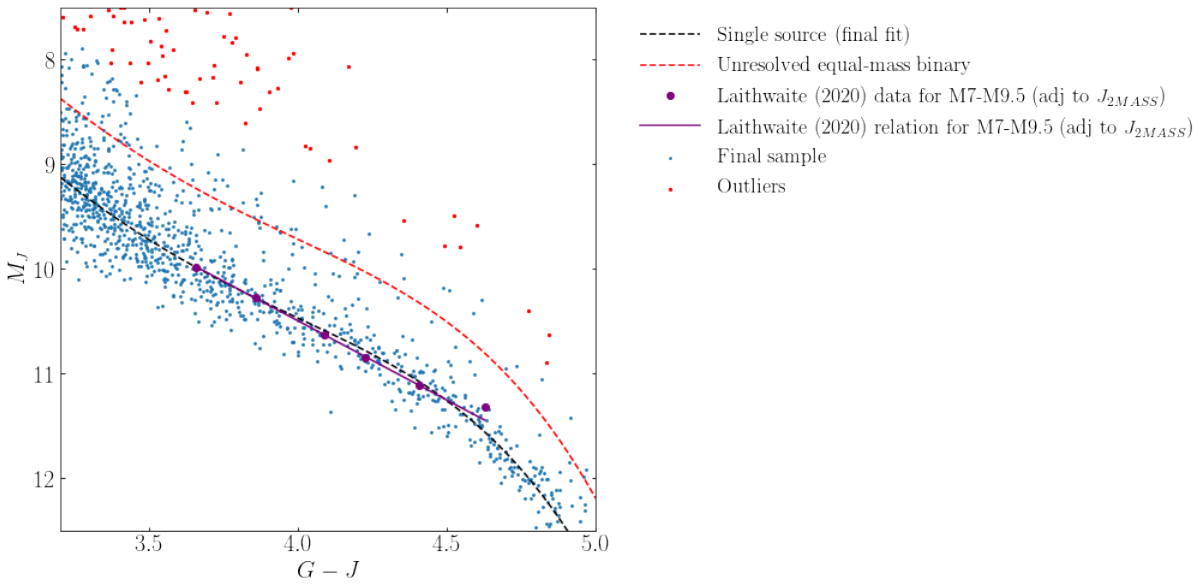

Figure 6.6: Maximum likelihood model fitted to the data with the quartic polynomial for single sources (black dashed) and equal-mass binaries (red dashed)shown as dotted green line. Overluminous outlier points removed from the final sample are shown as red points and the Laithwaite & Warren (2020) colour-magnitude relation (adjusted to J_{2MASS}) is shown as purple points and solid line.

3. $b_f(x;\ a,\ b) = a + bx$; the binary fraction relation; and,

4. A is a normalisation constant.

Following the iterative removal of outliers discussed in section 6.2.3 we determine the maximum likelihood fit of our model using a Poisson point process as shown in Figure 6.6. The polynomial colour magnitude fit for the single sources is shown and is a good match to the linear colour-magnitude relation found by Laithwaite & Warren (2020) over the overlapping G-J range. We examined the outliers (shown as red points in Figure 6.6) and found that they had either a poor positional match as measured by a $\sim 3\times$ larger than average angular matching distance, or that they had > 1 matching object within *Gaia* suggesting that they are contaminants in our sample.

We centre our sample in G-J space by applying an offset of -4. This provides better convergence of our parameters when fitting the model. Minimising the log likelihood yields the best fit parameters as shown in Table 6.1.

In addition we performed Bayesian parameter estimation using a Markov Chain Monte Carlo (MCMC) method based on the `emcee` sampler (Foreman-Mackey et al. 2013*a*) in order to generate the posterior distributions and the associated uncertainties for our parameters. We applied uniform physical priors for σ, μ, c, A, a >0 and b > -a to avoid sampling a negative binary fraction. In particular we checked for any correlation between our parameters and sought to estimate the uncertainties in our binary fraction parameters.

The results of the Bayesian parameter estimation show that the function is well-behaved and rapidly converges with minimal degeneracy between the parameters. All posterior distributions

Table 6.1: Best fit model parameters from the maximum likelihood fit of the function described by 6.4.

Model parameter	Best fit value
μ	3.585
c	0.972
a_0	0.329
a_1	0.813
a_2	0.000
a_3	1.334
a_4	10.468
σ	0.246
A	1151.343
a	0.138
b	-0.0739

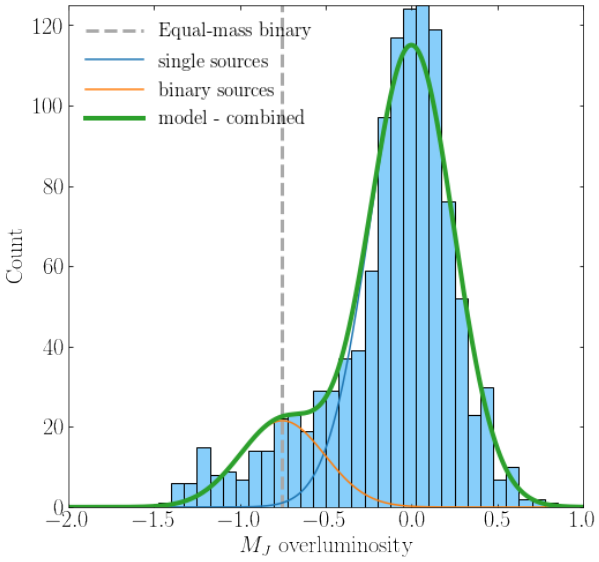

Figure 6.7: Distribution of overluminosity calculated as the difference between M_J and the polynomial fit of the single source distribution. As expected there is surplus of overluminous binary sources centred around the equal-mass binary position at -2.5log_{10}2.

are approximately normal and symmetrical as shown in Figure 6.8.

The binary fraction relation as a function of colour with 1σ and 2σ uncertainty bands is shown in Figure 6.9.

Since our $G-J$ range corresponds to spectral types in the range M7 through to $\sim$ L2.5, we note that the fitted binary fraction relation decreases steeply with spectral type.

In the next section we calculate the number of single stars and binary systems in magnitude intervals of M_J and M_G by probabilistically assigning each source as a single ($p(single)$) or binary ($p(binary)$). using our polynomial relation and the intrinsic scatter for both the single and binary populations we can now find a binned estimate of the luminosity function by using $p(single)$ and $p(binary)$ as illustrated by Figure 6.10. We are then able to directly compute the binary fraction and luminosity function within each magnitude interval.

The over-luminosity of each source ($\bar{M_J}$) compared to our single star polynomial relation is calculated as:

$$\bar{M_J} = M_J - q(x, a_0, a_1, a_2, a_3, a_4)$$

where $x = G - J$.

For each source we calculate $p(binary)$ and $p(single)$ as follows:

$$p(binary) = \frac{b_f e^{\frac{-(\bar{M_J}+2.5log_{10}2)^2}{2\sigma^2}}}{b_f e^{\frac{-(\bar{M_J}+2.5log_{10}2)^2}{2\sigma^2}} + (1-b_f)e^{\frac{-(\bar{M_J})^2}{2\sigma^2}}} \tag{6.4}$$

$$p(single) = 1 - p(binary) \tag{6.5}$$

Equation 6.5 describes the probability of a given source being a binary and is calculated as the proportion of the binary distribution to the total distribution for a given over-luminosity $\bar{M_J}$ and binary fraction $b_f = a + b(G-J)$ as shown in Figure 6.7. The resulting $p(binary)$ as a function over overluminosity in M_J is shown in Figure 6.11 with an average binary fraction of 15.5%. However the average binary fraction masks the binary fraction relation as a function of M_J as implied by the model fitting.

In order to calculate the luminosity function and binary fraction as a function of M_J we divide our sample into six 0.5 magnitude bins from M_J of 9.5 to 12.5. We calculate the number of single sources in a M_J interval as the sum of the probability of being a single as follows:

$$N_s = \sum_i p_i(single)$$

where i are the sources in a given M_J range. Similarly the number of binary sources is calculated

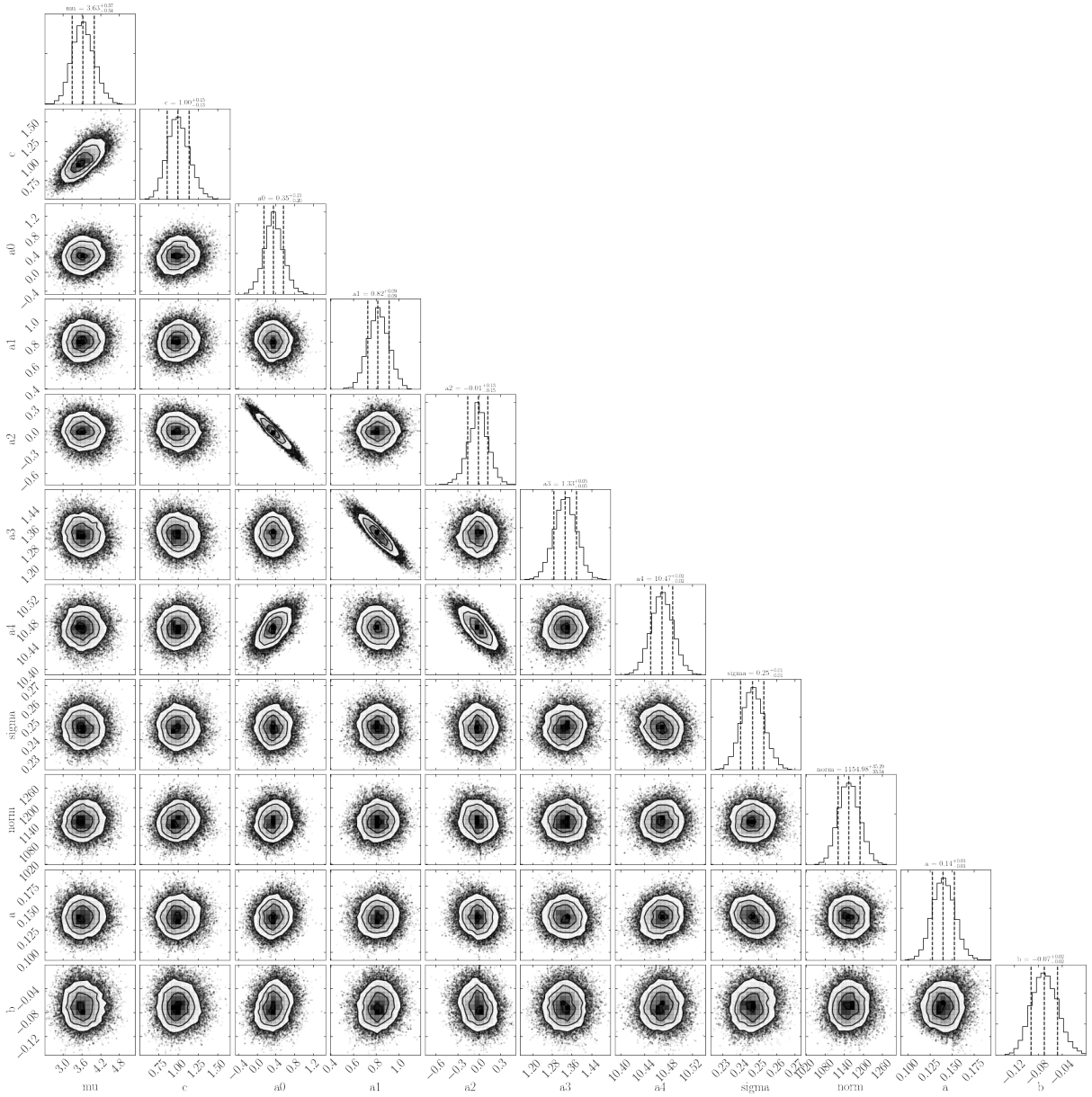

Figure 6.8: MCMC corner plot to determine parameter posterior distributions and uncertainty in the binary fraction relationship.

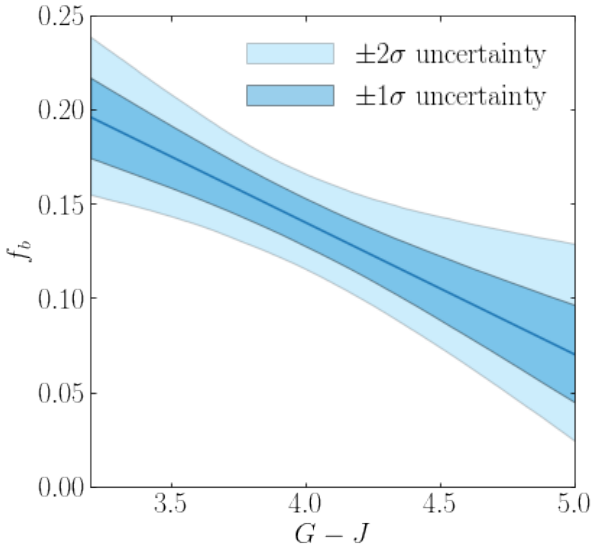

Figure 6.9: MCMC fitted binary fraction relationship as a function of $G-J$ with 1σ and 2σ uncertainty. This suggests that there is a steeply declining binary fraction over this range of $G-J$ and M_J magnitudes. Later we compare to the probabilistic count of singles and binaries.

as:

$$N_b = \sum_j p_j(binary)$$

where j are the number of sources in a M_J bin where M_J has been offset by $-2.5log_{10}2$, the difference in magnitude between a single star and an equal-mass binary of the same colour.

By summing the probabilities in an M_J interval we estimate the population of single and binary sources within the interval. Please note that Figure 6.10 assumes that any object with $p(binary) > 0.5$ is a binary. This is for illustrative purposes only. The method outlined above calculates the number of binaries in a given magnitude bin as the sum of $p(binary)$. Each source has variance p_i^2 therefore the Poisson errors of the probabilistic counts are determined as:

$$\sigma_{N_s} = \sqrt{\sum_i p_i(single)^2}$$

$$\sigma_{N_b} = \sqrt{\sum_j p_j(binary)^2}$$

The total 'probabilistic' number of stars in the given M_J interval is given by:

$$N = \sum_i p_i(single) + 2\sum_j p_j(binary)$$

The combined error calculated in quadrature as:

$$\sigma_N = \sqrt{(\sigma_{N_s})^2 + (2 * \sigma_{N_b})^2}$$

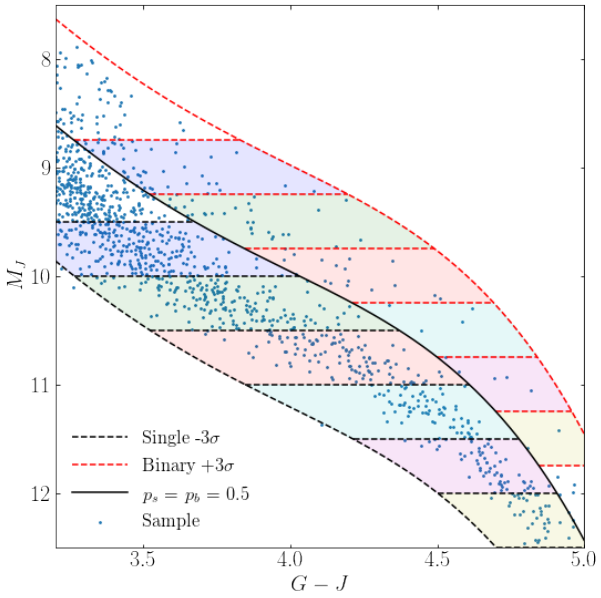

Figure 6.10: Sample plotted with shaded regions corresponding to p(single)>0.5 and corresponding offset region by $+2.5log_{10}2$ of sources shaded corresponding to p(binary)>0.5. For illustrative purposes only.

.

6.4 Results

6.4.1 Luminosity function and binary fraction in M_J and M_G

The luminosity function in six 0.5 M_J intervals from 9.5 to 12.5 and the corresponding calculated binary fraction in each interval are shown in Figures 6.12 and 6.13. As can be see from Figure 6.10, the M_J range from 9.5 to 12.5 is essentially complete for both the single and binary regions. This justifies our region of colour-magnitude space selected in Figure 6.2.

The equivalent luminosity function and binary fraction in 0.5 magnitude M_G intervals from 12.5 to 17.0 was calculated in exactly the same manner and is shown in Figures 6.14 and 6.15. In Figure 6.14 we compare our result to the luminosity function prepared by (Gaia Collaboration et al. 2020) using the full 100 pc GCNS catalogue. The upper grey points represent main sequence stars only with no correction for binaries. The lower green curve represents a subsample of the main sequence of assumed single stars using a parameter[2] that indicates that is may be a binary star. Our luminosity function is in good agreement with these curves but likely higher because of the more detailed treatment of binaries.

We also calculate the $\langle \frac{V}{V_{max}} \rangle$ statistic (Schmidt 1968) and corresponding uncertainty for each interval to determine the homogeneity in the spatial distribution of our sample. $\langle \frac{V}{V_{max}} \rangle$ should approach 0.5 for a uniformly distributed sample. Our sample shows good agreement with this limit across the J-band and G-band intervals as shown in Figures 6.12 and 6.14. The calculated

[2]ipd_frac_multi_peak

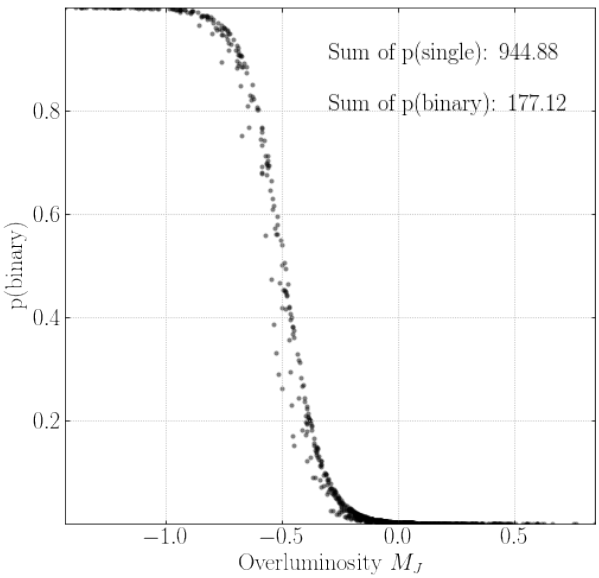

Figure 6.11: p(binary) for each source in our sample as a function of overluminosity in M_J.

binary fraction as a function of M_J and M_G mirror the best fit relationship as a function of $G - J$ shown in Figure 6.9.

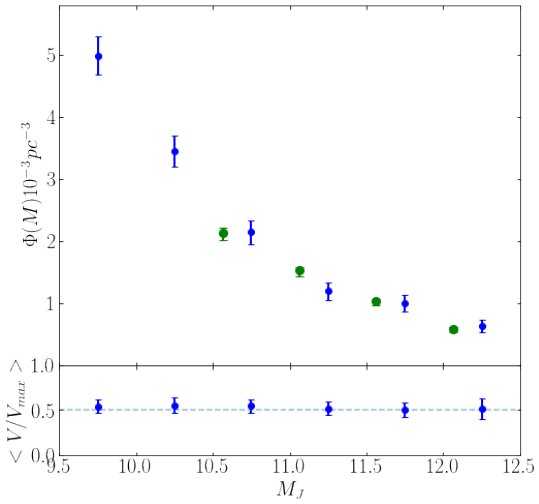

Figure 6.12: The luminosity function in 0.5 magnitude intervals for $M_J = 9.0$ to 12.5. We show the result of recent study by Warren et al. (2021).

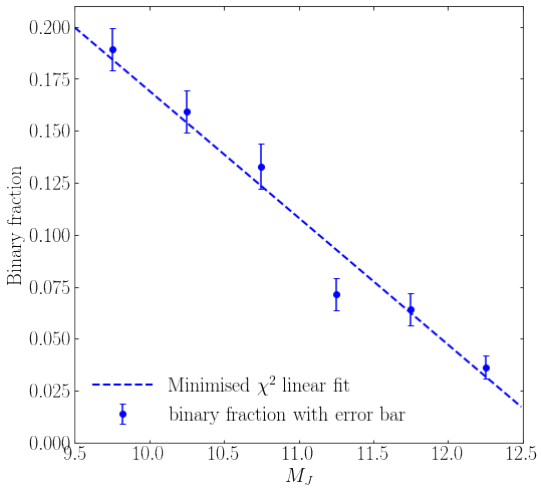

Figure 6.13: Calculated binary fraction for each M_J bin. A least squares linear fit is shown.

Table 6.2: Construction of the luminosity function in M_J bins. N_s is the number of single sources, N_b is the number of binary sources, and N is the total number of stars calculated as $N = N_s + 2N_b$. The completeness factor applied is 0.95 throughout. The implied binary fraction, b_f is calculated as $\frac{N_b}{N_s+N_b}$. The density $\Phi(M)$ and its error are in units of $10^{-3}pc^{-3}$.

M_J	N_s	N_b	σ_{N_s}	σ_{N_b}	N	σ_N	N_{adj}	$\sigma_{N_{adj}}$	b_f	σ_{b_f}
9.5	231.720	54.025	15.076	6.293	339.771	33.711	357.654	35.485	0.189	0.010
10.0	170.339	32.266	12.958	4.987	234.870	28.976	247.231	30.501	0.159	0.010
10.5	111.612	17.088	10.501	3.694	145.789	23.481	153.462	24.717	0.133	0.011
11.0	70.611	5.425	8.383	1.945	81.460	18.744	85.748	19.731	0.071	0.008
11.5	59.710	4.094	7.674	1.784	67.897	17.161	71.471	18.064	0.064	0.008
12.0	39.830	1.500	6.241	1.071	42.830	13.955	45.084	14.689	0.036	0.005

Table 6.3: The luminosity function in M_J bins with $\langle\frac{V}{V_{max}}\rangle$. The density $\Phi(M)$ and its error are in units of $10^{-3}pc^{-3}$.

M_J	$\Phi(M)$	$\sigma_{\Phi(M)}$	$\langle\frac{V}{V_{max}}\rangle$	$\sigma_{\langle\frac{V}{V_{max}}\rangle}$
9.5	4.991	0.495	0.522	0.075
10.0	3.450	0.426	0.534	0.091
10.5	2.142	0.345	0.527	0.074
11.0	1.197	0.275	0.500	0.072
11.5	0.997	0.252	0.487	0.083
12.0	0.629	0.205	0.498	0.113

Table 6.4: Binary fraction, luminosity function and $\langle V/V_{max}\rangle$ statistic in M_G bins with uncertainties. $\Phi(M)$ and its uncertainty are in units of $10^{-3}pc^{-3}$.

M_G	b_f	σ_{b_f}	$\Phi(M)$	$\sigma_{\Phi(M)}$	$\langle V/V_{max}\rangle$	$\sigma_{\langle V/V_{max}\rangle}$
12.5	0.188	0.011	8.381	0.569	0.548	0.102
13.0	0.144	0.010	6.450	0.487	0.552	0.053
13.5	0.189	0.015	4.672	0.425	0.533	0.072
14.0	0.163	0.015	3.568	0.366	0.555	0.074
14.5	0.160	0.017	2.666	0.316	0.577	0.067
15.0	0.104	0.012	2.045	0.267	0.517	0.053
15.5	0.056	0.007	1.730	0.237	0.492	0.061
16.0	0.075	0.011	1.488	0.223	0.524	0.067
16.5	0.025	0.004	1.350	0.204	0.499	0.086

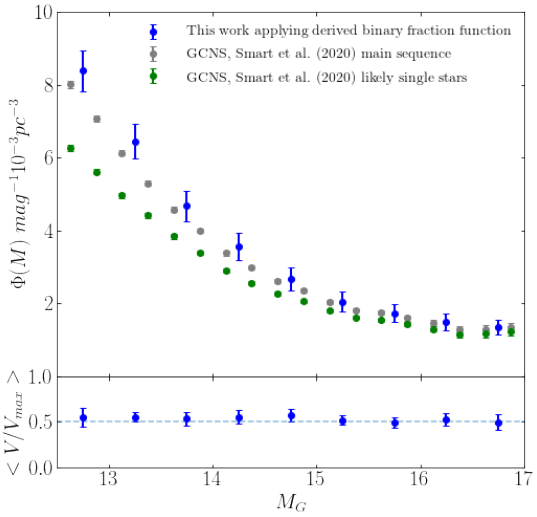

Figure 6.14: The luminosity function in 0.5 magnitude intervals of M_G.

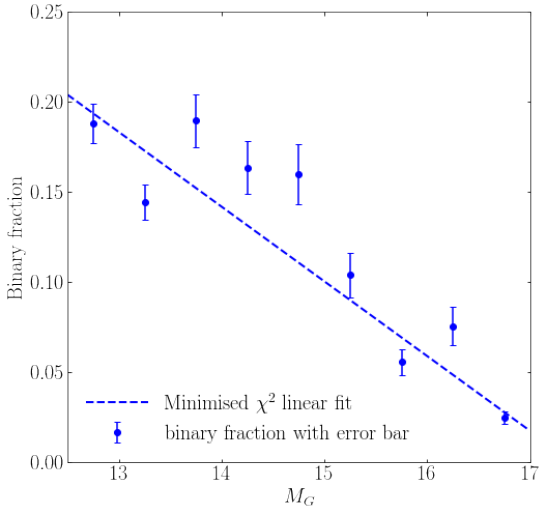

Figure 6.15: Calculated binary fraction with uncertainties for each M_G bin. A least squares linear fit is shown.

6.5 Discussion

6.5.1 Luminosity function

We compare our results to three other studies that seek to calculate the space density and luminosity function of the late-M and early-L dwarfs. Cruz et al. (2007) presents a 20 pc, volume-limited sample of 99 ultracool dwarfs in 91 systems and estimates the J-band luminosity function. As can be seen in Figure 6.16, our results compare favourably with Cruz et al. (2007) for $M_J > 10.5$ where this study begins.

Warren et al. (2021) estimate the luminosity function for a large homogeneous sample of ultracool dwarfs within 350 pc of the Galactic plane as part of their calculation of the local vertical density distribution. Again our results using *Gaia* EDR3 data closely match these results over the narrower M_J range 10.5 to 12.0. It should be noted that this study uses the binary fraction estimate from Laithwaite & Warren (2020) in its estimate.

As was discussed in Warren et al. (2021), our results are a factor of around two lower than a recent study by Bardalez Gagliuffi et al. (2019). This work presents a volume-limited sample of 410 ultracool dwarfs from M7 to L5 within 25 pc. The majority of this sample has astrometric distance measurements (80% from *Gaia* DR1 parallax measurements). The sample is determined to have completeness of 62% for the late-M dwarfs and 83% for the early-L dwarfs. This sample is compiled from a large number of individual surveys with a literature binary fraction of only $7.5^{+1.6}_{-1.4}$%. The authors state that they expect that the true ultracool binary fraction to be closer to 10%-20%.

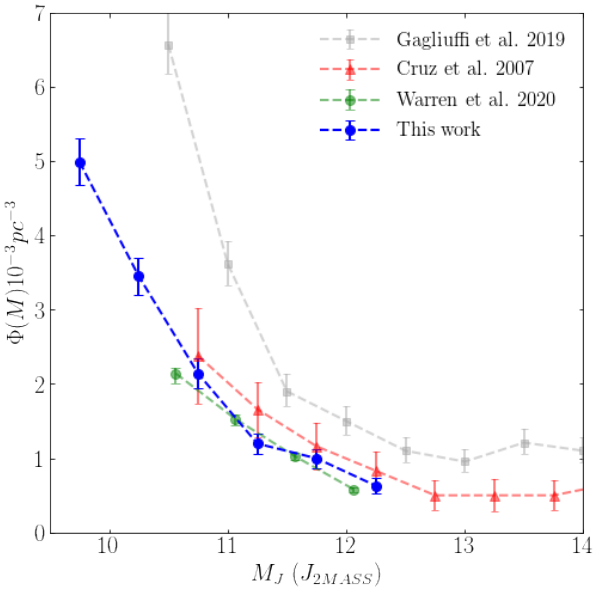

Figure 6.16: The luminosity function calculated in this paper compared to other similar calculations.

6.5.2 Wide binaries

The number of resolved binaries in our sample is expected to be very small. Typical mean separations for stellar masses in range 0.075-0.15 $M_{\odot}$ are around 7 AU with very few > 100 AU (Winters et al. 2019*a*). In order to identify all potential resolved wide binaries in our sample, we found sources with match radius < 50" to another sample source and calculated the distance between them. This wide match criterion would capture resolved wide binaries with separation distances of up to 500 AU at 10pc and 1500 AU at 30pc. With such a wide match radius we risk identifying chance matches. We found 7 candidates pairs in our sample and calculated the distance to each component of each pair. Each component in a wide binary should be at essentially the same distance in pc. In our sample, 95% of sources have a distance error (σ_{dist_50}) < 0.22 pc therefore any wide binary candidate system with Δ dist_50 > 0.22pc was treated as a chance matching and therefore removed as a wide binary candidate pair. 1 candidate system was removed as a chance matching. The remaining 6 systems represents an upper limit on the number of wide resolved binaries. Since this represents < 1% of our sample our results ignore potential resolved wide binaries.

6.5.3 Missing binaries

In order to check for potentially missing binaries we look at the distribution of singles and binaries in the final sample as a function of distance. First we stratify our final sample into 10-20 pc and 20-30 pc subsamples and calculate the overall binary fraction as well as the binary fraction as a function of M_J for each subsample showing the minimum χ^2 linear fit. We find an average binary fraction of 12.5% in the 10-20 pc range and 15.0% in the 20-30 pc range (compared to 14.3% for 10-30 pc) and the binary fraction as a function of M_J for each range is shown in Figure 6.17. There is little difference between the two samples (both in trend and binary fraction) and given the sample weighting towards sources > 20 pc, any potentially missing binaries in the range 10-20 pc has a relatively minor effect on the overall result.

6.5.4 Comparison of binary fraction to other studies

The binary (or multiplicity) fraction is the number of systems with a stellar companion to the total number of systems in a population. Equivalently the single star fraction is the fraction of stellar systems without a stellar companion. Strictly these definitions relate the multiplicity fraction (MF) and the fraction of multiple systems in a population. However multiple systems of higher orders than 2 are very rare (e.g. Laithwaite & Warren 2020, Winters et al. 2019*a*) and not considered for the purposes of this analysis. In effect we are assuming that the binary fraction is the same as the MF. It has been known for a long time that the multiplicity fraction of stars steeply increases with stellar mass (e.g. Duchêne & Kraus 2013*a*) with the lowest mass stars (M < $0.1M_{\odot}$) having a multiplicity fraction and companion frequency of $\sim$ 20-22% (Winters et al. 2019*a*). Our work suggests that this trend continues through the late-M dwarfs and early-L dwarfs right down to the stellar limit with the multiplicity fraction of the lowest mass stars < 10%.

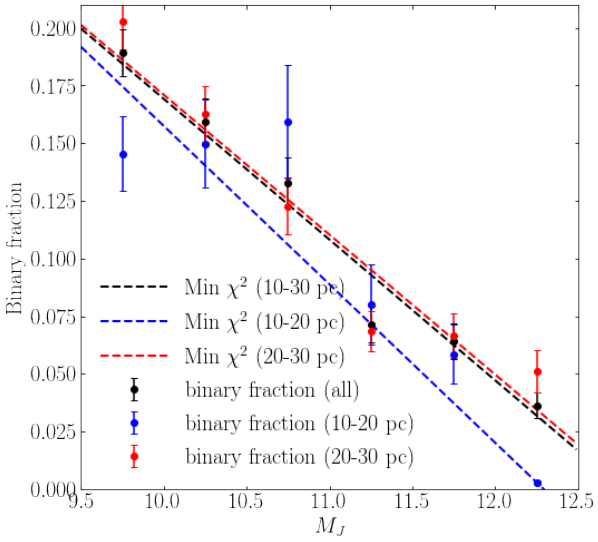

Figure 6.17: Binary fraction as a function of M_J for 10-20 pc and 20-30 pc

We compare our result to our previous work Laithwaite & Warren (2020) where we found a binary fraction of 16.5±0.8% for M7 to M9.5 with corresponding M_J of 9.92 to 11.25. Applying our binary fraction relation as a function of M_J as shown in Figure 6.13 to the sample of late M dwarfs from Laithwaite & Warren (2020) we calculate a weighted average binary fraction of 17.1% well within our uncertainty range and therefore consistent with our previous work.

Given the size and completeness of our sample, we take a statistical approach to determining the binary fraction based on over-luminosity and utilising the character of ultracool binary systems based on the binary mass fraction determined by Laithwaite & Warren (2020). This work showed that late-M dwarf binaries exist almost exclusively in equal-mass 'twin' systems.

The very low multiplicity fraction of the lowest mass stars has potential implications for the abundance of stable planetary systems. Single stars unperturbed by a companion are perhaps more likely to maintain stable and more populous planetary systems. There is also some evidence from Hardegree-Ullman et al. (2019) that planetary occurrence rates increase with declining mass through the M dwarfs.

6.6 Summary & conclusions

Using the Gaia Catalogue of Nearby Stars (GCNS) derived from *Gaia* EDR3, we prepared an all-sky, statistically complete (> 95%) sample of 1122 ultracool dwarfs from 10 to 30 pc. This is the largest and most complete sample of ultracool dwarfs in this range to date. From this sample we statistically identify single and binary systems and estimate the binary fraction as a function of M_J and M_G and calculate the field luminosity function in M_J and M_G of the ultracool dwarfs M7 to L2.5 . In line with other studies we show that the luminosity function falls steeply towards the end of the main sequence. We find a linear relation between binary fraction and absolute magnitude that falls sharply from $b_f \sim 20\%$ at an M_J =9.5 to b_f <5% for M_J >12 corresponding to spectral types ∼ M6.0 through L2.5. This is in line with our previous

work on the binary fraction for the late-M dwarfs (Laithwaite & Warren 2020).

Anticipated future work would involve extending this approach to determining the field luminosity function and binary fraction deeper into the ultracool dwarf population > L2.5. This is not yet possible with current *Gaia* data while maintaining a very high level of completeness. By loosening the completeness constraint it should be possible to prepare a sample of objects to $\sim$ L5 with around 50% completeness and handle the associated selection bias effects (Gaia Collaboration et al. 2020).

Chapter 7

Vertical density profile close to the galactic plane

7.1 Introduction

The exceptional astrometry and photometry available in *Gaia* EDR3 provides the opportunity to investigate, in fine detail, the vertical structure of the Milky Way and derive the star formation rate history of the local solar neighbourhood. For the first time we have accurate distance determinations using *Gaia* parallax measurements for millions of stars in the solar neighbourhood extending above and below the galactic plane.

The vertical density of stars for $|z| < 1$ kpc is often modelled by an exponential with scale height ~ 300 pc (e.g. Gilmore & Reid 1983, Bochanski et al. 2010) however such a functional form suggests a sharp peak in density at the galactic plane. Other authors (e.g. Ferguson et al. 2017, Bennett & Bovy 2019) have suggested a sech^2 distribution which softens the exponential close to the galactic plane. A more useful functional form to explore the density distribution close to the galactic plane is the generalised sech distribution proposed by van der Kruit (1988) and parameterised in the following form by Dobbie & Warren (2020) and Warren et al. (2021):

$$\rho(z) = 2^{-\alpha}\rho_0 \text{sech}^{\alpha}(z/\alpha z_h)$$

This function tends to an exponential distribution at large $|z|$ and the degree of softening close to z = 0 is controlled by the α parameter where $\alpha = 0$, 1 and 2 are equivalent to the exponential, sech and sech^2 distributions respectively as shown in Figure 7.1. Vertical density models that include both a thin and thick disk component contain two terms, combinations of sech^{α} and exponential, different scale height parameters and a factor f that controls the proportional of thick disk.

We proceed by first preparing a series of cylindrical, colour-dependent and volume-limited samples perpendicular to the plane taking account of *Gaia* magnitude completeness limits and reddening. Using these samples we calculate the vertical density profile in colour bins (equivalent

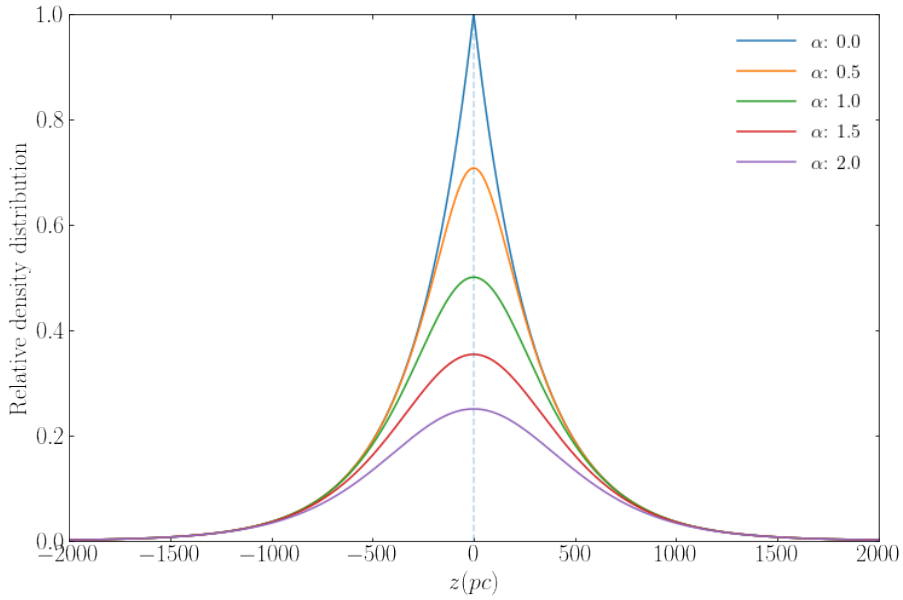

Figure 7.1: Illustrative vertical density distributions based on $sech^{\alpha}$ distribution at various α showing degree of softening in the central plane. The vertical scale height is assumed to be 300 pc (for illustrative purposes only).

to spectral type) and fit to various functional forms for the vertical density distribution. We aim to determine the softening parameter, α, close to the galactic plane and the thin disk scale height as a function of *Gaia* colour, $G_{BP}-G_{RP}$, from 0.50 to 1.30. Using this result we calculate integrated number counts in each colour bin, extending above and below the galactic plane, and compare to simulated sample of FGK stars based on an initial mass function and evolved with PARSEC isochrones. We fit count histograms of our simulated sample by colour bins at different ages to directly determine the star formation history in the solar neighbourhood in a manner not previously available.

7.2 The Data

7.2.1 The Sample

Initially we prepare colour samples of *Gaia* sources in a 500 pc radius cylindrical volume centred on the sun for G magnitudes between 7 and 17 using the query shown in Figure 7.2 (adapted from Bennett & Bovy 2019). The *Gaia* EDR3 catalogue is essentially complete between these magnitude limits (Bennett & Bovy 2019) and we further select stars with parallax > 0 and parallax over error > 5. A cylindrical volume is more suitable for investigating the vertical structure close to the plane than a conical volume due to the significantly higher number of objects at low $|z|$. *Gaia* offers the opportunity to create volume complete samples of stars over such a large cylindrical volume.

At this stage we are selecting a magnitude-limited set of objects across a wide range of M_G

in a particular colour range in $G_{BP} - G_{RP}$ where M_G calculated as

$$M_G = -5 * log_{10}(1000/\varpi) + 5 + G$$

between wide limits for M_G of 0 and 10. We then make distance cuts based on upper and lower M_G limits to get a complete volume-limited sample as shown in Figures 7.3 and 7.4. The median parallax over error for the combined sample is 97.7 (or parallax error of 1.02%).

```
SELECT bp_rp, (1/parallax)*sin(RADIANS(b)) as z,
(1/parallax)*cos(RADIANS(b)) as r,
phot_g_mean_mag as g, parallax, parallax_error,
(1000/parallax) as dist_pc, parallax_over_error,
-5*LOG(1000/parallax)/LOG(10)+5+phot_g_mean_mag as mg
FROM gaiaedr3.gaia_source
WHERE parallax > 0
AND parallax_over_error > 5
AND (1/parallax)*cos(RADIANS(b)) < 0.5
AND phot_g_mean_mag BETWEEN 7 and 17
AND bp_rp BETWEEN {bprp_min} AND {bprp_max}
AND mg BETWEEN 0 AND 10
```

Figure 7.2: *Gaia* query to select samples in a 500 pc cylindrical volume in a given $G_{BP} - G_{RP}$ colour and M_G range.

Within this cylindrical volume we select 16 colour bins in $G_{BP} - G_{RP}$ from 0.50 to 1.30 in 0.05 intervals. This colour range is chosen to ensure that the maximum vertical distance $|z|$ in each colour bin at the limiting magnitude of G = 17 is at least 1 kpc. These objects correspond to stars with spectral type from around F2V to K4V covering a mass range of 0.7 to 1.5 $M_\odot$ based on the updated *Mean Dwarf Stellar Color and Effective Temperature Sequence*[1] (Pecaut & Mamajek 2013).

7.2.2 Setting the bright and faint limits in M_G

In order to select main sequence stars only and not subgiants we make an upper and lower cut in M_G based on the cross-sectional number count of sources within each colour bin. As expected the number count distribution of sources peak sharply across a narrow range of absolute magnitudes representing the central main sequence band (see Figure 7.4). The earlier colour bins show a skew towards the brighter magnitudes as the older stars have begun to evolve off the main sequence. Following a similar method to Bennett & Bovy (2019) we perform a Gaussian fit to the number count distribution fixing the mean and amplitude of M_G at argmax(N) and max(N) respectively. We then set our upper and lower M_G limits based on a $\pm 1.5\sigma$ interval of this Gaussian fit as shown by the dotted orange lines in the plots in Figure 7.4.

The resulting colour magnitude sample regions are shown in Figure 7.3 as rectangles and comprise 3,387,000 sources. The maximum and minimum distance for which our colour samples

[1] `http://www.pas.rochester.edu/ emamajek/EEM_dwarf_UBVIJHK_colors_Teff.txt`

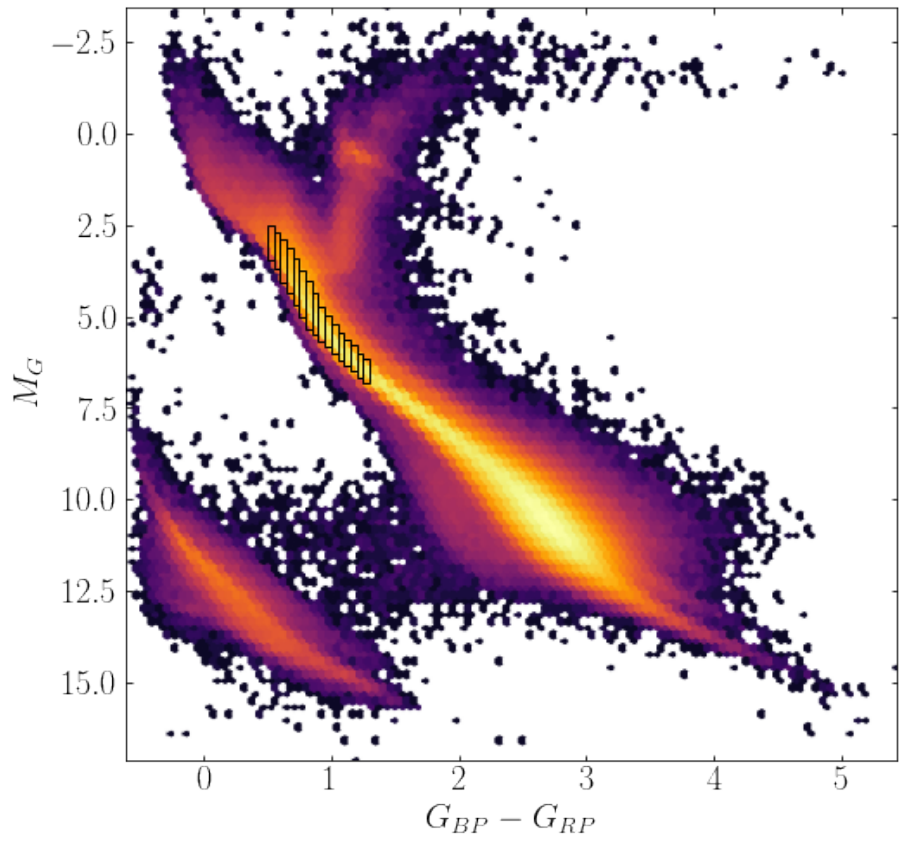

Figure 7.3: The 16 colour samples with $G_{BP} - G_{RP}$ from 0.50 to 1.30 and upper and lower M_G limits shown against the background of a *Gaia* colour-magnitude diagram.

are complete are determined by the associated bright and faint M_G limits.

$$d_{min} = 10^{\frac{G_{min} - M_{G,min} + 5}{5}}$$

$$d_{max} = 10^{\frac{G_{max} - M_{G,max} + 5}{5}}$$

and therefore,

$$|z|_{max} = \sqrt{d_{max}^2 - r_{cyl}^2}$$

.

where $G_{min} = 7$, $G_{max} = 17$ and $r_{cyl} = 500$pc.

The maximum vertical height $|z|$ ranges from 5,128 pc for the bluest $G_{BP} - G_{RP}$ 0.50-0.55 bin to 981 pc for the reddest $G_{BP} - G_{RP}$ 1.25-1.30 bin.

The minimum distance for each bin is < 80pc and much less than the radius of the cylindrical volume. As a result we are potentially missing objects within a small spherical volume around the sun embedded within our larger cylindrical volume. To correct for this we make a small volume-related adjustment to the number count close to the galactic plane in each colour bin.

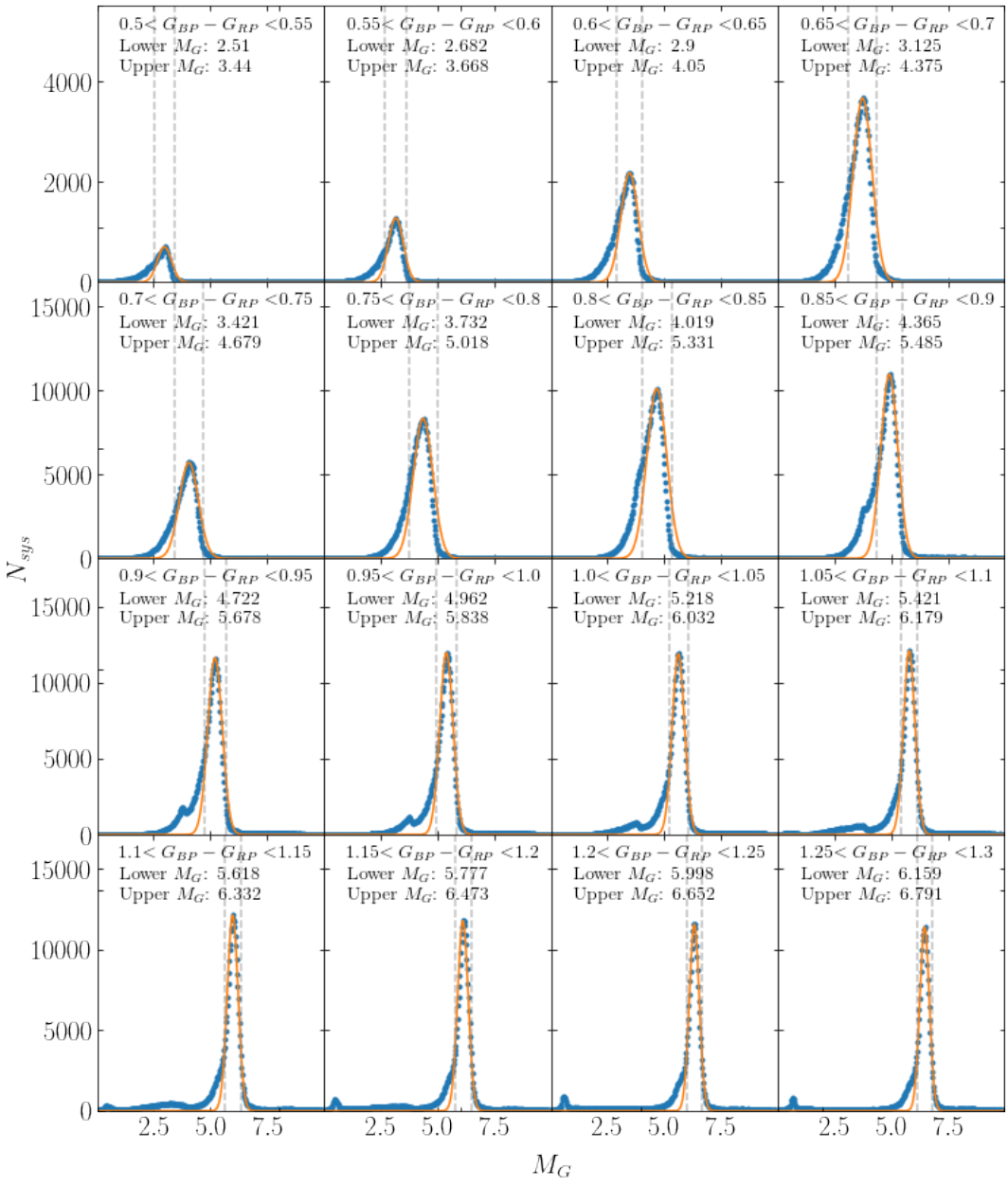

Figure 7.4: Histogram of counts in colour bins $G_{BP} - G_{RP}$ from 0.50 to 1.30 and absolute magnitude range M_G 0 to 10. These are vertical sections in the *Gaia* Colour-Magnitude diagram. We identify main sequence stars by determining upper and lower limit in M_G by fitting a Gaussian to this distribution and setting the range as $\pm$ 1.5σ from the mean M_G corresponding to maximum of N_{sys}.

7.2.3 Adjusting for reddening

Close to the galactic plane, reddening and extinction due to absorption by dust and gas are a concern. To quantify the effect of reddening we have calculated the cumulative reddening in magnitude units for points in a three-dimensional cylindrical volume around the sun with coordinates galactic longitude, l, radius in the galactic plane r, and vertical height z using the online tool[2] provided by Capitanio et al. (2017). The median and mean reddening for a given r and z, and averaged over l, is shown in Figure 7.5. We select the radii of our cylindrical volumes to ensure that the median reddening is $<< 0.05$. As expected, reddening is strongest close to the galactic plane where the density of dust and gas is greatest.

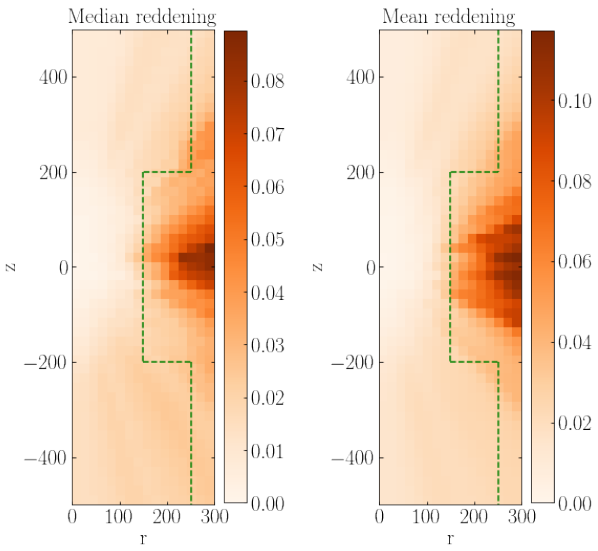

Figure 7.5: Median and mean reddening for a given radius, r, and vertical height z in pc from the galactic plane (Capitanio et al. 2017). Only the central region $|z| < 500$ pc is shown. Our radii limits for the cylindrical volumes are shown (green dotted lines)

To maximise the volume of our sample while minimising the effects of reddening we create three z-dependent cylindrical volumes and apply appropriate volume scaling factors. For $|z| <$ 200 we apply a radius of 150pc; for $|z|$ between 200 and 800pc we apply a radius of 250pc; and for $|z| >$ 800pc we apply a radius of 500pc. These limits are shown for the central region in Figure 7.5 as a green dotted line. Given that the greatest density of stars occurs in range $|z|$ $<$ 500pc, using a smaller volume close the plane has minimal effect on our number density and errors when we scale these to the larger radius volumes.

After selecting volumes to minimise reddening and z_{min} completeness, we transform our measured z distance to the galactic plane using $z_{\odot} = +20.3$pc (Bennett & Bovy 2019) and prepare a histogram of number counts by absolute vertical distance $|z|$ in 25pc intervals where we have scaled our number counts in the $r = 150$ pc and $r = 250$ cylinders to a cylinder of radius $r = 500$ pc. The furthest $|z|$ bin in each colour sample is determined by z_{max} rounded down to nearest 25pc. The result for the first seven bins for $|z|$ to 2 kpc is shown in Figure 7.6.

[2]https://stilism.obspm.fr/

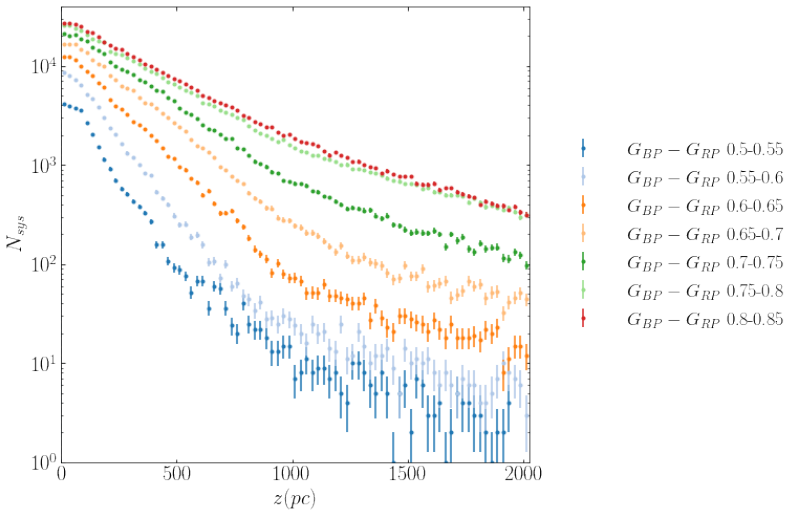

Figure 7.6: Histograms of number counts by $|z|$ for the first seven colour bins with BP-RP from 0.50 to 0.85 to limiting z_{max} for reddest bin of 2025pc. z_{max} is different in each case due to differing upper M_G limits and the faint G magnitude limit.

As observed in Figure 7.6, the first five bluest colour samples have a smaller scale height than the subsequent redder colour bins illustrating the scale height colour-dependence. We examine and quantify this relation in section 7.4.1.

7.3 Method

7.3.1 Selecting the Model

In order to select a suitable model for the vertical density distribution we select a 'test' colour bin and fit this to a number of commonly used functional forms from the literature. These include both two-component models (E.g. double exponential, double sech^2, sech^α + sech^β, sech^α + exponential) as well as one-component models (E.g. sech^α, Sersic models). We select the bin $G_{BP} - G_{RP}$ = 0.75-0.80 as our test sample as it has a sufficiently large maximum vertical distance with $|z_{max}| \sim 2.4$ kpc to accurately measure the thick disk component and shows relatively little evolved star depletion. We evaluate the fit of the various models against this 'test' sample with χ^2 and χ^2_ν statistics as shown in Figure 7.7

The sech^α + sech^β and the sech^α + exponential have almost identical χ^2_ν. After examining the posterior parameters distributions for both these functions, the beta parameter in the sech^α + sech^β was not particularly well constrained and close to zero. The sech^α plus exponential is a five-parameter model and special case of the general sech^α sech^β model where setting β equal to zero. In effect the second component becomes an exponential function. We therefore use the following five-parameter, two-component sech^α plus exponential model for the vertical number distribution:

$$N(z) = N_0 \left(\text{sech}^\alpha(\frac{z}{\alpha z_{thin}}) + f\text{exp}(\frac{-z}{z_{thick}}) \right)$$

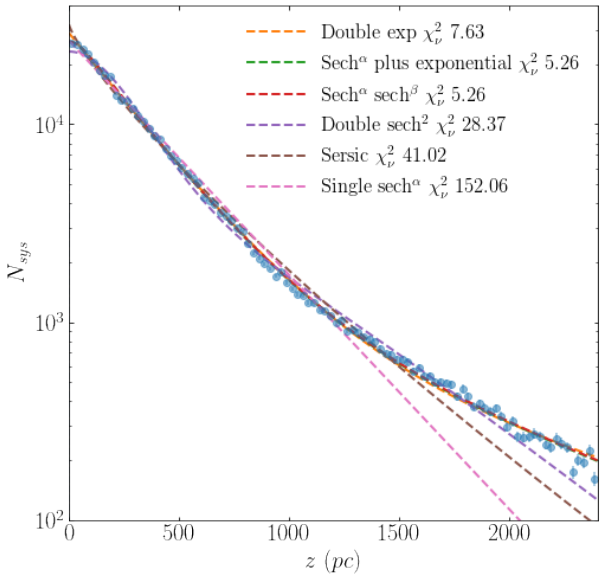

Figure 7.7: Various one- and two-component functional forms for the vertical density distribution fitted to 'test' colour sample with χ^2_ν statistics.

where N_0 is the normalisation constant; α is the shape parameter close to the galactic plane; z_{thin} is the thin disk scale height; z_{thick} is the thick disk scale height; and, f the fraction of the second or thick disk component to the total.

We use the following parameterisation for the sech$^\alpha$ density distribution following Dobbie & Warren (2020) as follows:

$$N(z) = N_0 \text{sech}^\alpha \left(\frac{z}{\alpha z_H} \right)$$

However also as noted in Dobbie & Warren (2020), sech$^\alpha \left(\frac{z}{\alpha z_H} \right)$ can be awkward to evaluate for small α and so we use the identity:

$$\text{sech}^\alpha \left(\frac{z}{\alpha z_H} \right) = 2^\alpha \exp(\frac{-z}{z_H}) \left(1 + \exp(\frac{-2z}{\alpha z_H}) \right)^{-\alpha}$$

This gives the following final functional form for our sech$^\alpha$ plus exponential model:

$$N(z) = N_0 \left(2^\alpha \exp(\frac{-z}{z_{thin}}) \left(1 + \exp(\frac{-2z}{\alpha z_{thin}}) \right)^{-\alpha} + f \exp(\frac{-z}{z_{thick}}) \right)$$

7.3.2 Determining the thick disk scale height

Since the primary aim of this work is to determine the thin disk scale height and shape parameter close to the galactic plane, it is necessary to identify and remove any thick disk component from our samples. We estimate the thick disk scale height by selecting those colour samples with sufficiently large $|z_{max}|$ that will allow a reasonable determination of this parameter. Given that the proportion of thick disk to total stars is on the order of 8% and an indicative z_{thick} of 1 kpc,

determining a robust estimate for scale thick disk requires at least 1.5 times this scale height. For this reason we select the colour bins with $|z_{max}| > 2$ kpc corresponding to the seven bluest with $G_{BP} - G_{RP}$ from 0.50 to 0.85 (see Figure 7.6).

Fitting the sech$^{\alpha}$ plus exponential model to these first seven bins using MCMC parameter estimation yields best fit parameters and their errors shown in Figure 7.8.

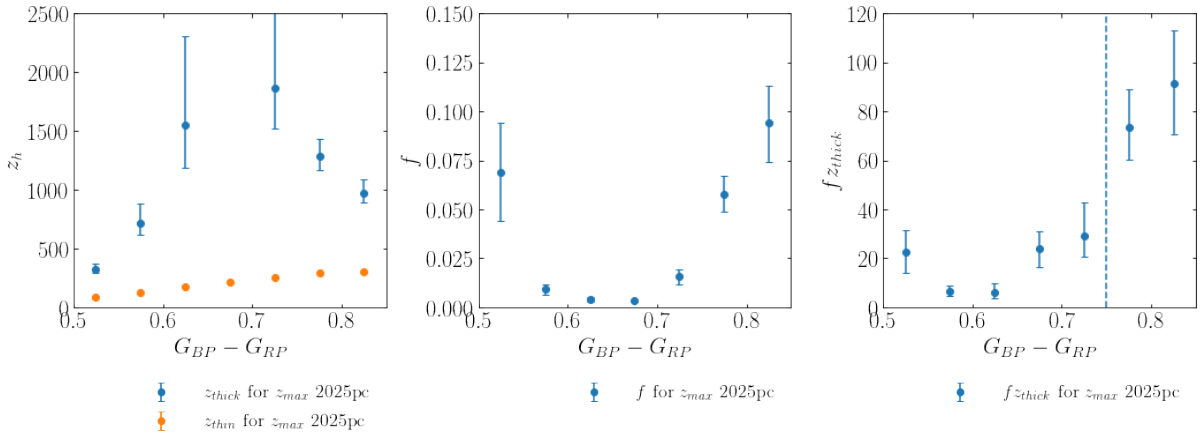

Figure 7.8: Fitted parameters for the seven bluest bins for $|z| < 2025$pc. These colour samples are used to determine where the thick disk is present and estimate z_{thick} and f. Plot shows median and 16th/84th percentile for each fitted parameter. The combined parameter f z_{thick} (right hand plot) shows that the thick disk is not present for $G_{BP} - G_{RP}$ colours bluer than 0.75 (blue dotted line) but is clearly present for redder colours.

The first five bins representing the bluest stars are distinct with a small value for f and/or a poorly constrained thick disk scale height. These bins represent the higher mass, shorter life stars of which the older stars in this sample will have evolved off the main sequence. We create a combined parameter, $f^{*}z_{thick}$ and their corresponding errors to demonstrate that there is effectively no thick disk component for colours $G_{BP} - G_{RP} < 0.75$ as expected given the estimated age of the thick disk. See section 7.5.4 for further discussion of this.

For $G_{BP} - G_{RP} \geq 0.75$, we estimate z_{thick} and f using an inverse-variance weighted average of our 0.75-0.80 and 0.80-0.85 samples. Using this method we find $z_{thick} = 1101$, and $f = 0.069$. As we are primarily interested in the thin disk and shape parameter close to the galactic plane (< 1 kpc) and therefore these approximate values are justified. We checked the sensitivity of our subsequent results for z_{thin} and α to changes in our estimated values for z_{thick} and f by applying upper and lower limits implied by our analysis above. We found that our results for z_{thin} and α were not particularly sensitive to changes in z_{thick} and f.

7.4 Results

7.4.1 The thin disk scale height and shape parameter close to the galactic plane

Using our estimate for z_{thick} and f we now determine the thin disk scale height and α parameter for each of our 16 colour bins. Again we fit using MCMC parameter estimation using the same sech$^{\alpha}$ plus exponential model but with z_{thick} and f fixed as described below. We assume that for bins where $G_{BP} - G_{RP} < 0.75$ (see Figure 7.8), f is effectively zero (i.e. there is no thick disk component) and so we are measuring the thin disk component only. For those bins where $G_{BP} - G_{RP} \geq 0.75$, we use our calculated values for z_{thick} and f above of 1101 pc and 0.069 respectively, and calculate z_{thin}, α and the normalisation as free parameters.

For this we consider the vertical density distribution $|z|$ from 0 to 1000pc in 25 pc distance bins adjusting for z_{min} completeness and $z_{\odot}$ as before. The posterior median and errors determined by 16th and 84th percentiles for each α and z_{thin} as a function of colour are shown in Figure 7.9. The corresponding functional fit using the median parameters are shown compared to the actual vertical density distribution data in Figure 7.10. We generate total thin disk number counts by integrating our sech$^{\alpha}$ thin disc model for a 500 pc cylinder in z from 0 to ∞ applying the best fit parameters for N_0, α, and z_{thin} for each $G_{BP} - G_{RP}$ bin. Our values for α, z_{thin} with their corresponding errors as well as our calculated integrated count of thin disk stars are shown in Table 7.1. In section 7.5.1 we use the parameterised model to calculated integrated count in each colour bin and fit to the simulated count histograms at various ages to directly derive the star formation history in the solar neighbourhood.

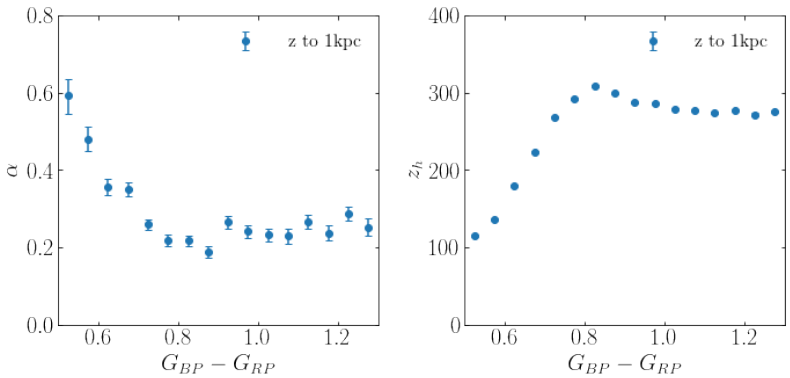

Figure 7.9: Fitted model parameters and associated errors from MCMC sampling for each of the 16 colour samples for $|z|$ to 1000pc.

We note that the values of α in table 7.1 are similar to the value found by Warren et al. (2021) of $0.29^{+0.12}_{-0.13}$ for a sample of 34,000 late M and early L-dwarfs within 350 pc of the galactic plane. This suggests that the value of α is fairly constant for stars redder than $G_{BP} - G_{RP}$ of ~ 0.75 covering a large range of masses from 1.1 $M_{\odot}$ down to the substellar limit.

We observe that z_{thin} exhibits a slight 'bump' in scale height at $G_{BP} - G_{RP}$ of ~ 0.8. We

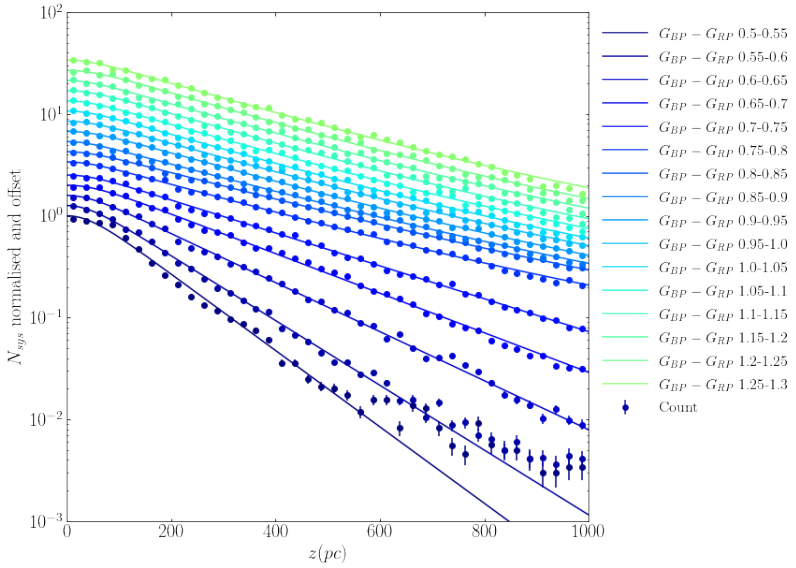

Figure 7.10: The plot shows the fitted model (solid colour lines) for each colour sample against the normalised histogram of number count. The histograms and fitted model are offset (on a logarithmic scale) to separate each sample.

performed various tests to check that this was a not an artefact of the data and found that this appears to be a real effect. While the thin disk scale height is remarkably constant for $G_{BP} - G_{RP} > 0.9$, the colour samples 0.75 to 0.900 show a slight increase in thin disk scale height peaking at around 0.8. The most likely explanation for this 'bump' is the presence of subgiants that have migrated into adjacent, bluer bins but not yet evolved out of our M_G limited regions. These objects would be some of the oldest stellar constituents of colour samples with BP-RP of 0.75-0.90 representing stars with main sequence lifetimes in excess of 8 Gyr.

7.5 Discussion

7.5.1 Direct determination of the star formation history and average age of the thin disk

A detailed description of the thin disk as it is today contains important evidence of its historical evolution and age. Typically assessments of the star formation history of the disk are made using velocity dispersion and heating mechanisms or a priori formation assumptions. We now use our structural parameters as a function of colour to directly determine the star formation history and average age profile of the thin disk.

To do this we create a synthetic population of stars based on a total initial total mass of 1 million $M_\odot$ using the broken power law Initial Mass Function (IMF) of Kroupa (2001)[3]. This translates to around 2.3m stars in total of which 333,000 have an initial mass in our range of interest from 0.5 to 2.0 $M_\odot$. For each source we randomly sample from a metallicity distribution based on a simple Gaussian distribution with mean [Fe/H] = -0.12 and dispersion 0.17

[3]Using python code adapted from https://github.com/keflavich/imf

Table 7.1: Best fit parameters for thin disk.

$G_{BP} - G_{RP}$	Integrated count	α	z_{thin} (pc)
0.525	28124.0	$0.592^{+0.042}_{-0.048}$	$115.7^{+1.7}_{-2.0}$
0.575	61411.0	$0.480^{+0.033}_{-0.032}$	$136.4^{+1.2}_{-1.2}$
0.625	113445.0	$0.356^{+0.022}_{-0.021}$	$180.2^{+1.1}_{-1.1}$
0.675	187861.0	$0.351^{+0.018}_{-0.018}$	$223.3^{+1.1}_{-1.1}$
0.725	266054.0	$0.259^{+0.014}_{-0.015}$	$268.5^{+1.1}_{-1.1}$
0.775	360433.0	$0.218^{+0.015}_{-0.014}$	$292.0^{+1.4}_{-1.2}$
0.825	399842.0	$0.218^{+0.013}_{-0.013}$	$308.7^{+1.4}_{-1.3}$
0.875	367918.0	$0.187^{+0.015}_{-0.015}$	$298.8^{+1.3}_{-1.4}$
0.925	334734.0	$0.265^{+0.015}_{-0.016}$	$286.8^{+1.4}_{-1.3}$
0.975	310833.0	$0.241^{+0.016}_{-0.016}$	$286.7^{+1.5}_{-1.5}$
1.025	292502.0	$0.233^{+0.016}_{-0.016}$	$278.4^{+1.4}_{-1.5}$
1.075	268492.0	$0.229^{+0.018}_{-0.019}$	$277.1^{+1.5}_{-1.5}$
1.125	253006.0	$0.266^{+0.019}_{-0.019}$	$273.6^{+1.5}_{-1.5}$
1.175	231477.0	$0.238^{+0.019}_{-0.019}$	$276.4^{+1.6}_{-1.6}$
1.225	222515.0	$0.287^{+0.018}_{-0.019}$	$271.7^{+1.7}_{-1.7}$
1.275	209870.0	$0.252^{+0.022}_{-0.021}$	$275.5^{+1.7}_{-1.7}$

dex (Aumer & Binney 2009). This Gaussian metallicity relation ignores the low metallicity tail commonly associated with thick disc stars but since we are exclusively concerned with modelling the thin disk this approximation is appropriate. Aumer & Binney (2009) and Holmberg et al. (2007) conclude that there is no significant dependence of mean metallicity with age in the solar neighbourhood and therefore the metallicity distribution may be used as a reasonable approximation for all ages. We interpolate the metal fraction Z from [Fe/H] using the conversion table provided in Aumer & Binney (2009) based on solar abundances $Z_{\odot} = 0.017$.

Our synthetic population represents a population of intermediate and low-mass stars at birth with a distribution of metallicities consistent with the thin disk in the solar neighbourhood.

We now seek to evolve this population forward using the state-of-the-art PARSEC (PAdova-TRieste Stellar Evolution Code) isochrones code (Bressan et al. 2012, Chen et al. 2014, 2015, Tang et al. 2014, Marigo et al. 2013, Pastorelli et al. 2019, Chen et al. 2019, Pastorelli et al. 2020) in the EDR3 photometric system[4].

We extract 60 isochrones corresponding to ages from 1 to 12 Gyr in 1 Gyr increments and with metallicities Z from 0.005 to 0.025 in five 0.005 increments. The resulting isochrones together with our colour-magnitude sample regions are shown in Figure 7.11 where we show the pre-main sequence, main sequence, and subgiant branch sections.

For each set of isochrones for a given age, we interpolate $G_{BP} - G_{RP}$ and M_G for every source in our simulated population of stars based on its mass (M) and metallicity (Z) using a bivariate B-spline representation of the isochrone surface. Figure 7.12 shows the resulting synthetic population in colour-magnitude space and the corresponding isochrones by age. We

[4]http://stev.oapd.inaf.it/cgi-bin/cmd

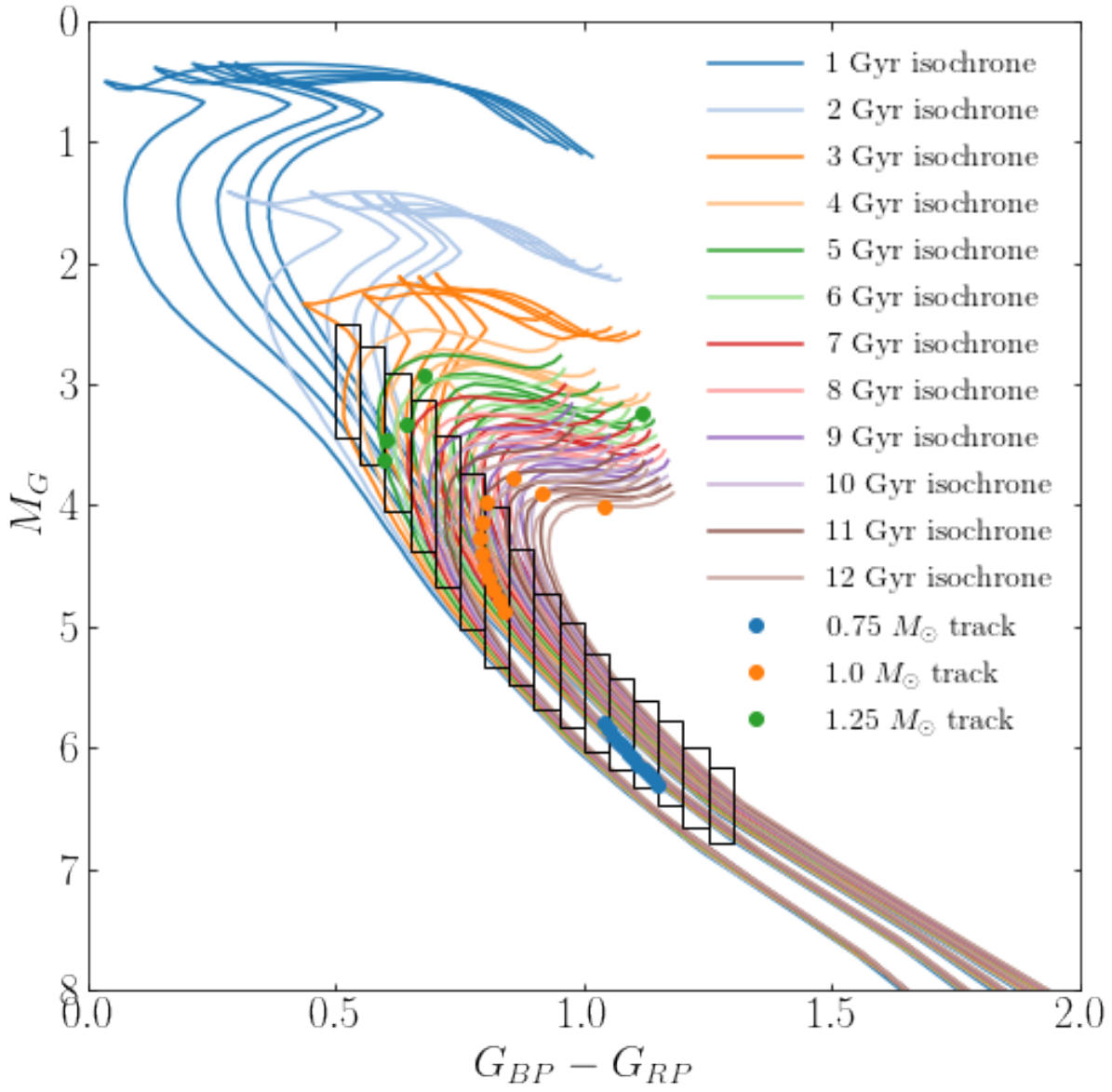

Figure 7.11: PARSEC isochrones by age and metallicity. For a given age, five metallicity isochrones have been extracted from the PARSEC code for Z from 0.005 to 0.025. The isochrones show the pre-main sequence, main sequence and subgiant branch sections only. The rectangles are our selected sample *Gaia* colour-magnitude regions for a given $G_{BP} - G_{RP}$ colour. For illustrative purposes we show the evolution of representative masses 0.75, 1.0, 1.25 $M_\odot$ (blue, orange and green dots).

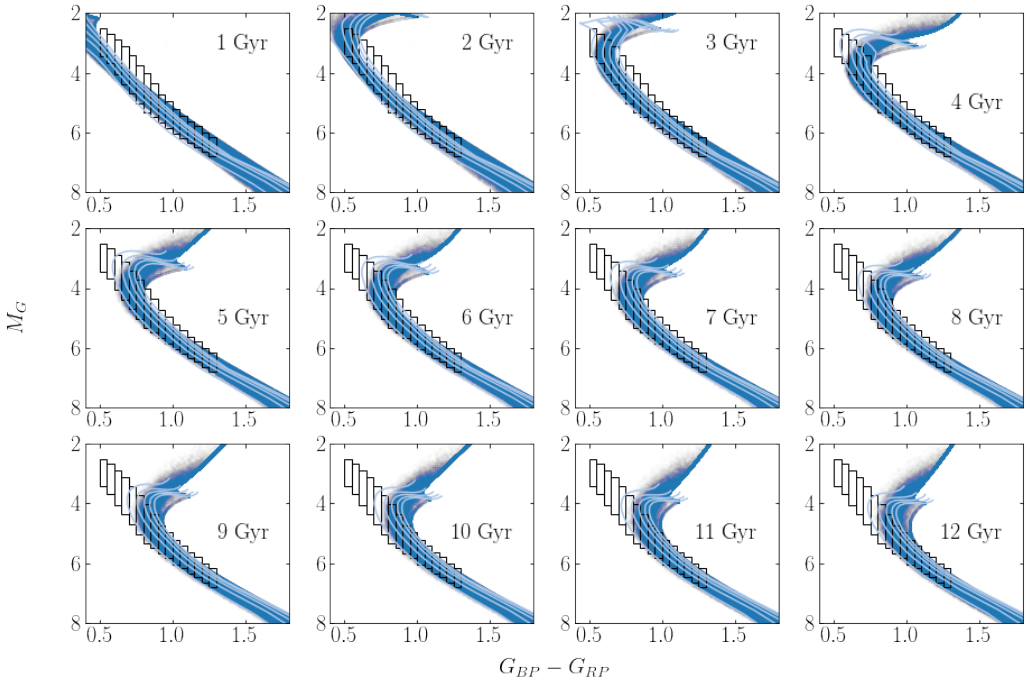

Figure 7.12: The synthetic population of stars at birth with masses between 0.5-2.0 M$\odot$ and [Fe/H] sampled from a gaussian distribution of metallcities with mean [Fe/H] = -0.12 and dispersion 0.17 dex (Aumer & Binney 2009) evolved using PARSEC isochrones (pale blue lines) from 1 to 12 Gyr. The rectangles are our selected sample *Gaia* colour-magnitude regions for a given $G_{BP} - G_{RP}$ colour.

then count the number of stars in each colour bin region after applying the upper and lower M_G limits, and plot histograms of our synthetic population as a function of colour and age as shown in Figure 7.13.

7.5.2 Selecting our colour range for the fit

Ideally we would use the full set of 16 colour bins with $G_{BP} - G_{RP}$ from 0.5 to 1.3 in fitting the age histograms to the integrated count data. However we found that there was very poor fit for $G_{BP} - G_{RP}$ beyond $\sim$ 1.15 which required further investigation. We traced this to an abrupt change in the gradient of the isochrone around 0.75 $M_\odot$ and $G_{BP} - G_{RP}$ between 1.2 and 1.3 as shown in the right hand plot of Figure 7.14. This creates a step in the histograms of number count in this colour range. We do not know what is causing this kink and it is unlikely to be a physical effect. We ruled out possible transitions between the PHOENIX and COMARCS spectral codes used to calculate the isochrones. One possibility suggested (Leo Girardi - private communication) is that at this $T_{\rm eff}$ some specific molecules are turned on in the PHOENIX spectral code as it is too time consuming to compute molecular equilibrium at higher $T_{\rm eff}$ where their impact is limited. Given the impact on our histograms for $G_{BP} - G_{RP} > 1.15$, we fit to the

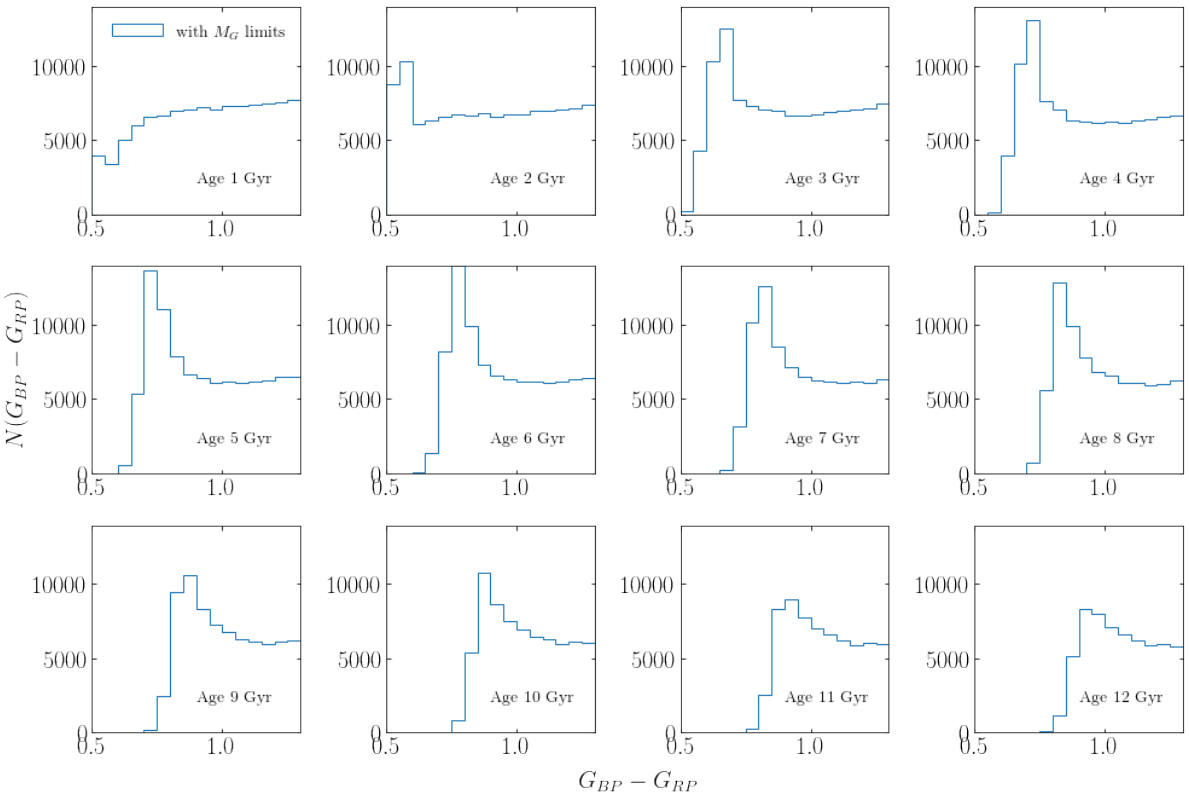

Figure 7.13: Histograms of number count for our synthetic population by 16 $G_{BP} - G_{RP}$ colour bins from 0.5 to 1.3 and by age.

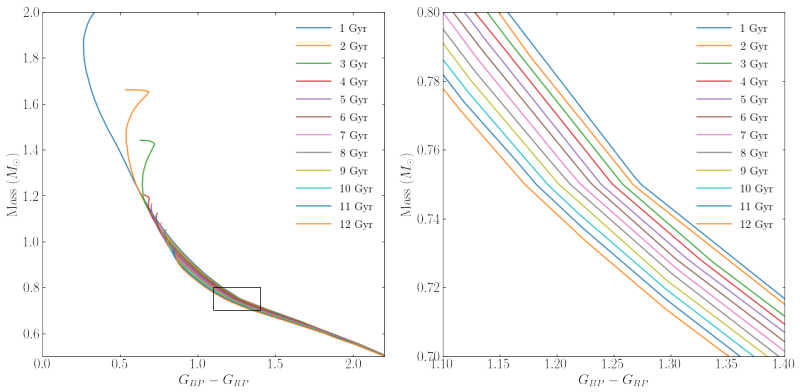

Figure 7.14: Isochrone of initial mass vs. $G_{BP} - G_{RP}$ for single metallicity (Z=0.015) for ages 1 to 12 Gyr. The right hand plot shows an enlargement of the boxed region. The isochrones show a abrupt change in gradient.

colour range 0.5 to 1.1 consisting of 12 data points for z_{thin} and including the region of rapidly increasing scale height peaking at a maximum and then falling slightly to a steady value.

7.5.3 Determining the integrated count error

Given the large number of stars in each colour bin sample, a Poisson error representing random errors would be unrealistically small. To try and quantify the systematic errors in the limit where the random errors are very small, we perform a simple least squares fit to the integrated count data for six of our histograms with ages 1, 3, 5, 7, 8, 11 Gyr. Based on this fit, we determine an error that ensures that the χ^2 of the overall fit is equal to six, the number of degrees of freedom for this fitting[5], as shown in the left hand plot of Figure 7.15.

7.5.4 Star formation history and average age of the thin disk

By finding the relative weighting of each age histogram (Figure 7.13) that fit the integrated counts of the thin disk we can directly determine both the star formation history (SFH) and the average age of stars as a function of colour.

We find the best fit weighting for six age histograms (i.e. 1, 3, 5, 7, 9, 11 Gyr) to the integrated counts using a Markov Chain Monte Carlo (MCMC) method based on the emcee sampler (Foreman-Mackey et al. 2013*b*) by minimising the χ^2. We use a subset of our available age histograms to prevent overfitting and degeneracy between adjacent age histograms. We adopt broad positive priors to ensure the histogram weightings are not negative.

The main results of this analysis are shown in Figure 7.15. The left hand plot shows the integrated number count of objects by colour bin (black circles) with the weighted age histograms shown as a stacked bar.

The weightings applied (and their respective errors) are shown in the centre plot. These are normalised by integrating to one for better comparison with the functional curves showing the

[5]In this case we have 12 data points and 6 histograms giving six degrees of freedom.

fitted star formation rate (based on a normalised gamma-distribution - see below). The resulting star formation history does not show a constant level of star formation over the life of the thin disk. We see maximum star formation rate occurs around 6-7 Gyr ago falling steeply towards older times with little star formation occurring $>$ 10 Gyr ago.

Using the weighting of each age histogram we calculate the average age of stars in each colour bin as shown in the right hand plot of Figure 7.15. The bluest bins containing the highest mass stars have the smallest average age as many of these stars formed when the star formation rate was at its greatest have since evolved off the main sequence.

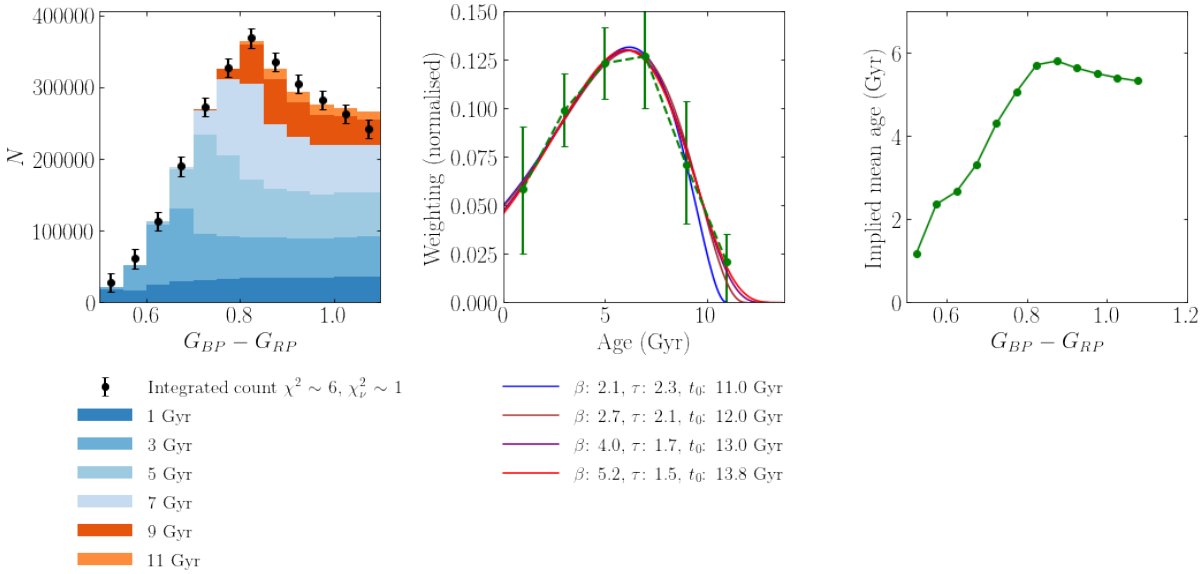

Figure 7.15: Left hand plot shows the integrated number count with errors for a 500 pc radius cylindrical volume with |z| from 0 to +inf (black dots and error bars) compared to the best fit weighted age histograms for 1, 3, 5, 7, 9, 11 Gyr. The central plot shows the histogram weightings by age shown as the median and 16th/84th percentiles of the posterior distributions. The histogram is normalised and represents the star formation history of the thin disk. The curves show fitted normalised gamma distributions with a range of parameters. The right hand plot shows the derived average age of the stars in each colour bin.

Our derived SFH is not consistent with the often used exponential star formation rate. We fit our histogram weightings to a normalised gamma-distribution, the functional form used by Ryan et al. (2017) for the star formation rate, as below:

$$\psi(t : N, \beta, \tau) = N \left(\frac{1}{\tau \Gamma(\beta + 1)} \right) \left(\frac{t}{\tau} \right)^{\beta} \exp \left(-\frac{t}{\tau} \right) \tag{7.1}$$

where t is the time since the formation of the thin disk of the Milky Way from $t = 0$ to t_0, the age of the thin disk. The parameter β represents the power law index in the early years, τ represents the exponential decay rate at later times, and $\Gamma(\beta + 1)$ is the gamma function normalisation. Given that our histogram weightings measure age as the time from today we

transform t in equation 7.1 using $t' = t_0 - t$. The parameter N is required to adjust the normalisation of our fit. Our histogram of star formation is normalised for positive t (i.e. the past), however our functional form is normalised for all times including t<0 i.e. the future. A proportion of the gamma distribution occurs in the future as shown in the central plot of Figure 7.15.

For every realisation of the star formation histogram weightings in our MCMC analysis we fit a normalised gamma distribution and determine the parameters N, β, and τ. We found leaving t_0, the age of the thin disk, as a free parameter generated values for t_0 much older than the age of the Universe due to the exponential decay of the gamma distribution at large t. We would anticipate that the value of t_0 would lie somewhere between 11 Gyr and 13.8 Gyr, between the oldest non-zero weighting and the canonical assumed age of the universe, so we apply values of t_0, representing the age of the thin disk, of 11, 12, 13, and 13.8 Gyr.

The resulting gamma distribution curves are plotted using the median parameter values from the MCMC realisations for each of $t_0 = 11$, 12, 13 and 13.8 Gyr are shown in Figure 7.15 (centre plot). Assuming, for example t_0 of 12 Gyr, the median parameters (N, β, τ) are (1.162, 2.744, 2.089). Maximum star formation occurs at $t_0 - \beta\tau$ suggesting that maximum star formation occurred 6.0 to 6.3 Gyr ago. Given how similar the fits are for $t_0 \geq 12$ Gyr and the exponential growth in the early formation of the thin disk, we are not sure on the validity of specifying an age of the thin disk.

Our SFH compares with recent estimates for the age of the thin disk of 7.4-8.2 Gyr (Kilic et al. 2017) and 7.5±0.7 Gyr (Liu & Chaboyer 2000) and 7.9±0.7 Gyr (Sandage et al. 2003). Our results are consistent with those of Haywood et al. (2013) that found, using an age-metallicity relation and age-vertical velocity dispersions, that the onset of thin disk star formation occurred between 8 - 10 Gyr ago and that thick disk star formation ceased altogether from $\sim$ 8 Gyr .

We can determine the average age of the thin disk as a function of colour by weighting the contribution of each histogram by its respective age. The resulting average age in each colour bin is shown in Figure 7.15 (right hand plot). As we would expect the average age for the bluest colours is young as many of the older stars will have evolved off the main sequence and only the more recently formed stars remain. Our average age profile peaks around $G_{BP} - GRP \sim$ 0.85 at 5.8 Gyr and declines slightly beyond that. Stars of this colour have a mass and main sequence lifetime similar to the sun.

7.5.5 Age-velocity dispersion relation

We now consider the other information in this dataset; the scale height as a function of colour. Combined with the SFH we can use this to derive the disk heating mechanism as follows. The age-velocity dispersion relation is often described using a simple power law $\sigma(\tau) \propto \tau^{\beta}$ where τ is age and β is the exponent of the velocity component. Hänninen & Flynn (2002) provide a summary of empirically derived values for β in the range 0.25 and 0.6. Recent observational values for β include 0.35 (Aumer & Binney 2009), 0.33 (Binney et al. 2000) and 0.34 (Nordström

et al. 2004). This relation between age and velocity dispersion suggests a heating mechanism by which velocity dispersion increases over time.

Theoretical models predict a range of values for β dependent on their underlying assumptions: $\beta_z \sim \frac{1}{4}$ (Lacey 1984, Hänninen & Flynn 2002), $\beta \sim \frac{1}{3}$ (Spitzer & Schwarzschild 1953), and $\beta \sim \frac{1}{2}$ (Wielen 1977, Fujimoto 1980). The age-velocity relation is explained using disk heating caused by gravitational perturbations of non-axisymmetric galactic structures, such as the spiral arms and central bar, giant molecular clouds (Spitzer & Schwarzschild 1951, Spitzer & Schwarzschild 1953) as well as satellite galaxies (Aumer et al. 2016, Hänninen & Flynn 2002) although this is far from being fully understood.

Using virialised equilibrium and simple dimensional arguments we show that the squared velocity dispersion (in the vertical direction) is proportion to the scale height as follows:

$$mgz \sim \frac{1}{2} m \langle v_z^2 \rangle \tag{7.2}$$

Assuming the mean velocity $\langle v_z \rangle = 0$, then:

$$\langle v_z^2 \rangle \sim \sigma_{v_z}^2 \sim z_h \sim \tau^{2\beta} \tag{7.3}$$

We take each histogram weighting vector from our MCMC chain in the SFH analysis above (after the burn-in period) and calculate the corresponding average age profile, $\langle \tau \rangle$. We then find the parameters β and normalisation N based on a maximum likelihood fit using the relation:

$$z = N \langle \tau \rangle^{2\beta} \tag{7.4}$$

This gives posterior distributions for β and N as shown in Figure 7.16. Using this method we find $\beta = 0.333 \pm 0.019$ based on the median and 16/84th percentile in line with other recent observational measurements (Aumer & Binney 2009, Binney et al. 2000, Nordström et al. 2004).

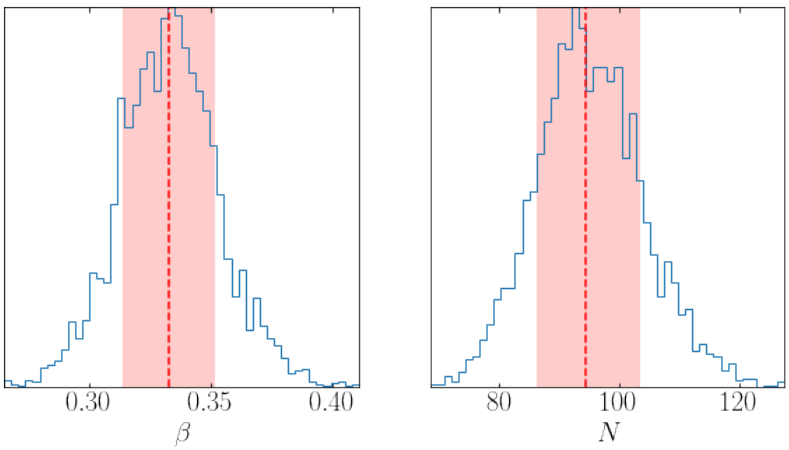

Figure 7.16: The distribution of maximum likelihood values for β and N using the MCMC chain of histogram weightings. The median (red dotted line) and 16th/84th percentile region (shaded region)

7.6 Summary & conclusions

The precise astrometry and photometry of the *Gaia* spacecraft has allowed us prepare large, colour-dependent and complete, cylindrical samples of FGK stars ($0.7 < \mathrm{M/M}\odot < 1.5$) for $|z|$ to 1 kpc. This has enabled us to measure the vertical density distribution, the thin disk scale height, and shape parameter of the solar neighbourhood in fine detail.

We find that the vertical density distribution for the thin disk is best described by a sech^{α} model where the α, the parameter that describes the softening close to the galactic plane, has a colour-dependence as shown in Figure 7.9 and Table 7.1.

In addition we find a colour-dependent thin disk scale height with a colour edge around $G_{BP} - GRP \sim 0.8$ representing a deficit of main sequence stars that have evolved off the main sequence. This has a direct relationship to the distribution of stars by colour and age in the main sequence.

We use our derived number density of stars by colour we fit to a series of simulated number count histograms representing the colour profile of stars at certain ages. We simulate these number count histograms using PARSEC isochrones in *Gaia* colours for a range of metallicities and ages. The best fit weightings of these age histograms allow us to directly determine the star formation rate history of the thin disk and its average age profile as a function of colour. We find a good fit to the star formation rate using a gamma distribution with maximum star formation occurring between 6.0 and 6.3 Gyr ago.

We hope that these results based on *Gaia* EDR3 data will be of use to theoretical studies of the Milky Way formation, evolution and history.

Chapter 8

UCD classification and anomaly detection

8.1 Introduction

The classification and ordering of observations is an important scientific process to help understand the underlying physical mechanisms and structure at work in any system. Historical examples include the taxonomy of all living things into Kingdom, Phylum, Class, Order, Family, Genus, and Species. Similarly the organisation of known elements into the periodic table led to a greater understanding of atomic structure. In astronomy we are faced with such a wide array of objects that accurate and consistent classification is an essential activity. The Morgan–Keenan (MK) system is the most widely used stellar classification scheme in astronomy today. It organises stars into spectral types described by letters OBAFGKM from the hottest (O) to the coolest (M). Since the discovery of very-low mass stars and brown dwarfs LTY classes have been added to this sequence. Within each spectral class, objects are further subdivided into types given by the numeric 0 (hottest) to 9 (coolest) as well as a luminosity class corresponding to its evolved state i.e. supergiants (I), bright giants (II), regular giants (III), subgiants (IV), main-sequence stars (V), subdwarfs (VI), white dwarfs (D). Some important features of the MK classification system are (i) that it is empirically derived based on observed spectral features and not tied to a physical interpretation; (ii) types are defined by a specific star's spectrum which acts as the standard or anchor for that type; and (iii) objects are classified by direct comparison to the standard.

Ultracool dwarf (UCD) spectra contain complex spectral features in the near IR driven by a mixture of deep atomic and molecular absorption bands and lines as well as rapidly changing spectral energy distribution (SED) due to evolving atmospheric composition, dynamics and clouds. UCD spectra are driven by complex interactions between mass, molecular composition, temperature, age, metallicity and magnetic properties that are not as prominent in higher mass stars. Figure 8.1 shows the standard spectra for spectral types M7 to T8 from 1 to 2.5 μm. As a result an accurate and homogeneous method of classifying ultracool dwarfs has been challenging to construct.

The initial L dwarf sequence was largely based on optical spectra (Kirkpatrick et al. 1999) which was was then extended into the NIR as discussed in Chapter 3. The standard template objects for the L and T dwarfs were constructed when only relatively few objects were known and these objects span a range of surface gravities and metallicities. It has been recognised for some time that the current classification system requires further refinement to account for gravity- and metallicity-dependent features (e.g. Kirkpatrick 2005; West et al. 2011; Allers & Liu 2013).

In this chapter we consider a range of alternative and automated methods of classification taking advantage of the larger samples now available. We aim to see if machine learning might offer alternative classification methods or teach us something new about the UCD sequence. We use both broad-band photometric and low resolution spectroscopic data in this work.

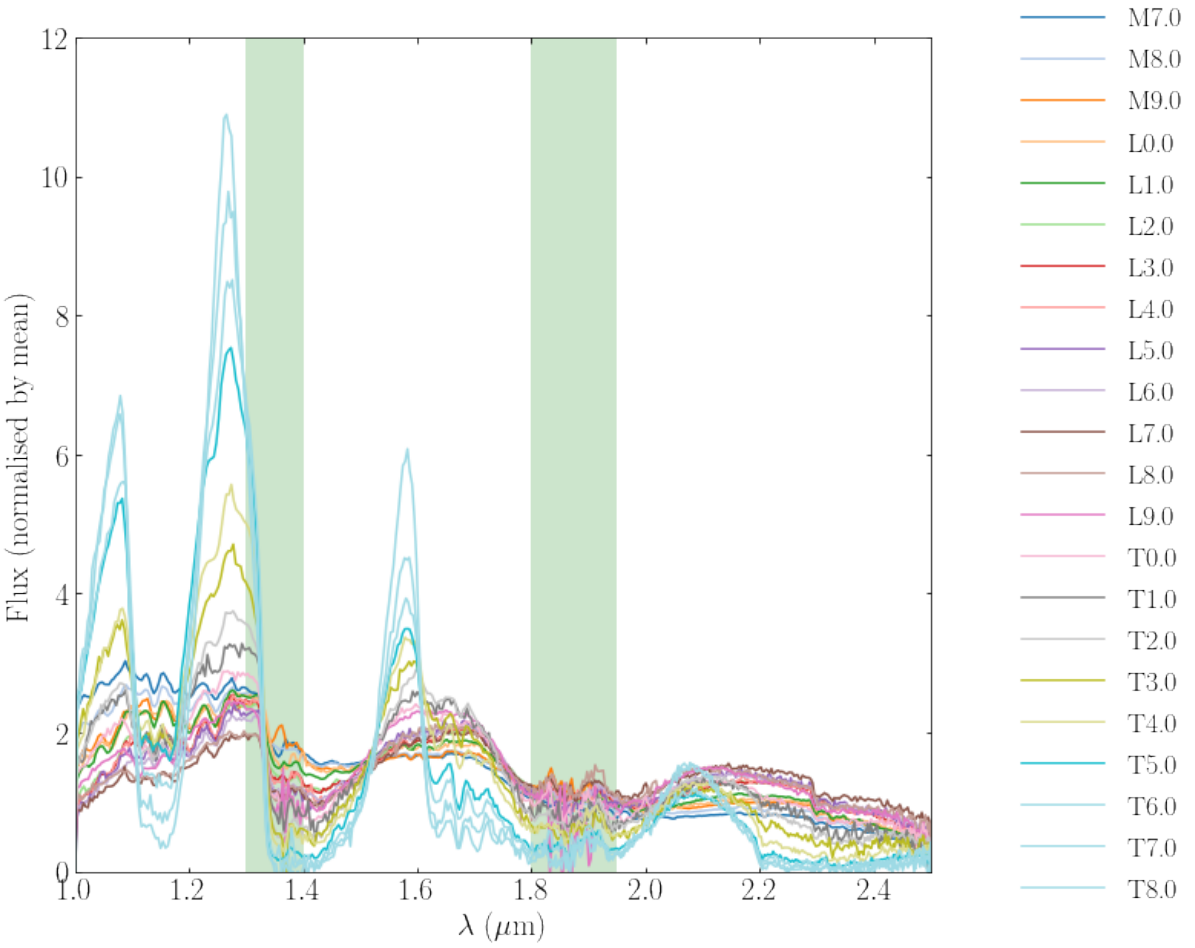

Figure 8.1: Spectra for SpeX standards M7 to T8 normalised by their mean flux. The telluric bands (green) are excluded from the calculation of the mean flux due to low S/N.

Historically substellar objects have been classified in one of four following ways: (i) by comparison to a specific 'standard' or 'anchor' objects (see Figure 8.1); (ii) by comparison to spectral indices (e.g. Burgasser, Geballe, Leggett, Kirkpatrick & Golimowski 2006; Allers & Liu

2013) in the form of flux density ratios of specific features and/or colour bands (see Table 8.1); (iii) by comparison to a set of synthetic standard spectra (e.g. Allard et al. 2012); and (iv) by comparison to a set of photometric template colours (e.g. Schmidt et al. 2015*a*; Skrzypek et al. 2015, Skrzypek et al. 2016).

8.2 Method

We perform a critical analysis of UCD classification methods for spectral types M7 to T9 in order to evaluate and propose alternative classification methods. We begin by evaluating the current spectral standards as a suitable sequence of benchmarks by:

1. Quantifying the evolution of the overall shape or morphology of the spectral energy distribution (SED) through the sequence;
2. Calculating new spectral indices based on ratios of the equivalent width of key absorption features; and,
3. Creating synthetic standard spectra using a recent sample of high quality and reclassified L-dwarf spectra (Schneider et al. 2014) and compare these to the current standards.

We then apply the following machine learning and deep learning methods to our UCD photometric and spectroscopic data in order to evaluate their potential for classification, feature extraction, anomaly detection and generating synthetic spectra:

1. Tree-based ensemble supervised machine learning;
2. Non-linear dimensionality reduction; and,
3. Variational autoencoders (VAEs), a type of artificial neural network.

From the population of brown dwarfs with an observed spectrum, spectral 'standard' objects have been selected as template spectra for a given spectral type e.g. Kirkpatrick et al. (1999) for the L-dwarfs; Burgasser et al. (2002) and Geballe et al. (2002) for T-dwarfs. New objects are classified by comparison to these standard spectra. This can be performed quantitatively by minimising χ^2 between the normalised standard and target object however this method is not always deemed to generate a correct classification due to low resolution observations, variability within a spectral type due to gravity or metallicity, and the number of peculiar objects. As a result the quantitative calculation is performed as a guide with the final classification performed by eye. As well as introducing inaccuracies and inconsistencies such a manual approach is not practical as the number of observations and candidate objects increase.

Constructing and measuring spectral indices is another convenient method to classify objects. This method also requires spectroscopic data in order to calculate these indices that are based on ratios between specific spectral features or bands which can be shown to follow a relation

by spectral type. For example Burgasser, Geballe, Leggett, Kirkpatrick & Golimowski (2006) constructed a series of spectral indices for the T-dwarfs (see Figure 8.1) and compared these to the SpeX standard objects (solid circles) and other SpeX spectra (see Figure 8.2) as a way of defining spectral types.

Index (1)	Numerator Range[a] (μm) (2)	Denominator Range[a] (μm) (3)	Feature (4)
H_2O-J[b]	1.140–1.165	1.260–1.285	1.15 μm H_2O
CH_4-J[b]	1.315–1.340	1.260–1.285	1.32 μm CH_4
H_2O-H[b]	1.480–1.520	1.560–1.600	1.4 μm H_2O
CH_4-H[b]	1.635–1.675	1.560–1.600	1.65 μm CH_4
H_2O-K	1.975–1.995	2.080–2.100	1.9 μm H_2O
CH_4-K[b]	2.215–2.255	2.080–2.120	2.2 μm CH_4
K/J	2.060–2.100	1.250–1.290	$J-K$ color

[a] Wavelength range over which flux density (f_λ) is integrated.
[b] Primary classification indices.

Table 8.1: Definitions of NIR spectral Indices for T-dwarfs. Numerator and denominator is the wavelength range over which the flux density is integrated. Indices in bold are those considered to be most accurate for classification. Table from Burgasser, Geballe, Leggett, Kirkpatrick & Golimowski (2006).

Photometric classification methods avoid the need for spectroscopy by using more readily available and often more accurate photometric data. This method uses a set of template colours to define a spectral type. Skrzypek et al. (2015) and Skrzypek et al. (2016) used eight colour bands drawn from UKIDSS, SDSS and ALLWISE data across the range 0.75 to 4.60μm to create template colours for the M5 to T8 dwarfs as shown in Figure 8.3. This method was shown to be accurate to within one spectral type.

Machine learning and deep learning as a classification method has been applied to a wide variety of astronomical objects in recent years. Common machine learning methods include random forests, Naive Bayes, neural networks and support vector machines (e.g. Dubath et al. 2011, Peng et al. 2012, Rimoldini et al. 2012). Deep learning methods such as convolutional neural networks (e.g. Pasquet-Itam & Pasquet 2018) and variational autoencoders (e.g. Portillo et al. 2020) are also being applied. Often the challenge with applying these methods is the explainability of the outcome. A summary of the machine learning and dimensionality reduction methods discussed in this chapter is included in appendix B.7.

Recently Aganze et al. (2021) attempted to identify and classify a remote population of ultracool dwarfs using the Hubble Space Telescopes' Wide Field Camera 3 (WFC3). They identified 164 ultracool dwarfs in 0.6 deg^2 using low-resolution near-infrared spectroscopic data from the WFC3 Infrared Spectroscopic Parallel Survey (WISPS) and the 3D-HST parallel survey. They used a variety of techniques to isolate and classify UCD sources from $>$ 200,000 spectra includ-

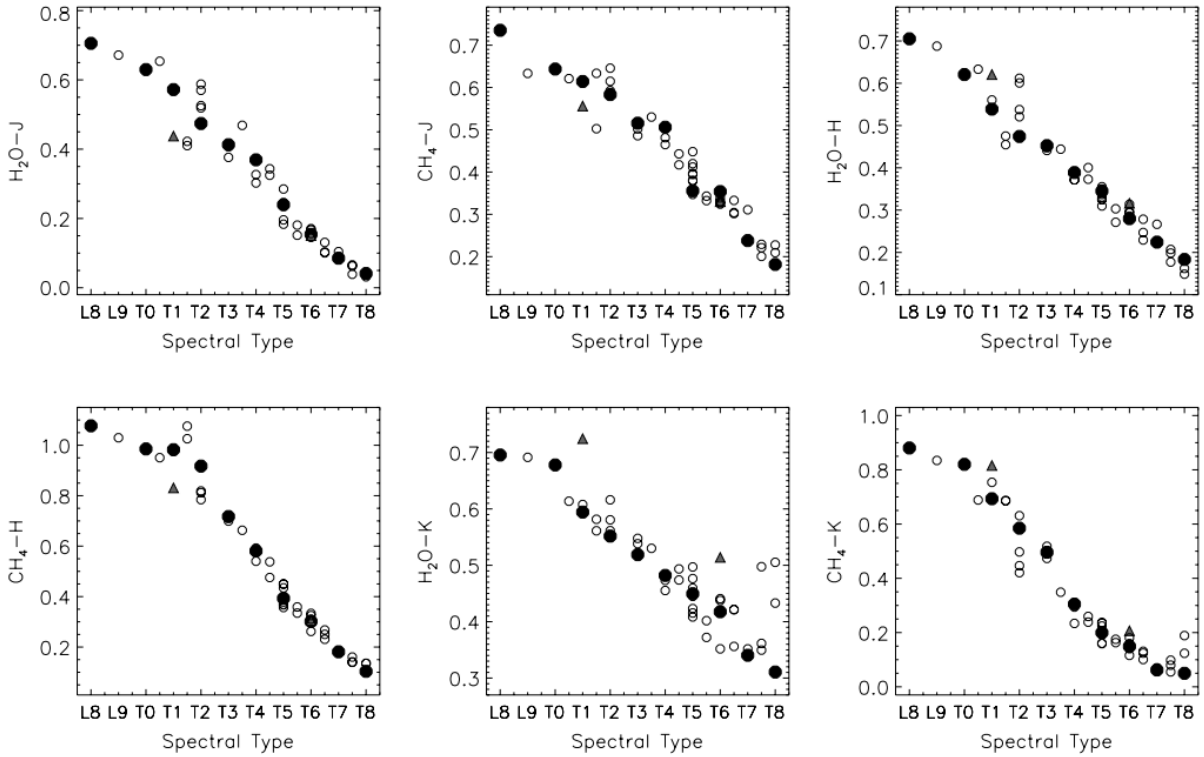

Figure 8.2: NIR spectral Indices as a function of spectral type. Solid circles are SpeX standard objects, unfilled circles are other SpeX prism objects; triangles are pecular objects. Figure from Burgasser, Geballe, Leggett, Kirkpatrick & Golimowski (2006).

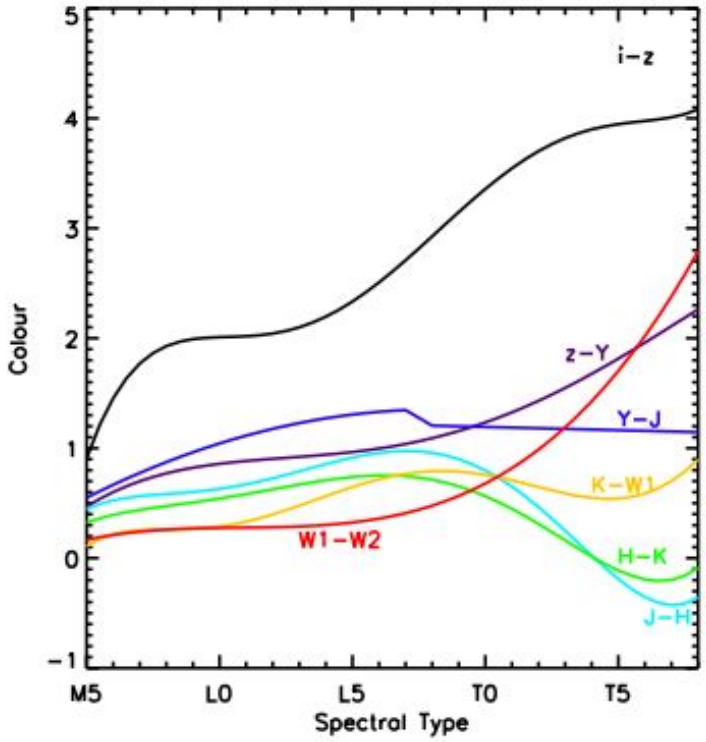

Figure 8.3: Template colours for photometric classification using $izYJHKW1W2$ passbands. Figure from Skrzypek et al. (2015)

ing spectral indices and supervised machine learning[1] trained on low-resolution spectra from the SpeX Prism Library demonstrating the potential of this technique for UCD identification using low-resolution spectroscopy.

8.3 Data

8.3.1 Photometry

Our photometric data set (Skrzypek et al. 2015, Skrzypek et al. 2016) consists of an homogeneous and classified sample of 1361 point sources of L and T dwarfs as described in 5.8. This photometric catalogue contains 8-band photometry $izyJHKW1W2$. The majority of sources have full 8-band photometry however a small number of sources are missing i, z, $W1$ or $W2$ data and these sources are removed. The sources cover a wide range of distances and so to remove the effect of distance we calculate a set of colours against the central J band e.g. $i - J$, $z - J$ etc. The remaining data consists of 1255 sources of 7 colours ('features') and a spectral sub-type ('class' or 'label').

For the ensemble supervised learning in section 8.8, we add photometry for 33,665 late-M dwarfs to the L and T dwarfs. This homogeneous sample of late-M dwarfs was prepared and

[1]Specifically random forest, deep neural network (DNN) and convolutional neural network (CNN)

classified by Ahmed & Warren (2019) using the same method as Skrzypek et al. (2015) above. Ahmed & Warren (2019) data includes $izYJHK$ bands but not $W1$ or $W2$. For the purposes of section 8.8 we use 6-band photometry to create 5 colours referenced to the J band (the 'features') with a spectral sub-type (the 'class' or 'label'). The resulting data consists of 35,026 UCD sources.

8.3.2 Spectroscopy

The primary source of UCD spectra for our analysis is the SpeX Prism Library (Burgasser 2014). The SpeX Prism Library is a repository of over 3000 low-resolution, near-infrared spectra, primarily of very-low mass dwarf stars and brown dwarfs, obtained with the SpeX spectrograph mounted on the 3m NASA Infrared Telescope Facility on Mauna Kea, Hawaii. Spectroscopic data is retrieved from the SpeX Prism Library using the SpeX Prism Library Analysis Toolkit (SPLAT) Burgasser & Splat Development Team (2017)[2]. SpeX data is prepared and processing as follows:

1. Extract all available raw spectra from SpeX library with SPLAT
2. Remove spectra with either null spectral type; spectral type outside the range M7.0 to T9.0; or, with missing or zero flux.
3. Select flux measurements between 0.9-2.4 microns. The vast majority of spectra have around 560 flux measurements in this range however they are not consistently spaced across wavelength.
4. Resample all spectra to 500 linearly spaced wavelengths between 0.9 and 2.4 microns using the *SpectRes* spectral resampling module (Carnall 2017).
5. Normalise spectra using the SPLAT normalize function.

The resulting sample contains 1696 normalised and resampled spectra for UCDs ranging from M7.0 to T9.0 as shown in table 8.2.

8.4 Spectral morphology

In this section, we investigate a number of approaches to quantify the overall morphology of the SED by spectral type. The SpeX prism library identifies a standard spectrum for each spectral type as shown in Figure 8.4. These are the sources that have been selected to most closely represent the ideal standard spectra for a given spectral type i.e. L3. and is often used as the primary source of comparison when classifying new sources. We show the main telluric regions[3] as well as some of the major CH_4, FeH and H_2O bands.

[2]The SpeX Prism Library Analysis Toolkit (SPLAT) is a python-based spectral access and analysis package designed to interface with the SpeX Prism Library. It is built on common python packages. Library was cloned from https://github.com/aburgasser/splat/ on 21 October 2021.

[3]The regions of high atmospheric absorption resulting in low S/N

Spectra type	Number
M7.0	109
M8.0	288
M9.0	113
L0.0	67
L1.0	234
L2.0	178
L3.0	61
L4.0	31
L5.0	82
L6.0	78
L7.0	112
L8.0	41
L9.0	45
T0.0	60
T1.0	19
T2.0	28
T3.0	17
T4.0	14
T5.0	35
T6.0	37
T7.0	28
T8.0	18
T9.0	1

Table 8.2: Number of spectra by spectral type in sample.

To quantify the morphology of the standard spectra from M7 to T9, we first normalise the flux by its mean over the range 1.0 to 2.5μm excluding the telluric regions between 1.35 and 1.40μm and 1.80 and 1.95μm. As a result the integrated flux for each standard is a constant value to aid comparison. From this we calculate the squared flux difference between adjacent standards as shown in Figure 8.5 and examine the resulting trend in Figure 8.6. There is a steady increase in the total root-squared flux difference as the sequence progresses that is approximately linear (as shown in the upper plot of Figure 8.6) however the difference in total absolute flux between adjacent types is highly uneven. For example the difference in flux between L2 to L3, L3 to L4, and L5 to L6 is particularly minor. The largest flux differences are seen from L1 to L2 and from T4 to T5. On this crude measure the evolution is far from smooth between adjacent standards although the evolution looks more consistent on a cumulative basis and increases as shown with the fitted exponential.

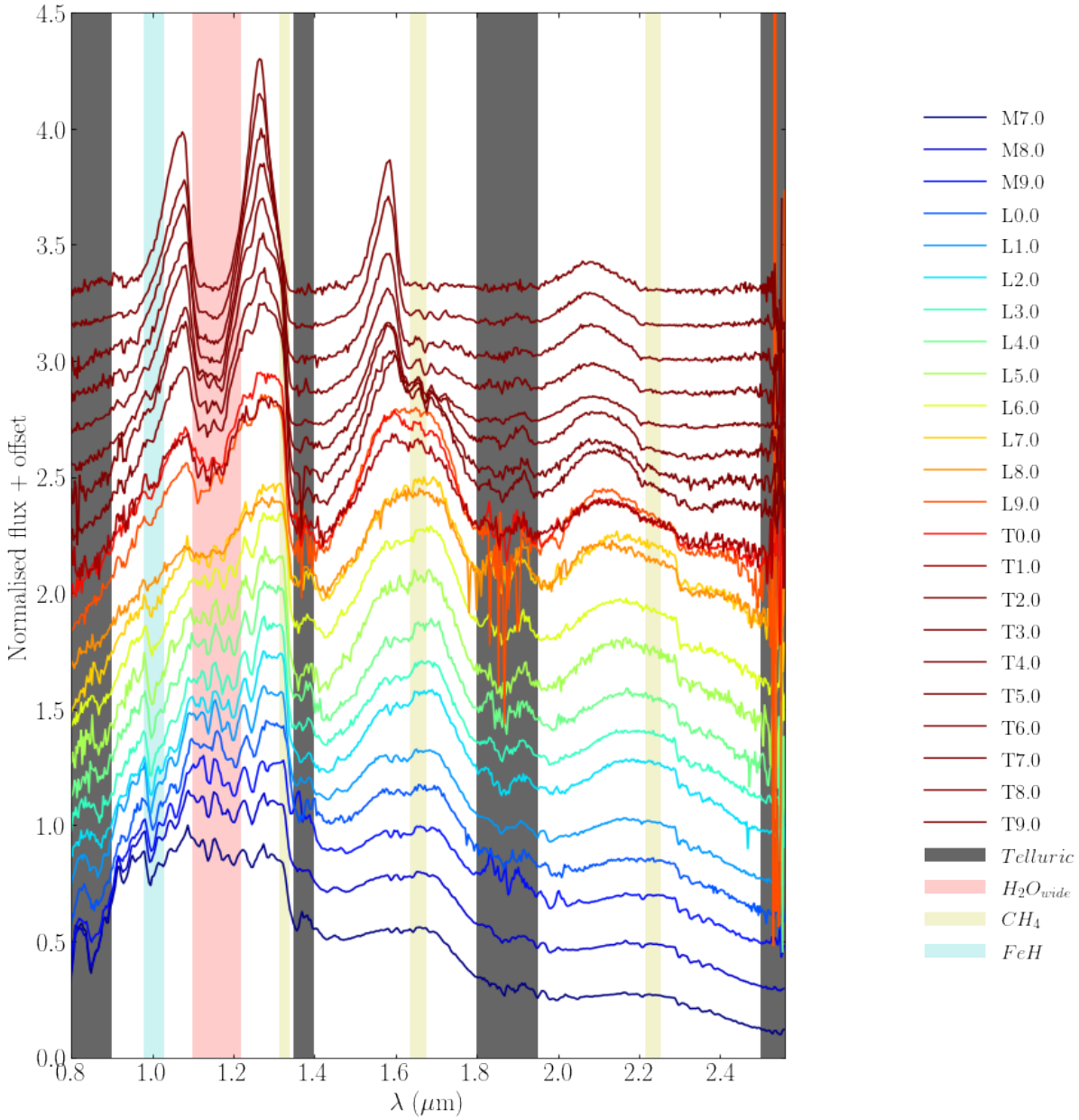

Figure 8.4: Standard spectra for M7.0 to T9.0 normalised and offset.

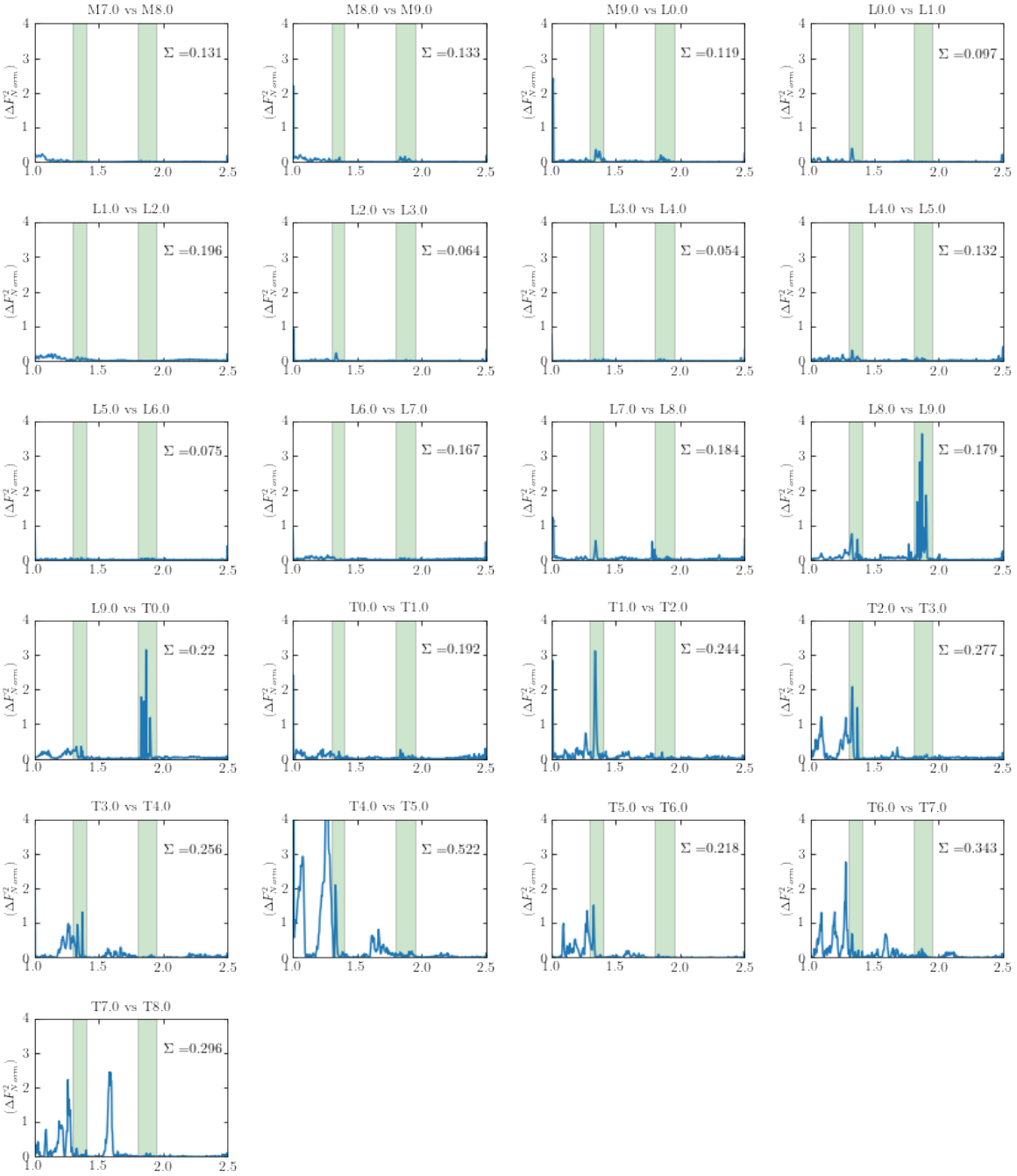

Figure 8.5: Comparison in normalised flux between adjacent SpeX standards shown as the root-squared difference. The telluric bands (green) are excluded from the difference due to noise.

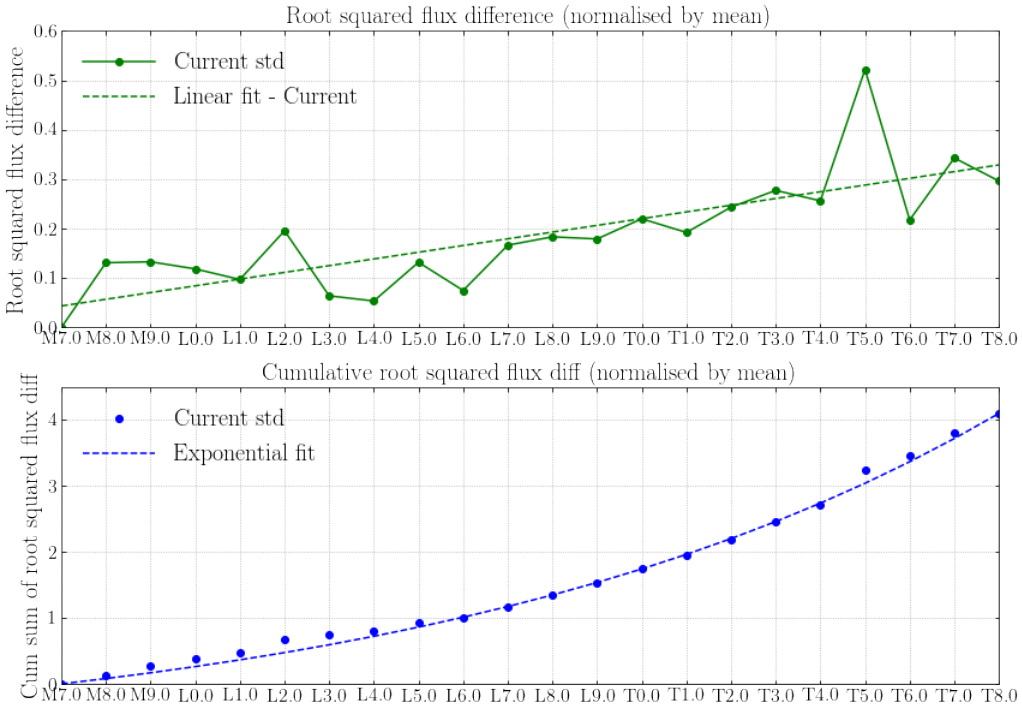

Figure 8.6: Trend in the difference in root-squared normalised flux between adjacent standards on individual and cumulative basis from M8 to T8.

8.5 Alternative spectral indices

Based on similar approaches by Burgasser, Geballe, Leggett, Kirkpatrick & Golimowski (2006) and Allers & Liu (2013), we calculate 18 candidate spectral indices for field dwarfs with spectral types L0 to T9 in order to identify potential trends and relationships that might be used for classification purposes. These indices are based on creating ratios from the integrated flux of key absorption lines as well as narrow-band and wide-band features as defined in table 8.3.

Name of feature or band	λ range (μm)	Additional information
J	1.260-1.285	
H	1.560-1.600	
K	2.080-2.100	
H_2O^1	1.140-1.165	1.15 μm H_2O line
H_2O^2	1.480-1.520	1.4 μm H_2O line
H_2O^3	1.975-1.995	1.9 μm H_2O line
CH_4^1	1.315-1.340	
CH_4^2	1.635-1.675	
CH_4^3	2.215-2.255	
FeH^1	0.980-1.030	0.99 μm Wing & Ford (1969)
FeH^2	1.190-1.250	
FeH^3	1.570-1.640	
CO	2.290-2.390	
CO_2	1.425-1.450	
J_{wide}	1.005-1.100, 1.260-1.285	
H_{wide}	1.520-1.640	
K_{wide}	2.080-2.200	
H_2O_{wide}	1.100-1.220	

Table 8.3: A list of absorption features and wide bands we have used in the construction of spectral indices.

The resulting values for these spectral indices are shown in Figures 8.7 and 8.8 for the standard spectra (shown as blue circles). We also calculate spectral indices for a sample of high signal-to-noise L dwarf spectra identified and classified by Schneider et al. (2014) to examine the degree of variability within a spectral type.

Suitable candidate indices would show both a clear increasing (or decreasing) trend and low variability. The strongest candidates are $H_2O^1 - J$, which was also identified by Burgasser, Geballe, Leggett, Kirkpatrick & Golimowski (2006)), and a potentially new index $CO_2 - H$ that meet this criteria. The Schneider L dwarf sample generally shows a high degree of variability demonstrating the challenge of using spectral indices. We did not identify any spectral indices that offer significant improvement on those already identified in the literature.

We now investigate using the equivalent width (EW) of two prominent absorption features for CH_4 and FeH across the range L0 to T9. The EW of each feature is calculated by deducting the integrated flux from the integrated flux of the local continuum across the feature. The local

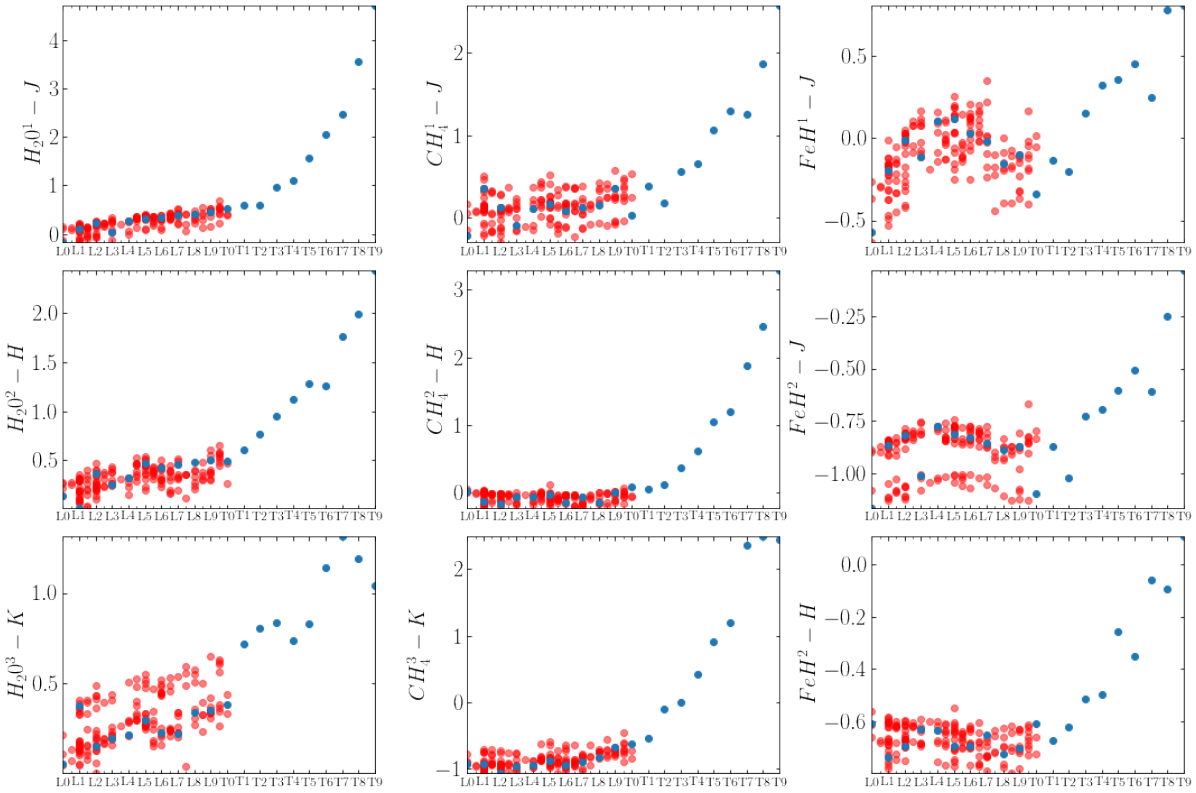

Figure 8.7: First set of prospective spectral indices for L0 to T9 SpeX standard objects (blue circles) and spectral indices calculated for the sample of high signal-to-noise L dwarf spectra identified by Schneider et al. (2014) (red circles)

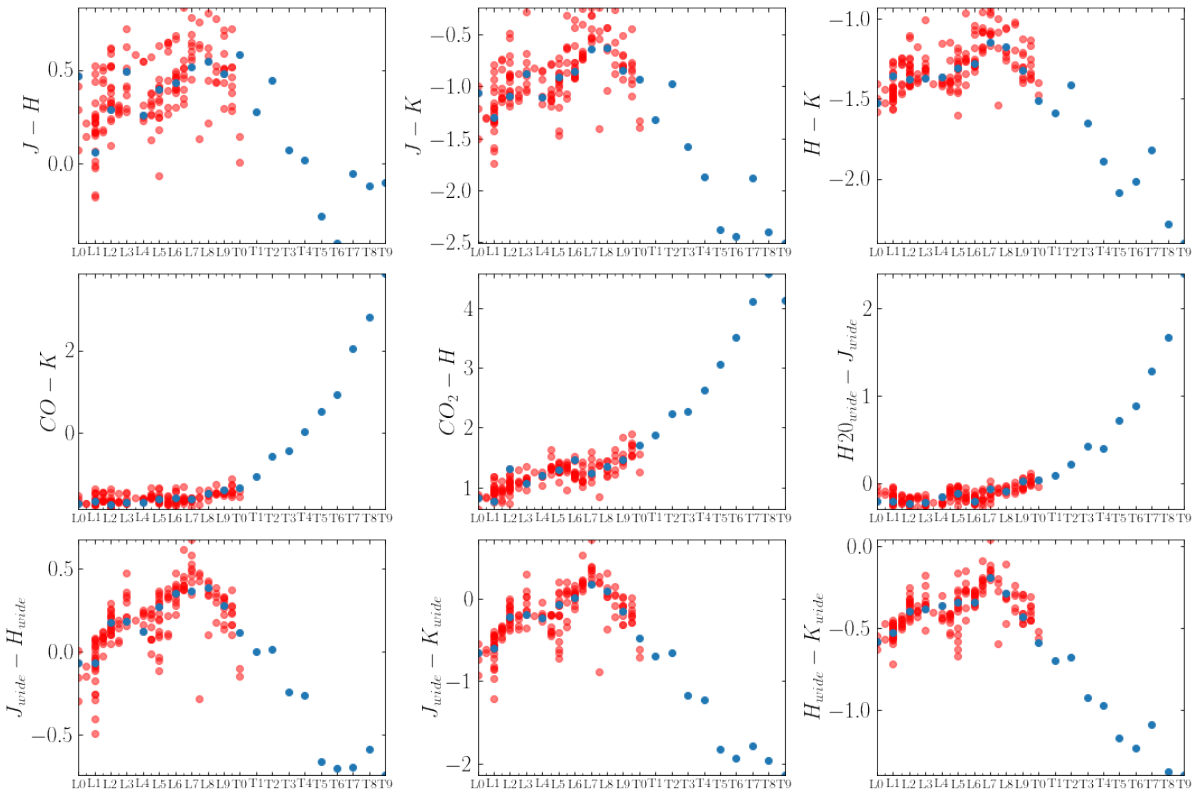

Figure 8.8: Second set of prospective spectral indices for L0 to T9 SpeX standard objects (blue circles) and spectral indices calculated for the sample of high signal-to-noise L dwarf spectra identified by Schneider et al. (2014) (red circles)

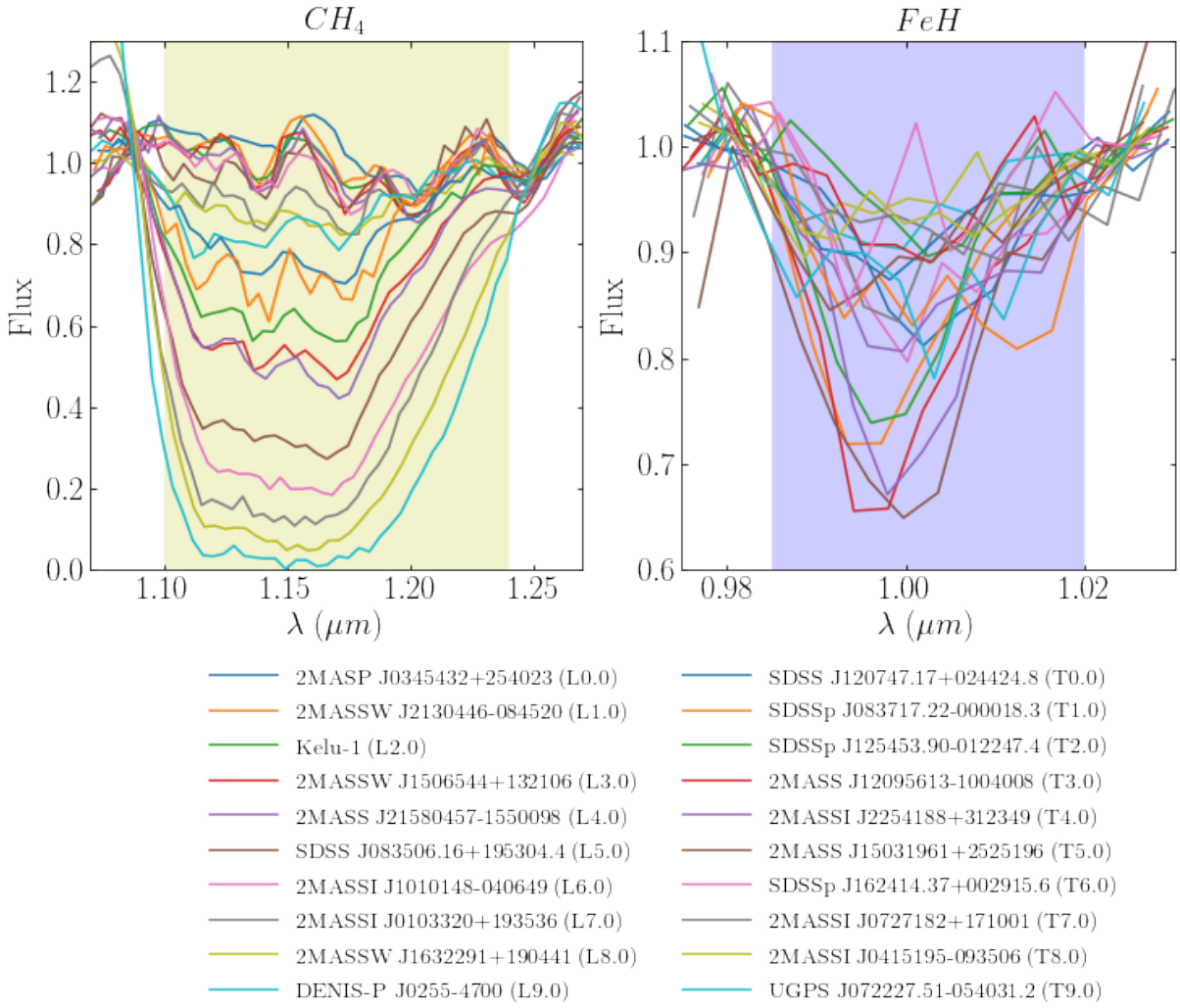

Figure 8.9: Depth of CH_4 absorption feature in range 1.10μm to 1.24μm across the spectral standards. Depth of FeH absorption feature in range 0.985μm to 1.020μm across the spectral standards.

continuum over the feature is defined as a linear fit across the feature using a small interval either side of the feature as shown in Figure 8.9. Allers & Liu (2013) showed that depth of absorption of the FeH feature at 0.998 μm, as well as VO and KI, have strong gravity sensitive features.

The evolution of the EW for each of these features is shown in Figure 8.10 along with a simple ratio between the EWs shown on a log scale. While a clear increasing trend is apparent, identifying clear continuum points across these features is challenging. In addition the relatively low resolution of the spectra in these narrow bands is a significant limitation in adopting this method and a source of variance in the result. We found that the resulting trend wasn't clear enough given the resolution make an effective classification method.

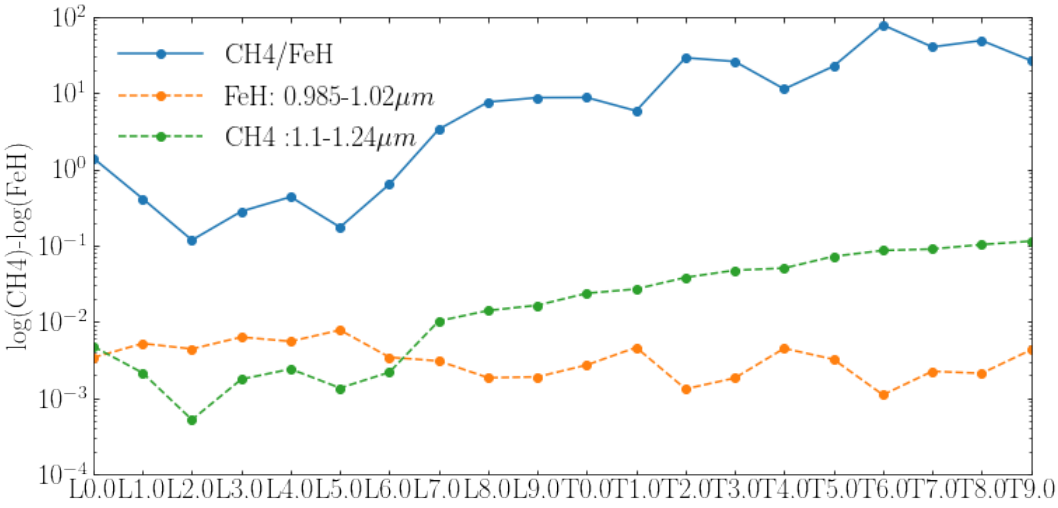

Figure 8.10: Evolution of equivalent width for CH_4 and FeH absorption feature across spectral sequence

8.6 Synthetic standard spectra

In order to attempt to address the apparent uneven evolution in overall spectral shape for the L-dwarf standards as highlighted in Figure 8.6, we construct a set of synthetic L-dwarf standards based on the sample of 174 high-quality L-dwarf spectra selected and classified by Schneider et al. (2014). We check and reclassify (where necessary) this sample to whole spectral types (e.g L2) by minimising the χ^2 between the normalised spectra and the current spectral standard after removing the telluric regions as shown in green in Figure 8.11. For each reclassified set of objects from L0 to L9 we calculate the median flux at each wavelength to construct a synthetic spectrum for that spectral type (see Figure 8.11). Taking the median flux for each spectral type helps negate the impact of outliers from peculiar, low gravity, or anomalous flux measurements. Our synthetic spectra are shown in Figure 8.11

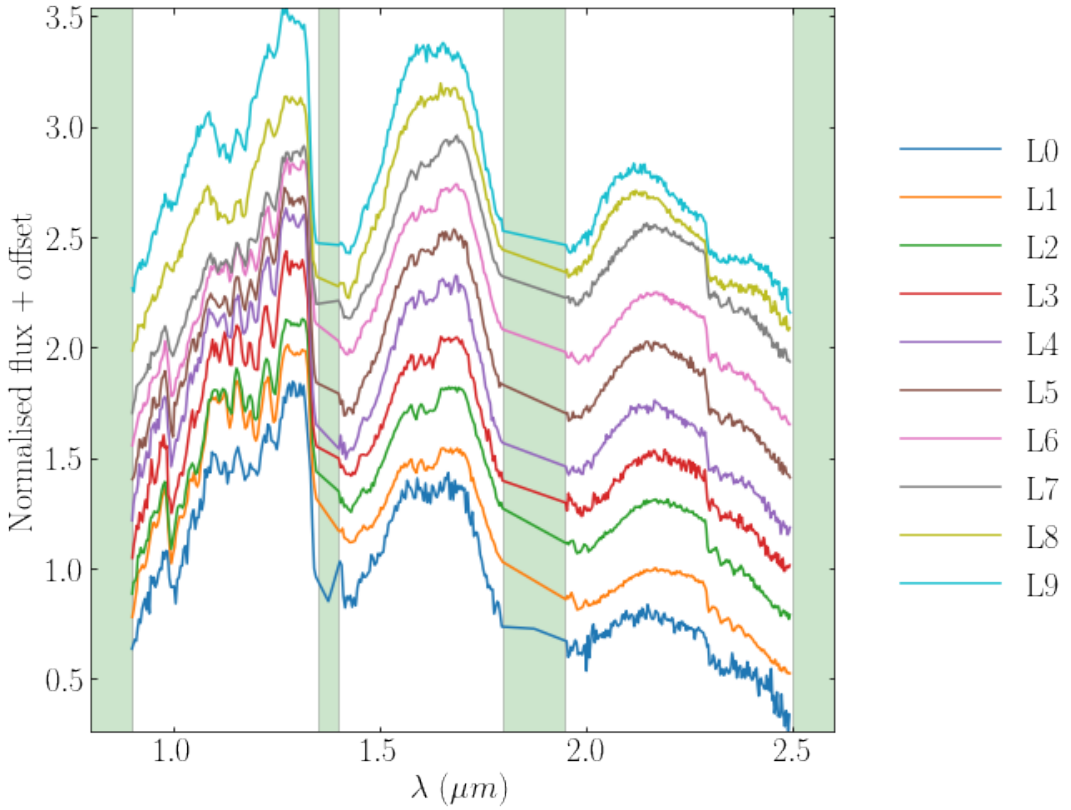

Figure 8.11: Synthetic L-dwarf standard spectra. Green shaded areas are telluric regions.

A comparison between the SpeX standard spectra and our synthetic standards is shown in Figure 8.12. This method yields synthetic standards that closely match those of the current standards suggesting that they are well-chosen even with the benefit of more accurate classifications. While this approach has some merit, the number of spectra available for each type to construct the synthetic standard remains fairly small. In addition this classification method is circular in the sense that spectra must first be classified in order to construct the synthetic standard which is then used to classify sources.

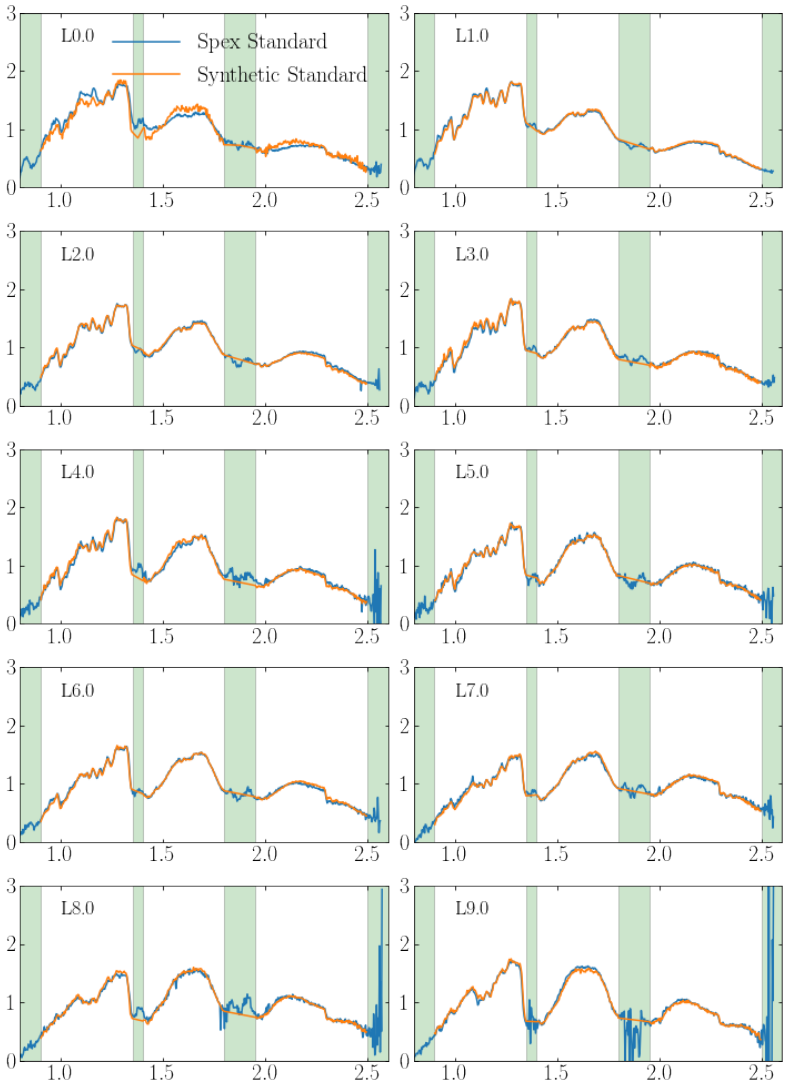

Figure 8.12: Comparison between SpeX standard and synthetic L-dwarf standard spectra.

8.7 Dimensionality reduction

Feature selection and dimensionality reduction (DR) are important processes in preparing data ahead of training a machine learning classification model. This is primarily in order to avoid the curse of dimensionality[4]. DR techniques attempt to represent high dimensional data by a smaller number of dimensions while retaining the important properties of the original data. As well as improving computational speed and reducing memory requirements, DR is commonly used to reduce overfitting and for data visualisation purposes. While computers can easily handle high dimensional data, humans have great difficulty in visualising data in greater than three dimensions.

Given that the features of our data comprise a set of photometric colours or spectral energy distributions, it is not obvious which features should be selected or deselected for classification, or indeed if the data can be meaningfully reduced to a smaller number of dimensions. Here we investigate and evaluate a range of linear and non-linear dimensionality reduction algorithms in order to visualise our UCD data and assess qualitatively: if the spectral types are well separated in lower dimensional space; if the order of the spectral types is maintained in some clearly separable curve; and if potential anomalies are clearly separated from the main clusters.

We will evaluate and visualise both the photometric and spectroscopic UCD data in two- and three-dimensions. Our data is already classified (i.e. labelled with a spectral type), however we will not use this in the dimensionality reduction. These labels will be overlaid on to the visualisations in order to evaluate for its performance against the criteria above. A description of each of the dimensionality reduction algorithms applied in this work is included in appendix B.5.

8.7.1 Dimensionality reduction of photometric data

For this analysis we use the L and T photometric data as described in section 8.3.1. Initially we calculate the principal components of the data and visualise their two and three principal components as shown in Figure 8.13. We show the spectral type of each source by colour and spectral type (L dwarfs are shown as circles and T dwarfs are shown as triangles). The centroid of each spectral type is shown as a labelled black star. Six DR algorithms have been applied to this photometric data: PCA and ICA are linear algorithms while t-SNE, ISOMAP, LLE, and UMAP are non-linear algorithms. Each calculates a projection of the data onto a 2D and 3D space. We qualitatively assess each method for its ability to (i) separate the spectral types into separable and clearly defined clusters, (ii) maintain the classification sequence, and (iii) appear to separate out peculiar or anomalous objects. Our results are summarised in Table 8.4.

[4]The curse of dimensionality describes the exponential growth in the volume of feature space with increasing features, or dimensions, and the subsequent issues related to sparsely populated data within that volume.

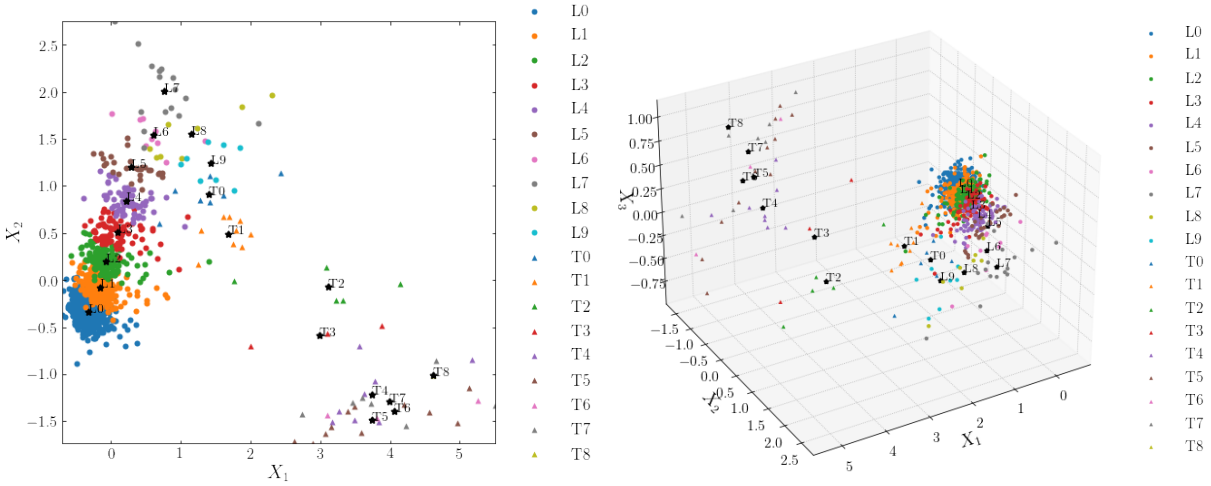

Figure 8.13: 2D (left plot) and 3D (right plot) PCA on photometric data. The centroid of each spectral type is shown (labelled black stars)

DR method	Sub-types well separated?	Sub-type order maintained?	Potentially anomalous objects separated?
PCA	Y (L0-T4)	Y (L0-T4)	Y
ICA	N	Y (T0-T8)	N
t-SNE (PCA-initiated)	N	N	N (One extreme point identified)
ISOMAP	Reasonably well	Y (L0-T1)	N
LLE	Y	Y	Y
UMAP	Y (L0-L8)	Y	N

Table 8.4: Qualitative evaluation of DR methods on photometric data

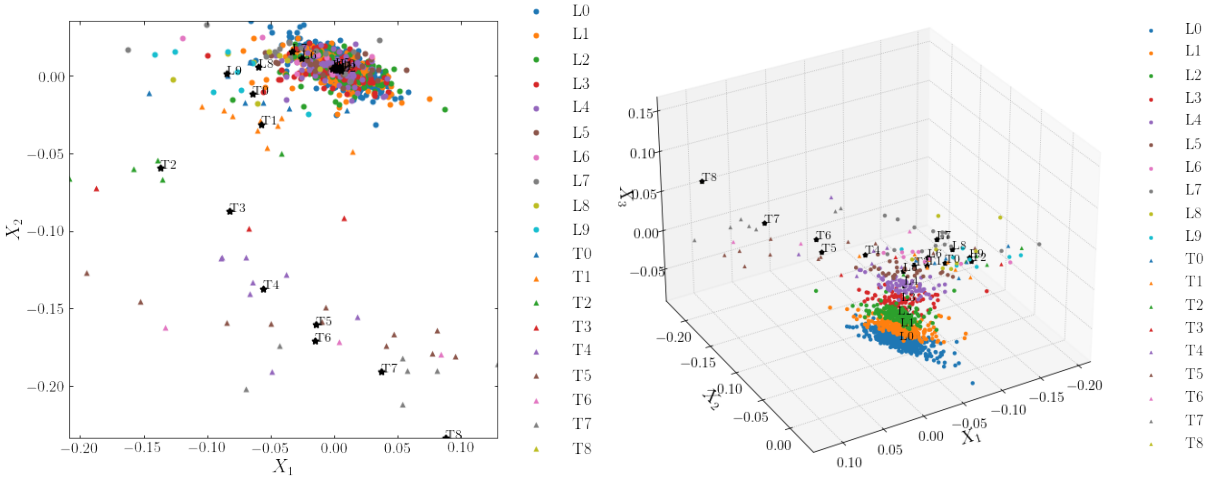

Figure 8.14: 2D (left plot) and 3D (right plot) ICA on photometric data. The centroid of each spectral type is shown (labelled black stars)

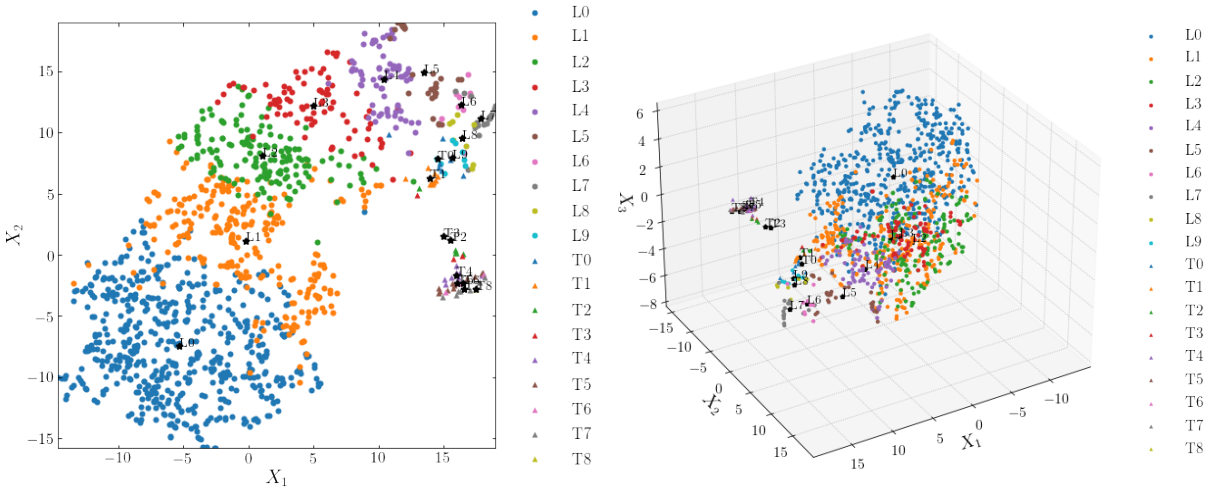

Figure 8.15: 2D (left plot) and 3D (right plot) t-SNE on photometric data. The centroid of each spectral type is shown (labelled black stars).

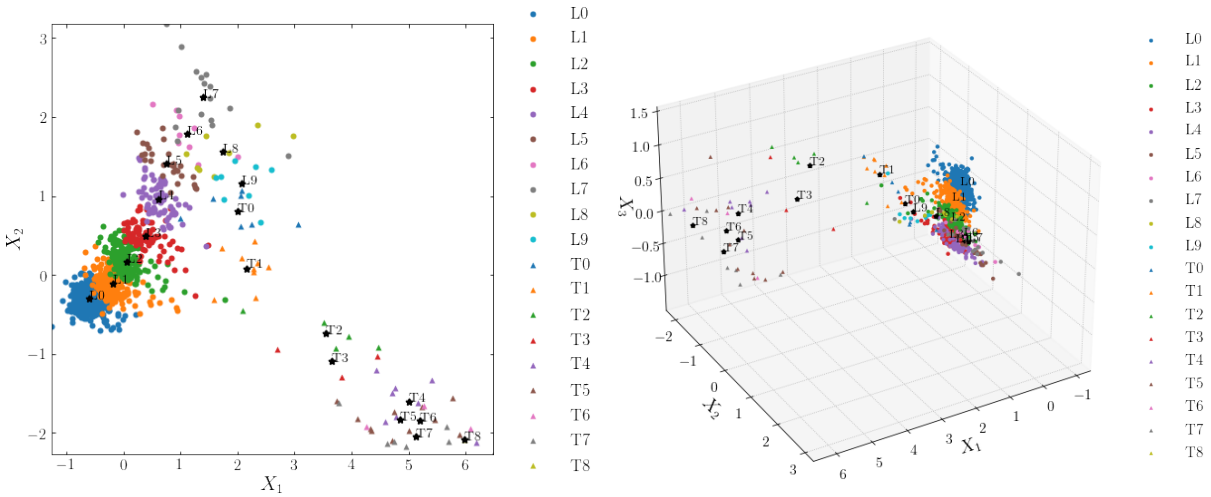

Figure 8.16: 2D (left plot) and 3D (right plot) ISOMAP on photometric data. The centroid of each spectral type is shown (labelled black stars)

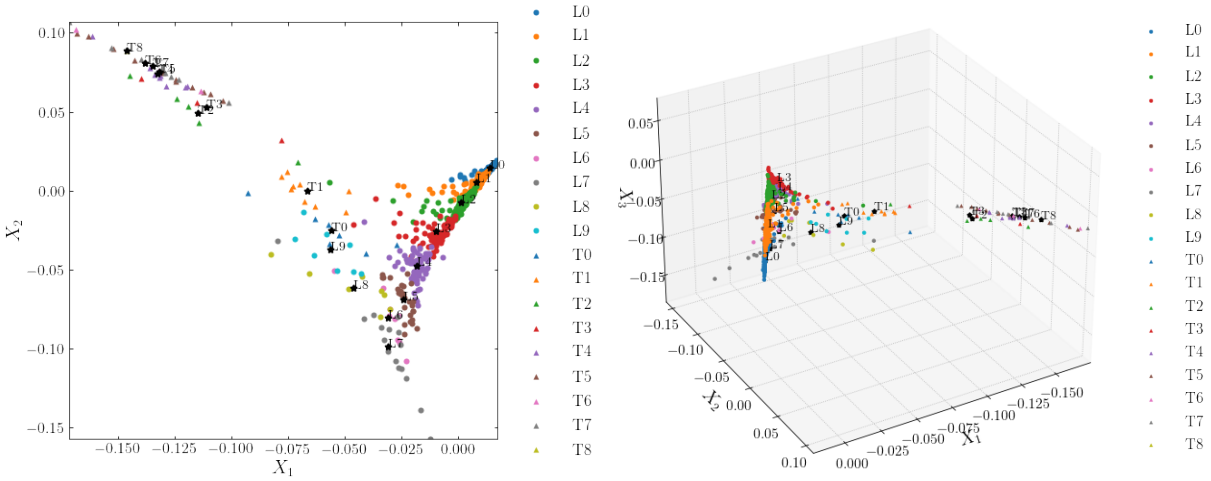

Figure 8.17: 2D (left plot) and 3D (right plot) LLE on photometric data. The centroid of each spectral type is shown (labelled black stars)

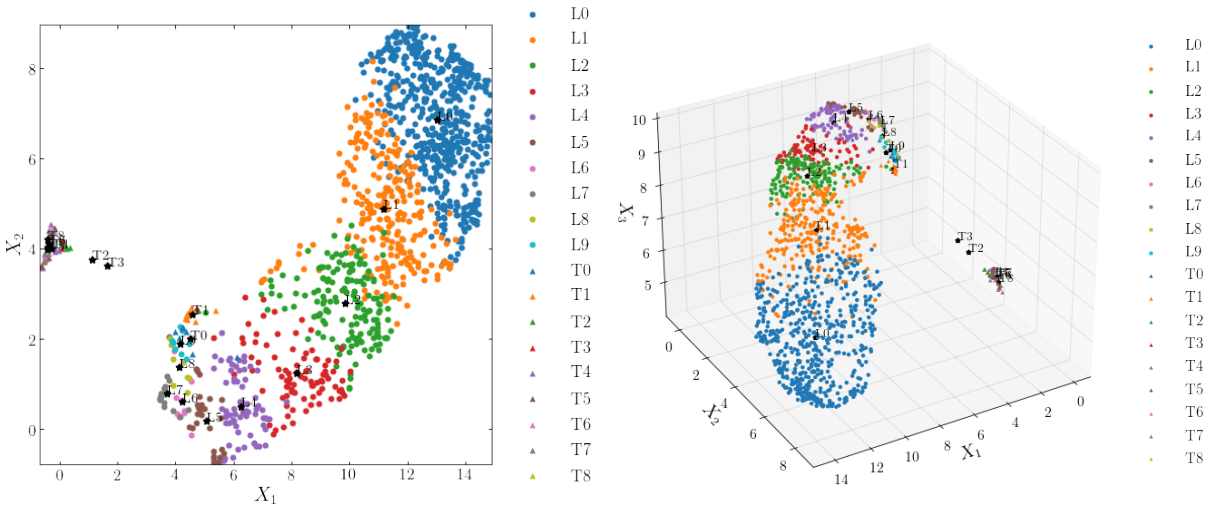

Figure 8.18: 2D (left plot) and 3D (right plot) UMAP on photometric data. The centroid of each spectral type is shown (labelled black stars).

8.7.2 Dimensionality reduction of spectroscopic data

We prepare our spectroscopic data by first extracting all available spectra from the SpeX library; 2203 UCD sources with spectral types M7 to T9. We normalise and select only those spectra with median signal-to-noise > 10 and those with sufficient flux measurements between 0.9 - 2.4 μm. Spectra with missing or a small number of flux measurements are removed from the sample. For each spectrum we remove the flux in the telluric regions between 1.35 - 1.40 μm and 1.80 - 1.95 μm as these regions contain excessive noise due to atmospheric absorption. The resulting sample consists of 981 spectra with the flux in three wavelength regions 0.9 - 1.35 μm, 1.40 - 1.80 μm and 1.95 - 2.40 μm representing the features. We again apply six DR reduction algorithms (PCA, ICA, t-SNE, ISOMAP, LLE, and UMAP) to this data and present the results visually in two- and three-dimensions for evaluation and overlaying the spectral type labels. We qualitatively evaluate each method as for the photometric data and summarise our results in Table 8.5.

DR method	Sub-types well separated?	Sub-type order maintained?	Potentially anomalous objects separated?
PCA	N	Partially	N
ICA	N	Y (L9-T4)	Y
t-SNE (PCA-initiated)	N	Y (M7-L9)	N
ISOMAP	N	Partially	Y
LLE	N	Partially	Y
UMAP	Partially	Y (M7-T1, L5 is anomaly)	N

Table 8.5: Qualitative evaluation of DR methods on spectroscopic data

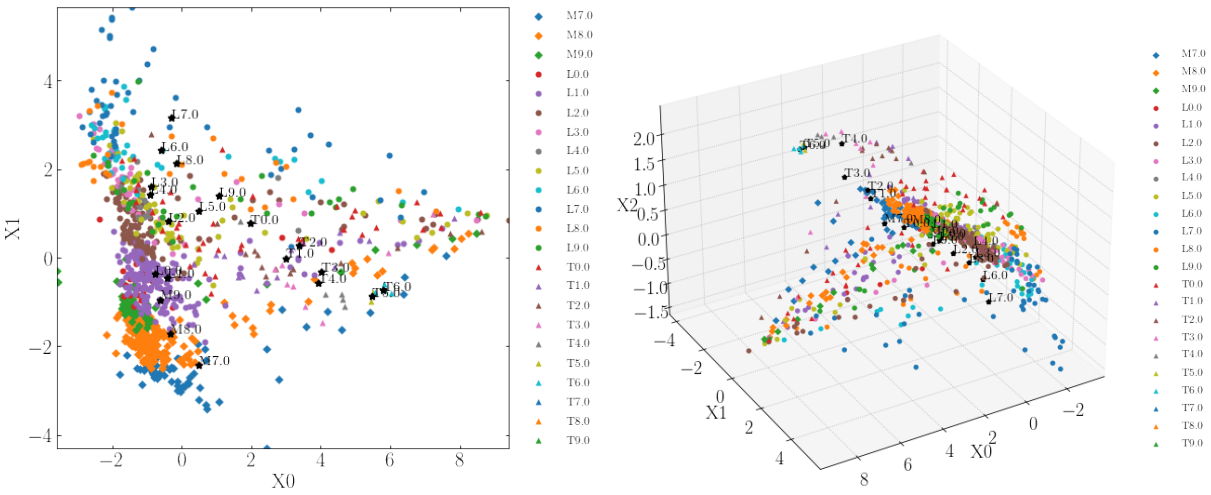

Figure 8.19: 2D (left plot) and 3D (right plot) PCA on SpeX spectroscopic data. The centroid of each spectral type is shown (labelled black stars).

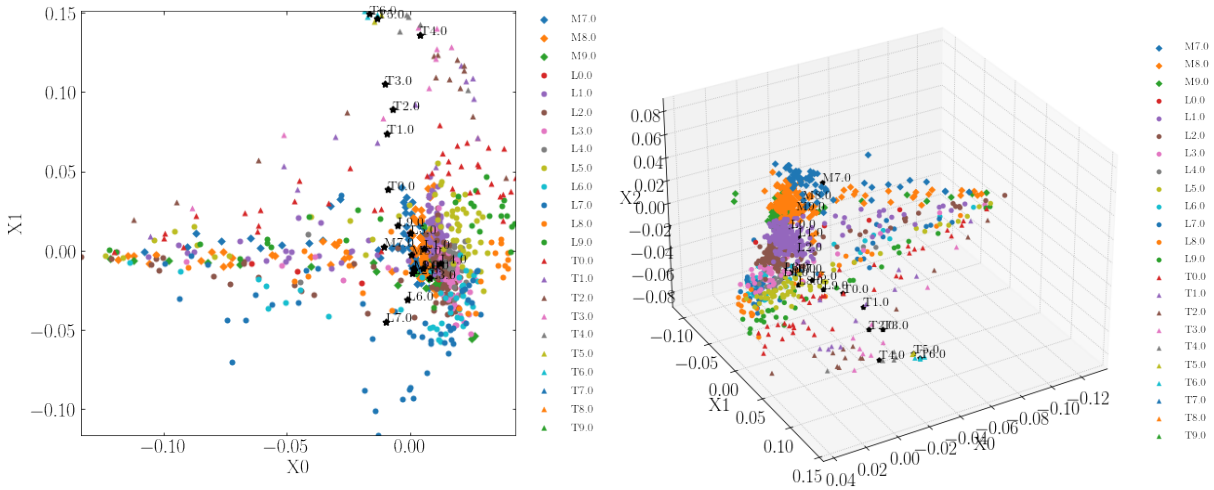

Figure 8.20: 2D (left plot) and 3D (right plot) ICA on SpeX spectroscopic data. The centroid of each spectral type is shown (labelled black stars).

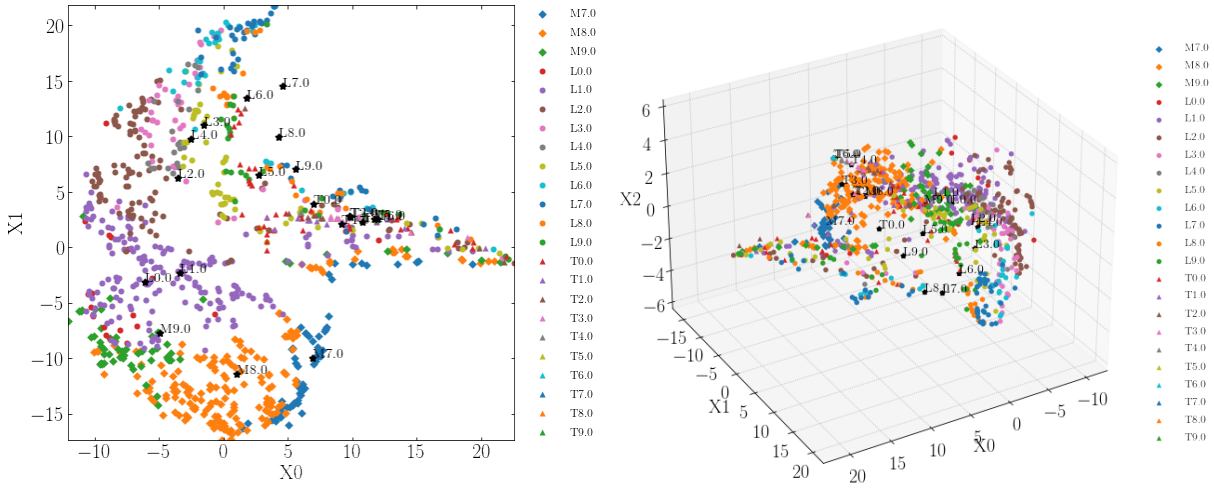

Figure 8.21: 2D (left plot) and 3D (right plot) t-SNE on SpeX spectroscopic data. The centroid of each spectral type is shown (labelled black stars).

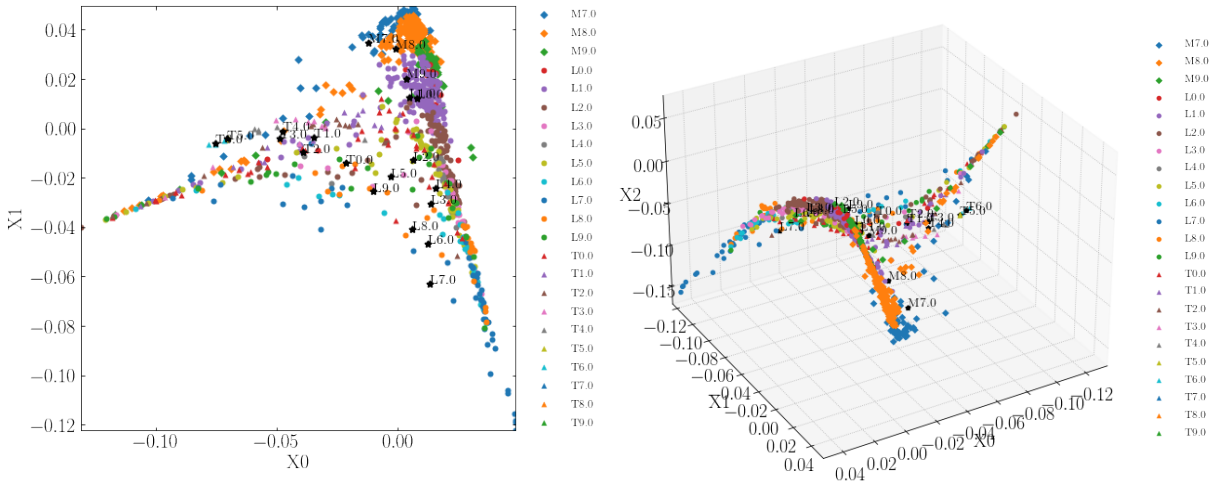

Figure 8.22: 2D (left plot) and 3D (right plot) LLE on SpeX spectroscopic data. The centroid of each spectral type is shown (labelled black stars).

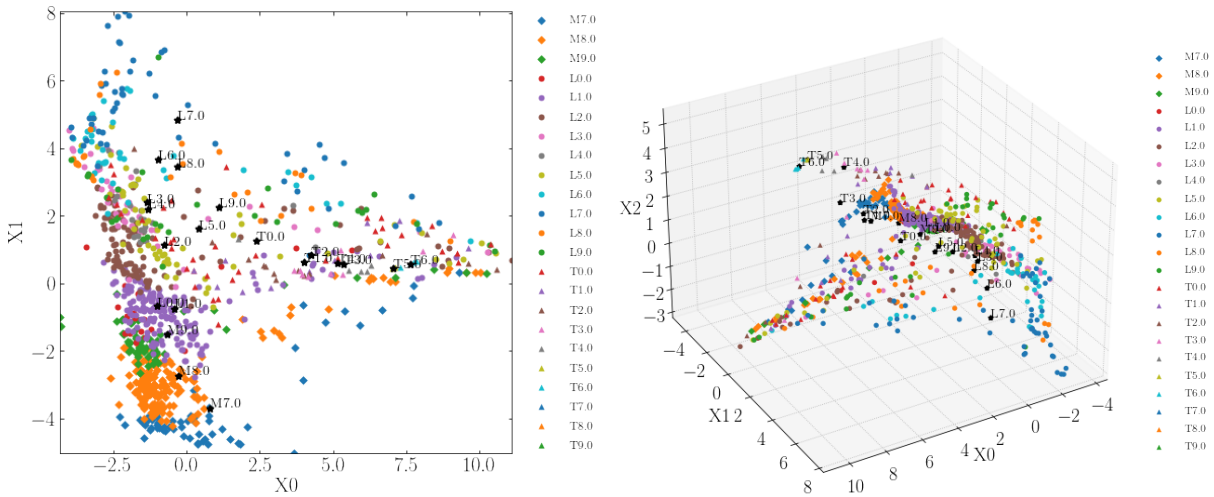

Figure 8.23: 2D (left plot) and 3D (right plot) ISOMAP on SpeX spectroscopic data. The centroid of each spectral type is shown (labelled black stars).

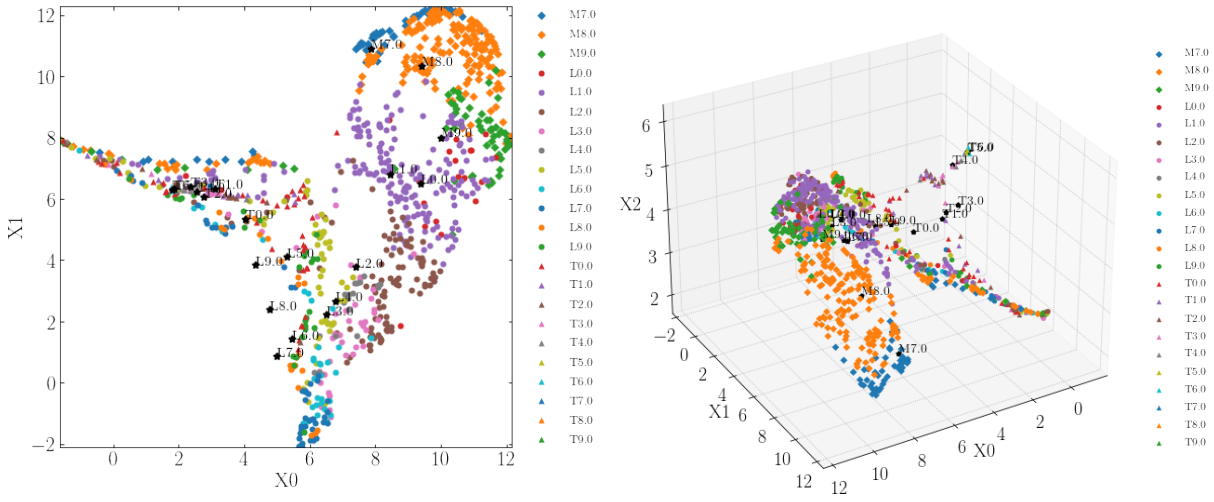

Figure 8.24: 2D (left plot) and 3D (right plot) UMAP on SpeX spectroscopic data. The centroid of each spectral type is shown (labelled black stars).

8.7.3 Discussion on dimensionality reduction methods

The primary purpose of visualising complex, multidimensional data in a lower dimensional space is to try and identify clusters and patterns in the data that might hint at some underlying structure or features that are not readily identifiable in its higher dimensional form. These methods are unsupervised; that is the algorithm does not know or use the classification labels (in this case the spectral type) in the data. We overlay the spectral type, shown by the colour of the data points, in order to assess how well the algorithm has maintained the spectral sequence and clustered the data correctly. The centroid of each spectral class is shown as a black star in order to trace the sequence in each Figure. It is interesting to note that most of the lower dimensional representations (e.g. Figures 8.13, 8.15, 8.16, 8.17, 8.19, 8.21, 8.22, 8.23, 8.24) show a clear cusp, or abrupt change in direction, around L7 and this is seen in both the photometric and spectroscopic analysis. This cusp corresponds to the point of maximum reddening and greatest variability at the L/T transition due to the heterogeneous settling of dusty condensates below the photosphere leading to regions of alternate thick, thin or clear atmosphere (Radigan et al. 2014).

We see tight clustering of spectral types L0 to L5 in the photometric analysis as shown in Figures 8.13, 8.16 and 8.18 with limited overlap in the clusters suggesting that these spectral types are well-defined and separable in colour space. Beyond $\sim$ L5 the clusters broadly maintain the correct sequence but there is little separation and they significantly overlap. For the spectroscopic analysis, clusters can be seen for M7 to L2 beyond which there is little separation. Even for those clusters that are generally tightly defined there are numerous outliers across this low dimensional space (e.g. M7 and M8 in Figures 8.19 and 8.22).

8.8 Tree-based supervised machine learning

Supervised classification tasks seek to correctly classify objects into categories based on their features using a machine learning model that has been trained on a, typically large, set of labelled objects ('the training set'). Extreme Gradient Boosting (XGBoost), Random Forests, and Adaptive Boosting (AdaBoost) are leading tree-based ensemble machine learning algorithms known for their high performance in supervised learning classification tasks. Please see Appendix B.4 for a brief explanation of these algorithms. We evaluate the performance of these algorithms as a classifier of UCD spectral type using both the photometric and spectroscopic data as described in sections 8.3.1 and 8.3.2. We use a simple Gaussian Naive Bayes method as our baseline classifier and randomly split our sample into a training and test set in the ratio 75:25. This is a multiclassification problem and we manually optimise the hyperparameters and evaluate each algorithm based on a simple accuracy metric i.e. the percentage of correctly classified sources.

For the photometric analysis we calculate the accuracy for the entire dataset i.e. 35,026 M, L and T dwarfs. However, given that the sample is heavily biased towards the late-M dwarfs, we also calculate the accuracy for the smaller number of L and T dwarfs only. Our spectroscopic data consists of 1696 resampled and normalised spectra (M7 to T9) as discussed earlier. A confusion matrix[5] and a histogram of the distance between the predicted and labelled spectral type is shown for the baseline and each ensemble tree-based classifier. The results trained on the photometric data are shown in Figures 8.25, 8.26, 8.27, 8.28 and the results trained on the spectroscopic data are shown in Figures 8.29, 8.30, 8.31, 8.32. The accuracy of the predicted class within one spectral type, represented numerically as a distance of ± 1, is also calculated. Summary results are shown in Table 8.6.

Dataset	Classifier	Accuracy (MLT)	Accuracy ± 1 sub-type (MLT)	Accuracy (LT only)
Photometric	Gaussian Naive Bayes (Baseline)	93.0%	99.7%	46.8%
Photometric	XGBoost	97.1%	99.9%	62.1%
Photometric	Random Forest	97.2%	99.9%	64.8%
Photometric	AdaBoost	81.9%	97.6%	24.2%
Spectroscopic	Gaussian Naive Bayes (Baseline)	62.5%	87.7%	n/a
Spectroscopic	XGBoost	76.9%	92.5%	n/a
Spectroscopic	Random Forest	78.3%	92.2%	n/a
Spectroscopic	AdaBoost	55.2%	83.7%	n/a

Table 8.6: Accuracy of tree-based classification methods

8.8.1 Discussion on ensemble, tree-based methods

The Gaussian Naive Bayes baseline classifier trained on the photometric data performed well with an overall accuracy of 93% however the accuracy fell sharply when evaluating the accuracy

[5] A confusion matrix provides a comparison between actual and predicted values. For a multiclassification task with N classes, the confusion matrix is a N x N matrix with the leading diagonal showing true positive values.

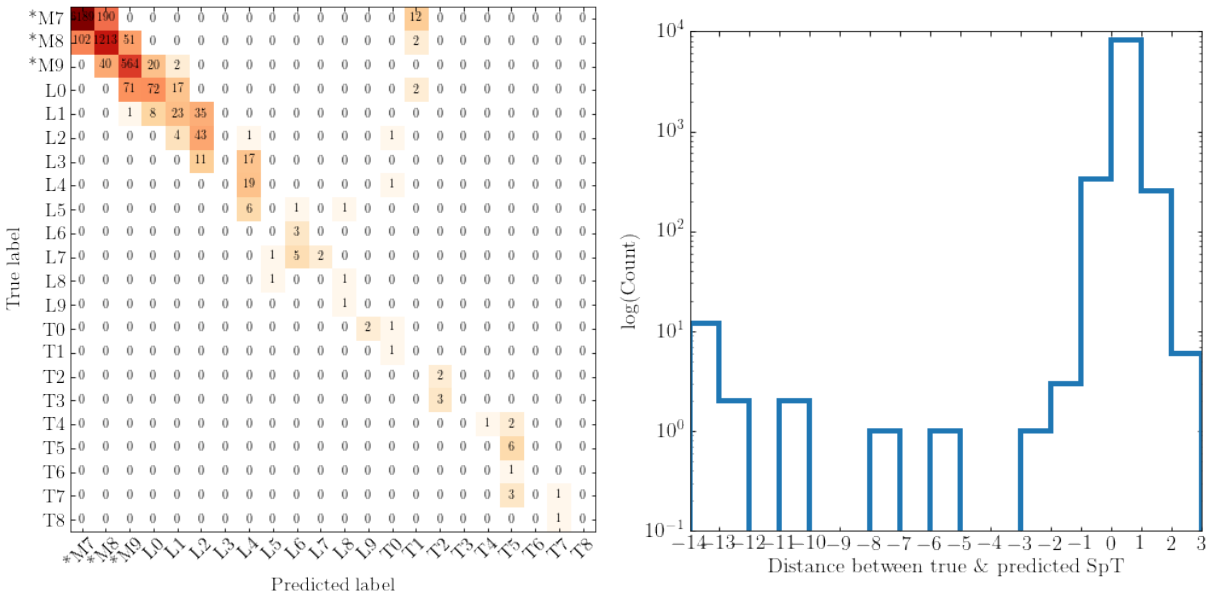

Figure 8.25: Confusion matrix for Gaussian Naive Bayes classifier applied to the photometric dataset (left plot) and histogram of the distance between predicted and labelled spectral types (right plot). Note that distance between one spectral type (e.g. from L4 to L5) is ±1.

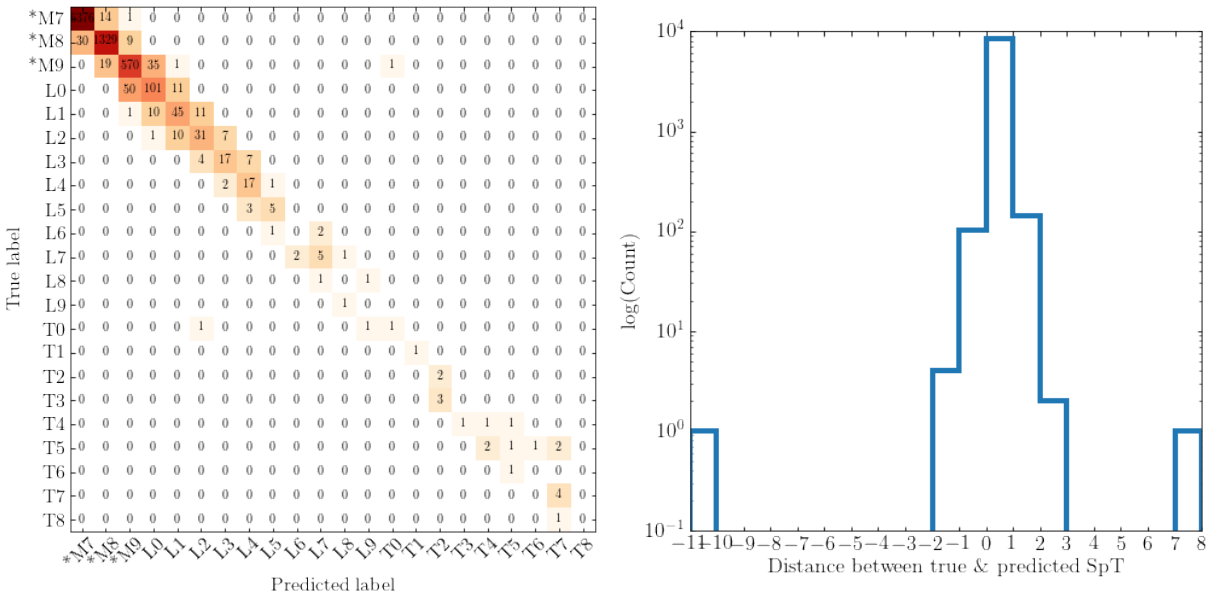

Figure 8.26: Confusion matrix for XGBoost classifier applied to the photometric dataset (left plot) and histogram of the distance between predicted and labelled spectral types (right plot). Note that distance between one spectral type (e.g. from L4 to L5) is ±1.

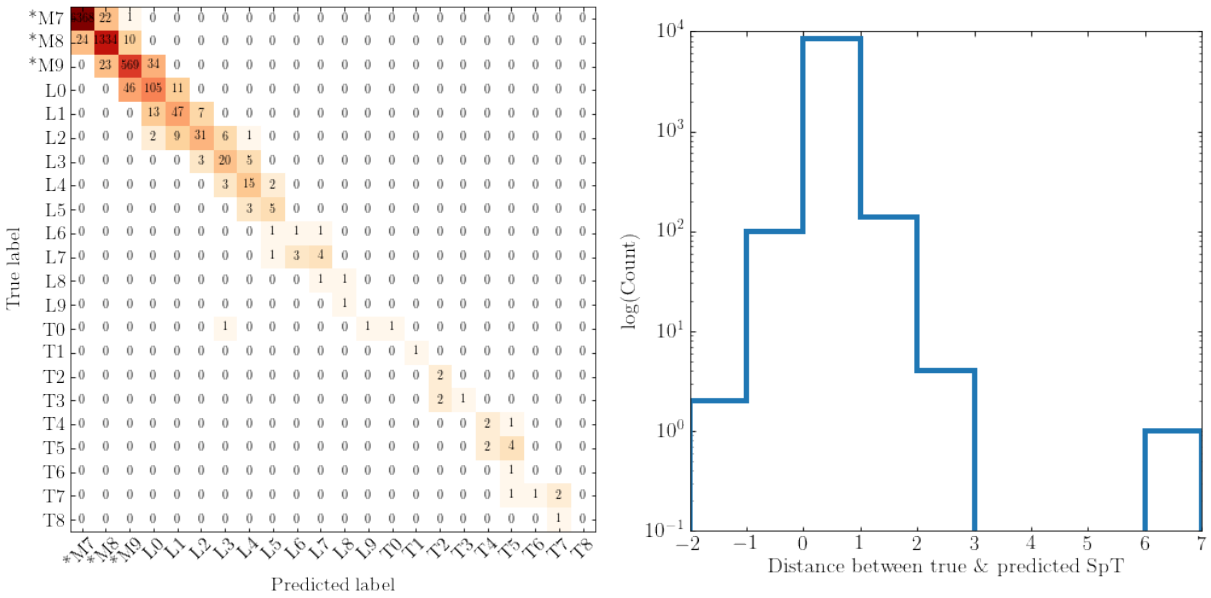

Figure 8.27: Confusion matrix for Random Forest classifier applied to the photometric dataset (left plot) and histogram of the distance between predicted and labelled spectral types (right plot). Note that distance between one spectral type (e.g. from L4 to L5) is ±1.

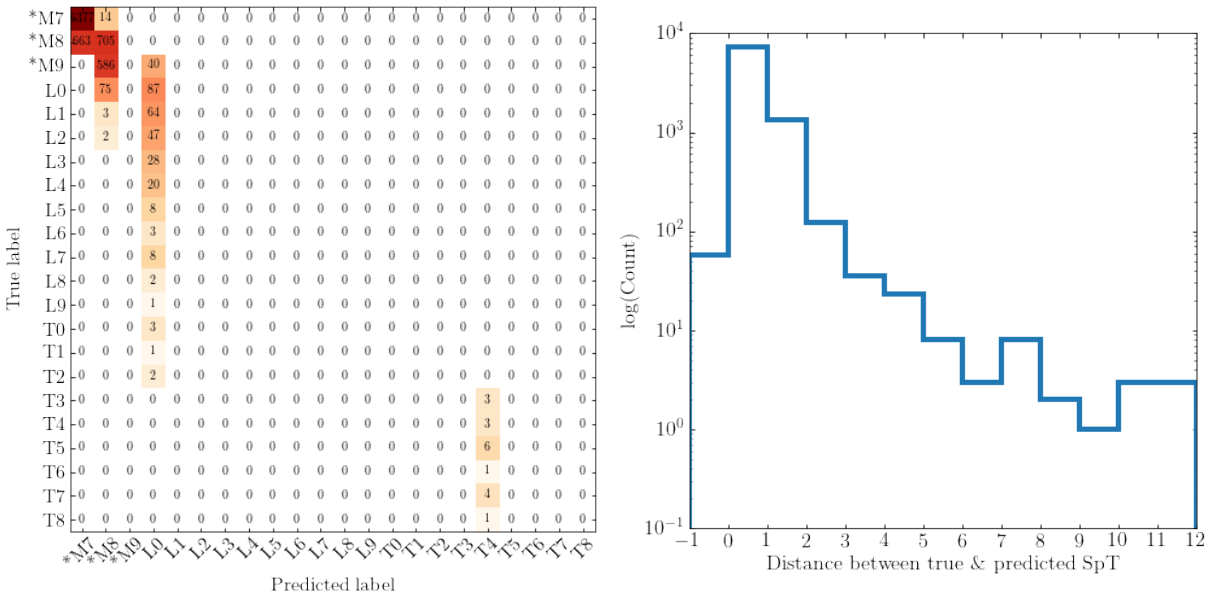

Figure 8.28: Confusion matrix for AdaBoost classifier applied to the photometric dataset (left plot) and histogram of the distance between predicted and labelled spectral types (right plot). Note that distance between one spectral type (e.g. from L4 to L5) is ±1.

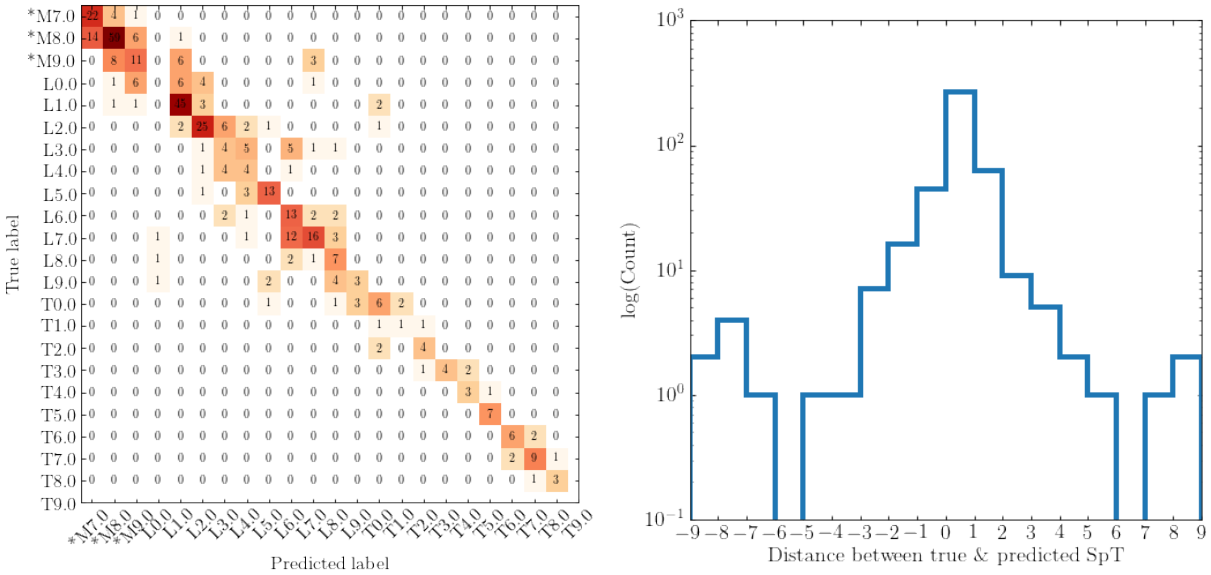

Figure 8.29: Confusion matrix for Gaussian Naive Bayes classifier applied to the spectroscopic dataset (left plot) and histogram of the distance between predicted and labelled spectral types (right plot). Note that distance between one spectral type (e.g. from L4 to L5) is ±1.

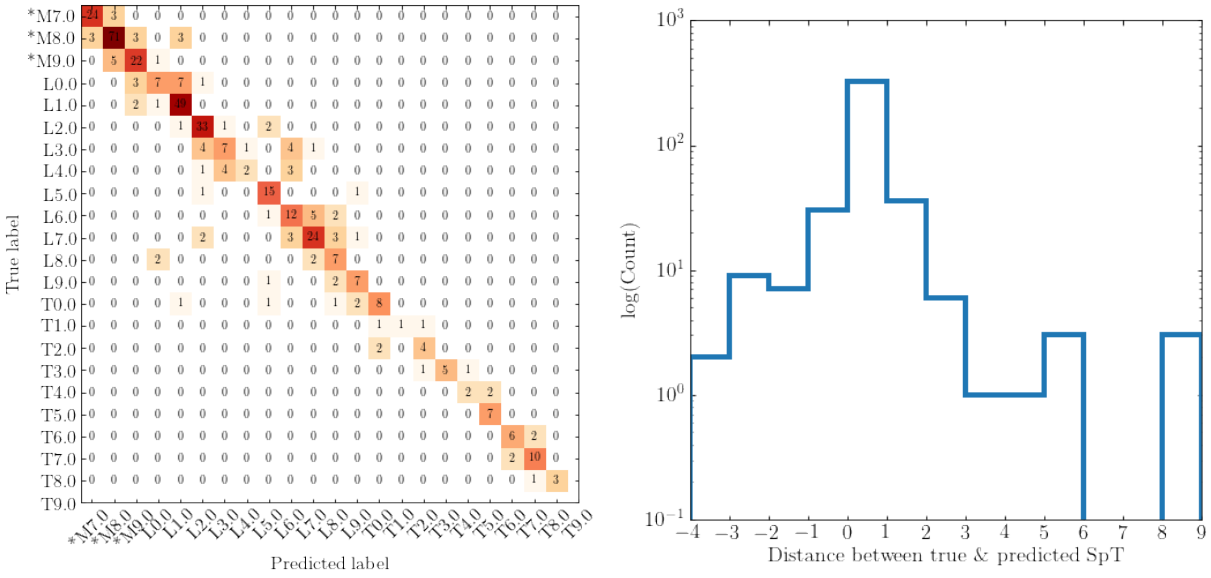

Figure 8.30: Confusion matrix for XGBoost classifier applied to the spectroscopic dataset (left plot) and histogram of the distance between predicted and labelled spectral types (right plot). Note that distance between one spectral type (e.g. from L4 to L5) is ±1.

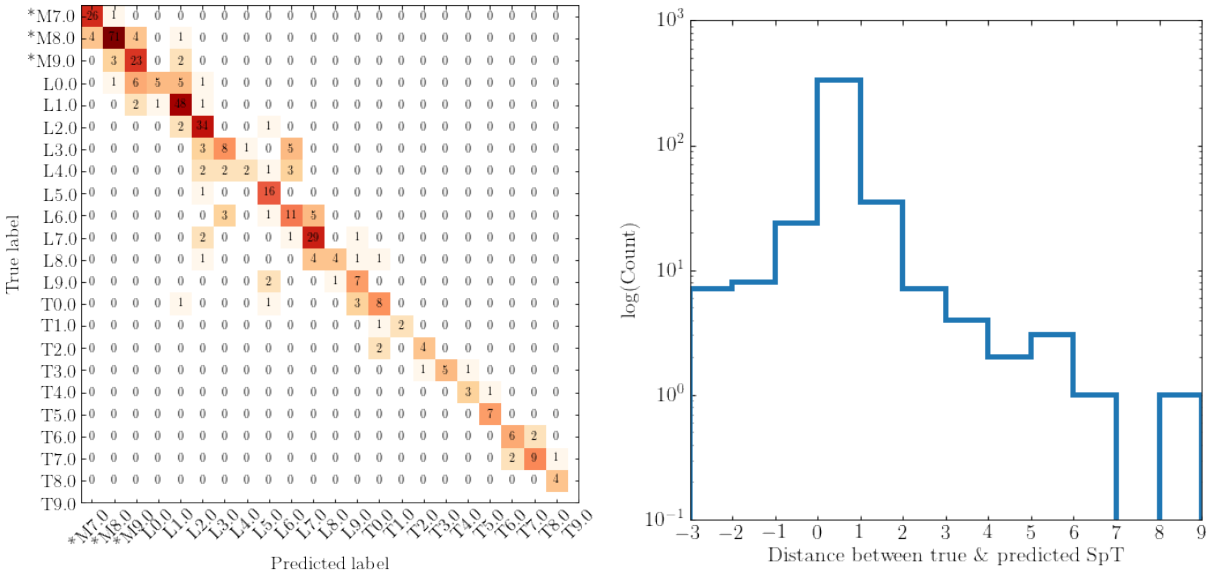

Figure 8.31: Confusion matrix for Random Forest classifier applied to the spectroscopic dataset (left plot) and histogram of the distance between predicted and labelled spectral types (right plot). Note that distance between one spectral type (e.g. from L4 to L5) is ±1.

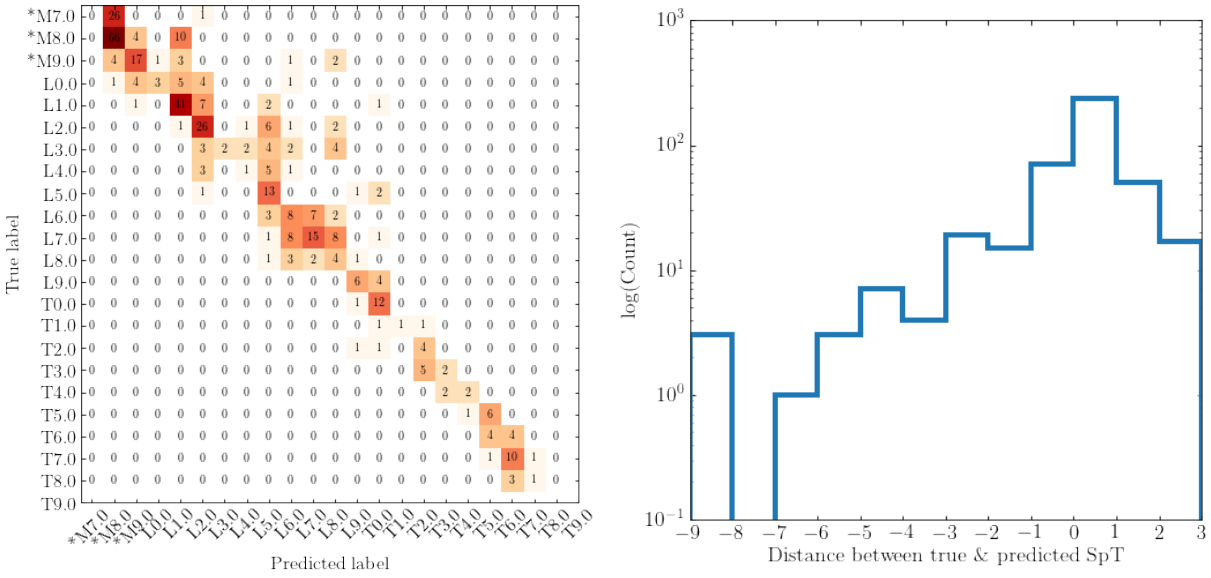

Figure 8.32: Confusion matrix for AdaBoost classifier applied to the spectroscopic dataset (left plot) and histogram of the distance between predicted and labelled spectral types (right plot). Note that distance between one spectral type (e.g. from L4 to L5) is ±1.

of the L and T dwarfs only. The XGBoost and Random Forest classifiers offered improved overall accuracy compared to the baseline and better accuracy for the L and T dwarfs of 62.1% and 64.8% respectively. Both classifiers made a small number of outlier classifications i.e. > 5 spectral types away from the 'true' label.

The spectroscopic data is less biased towards the late-M dwarfs and contains significantly more features than the photometric data. Dimensionality reduction algorithms were applied to the spectroscopic data ahead of training to reduce the number of features to 10-20 to see if this improved the performance however we found that this had little impact on the accuracy. The Random Forest classifier trained on the spectroscopic data (with no initial dimensionality reduction) achieved an overall accuracy of 78.3% and was more accurate in classifying the late-L and T dwarfs (see Figure 8.31). Many of the largest misclassifications occur in the L/T transition range from L6 to L9.

Overall we find that the random forest classifier had the highest overall performance with both the photometric and spectroscopic data with an accuracy of 97.2% and 78.3% respectively. However we note that the largest discrepancies occur across the L/T transition where rapid changes occur in the atmosphere and the greatest variability is observed. Accurate classification of L/T transition objects remains an interesting challenge.

8.9 Variational autoencoders (VAEs)

In contrast with other dimensionality reduction techniques, variational autocoders (VAEs) can capture nonlinear relationships between underlying parameters in a low dimensional latent space using deep neural networks. VAEs are a unsupervised, non-linear, deep learning technique where data features are mapped to a distribution in a lower dimensional latent space rather than a single point. These distributions are described by overlapping multivariate Gaussian distributions and the latent layer consists of neurons corresponding to the latent means and latent variances. The overlapping nature of these distributions allows meaningful interpolation between points in latent space which enables the construction of realistic and representative synthetic spectra. VAEs have the ability to compress and reconstruct spectra with a lower reconstruction error than other common dimensionality reduction algorithms that linearly decompose input data into a representative lower dimensional space. See appendix B.7 for a more detailed description of VAEs.

Portillo et al. (2020) found that a VAE approach performed well in reconstructing SDSS galaxy spectra with only six latent parameters, outperforming other methods such as PCA with a similar number of components. Different galaxy classes were naturally separated in this latent space, without applying class labels.

Our aim is to apply this technique to a sample of UCD spectra to try and establish a clear classification method based on a small number of underlying 'latent' parameters and use these to discover if they provide some insight into the underlying mechanisms occurring across the substellar spectral types M7 to T9. This work closely follows the approach developed by Portillo et al. (2020) and re-purposes much of the code used to train the VAEs and create the plots[6].

Again we use our sample of 1696 low resolution and resampled spectra from the SpeX library (section 8.3.2). This sample is randomly divided into a training and validation set in the ratio 75:25.
Following Portillo et al. (2020) we implement an Information Maximizing Variational Autoencoder (InfoVAE) approach developed by Zhao et al. (2017) using pytorch (Paszke et al. 2019). We train our VAE with two hidden layers for each of the encoder and decoder and using pytorch's built-in Adam optimiser. The size of the hidden layers are randomly assigned. All activations are the rectified linear unit (ReLU) except for the initial code layer and the reconstruction layer which use linear activations.
We train the VAE with 1 to 8 latent parameters and measure the reconstruction error of the validation set of spectra. We use the following three dimensionality reduction methods as a baseline for comparison purposes: Principle Component Analysis (PCA), truncated singular value decomposition (TSVD), and non-negative matrix factorisation (NMF). We find that the TSVD and NMF give the same result so refer to PCA and NMF for baseline comparison purposes. We

[6] `https://github.com/stephenportillo/SDSS-VAE`

find that the VAE with the best performance, i.e. the lowest MSE for the validation data, was a four-parameter VAE with a 500-441-383-4-383-441-500 layered architecture. For each spectral type from M7 to T8 (where M7 = 7 and L8 = 28), we show the average value of each latent parameter and its standard deviation in Figure 8.33. Each spectrum is described by these four parameters in latent space and can be reconstructed from the non-linear components shown in Figure 8.34.

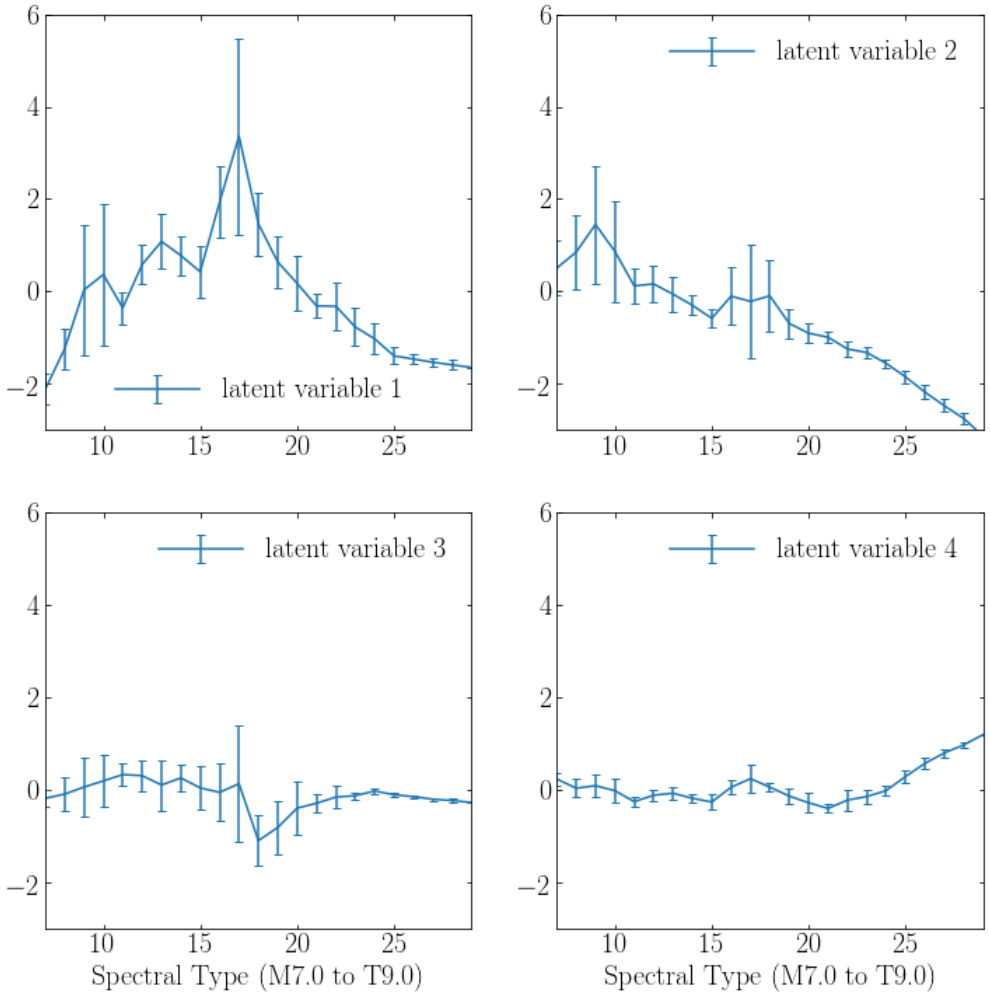

Figure 8.33: The average value for each latent variable as a function of spectral type with error bars indicating the standard deviation of latent values within each spectral type. The greatest variation in latent variable value within a given spectral type occurs around L7 (labelled 17 on the x-axis). This point also coincides with a change in direction in value in latent variable 1.

Spectra are not reconstructed as a linear combination of VAE parameters as with PCA

however we can illustrate how the non-linear components and latent parameters reconstruct a spectrum with Figure 8.34. A mean spectra forms the foundation, we then show the first latent parameter as it would be generated by the 1st, 16th, 50th, 86th and 99th percentile latent parameter value from our sample. We perform the same analysis for the second, third and forth VAE latent parameter. It can be seen that the later parameters contribute gradually smaller changes to the resulting spectrum.

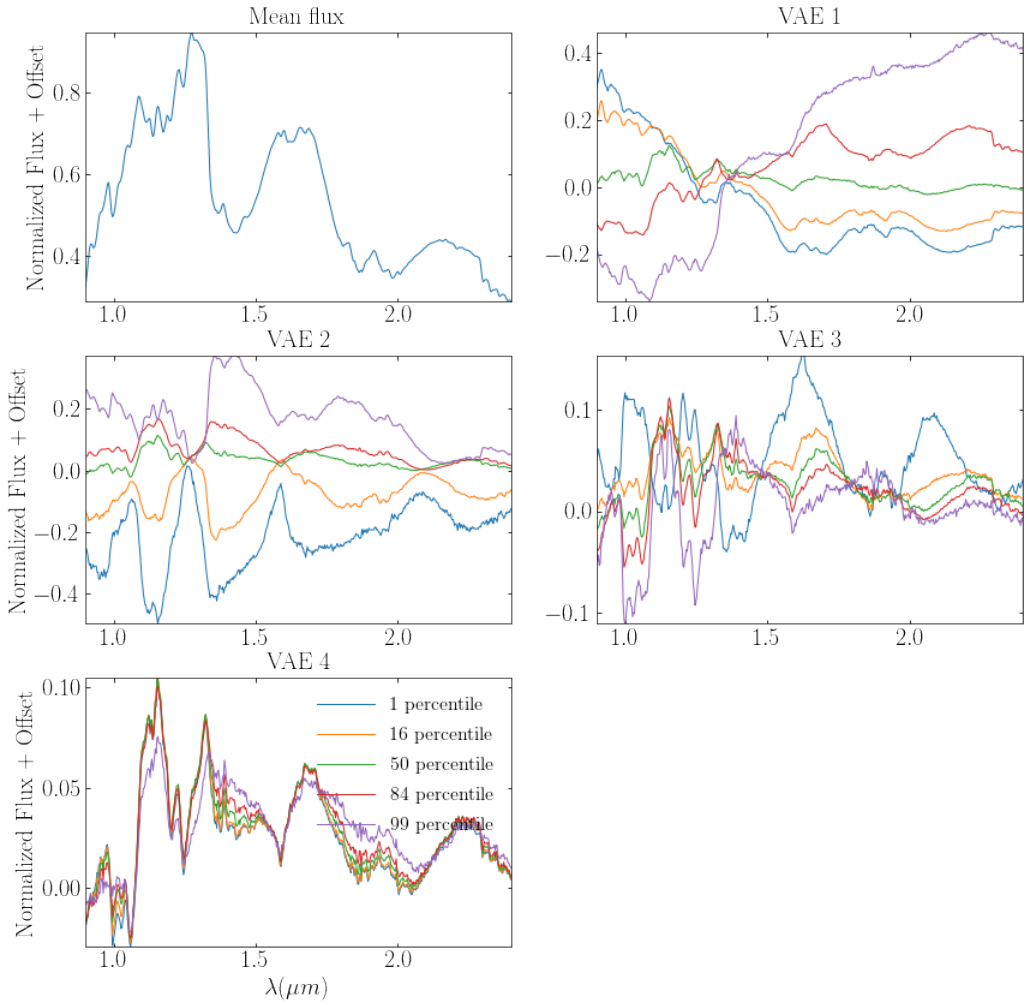

Figure 8.34: Non-linear components of the VAE trained model for a set of latent parameters as shown above. The mean spectra across all spectral type forms the foundation, we then show the first latent parameter as it would be generated by the 1st, 16th, 50th, 86th and 99th percentile parameter value from our sample. We perform the same analysis for the second, third and forth VAE latent parameter.

8.9.1 Discussion on VAE

In figures 8.35, 8.36 and 8.37 we show reconstructed spectra for M7 to T9 based on the mean latent parameters for a given spectral type. A simple visual inspection shows that the VAE has reconstructed the rapidly evolving spectra over this range of spectral types with a smooth and continuous evolution.

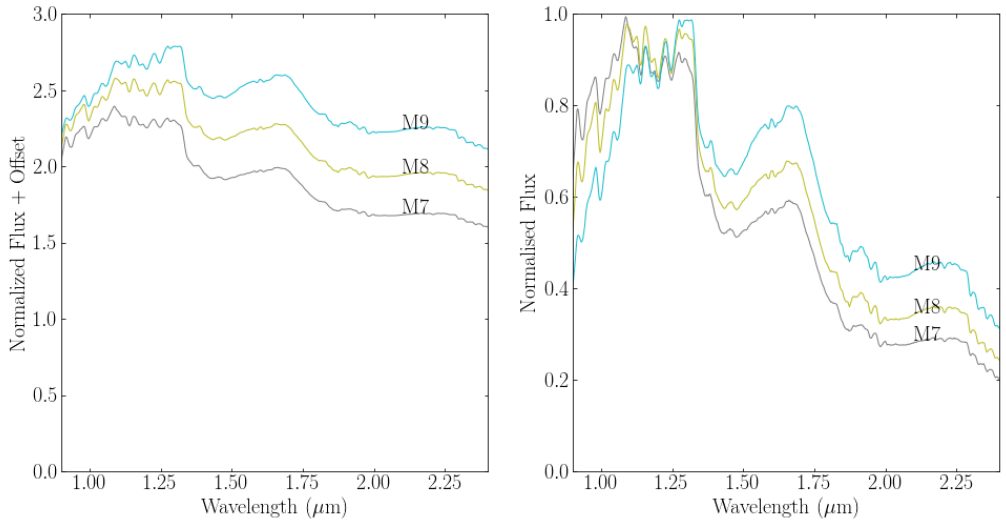

Figure 8.35: Reconstruction of the average spectrum for the M spectral types based on their mean latent parameters. The left hand plot shows the flux offset by 0.2 to show the evolution of the shape as we progress through the spectral types. The right hand plot shows the same spectra overlaid to illustrate the flux variation between spectral types at a given wavelength.

We compare the average reconstruction loss on the validation data to an equivalent reconstruction loss using PCA and NMF components trained on the training data and applied to the validation data. The results are shown in Figure 8.38. We find that the VAE significantly outperforms both PCA and NMF for the number of latent parameters ≤ 4 and that the performance becomes comparable for ≥ 5. For a given level of reconstruction loss, fewer latent variables are preferable as the observable data is represented as simply as possible making it more understandable and potentially uncovering underlying patterns and concepts in the data.

We measure the mean squared error (MSE) between the spectra and the VAE-reconstructed spectra for all 1696 samples and find a mean MSE of 2.44 and a median MSE of 1.88 as shown in figure 8.39.

Given the low mean reconstruction error and the improvement over other dimensionality reduction methods, this approach shows good promise as a classification method as well as generating realistic and representative synthetic spectra. That said, the current size of the available training set and low resolution of spectra limit the potential of this technique for

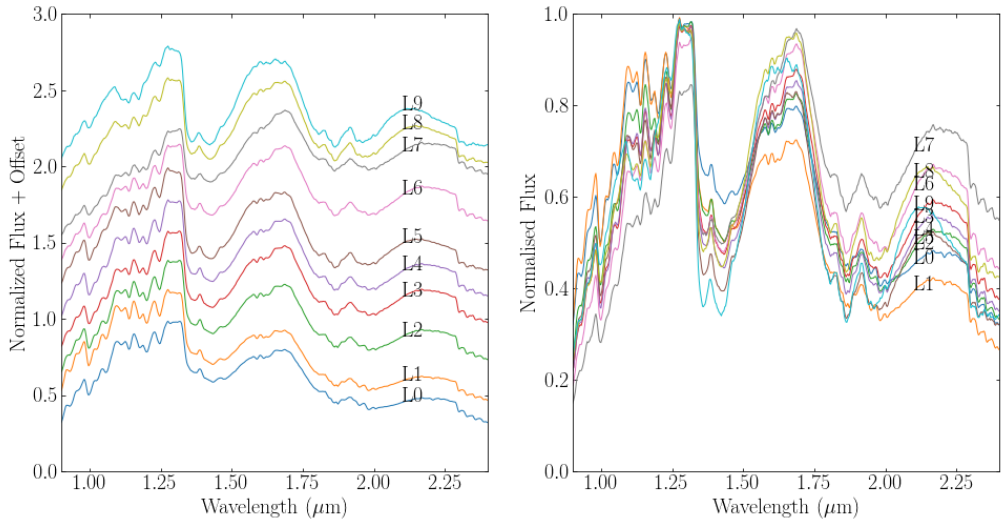

Figure 8.36: Reconstruction of the average spectrum for the L spectral types based on their mean latent parameters. The left hand plot shows the flux offset by 0.2 to show the evolution of the shape as we progress through the spectral types. The right hand plot shows the same spectra overlaid to illustrate the flux variation between spectral types at a given wavelength. The well-established reversal in spectral reddening around L7.0 is readily apparent.

identifying unusual or anomalous sources. Variation in gravity and metallicity within a given spectral type is captured in a non-specific manner in the dispersion of the latent variables. While the average reconstruction error across the sample is low, we find 11 sources with reconstructed spectra with MSE $>$ 15. We find that ten of these are classified as very low gravity objects. Figure 8.40 shows the comparison between the actual and VAE reconstructed spectra for the six spectra with the highest reconstruction error.

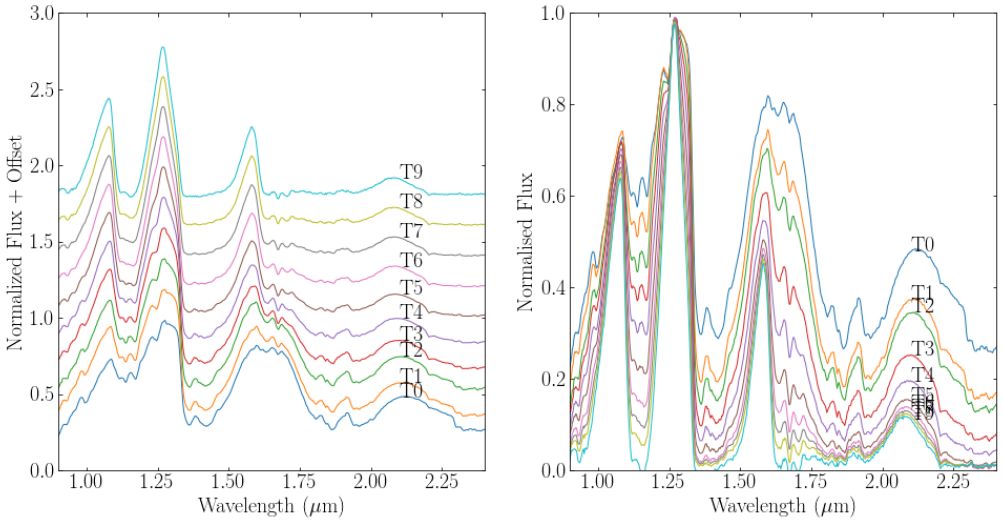

Figure 8.37: Reconstruction of the average spectrum for the T spectral types based on their mean latent parameters. The left hand plot shows the flux offset by 0.2 to show the evolution of the shape as we progress through the spectral types. The right hand plot shows the same spectra overlaid to illustrate the flux variation between spectral types at a given wavelength.

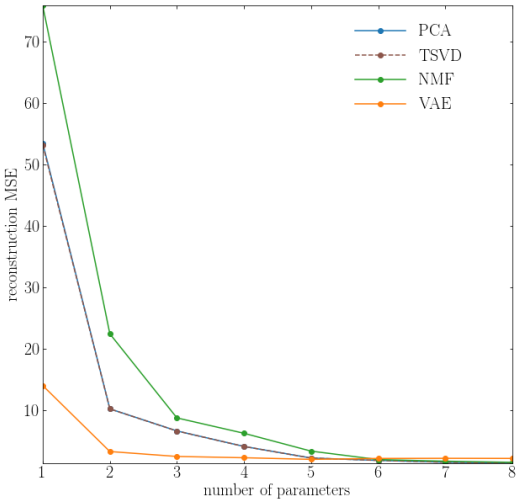

Figure 8.38: Mean squared reconstruction error for PCA, NMF and VAE. VAE significantly outperforms PCA, TSVD and NMF for < 5 latent parameters. This outperformance reduces and eventually underperforms as the number of parameters increases.

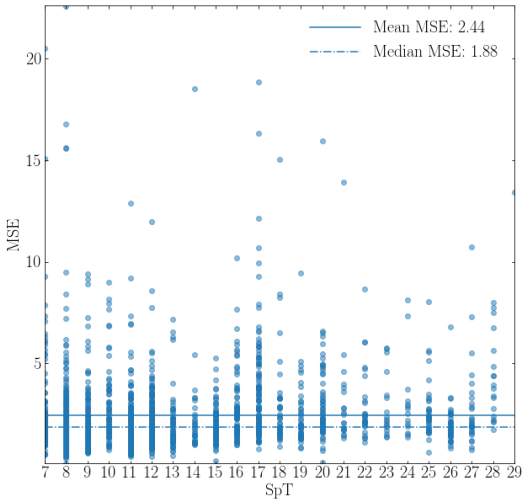

Figure 8.39: Plot shows mean squared error between resampled spectra and VAE-reconstructed spectrum for each spectra by spectral type (SpT) with numbering convention M7.0 = 7, L0.0 = 10, L9.0 = 19 and so on. The median and mean MSE across the entire sample is shown for the 4-parameter VAE model.

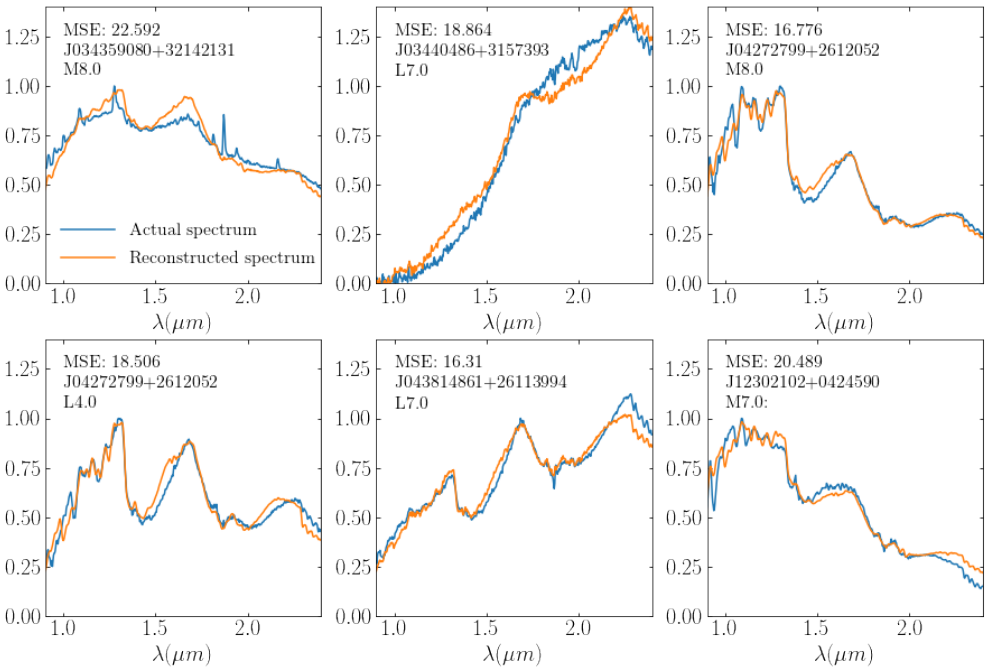

Figure 8.40: Six spectra with highest VAE reconstruction error

8.10 Summary & conclusions

In this chapter we have evaluated the current standard spectra used for UCD classification and performed a number of alternative traditional and machine learning approaches for UCD classification, feature extraction and anomaly detection. Given the variability in colour, molecular composition, gravity and metallicity in the spectra of UCDs, both across the spectral types and within an individual type, this is a challenging task. While we highlight a number of shortcomings in the existing qualitative and quantitative methods of classification, we were unable to sufficiently improve on these using alternative spectral indices, equivalent width features, or the construction of synthetic spectral standards. Turning to machine learning techniques, we found some promising approaches to classification through the application of supervised machine learning classifiers, in particular random forest and XGBoost, as well promising unsupervised dimensionality reduction and synthetic data generation with VAEs. However the supervised techniques rely on high quality and accurately labelled spectroscopic or photometric data. Spectroscopic methods are currently limited by the small number and fairly low quality of available spectra. We found that the spectra could be well represented, as measured by low reconstruction errors, by a small number of latent parameters using a VAE approach however we found that very low gravity objects were not well represented. The photometric samples are much larger and accurately classified however the sample size for spectral types later than L2 is small. We have shown that ensemble tree-based supervised machine learning and VAEs are promising approaches to explore further for classification however larger and higher resolution samples are required to improve overall accuracy. In addition gravity and metallicity cannot be ignored and must be taken into account.

Appendix A

Data, catalogues & surveys

This section describes the primary sources of data and catalogues that we have used in this research. In particular this research has relied heavily on utilising recent data releases from the European Space Agency (ESA) *Gaia* mission.

During the course of this work, the *Gaia* Data Processing and Analysis Consortium (DPAC) published two large data releases: *Gaia* Data Release 2 (DR2) on 28 April 2019 (Gaia Collaboration et al. 2016, Gaia Collaboration et al. 2018*b*, Lindegren et al. 2018, Evans et al. 2018), and *Gaia* Early Data Release 3 (EDR3) on 3 December 2020 (Gaia Collaboration et al. 2021, Riello et al. 2021, Gaia Collaboration et al. 2020).

The ESA's Gaia spacecraft is mapping the position, parallax and proper motion (5-parameter astrometric solution) of millions of sources with unprecedented accuracy from its position at the L2 Lagrange point. *Gaia* has been collecting data since July 2014. It's main photometric band, G, is a broad visible filter centred around 650 nm with sub filters G_{BP}, G_{RP} for the blue and red components respectively. It has a limiting magnitude of 21 at the faint end and a bright limit of 3. It is essentially complete for all sources between G=12 and G=17. *Gaia* also includes a radial velocity spectrometer (RVS) to measure radial velocity with low resolution spectra over the range 845-872 nm centred on a Calcium triplet. While *Gaia* was not specifically designed to detect exoplanets, this instrument is expected to catalogue tens of thousands of gas giant planets with separations between 1 and 4 AU (Reylé et al. 2021) using the radial velocity method of exoplanet detection. Data are anticipated in DR4. *Gaia* is not expected to detect super-Earths or sub-Neptunes.

EDR3 contains an updated sources list, astrometry and photometry in three passbands G, G_{BP}, G_{RP} for around 1.8 billion sources and represents an intermediate data release ahead of the full DR3 expected in early 2022. EDR3 includes a 30% improvement in parallax precision and a factor of 2 improvement in the precision of proper motion as well as significant reduction in systematic errors in astrometry, over DR2. Parallax uncertainties average 0.5 mas at G = 20. The photometry is significantly more homogeneous in colour, magnitude and sky position with less the 1% systemic errors.

One of the performance verification papers (Gaia Collaboration et al. 2020) released at the same time at EDR3 was particularly relevant to this research. This paper prepared a 100 pc

all-sky census of around 300,000 stars in our solar neighbourhood called the Gaia Catalogue of Nearby Stars (GCNS).

In addition to *Gaia* we use data from a number of other large area surveys including the Two Micron All Sky Survey '2MASS' (Skrutskie et al. 2006; the Sloan Digital Sky Survey 'SDSS' (Strauss et al. 1999, Hawley et al. 2002); the UK Infrared Deep Sky Survey 'UKIDSS' (Lawrence et al. 2007, Pinfield et al. 2008, Burningham et al. 2010); and the Wide-field Infrared Survey Explorer 'WISE' (Wright et al. 2010).

A.1 Photometric data

While every photometric measurement is specific to the measuring instrument, this research is primarily using the following wide and narrow bands:

Band	Survey	NIR photometric system	Calibration
G	Gaia	n/a	Vega
G_{BP}	Gaia	n/a	Vega
G_{RP}	Gaia	n/a	Vega
i	SDSS	MKO	AB
z	SDSS	MKO	AB
Y	UKIDSS	MKO	Vega
J	UKIDSS	MKO	Vega
H	UKIDSS	MKO	Vega
K	UKIDSS	MKO	Vega
J_{2MASS}	2MASS	2MASS	Vega
H_{2MASS}	2MASS	2MASS	Vega
Ks_{2MASS}	2MASS	2MASS	Vega
$W1$	WISE	n/a	Vega
$W2$	WISE	n/a	Vega

Table A.1: Photometric bands and instruments

The most common conversions required are to convert the SDSS iz AB magnitudes to Vega where the offsets in Hewett et al. (2006) are applied, and to transform the 2MASS photometry to the MKO system (Leggett et al. 2006).

A.2 Astrometric data

A typical 5-parameter astrometric solution comprises:

Symbol	Parameter
α	Equatorial longitude (Right Ascension)
δ	Equatorial latitude (Declination)
ϖ	Parallax (mas)
$\mu_{\alpha*}$	Proper motion in Right Ascension (mas/yr)
μ_δ	Proper motion in Declination (mas/yr)

Table A.2: Standard 5-parameter astrometric solution

Appendix B

Summary of statistical & machine learning techniques applied in this research

B.1 Introduction

The use of data science and statistic learning including sophisticated machine learning and artificial intelligence techniques is now widespread and pervasive in astronomical and astrophysical research. This discipline has always been heavily observational and data-driven although the volume of data now captured by modern instrumentation is increasing at an exponential rate. This deluge of data creates both opportunities and challenges. There are many definitions of machine learning (ML) and artificial intelligence (AI) however we choose to define these in line with Fluke & Jacobs (2019) as follows:
ML: automated processes that learn by example in order to classify, predict, discover or generate new data.
AL: methods by which a computer makes decisions or discoveries that would usually require human intelligence.

Here we describe the main statistical and machine learning techniques used in our research.

B.2 Bayesian parameter inference & Markov Chain Monte Carlo (MCMC)

Observational results need to be generalised to be scientifically useful. A theory is proposed and can be represented in a generalised functional form as a model of the underlying data-generating process. The objective of statistical inference is to estimate the unknown parameters of the model given the observational data.
Bayesian parameter estimation is an application of the product law of probability such that

the joint probability of two events, A and B is given by $P(A,B) = P(B,A) = P(A|B)P(B) = P(B|A)P(B)$. Rearranging this expression gives Bayes' Rule:

$$P(A|B) = \frac{P(B|A)P(A)}{P(B)}$$

In Bayesian parameter inference we apply Bayes' rule to determine a probability distribution for the parameters θ of a model M based on observed data d and prior information, I. This relation is described as follows:

$$P(\theta|d, M, I) = \frac{P(d|\theta, M, I)P(\theta|M, I)}{P(d|M, I)}$$

The likelihood $L(\theta) = \prod_i^n P(d_i|\theta, M, I)$ is a function of θ and is not a probability distribution. An important aspect of Bayes' Rule is that is allows us to update our estimate in the prescience of new information described by the prior $P(\theta|M, I)$. This is our unbiased estimate of the parameters prior to the new data.

The denominator is called the evidence. This has no θ dependence, is a normalisation constant and is often difficult to calculate in practice. As a result it is often ignored and relation below is used (dropping the model M and information I conditions).

$$P(\theta|d) \propto P(d|\theta)P(\theta)$$

where the maximum likelihood estimate (MLE) of θ is given by:

$$\hat{\theta} = \arg\max_{\theta} \; L(\theta) = \arg\max_{\theta} \; \prod_i^n P(d_i|\theta)$$

For many problems the likelihood is too complex for an analytical solution and numerical methods are used. Given the one-to-one relationship between the likelihood and the log likelihood, in practice the negative log likelihood is minimised to estimate $\hat{\theta}$ as follows:

$$\hat{\theta} = \arg\min_{\theta} \; ln(L(\theta)) = \arg\min_{\theta} \; \sum_i^n ln(P(d_i|\theta))$$

This is the basis of determining the best fit model parameters using MLE. This method is not strictly Bayesian as it does not include a prior term.

In practice, we can rarely infer the model parameters by solving the complex probability distribution analytically, and Markov Chain Monte Carlo (MCMC) methods are used instead. MCMC techniques randomly sample the parameter space using a guided random walk. Various algorithms exist to sample the parameter space efficiently e.g. Metropolis-Hastings, Hamiltonian MC, Gibbs. Each of these algorithms evaluate the function $f(\theta) = P(d|\theta)P(\theta)$ for an initial parameter vector $\theta = \{\theta_1, ..., \theta_N\}$, the subsequent θ_* is selected from a proposal distribution and evaluated as $f(\theta_*)$. This is compared to $f(\theta)$ to determine if the new parameter vector

is accepted or rejected. The methods by which these values are accepted or rejected and the subsequent choice of θ_* is dependent on the chosen MCMC algorithm.

Typically a large number of trials are run and the distributions of θ after an period of burn-in represent the posterior distributions for each θ_i. Posterior distributions are often shown visually as a corner plot with individual parameter distributions and two-dimensional contour plots for each combination of parameters.

While the entire posterior distribution for a given parameter is the result, it is often practical to summarise the estimate using either the maximum a posteriori (MAP), or median estimate with some dispersion interval.

B.3 Two-dimensional inhomogeneous Poisson point process

A two-dimensional inhomogeneous Poisson point process is one where an underlying Poisson process (e.g. independent count data) generates points on a two-dimensional mathematical plane and the points are not uniformly distributed (inhomogeneous). Inhomogeneous Poission point processes can be used to describe a wide variety of natural phenomenon subject to such underlying complexity or noise and where the underlying data-generating mechanisms are best described probabilistically. In general certain regions will contain a higher or lower density of points than elsewhere. We seek to fit a smooth, differentiable intensity function $\lambda(x, y)$ or normalised joint probability density function $f(x, y)$, to the observed data. An important and defining property of a Poisson point process is the complete independence of each point. Our data are measurements of absolute magnitude and colour where each observation is a separate and independent source measured by *Gaia* within a volume-complete region of the sky. In this instance we are not concerned with temporal inhomogeneity as the period over which the observations were taken is much shorter than the timescale over which the observed measurements change. A parameterised model is assumed to describe the joint probability function and fitted using a Monte Carlo Markov Chain (MCMC) Bayesian parameter estimation method.

B.4 Tree-based algorithms for supervised learning

B.4.1 Random Forest

Random forest (Breiman 2001) is a versatile and commonly used supervised learning algorithm built on the idea of a decision tree[1]. This method builds an ensemble of decision trees by selecting a random subset of features and observations and then trains each subtree by selecting the most important feature at each node. This is know as 'bagging'. The subtrees are combined by taking the majority vote of each subtree's prediction which results in a more accurate classifier than

[1] A decision tree is a hierarchical structure consisting of nodes (test for the value or category of a feature); branches (linking the nodes based on the outcome of the previous node test); and leaf nodes (predicted class or label).

any one subtree or a single decision tree trained on the entire dataset. Random forests can be used for both classification and regression tasks and they are generally robust to overfitting.

B.4.2 XGBoost

A leading gradient boosted tree algorithm is the eXtreme Gradient Boosted algorithm or XGBoost developed by Chen & Guestrin (2016). It builds a predictive model based on an ensemble of weaker predictive models similar to random forest. Instead of creating subsamples of data and training each independently, XGBoost uses a boosting method where each model iteration is evaluated with a loss function until the loss function is minimised. This is a numerical optimisation problem which minimises a differentiable loss function using gradient descent. Boosting describes the process where models are added sequentially to correct misclassifications. It achieves this by assigning more weight to points incorrectly classified which introduces new features (weak learners) to boost the performance of the algorithm for those incorrectly classified records.

B.4.3 AdaBoost

Adaptive boosting (AdaBoost) is another ensemble-based learning algorithm that uses boosting to sequentially correct predictions. AdaBoost builds small one-level decision trees that are individually weak classifiers but iteratively adds new trees to correct for the misclassification errors of previous trees by more heavily weighting the misclassified records. Unlike XGBoost, AdaBoost does not use gradient descent. It is generally more suited to binary classification tasks.

A full mathematical description of the Random Forest, AdaBoost and XGBoost algorithms is beyond the scope of this work.

B.5 Dimensionality reduction

B.5.1 Principal Component Analysis (PCA)

PCA creates a set of new independent features that are linear combinations of the original features. The idea is to find a subspace spanned by an orthogonal basis of new features that minimises the errors of projecting the data onto this subspace. We determine the principal components as the eigenvectors of the features covariance matrix ordered by the largest eigenvalue. Each eigenvalue describes the amount of variance in the original feature space explained by including the corresponding eigenvector in the basis of the subspace. For example the first principal component explains the greatest amount of variance in the data. Principal components with very small, near zero eigenvalues are not included.

B.5.2 Independent Components Analysis (ICA)

ICA assumes that the data is a mixture of independent signals or components. It seeks to separate and recover these. In common with PCA, ICA tries to identify a set of basis vectors to describe the data in a lower dimensional space. However ICA does not require that the basis vectors be orthogonal. ICA requires that the signals are statistically independent and maximises non-gaussianity.

B.5.3 t-Distributed Stochastic Neighbour Embedding (t-SNE)

t-SNE developed by van der Maaten & Hinton (2008) is often used to visualise clusters in a high-dimensional data. It works by trying to keep similar instances close and dissimilar instances apart by minimising the Kullback-Leibler[2] divergence between the joint probabilities of the low-dimensional embedding and the high-dimensional data. Note that the cost function often have local minima so that different initialisations can lead to different embeddings.

B.5.4 Locally Linear Embedding (LLE)

LLE (Roweis & Saul 2000) works by measuring how each instance linearly relates to its closest neighbours in the higher dimensional space, and then looks for a lower-dimensional representation of the data where these local relationships are best preserved. This method is particularly good at representing twisted or folded manifolds.

B.5.5 ISOMAP

Isometric feature mapping (ISOMAP) developed by Tenenbaum et al. (2000) is a non-linear dimensionality reduction algorithm that preserves the geodesic distance rather than the Euclidean distance between points in the higher dimensional space. The geodesic distance between two data points is the shortest distance along the manifold on which the points lie. Unfortunately the true manifold is often not known and therefore the geodesic distance is estimated using a nearest neighbour graph (e.g. k-Nearest Neighbour). It is particularly good at capturing data lying on a curved global geometry.

B.5.6 UMAP

Uniform Manifold Approximation and Projection (UMAP) is a non-linear dimensionality reduction algorithm presented by McInnes et al. (2018) used primarily for visualisation and exploring high dimensional data. It is similar to t-SNE in that it uses a high dimensional graph to represent the data before organising into a lower dimensional space. The key difference is that UMAP constructs a weighted graph with each edge weighting representing the likelihood of connectedness with the other point. Only the n-nearest neighbouring points are connected by setting a local radius out from each point (Coenen & Pearce 2019). UMAP assumes data is uniformly distributed on a Riemannian manifold. It is more generally applicable and has better performance than t-SNE.

B.6 Autoencoders

Autoencoders are a deep learning neural network architecture comprising an encoder and decoder. They aim to learn a compressed representation of the input data and then recreate a copy of the input as an output.

The data are not labelled but since they are trained on their own input data it is a self-supervised learning method. Uses include feature extraction, classification, anomaly detection, image compression and denoising, and as a dimensionality reduction technique as preparation for a predictive model. The basic architecture of an autoencoder consists of an input layer, an output layer and a bottleneck layer separated by one or more hidden layers of perceptrons. The bottleneck layer or latent space consists of a low-dimension vector capturing a compressed version of the input data. This latent space representation can be decoded to recreate the input with some reconstruction loss. The learning part minimises the reconstruction loss via some loss function. The four hyperparameters required in an autoencoder are (i) size of the bottleneck vector; (ii) number of layers; (iii) number of nodes per layer; and (iv) the reconstruction loss function. The encoder and decoder have the same number of layers and the same number of nodes per layer; they are in a sense mirror images of each other.

B.7 Variational autoencoders

Variation autoencoders (VAEs) (Paszke et al. 2019) are built on the same principles as autoencoders however the latent space is regularised allowing the model to generate representative new data. The ability to create synthetic data sets VAEs apart from autoencoders. In principle autoencoders could be used to generate synthetic data however the regularity of the latent space is highly dependent on the initial data and the architecture of the encoder/decoder. Selecting a random point in latent space may produce meaningless outputs. VAEs achieve regularity in latent space by encoding the input data as a distribution over the latent space rather than a single point. It achieves this by sampling from the encoded latent distribution, calculating the reconstruction error of the decoded sample and propagating this back through the neural network. The encoded latent spaces are generally Gaussian distributions and as such a mean and variance are returned. The latent variables are then sampled from these distributions and decoded as shown in Figure B.1.

The VAE is trained by minimising a loss function comprising the reconstruction error on the output and a regularisation term on the latent space as shown in equation B.1 using gradient descent. The regularisation term ensures that the latent distributions are close to a standard normal by minimising the Kullback-Leibler divergence[2].

$$\mathcal{L} = \|\mathbf{x} - \hat{\mathbf{x}}\|^2 + KL[\mathcal{N}(\mu, \sigma^2),\ \mathcal{N}(0, \mathbf{I})] \tag{B.1}$$

Regularity in latent space achieves both continuity and completeness. Continuity ensures

[2]The Kullback-Leibler divergence, or relative entropy, measures how one probability distribution differs from a second, reference distrbution. A value of 0 indicates that the distributions have the same information content.

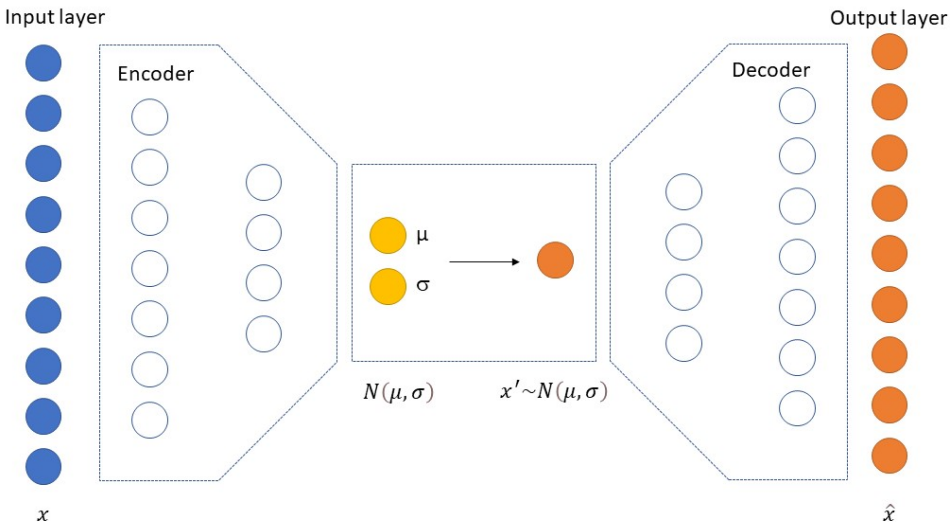

Figure B.1: Illustrative diagram of variational autoencoder architecture.

that close points in latent space generate similar outputs. Completeness ensures that points sampled from the latent distributions should generative valid outputs.

Appendix C

Telescope proposals

C.1 The L-T transition and extreme red objects

Using the catalogue of L and T dwarfs (Skrzypek et al. 2015, 2016) we show colour evolution ($Y-H$ and $J-K$) from L0 to T8 (see Figures C.1 and C.2). We can see the steady reddening from L0 through L7 with the largest dispersion occurring for L7 objects. This is followed by sudden reversal from gradual reddening to becoming increasingly blue from L8 to T8. While this trend is not unexpected there are hints that some extreme red objects are being classified within the L7 subcategory. These may be very young objects or extreme examples of the atmospheric processes occurring just before the onset of the observed changes identified with the L/T transition.

We have identified the most extreme red objects in the sample using a Y-W1 vs. W1-W2 two-colour plot (see Figure C.3). This Figure illustrates the rapid change in Y-W1 magnitude around L7 and a spur of objects continuing above the general trend. We believe that some of these objects are at the cusp of the L/T transition and may hold important clues as to the mechanisms driving this rapid change.

From our analysis we have identified 16 objects with Y-W1>4.0 and over 2σ redder than the L7 photometric standard colour (shown in orange). These objects include two previously identified young, very low-gravity objects:

- J0055+0134 classified as L2γ (Skrzypek et al. 2016)
- J0126+1428 classified as L2γ (Metchev et al. 2008)

These objects are positioned across the sky and are therefore not all observable at the same time or hemisphere. We submitted two telescope proposals to obtain high quality spectra of these objects for detailed further analysis.

We anticipate that these objects are a mixture of potentially very young objects as well as those with the most extreme cloudy condensate-rich atmospheres however future high-resolution spectra are required to understand the processes occurring in the atmospheres of these objects.

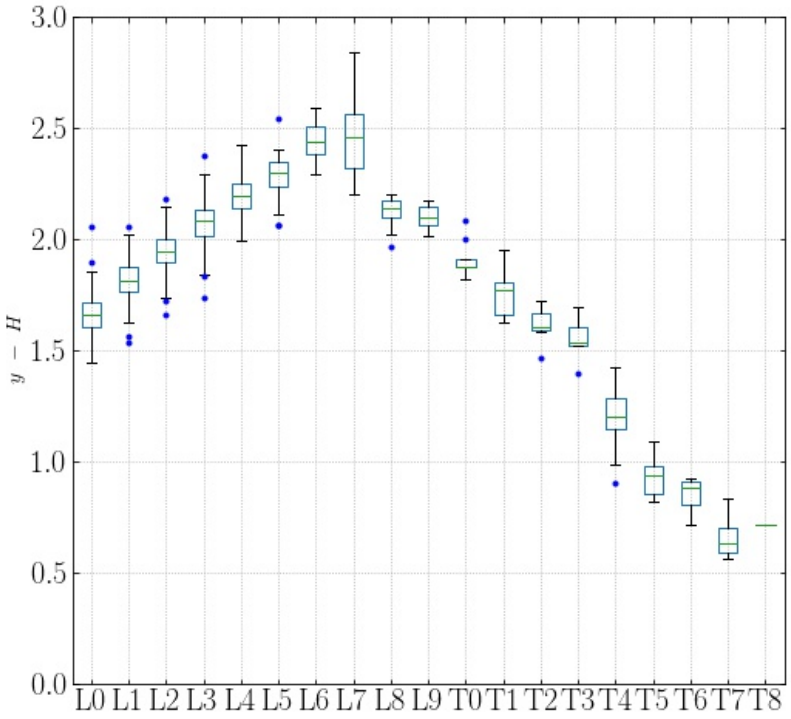

Figure C.1: Box plot showing the evolution of $Y-H$ colour with spectral type for a homogeneous sample of 1361 L & T dwarfs. Box extends from the lower to upper quartile showing median (red line). The whiskers show the range of the data with outliers highlighted as points.

Eight of our 16 extreme red objects identified in Figure C.3 have spectra in the SpeX Prism library[1] (Burgasser 2014). We compare these SpeX spectra to the L7 standard object in Figure C.4 highlighting the main molecular absorption and telluric regions.

C.2 Submission of ESO VLT proposal

We submitted a proposal for 12.1 hours of observing time in period 104A[2] at the ESO Very Large Telescope (VLT) using the X-Shooter instrument. We proposed to obtain high S/N, high resolution spectra for 12 extremely red L/T transition objects observable from the VLT site in Paranal, Chile (see Table *C*.1 objects S1-S12). In addition we will also obtain spectra for the standard L6-L8 objects observable from Paranal (see Table *C*.1 objects L6-L8). Note that high S/N, high quality spectra is already available for the standard L9 object. We will compare the observed spectra to the SpeX standards and analyse differences in the strength of absorption lines for FeH, metal oxides using our results to constrain or support various L/T transition mechanisms including cloud breaking; surface features; cloud-free convective instablilities. In addition we will measure the spectral indices and compare to the classification standards defined by (Geballe et al. 2002), (Cruz et al. 2009) and (Allers & Liu 2013) to assess whether they

[1]The SpeX Prism Library is a repository of low-resolution, near-infrared spectra of ultracool dwarfs obtained with the SpeX spectrograph instrument attached to the 3m NASA Infrared Telescope Facility on Mauna Kea, Hawaii

[2]Observing period 1 October 2019 to 31 March 2020

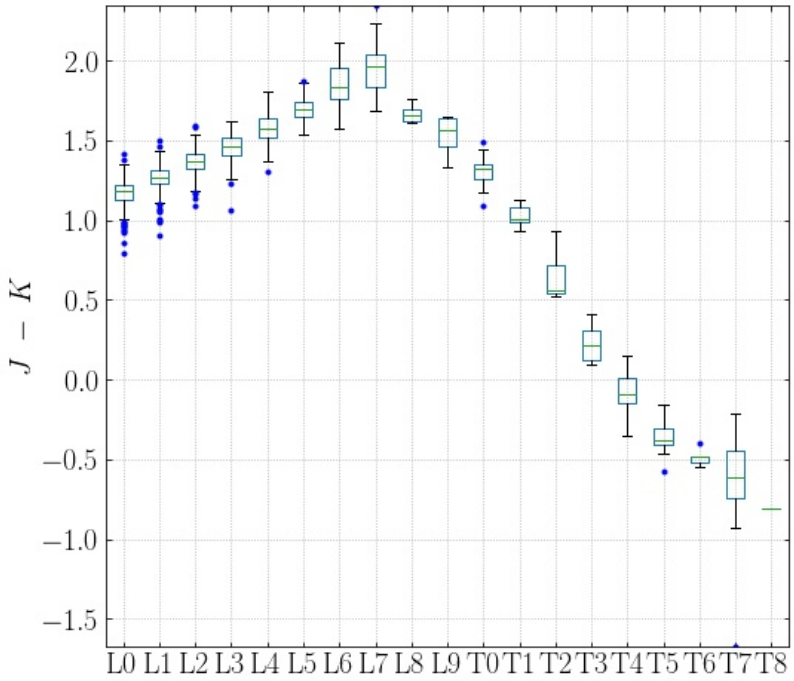

Figure C.2: Box plot showing the evolution of $J - K$ with spectral type for a homogeneous sample of 1361 L & T dwarfs. Box extends from the lower to upper quartile showing median (red line). The whiskers show the range of the data with outliers highlighted as points.

current standards sufficiently recognise these objects and inform if they are unusual/peculiar, or represent a unrecognised class of objects between L7 and L8.

Unfortunately this telescope proposal was not successful.

C.3 Submission of NASA Infrared Telescope Facility (IRTF) proposal

A telescope proposal was submitted to NASA IRTF for 6 hours of observing time using the SpeX instrument. This was the first of two proposals to observe those objects observable from the Mauna Kea in Hawaii during the observing period 1 Aug 2019 to 31 January 2020. A second proposal was to be submitted for the following observing period.
Of the five target objects, four do not have existing SpeX spectra. Object S2 (see Table C.2) does have spectra but with low S/N. We would like to obtain consistent, higher resolution spectra for all five objects in our sample.

This proposal was successfully awarded for 7 August 2019. Unfortunately during July and August all the astronomical facilities on Mauna Kea were evacuated and temporarily closed due to protesters blocking the access road. Despite a long history of astronomy and astronomical facilities on Mauna Kea, some environmental groups and Native Hawaiians oppose the ongoing development of Mauna Kea due to concerns around protecting their cultural heritage as well as

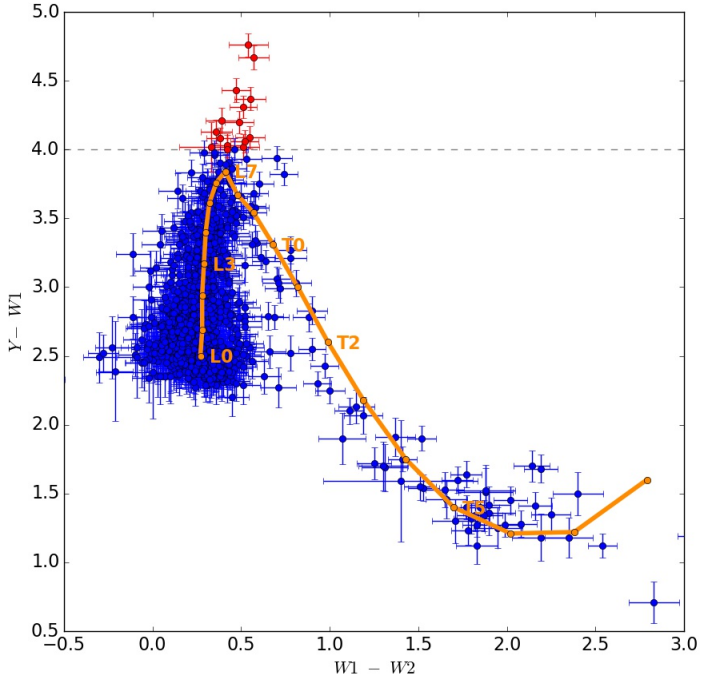

Figure C.3: Objects with $Y - W1 > 4.0$ (coloured red with error bars). Also shown are the photometric template colours for L0 to T9 (orange solid line). Other objects shown in blue with error bars.

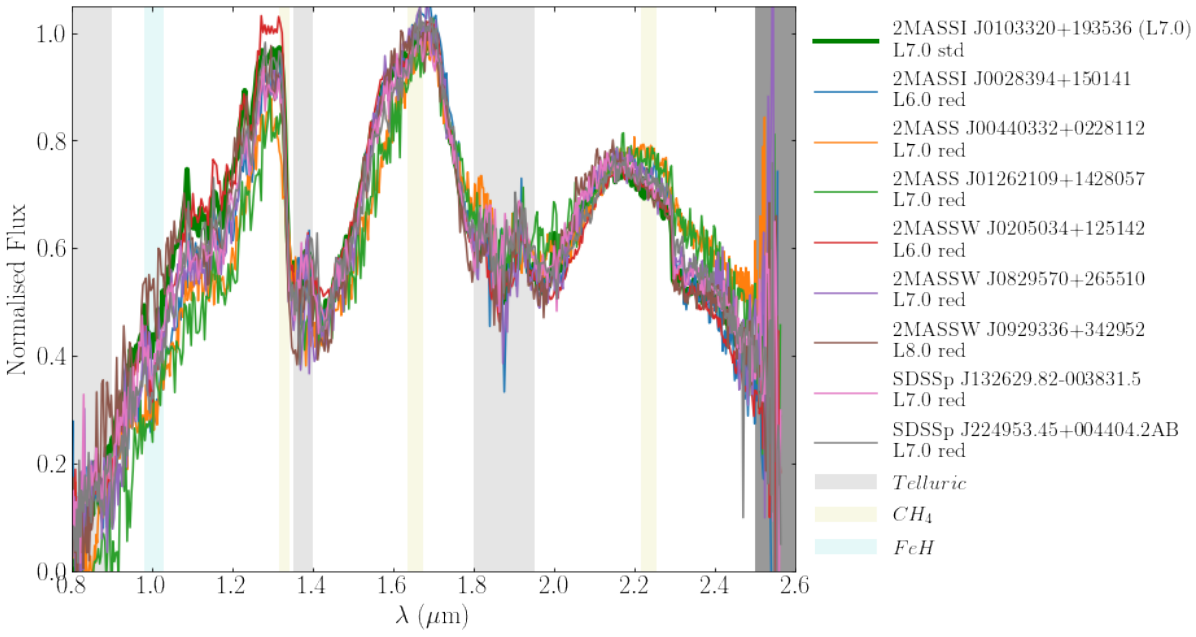

Figure C.4: SpeX spectra of selected extreme red objects compared to standard L7 object. Telluric and significant molecular absorption regions are shown.

Target	RA(J2000)	DEC(J2000)	Mag	Integration Time
J0028+1501(S1)	00 28 39.5	+15 01 41	J=16.6	700s
J0044+0228(S2)	00 44 03.4	+02 28 11	J=17.1	1600s
J0055+0134(S3)	00 55 05.7	+01 34 36	J=16.4	600s
J0126+1428(S4)	01 26 21.1	+14 28 06	J=17.5	3400s
J0205+1251(S5)	02 05 03.7	+12 51 42	J=15.6	600s
J1159+1432(S6)	11 59 53.5	+14 32 03	J=17.4	2800s
J1326−0038(S7)	13 26 29.7	-00 38 33	J=16.2	600s
J1344+0924(S8)	13 44 14.9	+09 24 05	J=17.3	2500s
J1509+0344(S9)	15 09 27.8	+03 44 50	J=17.2	2500s
J2237+0716(S10)	22 37 56.9	+07 16 57	J=17.5	3600s
J2249+0044(S11)	22 49 53.5	+00 44 05	J=16.5	600s
J2334+1313(S12)	23 34 32.5	+13 13 15	J=16.6	700s
J1010−0406(L6)	10 10 48.0	-04 06 50	J=15.5	600s
J0103+1935(L7)	01 03 32.0	+19 35 36	J=16.3	600s
J1632+1904(L8)	16 32 29.1	+19 04 41	J=15.9	600s

Table C.1: List of target objects submitted to ESO VLT

Target	Coordinates	Mag	Integration Time
J0001+1535 (S1)	$0^h\ 1^m\ 12^s$, +15.59°	J=15.5	0.2 hr
J0044+0228 (S2)	$0^h\ 44^m\ 3^s$, +2.50°	J=17.1	1.0 hr
J0151+1131 (S3)	$1^h\ 51^m\ 29^s$, +11.52°	J=16.8	0.7 hr
J2237+0716 (S4)	$22^h\ 37^m\ 57^s$, +7.28°	J=17.5	1.0 hr
J2334+1313 (S5)	$23^h\ 34^m\ 33^s$, +13.22°	J=16.6	0.5 hr

Table C.2: List of target objects submitted to NASA SPEX

potential damage to the local environment. This peaceful protest against the construction of the Thirty Meter Telescope (TMT) disrupted scheduled observations for a period of months. This remains a highly controversial issue with strong support both for and against the construction of the TMT amongst Hawaiian residents[3].

[3]https://www.westhawaiitoday.com/2020/05/28/hawaii-news/ward-research-shows-citizens-2-to-1-favor-of-telescope/

Bibliography

Ackerman, A. S. & Marley, M. S. (2001*a*), 'Precipitating Condensation Clouds in Substellar Atmospheres', **556**(2), 872–884.

Ackerman, A. S. & Marley, M. S. (2001*b*), 'Precipitating Condensation Clouds in Substellar Atmospheres', **556**(2), 872–884.

Adams, F. C., Batygin, K. & Bloch, A. M. (2020), 'Energy optimization in binary star systems: explanation for equal mass members in close orbits', **494**(2), 2289–2298.

Aganze, C., Burgasser, A. J., Malkan, M., Theissen, C. A., Tejada Arevalo, R. A., Hsu, C.-C., Bardalez Gagliuffi, D. C., E Ryan, Russell, J. & Holwerda, B. (2021), 'Beyond the Local Volume I: Surface Densities of Ultracool Dwarfs in Deep HST/WFC3 Parallel Fields', *arXiv e-prints* p. arXiv:2110.07672.

Ahmed, S. & Warren, S. J. (2019), 'A homogeneous sample of 34 000 M7-M9.5 dwarfs brighter than J = 17.5 with accurate spectral types', **623**, A127.

Allard, F., Hauschildt, P. H., Alexander, D. R. & Starrfield, S. (1997), 'Model Atmospheres of Very Low Mass Stars and Brown Dwarfs', **35**, 137–177.

Allard, F., Hauschildt, P. H., Alexander, D. R., Tamanai, A. & Schweitzer, A. (2001), 'The Limiting Effects of Dust in Brown Dwarf Model Atmospheres', **556**(1), 357–372.

Allard, F., Homeier, D. & Freytag, B. (2012), 'Models of very-low-mass stars, brown dwarfs and exoplanets', *Philosophical Transactions of the Royal Society of London Series A* **370**(1968), 2765–2777.

Allen, J. T., Hewett, P. C., Richardson, C. T., Ferland, G. J. & Baldwin, J. A. (2013), 'Classification and analysis of emission-line galaxies using mean field independent component analysis', **430**(4), 3510–3536.

Allen, P. R. (2007), 'Star Formation via the Little Guy: A Bayesian Study of Ultracool Dwarf Imaging Surveys for Companions', **668**(1), 492–506.

Allen, P. R., Koerner, D. W., Reid, I. N. & Trilling, D. E. (2005), 'The Substellar Mass Function: A Bayesian Approach', **625**(1), 385–397.

Allen, P. R. & Reid, I. N. (2008), 'Spitzer/irac Search for Companions to Nearby, Young M Dwarfs', **135**(6), 2024–2032.

Allen, P. R., Reid, I. N. & Koerner, D. W. (2005), The distribution of companions to ultracool dwarfs, *in* F. Favata, G. A. J. Hussain & B. Battrick, eds, '13th Cambridge Workshop on Cool Stars, Stellar Systems and the Sun', Vol. 560 of *ESA Special Publication*, p. 385.

Allers, K. N. & Liu, M. C. (2013), 'A Near-infrared Spectroscopic Study of Young Field Ultracool Dwarfs', **772**(2), 79.

Ambartsumian, V. A. (1937), 'On the Statistics of Double Stars', **14**, 207–219.

Apai, D., Karalidi, T., Marley, M. S., Yang, H., Flateau, D., Metchev, S., Cowan, N. B., Buenzli, E., Burgasser, A. J., Radigan, J., Artigau, E. & Lowrance, P. (2017*a*), 'Zones, spots, and planetary-scale waves beating in brown dwarf atmospheres', *Science* **357**(6352), 683–687.

Apai, D., Karalidi, T., Marley, M. S., Yang, H., Flateau, D., Metchev, S., Cowan, N. B., Buenzli, E., Burgasser, A. J., Radigan, J., Artigau, E. & Lowrance, P. (2017*b*), 'Zones, spots, and planetary-scale waves beating in brown dwarf atmospheres', *Science* **357**(6352), 683–687. **URL:** *http://science.sciencemag.org/content/357/6352/683*

Apai, D., Radigan, J., Buenzli, E., Burrows, A., Reid, I. N. & Jayawardhana, R. (2013), 'HST Spectral Mapping of L/T Transition Brown Dwarfs Reveals Cloud Thickness Variations', **768**(2), 121.

Artigau, É. (2018), Variability of Brown Dwarfs, *in* H. J. Deeg & J. A. Belmonte, eds, 'Handbook of Exoplanets', p. 94.

Aumer, M. & Binney, J. J. (2009), 'Kinematics and history of the solar neighbourhood revisited', **397**(3), 1286–1301.

Aumer, M., Binney, J. & Schönrich, R. (2016), 'Age-velocity dispersion relations and heating histories in disc galaxies', **462**(2), 1697–1713.

Bahcall, J. N. (1986), 'Star counts and galactic structure.', **24**, 577–611.

Bahcall, J. N. & Soneira, R. M. (1980), 'The universe at faint magnitudes. I. Models for the Galaxy and the predicted star counts.', **44**, 73–110.

Bahcall, J. N. & Soneira, R. M. (1984), 'Comparisons of a standard galaxy model with stellar observations in five fields.', **55**, 67–99.

Bailer-Jones, C. A. L. (2015), 'Estimating Distances from Parallaxes', **127**(956), 994.

Bailer-Jones, C. A. L., Rybizki, J., Fouesneau, M., Mantelet, G. & Andrae, R. (2018), 'Estimating Distance from Parallaxes. IV. Distances to 1.33 Billion Stars in Gaia Data Release 2', **156**(2), 58.

Baraffe, I. & Chabrier, G. (1996), 'Mass–Spectral Class Relationship for M Dwarfs', **461**, L51.

Baraffe, I., Chabrier, G., Allard, F. & Hauschildt, P. H. (1998), 'Evolutionary models for solar metallicity low-mass stars: mass-magnitude relationships and color-magnitude diagrams', **337**, 403–412.

Baraffe, I., Chabrier, G., Barman, T. S., Allard, F. & Hauschildt, P. H. (2003), 'Evolutionary models for cool brown dwarfs and extrasolar giant planets. The case of HD 209458', **402**, 701–712.

Baraffe, I., Homeier, D., Allard, F. & Chabrier, G. (2015), 'New evolutionary models for pre-main sequence and main sequence low-mass stars down to the hydrogen-burning limit', **577**, A42.

Bardalez Gagliuffi, D. C., Burgasser, A. J., Schmidt, S. J., Theissen, C., Gagne, J., Gillon, M., Sahlmann, J., Faherty, J. K., Gelino, C. & Cruz, K. L. (2019), 'The Ultracool SpeXtroscopic Survey. I. Volume-Limited Spectroscopic Sample and Luminosity Function of M7−L5 Ultracool Dwarfs', *arXiv e-prints* p. arXiv:1906.04166.

Bardalez Gagliuffi, D. C., Faherty, J. K., Schneider, A. C., Meisner, A., Caselden, D., Colin, G., Goodman, S., Kirkpatrick, J. D., Kuchner, M., Gagné, J., Logsdon, S. E., Burgasser, A. J., Allers, K., Debes, J., Wisniewski, J., Rothermich, A., Andersen, N. S., Thévenot, M., Walla, J. & Backyard Worlds: Planet 9 Collaboration (2020), 'WISEA J083011.95+283716.0: A Missing Link Planetary-mass Object', **895**(2), 145.

Bastian, N., Covey, K. R. & Meyer, M. R. (2010), 'A Universal Stellar Initial Mass Function? A Critical Look at Variations', **48**, 339–389.

Bate, M. R. (2012), 'Stellar, brown dwarf and multiple star properties from a radiation hydrodynamical simulation of star cluster formation', **419**(4), 3115–3146.

Bate, M. R., Bonnell, I. A. & Bromm, V. (2002), 'The formation of close binary systems by dynamical interactions and orbital decay', **336**(3), 705–713.

Belokurov, V., Erkal, D., Evans, N. W., Koposov, S. E. & Deason, A. J. (2018), 'Co-formation of the disc and the stellar halo', **478**(1), 611–619.

Bennett, M. & Bovy, J. (2019), 'Vertical waves in the solar neighbourhood in Gaia DR2', **482**(1), 1417–1425.

Best, W. M. J., Liu, M. C., Magnier, E. A. & Dupuy, T. J. (2020*a*), 'A Volume-Limited Sample of L0-T8 Dwarfs. I. Construction, Space Density, and a Gap in the L/T Transition', *arXiv e-prints* p. arXiv:2010.15853.

Best, W. M. J., Liu, M. C., Magnier, E. A. & Dupuy, T. J. (2020*b*), 'The Hawaii Infrared Parallax Program. IV. A Comprehensive Parallax Survey of L0-T8 dwarfs with UKIRT', *arXiv e-prints* p. arXiv:2010.15850.

Biller, B. (2017*a*), 'The time domain for brown dwarfs and directly imaged giant exoplanets: the power of variability monitoring', *The Astronomical Review* **13**(1), 1–27.

Biller, B. (2017*b*), 'The time domain for brown dwarfs and directly imaged giant exoplanets: the power of variability monitoring', *The Astronomical Review* **13**(1), 1–27.

Biller, B. A., Kasper, M., Close, L. M., Brandner, W. & Kellner, S. (2006), 'Discovery of a Brown Dwarf Very Close to the Sun: A Methane-rich Brown Dwarf Companion to the Low-Mass Star SCR 1845-6357', **641**(2), L141–L144.

Binney, J., Dehnen, W. & Bertelli, G. (2000), 'The age of the solar neighbourhood', **318**(3), 658–664.

Binney, J. & Merrifield, M. (1998), *Galactic Astronomy*.

Blake, C. H., Charbonneau, D., White, R. J., Torres, G., Marley, M. S. & Saumon, D. (2008), 'A Spectroscopic Binary at the M/L Transition', **678**(2), L125.

Bochanski, J. J., Hawley, S. L., Covey, K. R., West, A. A., Reid, I. N., Golimowski, D. A. & Ivezić, Ž. (2010), 'The Luminosity and Mass Functions of Low-mass Stars in the Galactic Disk. II. The Field', **139**(6), 2679–2699.

Bonfils, X., Delfosse, X., Udry, S., Forveille, T., Mayor, M., Perrier, C., Bouchy, F., Gillon, M., Lovis, C., Pepe, F., Queloz, D., Santos, N. C., Ségransan, D. & Bertaux, J. L. (2013), 'The HARPS search for southern extra-solar planets. XXXI. The M-dwarf sample', **549**, A109.

Bouy, H., Brandner, W., Martín, E. L., Delfosse, X., Allard, F. & Basri, G. (2003), 'Multiplicity of Nearby Free-Floating Ultracool Dwarfs: A Hubble Space Telescope WFPC2 Search for Companions', **126**(3), 1526–1554.

Bouy, H., Martín, E. L., Brandner, W. & Bouvier, J. (2005), 'A Possible Third Component in the L Dwarf Binary System DENIS-P J020529.0-115925 Discovered with the Hubble Space Telescope', **129**(1), 511–517.

Bovy, J. (2017), 'Stellar inventory of the solar neighbourhood using Gaia DR1', **470**(2), 1360–1387.

Bovy, J., Nidever, D. L., Rix, H.-W., Girardi, L., Zasowski, G., Chojnowski, S. D., Holtzman, J., Epstein, C., Frinchaboy, P. M., Hayden, M. R., Rodrigues, T. S., Majewski, S. R., Johnson, J. A., Pinsonneault, M. H., Stello, D., Allende Prieto, C., Andrews, B., Basu, S., Beers, T. C., Bizyaev, D., Burton, A., Chaplin, W. J., Cunha, K., Elsworth, Y., García, R. A., García-Herńandez, D. A., García Pérez, A. E., Hearty, F. R., Hekker, S., Kallinger, T., Kinemuchi, K., Koesterke, L., Mészáros, S., Mosser, B., O'Connell, R. W., Oravetz, D., Pan, K., Robin, A. C., Schiavon, R. P., Schneider, D. P., Schultheis, M., Serenelli, A., Shetrone, M., Silva Aguirre, V., Simmons, A., Skrutskie, M., Smith, V. V., Stassun, K., Weinberg, D. H., Wilson, J. C. & Zamora, O. (2014), 'The APOGEE Red-clump Catalog: Precise Distances, Velocities,

and High-resolution Elemental Abundances over a Large Area of the Milky Way's Disk', **790**(2), 127.

Bovy, J., Rix, H.-W. & Hogg, D. W. (2012), 'The Milky Way Has No Distinct Thick Disk', **751**(2), 131.

Breiman, L. (2001), 'Random Forests.', *Machine Learning* **45**, 5–32.

Bressan, A., Marigo, P., Girardi, L., Salasnich, B., Dal Cero, C., Rubele, S. & Nanni, A. (2012), 'PARSEC: stellar tracks and isochrones with the PAdova and TRieste Stellar Evolution Code', **427**(1), 127–145.

Brook, C. B., Kawata, D., Gibson, B. K. & Freeman, K. C. (2004), 'The Emergence of the Thick Disk in a Cold Dark Matter Universe', **612**(2), 894–899.

Burgasser, A. (2007*a*), Gravity and Metallicity Effects in T Dwarfs, *in* 'American Astronomical Society Meeting Abstracts #210', Vol. 210 of *American Astronomical Society Meeting Abstracts*, p. 69.04.

Burgasser, A. J. (2007*b*), 'Binaries and the L Dwarf/T Dwarf Transition', **659**(1), 655–674.

Burgasser, A. J. (2008*a*), Ultracool Subdwarfs: Subsolar Metallicity Objects Down to Substellar Masses, *in* G. van Belle, ed., '14th Cambridge Workshop on Cool Stars, Stellar Systems, and the Sun', Vol. 384 of *Astronomical Society of the Pacific Conference Series*, p. 126.

Burgasser, A. J. (2008*b*), Ultracool Subdwarfs: Subsolar Metallicity Objects Down to Substellar Masses, *in* G. van Belle, ed., '14th Cambridge Workshop on Cool Stars, Stellar Systems, and the Sun', Vol. 384 of *Astronomical Society of the Pacific Conference Series*, p. 126.

Burgasser, A. J. (2014), The SpeX Prism Library: 1000+ low-resolution, near-infrared spectra of ultracool M, L, T and Y dwarfs, *in* 'Astronomical Society of India Conference Series', Vol. 11 of *Astronomical Society of India Conference Series*, pp. 7–16.

Burgasser, A. J., Geballe, T. R., Leggett, S. K., Kirkpatrick, J. D. & Golimowski, D. A. (2006), 'A Unified Near-Infrared Spectral Classification Scheme for T Dwarfs', **637**(2), 1067–1093.

Burgasser, A. J., Gillon, M., Melis, C., Bowler, B. P., Michelsen, E. L., Bardalez Gagliuffi, D., Gelino, C. R., Jehin, E., Delrez, L., Manfroid, J. & Blake, C. H. (2015), 'WISE J072003.20-084651.2: an Old and Active M9.5 + T5 Spectral Binary 6 pc from the Sun', **149**(3), 104.

Burgasser, A. J., Kirkpatrick, J. D., Brown, M. E., Reid, I. N., Burrows, A., Liebert, J., Matthews, K., Gizis, J. E., Dahn, C. C., Monet, D. G., Cutri, R. M. & Skrutskie, M. F. (2002), 'The Spectra of T Dwarfs. I. Near-Infrared Data and Spectral Classification', **564**(1), 421–451.

Burgasser, A. J., Kirkpatrick, J. D., Cruz, K. L., Reid, I. N., Leggett, S. K., Liebert, J., Burrows, A. & Brown, M. E. (2006), 'Hubble Space Telescope NICMOS Observations of T Dwarfs: Brown Dwarf Multiplicity and New Probes of the L/T Transition', **166**(2), 585–612.

Burgasser, A. J., Luk, C., Dhital, S., Bardalez Gagliuffi, D., Nicholls, C. P., Prato, L., West, A. A. & Lépine, S. (2012*a*), 'Discovery of a Very Low Mass Triple with Late-M and T Dwarf Components: LP 704-48/SDSS J0006-0852AB', **757**(2), 110.

Burgasser, A. J., Luk, C., Dhital, S., Bardalez Gagliuffi, D., Nicholls, C. P., Prato, L., West, A. A. & Lépine, S. (2012*b*), 'Discovery of a Very Low Mass Triple with Late-M and T Dwarf Components: LP 704-48/SDSS J0006-0852AB', **757**(2), 110.

Burgasser, A. J., Reid, I. N., Siegler, N., Close, L., Allen, P., Lowrance, P. & Gizis, J. (2007), Not Alone: Tracing the Origins of Very-Low-Mass Stars and Brown Dwarfs Through Multiplicity Studies, *in* B. Reipurth, D. Jewitt & K. Keil, eds, 'Protostars and Planets V', p. 427.

Burgasser, A. J., Sheppard, S. S. & Luhman, K. L. (2013), 'Resolved Near-infrared Spectroscopy of WISE J104915.57-531906.1AB: A Flux-reversal Binary at the L dwarf/T Dwarf Transition', **772**(2), 129.

Burgasser, A. J. & Splat Development Team (2017), The SpeX Prism Library Analysis Toolkit (SPLAT): A Data Curation Model, *in* 'Astronomical Society of India Conference Series', Vol. 14 of *Astronomical Society of India Conference Series*, pp. 7–12.

Burningham, B., Pinfield, D. J., Lucas, P. W., Leggett, S. K., Deacon, N. R., Tamura, M., Tinney, C. G., Lodieu, N., Zhang, Z. H., Huelamo, N., Jones, H. R. A., Murray, D. N., Mortlock, D. J., Patel, M., Barrado Y Navascués, D., Zapatero Osorio, M. R., Ishii, M., Kuzuhara, M. & Smart, R. L. (2010), '47 new T dwarfs from the UKIDSS Large Area Survey', **406**(3), 1885–1906.

Burrows, A., Hubbard, W. B., Lunine, J. I. & Liebert, J. (2001), 'The theory of brown dwarfs and extrasolar giant planets', *Reviews of Modern Physics* **73**(3), 719–765.

Burrows, A., Marley, M., Hubbard, W. B., Lunine, J. I., Guillot, T., Saumon, D., Freedman, R., Sudarsky, D. & Sharp, C. (1997), 'A Nongray Theory of Extrasolar Giant Planets and Brown Dwarfs', **491**(2), 856–875.

Burrows, A., Marley, M. S. & Sharp, C. M. (2000), 'The Near-Infrared and Optical Spectra of Methane Dwarfs and Brown Dwarfs', **531**(1), 438–446.

Canty, J. I., Lucas, P. W., Roche, P. F. & Pinfield, D. J. (2013*a*), 'Towards precise ages and masses of Free Floating Planetary Mass Brown Dwarfs', **435**(3), 2650–2664.

Canty, J. I., Lucas, P. W., Roche, P. F. & Pinfield, D. J. (2013*b*), 'Towards precise ages and masses of Free Floating Planetary Mass Brown Dwarfs', **435**(3), 2650–2664.

Canty, J. I., Lucas, P. W., Yurchenko, S. N., Tennyson, J., Leggett, S. K., Tinney, C. G., Jones, H. R. A., Burningham, B., Pinfield, D. J. & Smart, R. L. (2015*a*), 'Methane and ammonia in the near-infrared spectra of late-T dwarfs', **450**(1), 454–480.

Canty, J. I., Lucas, P. W., Yurchenko, S. N., Tennyson, J., Leggett, S. K., Tinney, C. G., Jones, H. R. A., Burningham, B., Pinfield, D. J. & Smart, R. L. (2015*b*), 'Methane and ammonia in the near-infrared spectra of late-T dwarfs', **450**(1), 454–480.

Capitanio, L., Lallement, R., Vergely, J. L., Elyajouri, M. & Monreal-Ibero, A. (2017), 'Three-dimensional mapping of the local interstellar medium with composite data', **606**, A65.

Carmichael, T. W., Latham, D. W. & Vanderburg, A. M. (2019), 'New Substellar Discoveries from Kepler and K2: Is There a Brown Dwarf Desert?', **158**(1), 38.

Carmichael, T. W., Quinn, S. N., Zhou, G., Grieves, N., Irwin, J. M., Stassun, K. G., Vanderburg, A. M., Winn, J. N., Bouchy, F., Brasseur, C. E., Briceño, C., Caldwell, D. A., Charbonneau, D., Collins, K. A., Colon, K. D., Eastman, J. D., Fausnaugh, M., Fong, W., Fűrész, G., Huang, C., Jenkins, J. M., Kielkopf, J. F., Latham, D. W., Law, N., Lund, M. B., Mann, A. W., Ricker, G. R., Rodriguez, J. E., Schwarz, R. P., Shporer, A., Tenenbaum, P., Wood, M. L. & Ziegler, C. (2021), 'TOI-811b and TOI-852b: New Transiting Brown Dwarfs with Similar Masses and Very Different Radii and Ages from the TESS Mission', **161**(2), 97.

Carnall, A. C. (2017), 'SpectRes: A Fast Spectral Resampling Tool in Python', *arXiv e-prints* p. arXiv:1705.05165.

Carnero Rosell, A., Santiago, B., dal Ponte, M., Burningham, B., da Costa, L. N., James, D. J., Marshall, J. L., McMahon, R. G., Bechtol, K., De Paris, L., Li, T., Pieres, A., García-Bellido, J., Abbott, T. M. C., Annis, J., Avila, S., Bernstein, G. M., Brooks, D., Burke, D. L., Carrasco Kind, M., Carretero, J., De Vicente, J., Drlica-Wagner, A., Fosalba, P., Frieman, J., Gaztanaga, E., Gruendl, R. A., Gschwend, J., Gutierrez, G., Hollowood, D. L., Maia, M. A. G., Menanteau, F., Miquel, R., Plazas, A. A., Roodman, A., Sanchez, E., Scarpine, V., Schindler, R., Serrano, S., Sevilla-Noarbe, I., Smith, M., Sobreira, F., Soares-Santos, M., Suchyta, E., Swanson, M. E. C., Tarle, G., Vikram, V., Walker, A. R. & DES Collaboration (2019), 'Brown dwarf census with the Dark Energy Survey year 3 data and the thin disc scale height of early L types', **489**(4), 5301–5325.

Carraro, G., Girardi, L. & Chiosi, C. (1999), 'Is the Galactic disc older than the halo?', **309**(2), 430–442.

Casewell, S. L., Burleigh, M. R., Lawrie, K. A., Maxted, P. F. L., Dobbie, P. D. & Napiwotzki, R. (2013), 'Irradiated brown dwarfs', **84**(4), 1022.

Casewell, S. L., Lawrie, K. A., Maxted, P. F. L., Marley, M. S., Fortney, J. J., Rimmer, P. B., Littlefair, S. P., Wynn, G., Burleigh, M. R. & Helling, C. (2015), 'Multiwaveband photometry of the irradiated brown dwarf WD0137-349B', **447**(4), 3218–3226.

Casewell, S. L., Littlefair, S. P., Parsons, S. G., Marsh, T. R., Fortney, J. J. & Marley, M. S. (2018), 'The direct detection of the irradiated brown dwarf in the white dwarf-brown dwarf binary SDSS J141126.20+200911.1', **481**(4), 5216–5222.

Chabrier, G. (2003), 'Galactic Stellar and Substellar Initial Mass Function', **115**(809), 763–795.

Chabrier, G. & Baraffe, I. (1997), 'Structure and evolution of low-mass stars', **327**, 1039–1053.

Chabrier, G., Baraffe, I., Allard, F. & Hauschildt, P. (2000), 'Evolutionary Models for Very Low-Mass Stars and Brown Dwarfs with Dusty Atmospheres', **542**(1), 464–472.

Chabrier, G., Gallardo, J. & Baraffe, I. (2007), 'Evolution of low-mass star and brown dwarf eclipsing binaries', **472**(2), L17–L20.

Chen, T. & Guestrin, C. (2016), 'XGBoost: A Scalable Tree Boosting System', *arXiv e-prints* p. arXiv:1603.02754.

Chen, Y., Bressan, A., Girardi, L., Marigo, P., Kong, X. & Lanza, A. (2015), 'PARSEC evolutionary tracks of massive stars up to 350 $M_\odot$ at metallicities $0.0001 \leq Z \leq 0.04$', **452**(1), 1068–1080.

Chen, Y., Girardi, L., Bressan, A., Marigo, P., Barbieri, M. & Kong, X. (2014), 'Improving PARSEC models for very low mass stars', **444**(3), 2525–2543.

Chen, Y., Girardi, L., Fu, X., Bressan, A., Aringer, B., Dal Tio, P., Pastorelli, G., Marigo, P., Costa, G. & Zhang, X. (2019), 'YBC: a stellar bolometric corrections database with variable extinction coefficients. Application to PARSEC isochrones', **632**, A105.

Christensen, U. R., Holzwarth, V. & Reiners, A. (2009), 'Energy flux determines magnetic field strength of planets and stars', **457**(7226), 167–169.

Close, L. M., Siegler, N., Freed, M. & Biller, B. (2003), 'Detection of Nine M8.0-L0.5 Binaries: The Very Low Mass Binary Population and Its Implications for Brown Dwarf and Very Low Mass Star Formation', **587**(1), 407–422.

Coenen, A. & Pearce, A. (2019), 'Understanding umap'.
URL: *https://pair-code.github.io/understanding-umap/*

Covey, K. R., Hawley, S. L., Bochanski, J. J., West, A. A., Reid, I. N., Golimowski, D. A., Davenport, J. R. A., Henry, T., Uomoto, A. & Holtzman, J. A. (2008), 'The Luminosity and Mass Functions of Low-Mass Stars in the Galactic Disk. I. The Calibration Region', **136**(5), 1778–1798.

Crossfield, I. J. M., Biller, B., Schlieder, J. E., Deacon, N. R., Bonnefoy, M., Homeier, D., Allard, F., Buenzli, E., Henning, T., Brandner, W., Goldman, B. & Kopytova, T. (2014*a*), 'A global cloud map of the nearest known brown dwarf', **505**(7485), 654–656.

Crossfield, I. J. M., Biller, B., Schlieder, J. E., Deacon, N. R., Bonnefoy, M., Homeier, D., Allard, F., Buenzli, E., Henning, T., Brandner, W., Goldman, B. & Kopytova, T. (2014*b*), 'A global cloud map of the nearest known brown dwarf', **505**(7485), 654–656.

Cruz, K. L., Kirkpatrick, J. D. & Burgasser, A. J. (2009), 'Young L Dwarfs Identified in the Field: A Preliminary Low-Gravity, Optical Spectral Sequence from L0 to L5', **137**(2), 3345–3357.

Cruz, K. L., Reid, I. N., Kirkpatrick, J. D., Burgasser, A. J., Liebert, J., Solomon, A. R., Schmidt, S. J., Allen, P. R., Hawley, S. L. & Covey, K. R. (2007), 'Meeting the Cool Neighbors. IX. The Luminosity Function of M7-L8 Ultracool Dwarfs in the Field', **133**(2), 439–467.

Cruz, K., Reid, I. N. & Liebert, J. (2005), The luminosity function of ultracool dwarfs, *in* F. Favata, G. A. J. Hussain & B. Battrick, eds, '13th Cambridge Workshop on Cool Stars, Stellar Systems and the Sun', Vol. 560 of *ESA Special Publication*, p. 271.

Cushing, M. C., Hardegree-Ullman, K. K., Trucks, J. L., Morley, C. V., Gizis, J. E., Marley, M. S., Fortney, J. J., Kirkpatrick, J. D., Gelino, C. R., Mace, G. N. & Carey, S. J. (2016), 'The First Detection of Photometric Variability in a Y Dwarf: WISE J140518.39+553421.3', **823**(2), 152.

Cushing, M. C., Kirkpatrick, J. D., Gelino, C. R., Griffith, R. L., Skrutskie, M. F., Mainzer, A., Marsh, K. A., Beichman, C. A., Burgasser, A. J., Prato, L. A., Simcoe, R. A., Marley, M. S., Saumon, D., Freedman, R. S., Eisenhardt, P. R. & Wright, E. L. (2011), 'The Discovery of Y Dwarfs using Data from the Wide-field Infrared Survey Explorer (WISE)', **743**(1), 50.

Cushing, M. C., Rayner, J. T., Davis, S. P. & Vacca, W. D. (2003), 'FeH Absorption in the Near-Infrared Spectra of Late M and L Dwarfs', **582**(2), 1066–1072.

Day-Jones, A. C., Marocco, F., Pinfield, D. J., Zhang, Z. H., Burningham, B., Deacon, N., Ruiz, M. T., Gallardo, J., Jones, H. R. A., Lucas, P. W. L., Jenkins, J. S., Gomes, J., Folkes, S. L. & Clarke, J. R. A. (2013*a*), 'The sub-stellar birth rate from UKIDSS', **430**(2), 1171–1187.

Day-Jones, A. C., Marocco, F., Pinfield, D. J., Zhang, Z. H., Burningham, B., Deacon, N., Ruiz, M. T., Gallardo, J., Jones, H. R. A., Lucas, P. W. L., Jenkins, J. S., Gomes, J., Folkes, S. L. & Clarke, J. R. A. (2013*b*), 'The sub-stellar birth rate from UKIDSS', **430**(2), 1171–1187.

Day-Jones, A., Marocco, F., Pinfield, D., Zhang, Z., Burningham, B., Deacon, N., Ruiz, M.-T., Gallardo, J., Jones, H., Lucas, P., Jenkins, J., Gomes, J., Folkes, S. & Clarke, J. (2013*c*), Measuring ultracool properties from the UKIDSS Large Area Survey, *in* 'European Physical Journal Web of Conferences', Vol. 47, p. 06003.

De Luca, A., Stelzer, B., Burgasser, A. J., Pizzocaro, D., Ranalli, P., Raetz, S., Marelli, M., Novara, G., Vignali, C., Belfiore, A., Esposito, P., Franzetti, P., Fumana, M., Gilli, R., Salvaterra, R. & Tiengo, A. (2020), 'EXTraS discovery of an X-ray superflare from an L dwarf', **634**, L13.

de Pater, I., Fletcher, L. N., Luszcz-Cook, S., DeBoer, D., Butler, B., Hammel, H. B., Sitko, M. L., Orton, G. & Marcus, P. S. (2014), 'Neptune's global circulation deduced from multi-wavelength observations', **237**, 211–238.

Deacon, N. R. & Hambly, N. C. (2006), 'The possiblity of detection of ultracool dwarfs with the UKIRT Infrared Deep Sky Survey', **371**(4), 1722–1730.

Dieterich, S. B., Henry, T. J., Golimowski, D. A., Krist, J. E. & Tanner, A. M. (2012), 'The Solar Neighborhood. XXVIII. The Multiplicity Fraction of Nearby Stars from 5 to 70 AU and the Brown Dwarf Desert around M Dwarfs', **144**(2), 64.

Ding, P.-J., Zhu, Z. & Liu, J.-C. (2019), 'Local standard of rest based on Gaia DR2 catalog', *Research in Astronomy and Astrophysics* **19**(5), 068.

Dittmann, J. A., Irwin, J. M., Charbonneau, D., Bonfils, X., Astudillo-Defru, N., Haywood, R. D., Berta-Thompson, Z. K., Newton, E. R., Rodriguez, J. E., Winters, J. G., Tan, T.-G., Almenara, J.-M., Bouchy, F., Delfosse, X., Forveille, T., Lovis, C., Murgas, F., Pepe, F., Santos, N. C., Udry, S., Wünsche, A., Esquerdo, G. A., Latham, D. W. & Dressing, C. D. (2017), 'A temperate rocky super-Earth transiting a nearby cool star', **544**(7650), 333–336.

Dobbie, P. S. & Warren, S. J. (2020), 'A Bayesian Approach to the Vertical Structure of the Disk of the Milky Way', *The Open Journal of Astrophysics* **3**(1), 5.

Dressing, C. D. & Charbonneau, D. (2015), 'The Occurrence of Potentially Habitable Planets Orbiting M Dwarfs Estimated from the Full Kepler Dataset and an Empirical Measurement of the Detection Sensitivity', **807**(1), 45.

Dubath, P., Rimoldini, L., Süveges, M., Blomme, J., López, M., Sarro, L. M., De Ridder, J., Cuypers, J., Guy, L., Lecoeur, I., Nienartowicz, K., Jan, A., Beck, M., Mowlavi, N., De Cat, P., Lebzelter, T. & Eyer, L. (2011), 'Random forest automated supervised classification of Hipparcos periodic variable stars', **414**(3), 2602–2617.

Duchêne, G. & Kraus, A. (2013*a*), 'Stellar Multiplicity', **51**(1), 269–310.

Duchêne, G. & Kraus, A. (2013*b*), 'Stellar Multiplicity', **51**(1), 269–310.

Dupuy, T. J. & Kraus, A. L. (2013), 'Distances, Luminosities, and Temperatures of the Coldest Known Substellar Objects', *Science* **341**(6153), 1492–1495.

Dupuy, T. J. & Liu, M. C. (2011), 'On the Distribution of Orbital Eccentricities for Very Low-mass Binaries', **733**(2), 122.

Dupuy, T. J. & Liu, M. C. (2012), 'The Hawaii Infrared Parallax Program. I. Ultracool Binaries and the L/T Transition', **201**(2), 19.

Evans, D. W., Riello, M., De Angeli, F., Carrasco, J. M., Montegriffo, P., Fabricius, C., Jordi, C., Palaversa, L., Diener, C., Busso, G., Cacciari, C., van Leeuwen, F., Burgess, P. W., Davidson, M., Harrison, D. L., Hodgkin, S. T., Pancino, E., Richards, P. J., Altavilla, G., Balaguer-Núñez, L., Barstow, M. A., Bellazzini, M., Brown, A. G. A., Castellani, M., Cocozza, G., De Luise, F., Delgado, A., Ducourant, C., Galleti, S., Gilmore, G., Giuffrida, G., Holl, B., Kewley, A., Koposov, S. E., Marinoni, S., Marrese, P. M., Osborne, P. J., Piersimoni, A., Portell, J.,

Pulone, L., Ragaini, S., Sanna, N., Terrett, D., Walton, N. A., Wevers, T. & Wyrzykowski, Ł. (2018), 'Gaia Data Release 2. Photometric content and validation', **616**, A4.

Evans, T. M., Ireland, M. J., Kraus, A. L., Martinache, F., Stewart, P., Tuthill, P. G., Lacour, S., Carpenter, J. M. & Hillenbrand, L. A. (2012), 'Mapping the Shores of the Brown Dwarf Desert. III. Young Moving Groups', **744**(2), 120.

Faherty, J., Allers, K., Bardalez Gagliuffi, D., Burgasser, A. J., Gagne, J., Gizis, J., Kirkpatrick, J. D., Riedel, A., Schneider, A. & Vos, J. (2019), Brown Dwarfs and Directly Imaged Exoplanets in Young Associations, *in* '', Vol. 51, p. 286.

Faherty, J. K., Burgasser, A. J., Cruz, K. L., Shara, M. M., Walter, F. M. & Gelino, C. R. (2009), 'The Brown Dwarf Kinematics Project I. Proper Motions and Tangential Velocities for a Large Sample of Late-Type M, L, and T Dwarfs', **137**(1), 1–18.

Faherty, J. K., Burgasser, A. J., Walter, F. M., der Bliek, N. V., Shara, M. M., Cruz, K. L., West, A. A., Vrba, F. J. & Anglada-Escudé, G. (2012), 'The brown dwarf kinematics project (bdkp) iii. parallaxes for 70 ultracool dwarfs', *The Astrophysical Journal* **752**(1), 56.
URL: *https://doi.org/10.1088*

Faherty, J. K., Burgasser, A. J., West, A. A., Bochanski, J. J., Cruz, K. L., Shara, M. M. & Walter, F. M. (2010), 'The Brown Dwarf Kinematics Project. II. Details on Nine Wide Common Proper Motion Very Low Mass Companions to Nearby Stars', **139**(1), 176–194.

Faherty, J. K., Cruz, K. L., Rice, E. L. & Riedel, A. (2013), 'Young brown dwarfs as giant exoplanet analogs', **84**(4), 955.

Faherty, J. K., Riedel, A. R., Cruz, K. L., Gagne, J., Filippazzo, J. C., Lambrides, E., Fica, H., Weinberger, A., Thorstensen, J. R., Tinney, C. G., Baldassare, V., Lemonier, E. & Rice, E. L. (2016), 'Population Properties of Brown Dwarf Analogs to Exoplanets', **225**(1), 10.

Faherty, J. K., Tinney, C. G., Skemer, A. & Monson, A. J. (2014), 'Indications of Water Clouds in the Coldest Known Brown Dwarf', **793**(1), L16.

Ferguson, D., Gardner, S. & Yanny, B. (2017), 'Milky Way Tomography with K and M Dwarf Stars: The Vertical Structure of the Galactic Disk', **843**(2), 141.

Fluke, C. J. & Jacobs, C. (2019), 'Surveying the reach and maturity of machine learning and artificial intelligence in astronomy', *arXiv e-prints* p. arXiv:1912.02934.

Flynn, C., Holmberg, J., Portinari, L., Fuchs, B. & Jahreiß, H. (2006), 'On the mass-to-light ratio of the local Galactic disc and the optical luminosity of the Galaxy', **372**(3), 1149–1160.

Foreman-Mackey, D., Hogg, D. W., Lang, D. & Goodman, J. (2013*a*), 'emcee: The MCMC Hammer', **125**(925), 306.

Foreman-Mackey, D., Hogg, D. W., Lang, D. & Goodman, J. (2013*b*), 'emcee: The MCMC Hammer', **125**(925), 306.

Fujimoto, M. (1980), 'Diffusion of Stellar Orbits and Velocities by Random Gravitational Forces of Short Duration - Application to the Giant CO Clouds', **32**, 89.

Gaia Collaboration, Smart, R. L. et al. (2020), 'Gaia Early Data Release 3: The Gaia Catalogue of Nearby Stars', *arXiv e-prints* p. arXiv:2012.02061.

Gaia Collaboration et al. (2016), 'The Gaia mission', **595**, A1.

Gaia Collaboration et al. (2018*a*), 'Gaia Data Release 2. Observational Hertzsprung-Russell diagrams', **616**, A10.

Gaia Collaboration et al. (2018*b*), 'Gaia Data Release 2. Summary of the contents and survey properties', **616**, A1.

Gaia Collaboration et al. (2021), 'Gaia Early Data Release 3. Summary of the contents and survey properties', **649**, A1.

Geballe, T. R., Knapp, G. R., Leggett, S. K., Fan, X., Golimowski, D. A., Anderson, S., Brinkmann, J., Csabai, I., Gunn, J. E., Hawley, S. L., Hennessy, G., Henry, T. J., Hill, G. J., Hindsley, R. B., Ivezić, Ž., Lupton, R. H., McDaniel, A., Munn, J. A., Narayanan, V. K., Peng, E., Pier, J. R., Rockosi, C. M., Schneider, D. P., Smith, J. A., Strauss, M. A., Tsvetanov, Z. I., Uomoto, A., York, D. G. & Zheng, W. (2002), 'Toward Spectral Classification of L and T Dwarfs: Infrared and Optical Spectroscopy and Analysis', **564**(1), 466–481.

Geballe, T. R., Noll, K. S., Leggett, S. K., Knapp, G. R., Fan, X. & Golimowski, D. (2001), Infrared Spectroscopy of Brown Dwarfs: the Onset of CH_4 Absorption in L Dwarfs and the L/T Transition, *in* H. R. A. Jones & I. A. Steele, eds, 'Ultracool Dwarfs: New Spectral Types L and T', p. 83.

Gerhard, O. (2002), 'Mass distribution in our Galaxy', **100**, 129–138.

Gillon, M., Jehin, E., Lederer, S. M., Delrez, L., de Wit, J., Burdanov, A., Van Grootel, V., Burgasser, A. J., Triaud, A. H. M. J., Opitom, C., Demory, B.-O., Sahu, D. K., Bardalez Gagliuffi, D., Magain, P. & Queloz, D. (2016), 'Temperate Earth-sized planets transiting a nearby ultracool dwarf star', **533**(7602), 221–224.

Gilmore, G. (1984), 'New light on faint stars - VI. Structure and evolution of the Galactic spheroid.', **207**, 223–240.

Gilmore, G. & Reid, N. (1983), 'New light on faint stars - III. Galactic structure towards the South Pole and the Galactic thick disc.', **202**, 1025–1047.

Gilmore, G., Wyse, R. F. G. & Kuijken, K. (1989), 'Kinematics, chemistry, and structure of the Galaxy.', **27**, 555–627.

Gizis, J. E. & Harvin, J. (2006), 'Halo Stars near the Hydrogen-burning Limit: The M/L Subdwarf Transition', **132**(6), 2372–2375.

Gizis, J. E., Reid, I. N., Knapp, G. R., Liebert, J., Kirkpatrick, J. D., Koerner, D. W. & Burgasser, A. J. (2003), 'Hubble Space Telescope Observations of Binary Very Low Mass Stars and Brown Dwarfs', **125**(6), 3302–3310.

Golimowski, D. A., Leggett, S. K., Marley, M. S., Fan, X., Geballe, T. R., Knapp, G. R., Vrba, F. J., Henden, A. A., Luginbuhl, C. B., Guetter, H. H., Munn, J. A., Canzian, B., Zheng, W., Tsvetanov, Z. I., Chiu, K., Glazebrook, K., Hoversten, E. A., Schneider, D. P. & Brinkmann, J. (2004), 'L' and M' Photometry of Ultracool Dwarfs', **127**(6), 3516–3536.

Goodwin, S. P. & Kroupa, P. (2005), 'Limits on the primordial stellar multiplicity', **439**(2), 565–569.

Grether, D. & Lineweaver, C. H. (2006), 'How Dry is the Brown Dwarf Desert? Quantifying the Relative Number of Planets, Brown Dwarfs, and Stellar Companions around Nearby Sun-like Stars', **640**(2), 1051–1062.

Grosso, N., Briggs, K. R., Güdel, M., Guieu, S., Franciosini, E., Palla, F., Dougados, C., Monin, J. L., Ménard, F., Bouvier, J., Audard, M. & Telleschi, A. (2007), 'X-ray emission from the young brown dwarfs of the Taurus molecular cloud', **468**(2), 391–403.

Guirado, J. C., Azulay, R., Gauza, B., Pérez-Torres, M. A., Rebolo, R., Climent, J. B. & Zapatero Osorio, M. R. (2018), 'Radio emission in ultracool dwarfs: The nearby substellar triple system VHS 1256-1257', **610**, A23.

Hallinan, G., Antonova, A., Doyle, J. G., Bourke, S., Lane, C. & Golden, A. (2008), 'Confirmation of the Electron Cyclotron Maser Instability as the Dominant Source of Radio Emission from Very Low Mass Stars and Brown Dwarfs', **684**(1), 644–653.

Hallinan, G., Littlefair, S. P., Cotter, G., Bourke, S., Harding, L. K., Pineda, J. S., Butler, R. P., Golden, A., Basri, G., Doyle, J. G., Kao, M. M., Berdyugina, S. V., Kuznetsov, A., Rupen, M. P. & Antonova, A. (2015), 'Magnetospherically driven optical and radio aurorae at the end of the stellar main sequence', **523**(7562), 568–571.

Hänninen, J. & Flynn, C. (2002), 'Simulations of the heating of the Galactic stellar disc', **337**(2), 731–742.

Hardegree-Ullman, K. K., Cushing, M. C., Muirhead, P. S. & Christiansen, J. L. (2019), 'Kepler Planet Occurrence Rates for Mid-type M Dwarfs as a Function of Spectral Type', **158**(2), 75.

Hawley, S. L., Covey, K. R., Knapp, G. R., Golimowski, D. A., Fan, X., Anderson, S. F., Gunn, J. E., Harris, H. C., Ivezić, Ž., Long, G. M., Lupton, R. H., McGehee, P. M., Narayanan, V., Peng, E., Schlegel, D., Schneider, D. P., Spahn, E. Y., Strauss, M. A., Szkody, P., Tsvetanov, Z., Walkowicz, L. M., Brinkmann, J., Harvanek, M., Hennessy, G. S., Kleinman, S. J., Krzesinski, J., Long, D., Neilsen, E. H., Newman, P. R., Nitta, A., Snedden, S. A. & York, D. G. (2002), 'Characterization of M, L, and T Dwarfs in the Sloan Digital Sky Survey', **123**(6), 3409–3427.

Haywood, M., Di Matteo, P., Lehnert, M. D., Katz, D. & Gómez, A. (2013), 'The age structure of stellar populations in the solar vicinity. Clues of a two-phase formation history of the Milky Way disk', **560**, A109.

Heggie, D. C. (1975), 'Binary evolution in stellar dynamics.', **173**, 729–787.

Helling, C., Ackerman, A., Allard, F., Dehn, M., Hauschildt, P., Homeier, D., Lodders, K., Marley, M., Rietmeijer, F., Tsuji, T. & Woitke, P. (2008), 'A comparison of chemistry and dust cloud formation in ultracool dwarf model atmospheres', **391**(4), 1854–1873.

Helling, C. & Casewell, S. (2014), 'Atmospheres of brown dwarfs', **22**, 80.

Helling, C., Klein, R., Woitke, P., Nowak, U. & Sedlmayr, E. (2004), 'Dust in brown dwarfs. IV. Dust formation and driven turbulence on mesoscopic scales', **423**, 657–675.

Helling, C., Oevermann, M., Lüttke, M. J. H., Klein, R. & Sedlmayr, E. (2001), 'Dust in brown dwarfs. I. Dust formation under turbulent conditions on microscopic scales', **376**, 194–212.

Helling, C. & Woitke, P. (2006), 'Dust in brown dwarfs. V. Growth and evaporation of dirty dust grains', **455**(1), 325–338.

Helmi, A., Babusiaux, C., Koppelman, H. H., Massari, D., Veljanoski, J. & Brown, A. G. A. (2018), 'The merger that led to the formation of the Milky Way's inner stellar halo and thick disk', **563**(7729), 85–88.

Hewett, P. C., Warren, S. J., Leggett, S. K. & Hodgkin, S. T. (2006), 'The UKIRT Infrared Deep Sky Survey ZY JHK photometric system: passbands and synthetic colours', **367**(2), 454–468.

Hills, J. G. (1990), 'Encounters between Single and Binary Stars: The Effect of Intruder Mass on the Maximum Impact Velocity for Which the Mean Change in Binding Energy is Positive', **99**, 979.

Hodgkin, S. T., Irwin, M. J., Hewett, P. C. & Warren, S. J. (2009), 'The UKIRT wide field camera ZYJHK photometric system: calibration from 2MASS', **394**(2), 675–692.

Hogg, M. A., Casewell, S. L., Wynn, G. A., Longstaff, E. S., Braker, I. P., Burleigh, M. R., Tilbrook, R. H., Geier, S., Koester, D., Debes, J. H. & Lodieu, N. (2020), 'Confirming new white dwarf-ultracool dwarf binary candidates', **498**(1), 12–24.

Holmberg, J., Nordström, B. & Andersen, J. (2007), 'The Geneva-Copenhagen survey of the Solar neighbourhood II. New uvby calibrations and rediscussion of stellar ages, the G dwarf problem, age-metallicity diagram, and heating mechanisms of the disk', **475**(2), 519–537.

Hu, N., Su, S.-S. & Kong, X. (2016), 'Spectral Synthesis via Mean Field approach to Independent Component Analysis', *Research in Astronomy and Astrophysics* **16**(3), 42.

Jeans, J. H. (1919), 'The origin of binary systems', **79**, 408.

Jimenez, R., Flynn, C. & Kotoneva, E. (1998), 'HIPPARCOS and the age of the Galactic disc', **299**(2), 515–519.

Jones, B. J. T. & Wyse, R. F. G. (1983), 'The formation of disc galaxies.', **120**, 165–180.

Jones, H. R. A. & Tsuji, T. (1997), 'Spectral Evidence for Dust in Late-Type M Dwarfs', **480**(1), L39–L41.

Just, A. & Jahreiss, H. (2007), 'The local star formation history of the thin disc derived from kinematic data', *arXiv e-prints* p. arXiv:0706.3850.

Karim, T. & Mamajek, E. E. (2017), 'Revised geometric estimates of the North Galactic Pole and the Sun's height above the Galactic mid-plane', **465**(1), 472–481.

Kellogg, K., Metchev, S., Miles-Páez, P. A. & Tannock, M. E. (2017), 'A statistical survey of peculiar L and T dwarfs in SDSS, 2MASS, and WISE', *The Astronomical Journal* **154**(3), 112. **URL:** *https://doi.org/10.3847*

Khodachenko, M. L., Ribas, I., Lammer, H., Grießmeier, J.-M., Leitner, M., Selsis, F., Eiroa, C., Hanslmeier, A., Biernat, H. K., Farrugia, C. J. & Rucker, H. O. (2007), 'Coronal Mass Ejection (CME) Activity of Low Mass M Stars as An Important Factor for The Habitability of Terrestrial Exoplanets. I. CME Impact on Expected Magnetospheres of Earth-Like Exoplanets in Close-In Habitable Zones', *Astrobiology* **7**(1), 167–184.

Kilic, M., Bergeron, P., Dame, K., Hambly, N. C., Rowell, N. & Crawford, C. L. (2019), 'The age of the Galactic stellar halo from Gaia white dwarfs', **482**(1), 965–979.

Kilic, M., Munn, J. A., Harris, H. C., von Hippel, T., Liebert, J. W., Williams, K. A., Jeffery, E. & DeGennaro, S. (2017), 'The Ages of the Thin Disk, Thick Disk, and the Halo from Nearby White Dwarfs', **837**(2), 162.

Kirkpatrick, J. D. (2005), 'New Spectral Types L and T', **43**(1), 195–245.

Kirkpatrick, J. D., Cruz, K. L., Barman, T. S., Burgasser, A. J., Looper, D. L., Tinney, C. G., Gelino, C. R., Lowrance, P. J., Liebert, J., Carpenter, J. M., Hillenbrand, L. A. & Stauffer, J. R. (2008), 'A Sample of Very Young Field L Dwarfs and Implications for the Brown Dwarf "Lithium Test" at Early Ages', **689**(2), 1295–1326.

Kirkpatrick, J. D., Gelino, C. R., Cushing, M. C., Mace, G. N., Griffith, R. L., Skrutskie, M. F., Marsh, K. A., Wright, E. L., Eisenhardt, P. R., McLean, I. S., Mainzer, A. K., Burgasser, A. J., Tinney, C. G., Parker, S. & Salter, G. (2012), 'Further Defining Spectral Type "Y" and Exploring the Low-mass End of the Field Brown Dwarf Mass Function', **753**(2), 156.

Kirkpatrick, J. D., Gelino, C. R., Faherty, J. K., Meisner, A. M., Caselden, D., Schneider, A. C., Marocco, F., Cayago, A. J., Smart, R. L., Eisenhardt, P. R., Kuchner, M. J., Wright, E. L., Cushing, M. C., Allers, K. N., Bardalez Gagliuffi, D. C., Burgasser, A. J., Gagné, J., Logsdon, S. E., Martin, E. C., Ingalls, J. G., Lowrance, P. J., Abrahams, E. S., Aganze, C., Gerasimov,

R., Gonzales, E. C., Hsu, C.-C., Kamraj, N., Kiman, R., Rees, J., Theissen, C., Ammar, K., Andersen, N. S., Beaulieu, P., Colin, G., Elachi, C. A., Goodman, S. J., Gramaize, L., Hamlet, L. K., Hong, J., Jonkeren, A., Khalil, M., Martin, D. W., Pendrill, W., Pumphrey, B., Rothermich, A., Sainio, A., Stenner, A., Tanner, C., Thévenot, M., Voloshin, N. V., Walla, J., Wedracki, Z. & Backyard Worlds: Planet 9 Collaboration (2021), 'The Field Substellar Mass Function Based on the Full-sky 20 pc Census of 525 L, T, and Y Dwarfs', **253**(1), 7.

Kirkpatrick, J. D., Looper, D. L., Burgasser, A. J., Schurr, S. D., Cutri, R. M., Cushing, M. C., Cruz, K. L., Sweet, A. C., Knapp, G. R., Barman, T. S., Bochanski, J. J., Roellig, T. L., McLean, I. S., McGovern, M. R. & Rice, E. L. (2010), 'Discoveries from a Near-infrared Proper Motion Survey Using Multi-epoch Two Micron All-Sky Survey Data', **190**(1), 100–146.

Kirkpatrick, J. D., Martin, E. C., Smart, R. L., Cayago, A. J., Beichman, C. A., Marocco, F., Gelino, C. R., Faherty, J. K., Cushing, M. C., Schneider, A. C., Mace, G. N., Tinney, C. G., Wright, E. L., Lowrance, P. J., Ingalls, J. G., Vrba, F. J., Munn, J. A., Dahm, S. E. & McLean, I. S. (2019), 'Preliminary Trigonometric Parallaxes of 184 Late-T and Y Dwarfs and an Analysis of the Field Substellar Mass Function into the "Planetary" Mass Regime', **240**(2), 19.

Kirkpatrick, J. D., Reid, I. N., Liebert, J., Cutri, R. M., Nelson, B., Beichman, C. A., Dahn, C. C., Monet, D. G., Gizis, J. E. & Skrutskie, M. F. (1999), 'Dwarfs Cooler than "M": The Definition of Spectral Type "L" Using Discoveries from the 2 Micron All-Sky Survey (2MASS)', **519**(2), 802–833.

Knapp, G. R., Leggett, S. K., Fan, X., Marley, M. S., Geballe, T. R., Golimowski, D. A., Finkbeiner, D., Gunn, J. E., Hennawi, J., Ivezić, Z., Lupton, R. H., Schlegel, D. J., Strauss, M. A., Tsvetanov, Z. I., Chiu, K., Hoversten, E. A., Glazebrook, K., Zheng, W., Hendrickson, M., Williams, C. C., Uomoto, A., Vrba, F. J., Henden, A. A., Luginbuhl, C. B., Guetter, H. H., Munn, J. A., Canzian, B., Schneider, D. P. & Brinkmann, J. (2004), 'Near-Infrared Photometry and Spectroscopy of L and T Dwarfs: The Effects of Temperature, Clouds, and Gravity', **127**(6), 3553–3578.

Kraus, A. L., Ireland, M. J., Martinache, F. & Lloyd, J. P. (2008), 'Mapping the Shores of the Brown Dwarf Desert. I. Upper Scorpius', **679**(1), 762–782.

Kroupa, P. (2001), 'On the variation of the initial mass function', **322**(2), 231–246.

Kuchner, M. J., Faherty, J. K., Schneider, A. C., Meisner, A. M., Filippazzo, J. C., Gagné, J., Trouille, L., Silverberg, S. M., Castro, R., Fletcher, B., Mokaev, K. & Stajic, T. (2017), 'The First Brown Dwarf Discovered by the Backyard Worlds: Planet 9 Citizen Science Project', **841**(2), L19.

Lacey, C. G. (1984), 'The influence of massive gas clouds on stellar velocity dispersions in galactic discs', **208**, 687–707.

Lada, C. J. (2006), 'Stellar Multiplicity and the Initial Mass Function: Most Stars Are Single', **640**(1), L63–L66.

Laithwaite, R. C. & Warren, S. J. (2020), 'The absolute magnitudes M_J, the binary fraction, and the binary mass ratios of M7-M9.5 dwarfs', **499**(2), 2587–2597.

Lammer, H., Lichtenegger, H. I. M., Kulikov, Y. N., Grießmeier, J.-M., Terada, N., Erkaev, N. V., Biernat, H. K., Khodachenko, M. L., Ribas, I., Penz, T. & Selsis, F. (2007), 'Coronal Mass Ejection (CME) Activity of Low Mass M Stars as An Important Factor for The Habitability of Terrestrial Exoplanets. II. CME-Induced Ion Pick Up of Earth-like Exoplanets in Close-In Habitable Zones', *Astrobiology* **7**(1), 185–207.

Laughlin, G., Bodenheimer, P. & Adams, F. C. (1997), 'The End of the Main Sequence', **482**(1), 420–432.

Law, N. M., Hodgkin, S. T. & Mackay, C. D. (2006), 'Discovery of five very low mass close binaries, resolved in the visible with lucky imaging*', **368**(4), 1917–1924.

Law, N. M., Hodgkin, S. T. & Mackay, C. D. (2008), 'The LuckyCam survey for very low mass binaries - II. 13 new M4.5-M6.0 binaries', **384**(1), 150–160.

Lawrence, A., Warren, S. J., Almaini, O., Edge, A. C., Hambly, N. C., Jameson, R. F., Lucas, P., Casali, M., Adamson, A., Dye, S., Emerson, J. P., Foucaud, S., Hewett, P., Hirst, P., Hodgkin, S. T., Irwin, M. J., Lodieu, N., McMahon, R. G., Simpson, C., Smail, I., Mortlock, D. & Folger, M. (2007), 'The UKIRT Infrared Deep Sky Survey (UKIDSS)', **379**(4), 1599–1617.

Leggett, S., Apai, D., Burgasser, A., Cushing, M., Dupuy, T., Faherty, J., Gizis, J., Kirkpatrick, J. D., Marley, M., Morley, C., Schneider, A. & Sousa-Silva, C. (2019), 'Discovery of Cold Brown Dwarfs or Free-Floating Giant Planets Close to the Sun', **51**(3), 95.

Leggett, S. K., Currie, M. J., Varricatt, W. P., Hawarden, T. G., Adamson, A. J., Buckle, J., Carroll, T., Davies, J. K., Davis, C. J., Kerr, T. H., Kuhn, O. P., Seigar, M. S. & Wold, T. (2006), 'JHK observations of faint standard stars in the Mauna Kea Observatories near-infrared photometric system', **373**(2), 781–792.

Leggett, S. K., Cushing, M. C., Hardegree-Ullman, K. K., Trucks, J. L., Marley, M. S., Morley, C. V., Saumon, D., Carey, S. J., Fortney, J. J., Gelino, C. R., Gizis, J. E., Kirkpatrick, J. D. & Mace, G. N. (2016), 'Observed Variability at 1 and 4 μm in the Y0 Brown Dwarf WISEP J173835.52+273258.9', **830**(2), 141.

Leggett, S. K., Ruiz, M. T. & Bergeron, P. (1998), 'The Cool White Dwarf Luminosity Function and the Age of the Galactic Disk', **497**(1), 294–302.

Leggett, S. K., Tremblin, P., Esplin, T. L., Luhman, K. L. & Morley, C. V. (2017), 'The Y-type Brown Dwarfs: Estimates of Mass and Age from New Astrometry, Homogenized Photometry, and Near-infrared Spectroscopy', **842**(2), 118.

Lindegren, L., Hernández, J., Bombrun, A., Klioner, S., Bastian, U., Ramos-Lerate, M., de Torres, A., Steidelmüller, H., Stephenson, C., Hobbs, D., Lammers, U., Biermann, M., Geyer, R., Hilger, T., Michalik, D., Stampa, U., McMillan, P. J., Castañeda, J., Clotet, M., Comoretto, G., Davidson, M., Fabricius, C., Gracia, G., Hambly, N. C., Hutton, A., Mora, A., Portell, J., van Leeuwen, F., Abbas, U., Abreu, A., Altmann, M., Andrei, A., Anglada, E., Balaguer-Núñez, L., Barache, C., Becciani, U., Bertone, S., Bianchi, L., Bouquillon, S., Bourda, G., Brüsemeister, T., Bucciarelli, B., Busonero, D., Buzzi, R., Cancelliere, R., Carlucci, T., Charlot, P., Cheek, N., Crosta, M., Crowley, C., de Bruijne, J., de Felice, F., Drimmel, R., Esquej, P., Fienga, A., Fraile, E., Gai, M., Garralda, N., González-Vidal, J. J., Guerra, R., Hauser, M., Hofmann, W., Holl, B., Jordan, S., Lattanzi, M. G., Lenhardt, H., Liao, S., Licata, E., Lister, T., Löffler, W., Marchant, J., Martin-Fleitas, J. M., Messineo, R., Mignard, F., Morbidelli, R., Poggio, E., Riva, A., Rowell, N., Salguero, E., Sarasso, M., Sciacca, E., Siddiqui, H., Smart, R. L., Spagna, A., Steele, I., Taris, F., Torra, J., van Elteren, A., van Reeven, W. & Vecchiato, A. (2018), 'Gaia Data Release 2. The astrometric solution', **616**, A2.

Lineweaver, C. H. & Grether, D. (2005), How Dry is the Brown Dwarf Desert? Quantifying the Relative Number of Planets, Brown Dwarfs and Stellar Companions Around Nearby Sun-like Stars, *in* 'Protostars and Planets V Posters', p. 8252.

Lingam, M. & Loeb, A. (2019*a*), 'Brown Dwarf Atmospheres as the Potentially Most Detectable and Abundant Sites for Life', **883**(2), 143.

Lingam, M. & Loeb, A. (2019*b*), 'Photosynthesis on habitable planets around low-mass stars', **485**(4), 5924–5928.

Liu, B., Lambrechts, M., Johansen, A., Pascucci, I. & Henning, T. (2020), 'Pebble-driven Planet Formation around Very Low-mass Stars and Brown Dwarfs', *arXiv e-prints* p. arXiv:2004.07239.

Liu, M. C., Dupuy, T. J. & Allers, K. N. (2016), 'The Hawaii Infrared Parallax Program. II. Young Ultracool Field Dwarfs', **833**(1), 96.

Liu, M. C., Dupuy, T. J. & Leggett, S. K. (2010), 'Discovery of a Highly Unequal-mass Binary T Dwarf with Keck Laser Guide Star Adaptive Optics: A Coevality Test of Substellar Theoretical Models and Effective Temperatures', **722**(1), 311–328.

Liu, M. C., Magnier, E. A., Deacon, N. R., Allers, K. N., Dupuy, T. J., Kotson, M. C., Aller, K. M., Burgett, W. S., Chambers, K. C., Draper, P. W., Hodapp, K. W., Jedicke, R., Kaiser, N., Kudritzki, R. P., Metcalfe, N., Morgan, J. S., Price, P. A., Tonry, J. L. & Wainscoat, R. J. (2013), 'The Extremely Red, Young L Dwarf PSO J318.5338-22.8603: A Free-floating Planetary-mass Analog to Directly Imaged Young Gas-giant Planets', **777**(2), L20.

Liu, W. M. & Chaboyer, B. (2000), 'The Relative Age of the Thin and Thick Galactic Disks', **544**(2), 818–829.

Lodders, K. (1999), 'Alkali Element Chemistry in Cool Dwarf Atmospheres', **519**(2), 793–801.

Lodders, K. & Fegley, B. (2002), 'Atmospheric Chemistry in Giant Planets, Brown Dwarfs, and Low-Mass Dwarf Stars. I. Carbon, Nitrogen, and Oxygen', **155**(2), 393–424.

Loebman, S. R., Roškar, R., Debattista, V. P., Ivezić, Ž., Quinn, T. R. & Wadsley, J. (2011), 'The Genesis of the Milky Way's Thick Disk Via Stellar Migration', **737**(1), 8.

Longstaff, E. S., Casewell, S. L., Wynn, G. A., Maxted, P. F. L. & Helling, C. (2017), 'Emission lines in the atmosphere of the irradiated brown dwarf WD0137-349B', **471**(2), 1728–1736.

Luhman, K. L. (2012), 'The Formation and Early Evolution of Low-Mass Stars and Brown Dwarfs', **50**, 65–106.

Luhman, K. L. (2014), 'Discovery of a ~250 K Brown Dwarf at 2 pc from the Sun', **786**(2), L18.

Luri, X., Brown, A. G. A., Sarro, L. M., Arenou, F., Bailer-Jones, C. A. L., Castro-Ginard, A., de Bruijne, J., Prusti, T., Babusiaux, C. & Delgado, H. E. (2018), 'Gaia Data Release 2. Using Gaia parallaxes', **616**, A9.

Ma, B. & Ge, J. (2014), 'Statistical properties of brown dwarf companions: implications for different formation mechanisms', **439**(3), 2781–2789.

Majewski, S. R. (1993), 'Galactic structure surveys and the evolution of the Milky Way.', **31**, 575–638.

Marigo, P., Bressan, A., Nanni, A., Girardi, L. & Pumo, M. L. (2013), 'Evolution of thermally pulsing asymptotic giant branch stars - I. The COLIBRI code', **434**(1), 488–526.

Marley, M. (2000*a*), The Role of Condensates in L- and T-dwarf Atmospheres, *in* C. A. Griffith & M. S. Marley, eds, 'From Giant Planets to Cool Stars', Vol. 212 of *Astronomical Society of the Pacific Conference Series*, p. 152.

Marley, M. (2000*b*), The Role of Condensates in L- and T-dwarf Atmospheres, *in* C. A. Griffith & M. S. Marley, eds, 'From Giant Planets to Cool Stars', Vol. 212 of *Astronomical Society of the Pacific Conference Series*, p. 152.

Marley, M. S. & Ackerman, A. S. (2001), 'The Role of Clouds in Brown Dwarf and Extrasolar Giant Planet Atmospheres', *arXiv e-prints* pp. astro–ph/0103269.

Marley, M. S., Ackerman, A. S., Burgasser, A. J., Saumon, D., Lodders, K. & Freedman, R. (2003), Clouds and Clearings in the Atmospheres of the L and T Dwarfs, *in* E. Martín, ed., 'Brown Dwarfs', Vol. 211, p. 333.

Marley, M. S., Gelino, C., Stephens, D., Lunine, J. I. & Freedman, R. (1999), 'Reflected Spectra and Albedos of Extrasolar Giant Planets. I. Clear and Cloudy Atmospheres', **513**(2), 879–893.

Marley, M. S. & Robinson, T. D. (2015*a*), 'On the Cool Side: Modeling the Atmospheres of Brown Dwarfs and Giant Planets', **53**, 279–323.

Marley, M. S. & Robinson, T. D. (2015*b*), 'On the Cool Side: Modeling the Atmospheres of Brown Dwarfs and Giant Planets', **53**, 279–323.

Marley, M. S., Saumon, D., Visscher, C., Lupu, R., Freedman, R., Morley, C., Fortney, J. J., Seay, C., Smith, A. J. R. W., Teal, D. J. & Wang, R. (2021), 'The Sonora Brown Dwarf Atmosphere and Evolution Models. I. Model Description and Application to Cloudless Atmospheres in Rainout Chemical Equilibrium', **920**(2), 85.

Marley, M. S., Seager, S., Saumon, D., Lodders, K., Ackerman, A. S., Freedman, R. S. & Fan, X. (2002), 'Clouds and Chemistry: Ultracool Dwarf Atmospheric Properties from Optical and Infrared Colors', **568**(1), 335–342.

Marocco, F., Jones, H. R. A., Day-Jones, A. C., Pinfield, D. J., Lucas, P. W., Burningham, B., Zhang, Z. H., Smart, R. L., Gomes, J. I. & Smith, L. (2015), 'A large spectroscopic sample of L and T dwarfs from UKIDSS LAS: peculiar objects, binaries, and space density', **449**(4), 3651–3692.

Marshall, H. L., Tananbaum, H., Avni, Y. & Zamorani, G. (1983), 'Analysis of complete quasar samples to obtain parameters of luminosity and evolution functions', **269**, 35–41.

Martin, E. C., Mace, G. N., McLean, I. S., Logsdon, S. E., Rice, E. L., Kirkpatrick, J. D., Burgasser, A. J., McGovern, M. R. & Prato, L. (2017*a*), 'Surface Gravities for 228 M, L, and T Dwarfs in the NIRSPEC Brown Dwarf Spectroscopic Survey', **838**(1), 73.

Martin, E. C., Mace, G. N., McLean, I. S., Logsdon, S. E., Rice, E. L., Kirkpatrick, J. D., Burgasser, A. J., McGovern, M. R. & Prato, L. (2017*b*), 'Surface Gravities for 228 M, L, and T Dwarfs in the NIRSPEC Brown Dwarf Spectroscopic Survey', **838**(1), 73.

Martín, E. L. & Bouy, H. (2002*a*), 'XMM-Newton observations of the nearby brown dwarf LP 944-20', **7**(8), 595–602.

Martín, E. L. & Bouy, H. (2002*b*), 'XMM-Newton observations of the nearby brown dwarf LP 944-20', *New Astronomy* **7**(8), 595–602.

Martín, E. L., Delfosse, X., Basri, G., Goldman, B., Forveille, T. & Zapatero Osorio, M. R. (1999), 'Spectroscopic Classification of Late-M and L Field Dwarfs', **118**(5), 2466–2482.

Martín, E. L., Lodieu, N. & del Burgo, C. (2021), 'New constraints on the minimum mass for thermonuclear lithium burning in brown dwarfs', .

McInnes, L., Healy, J. & Melville, J. (2018), 'UMAP: Uniform Manifold Approximation and Projection for Dimension Reduction', *arXiv e-prints* p. arXiv:1802.03426.

McKee, C. F., Parravano, A. & Hollenbach, D. J. (2015), 'Stars, gas, and dark matter in the solar neighborhood', *The Astrophysical Journal* **814**(1), 13.
URL: *http://dx.doi.org/10.1088/0004-637X/814/1/13*

Meisner, A. M., Faherty, J. K., Kirkpatrick, J. D., Schneider, A. C., Caselden, D., Gagné, J., Kuchner, M. J., Burgasser, A. J., Casewell, S. L., Debes, J. H., Artigau, É., Bardalez Gagliuffi, D. C., Logsdon, S. E., Kiman, R., Allers, K., Hsu, C.-c., Wisniewski, J. P., Allen, M. B., Beaulieu, P., Colin, G., Durantini Luca, H. A., Goodman, S., Gramaize, L., Hamlet, L. K., Hinckley, K., Kiwy, F., Martin, D. W., Pendrill, W., Rothermich, A., Sainio, A., Schümann, J., Andersen, N. S., Tanner, C., Thakur, V., Thévenot, M., Walla, J., Wedracki, Z., Aganze, C., Gerasimov, R., Theissen, C. & Backyard Worlds: Planet 9 Collaboration (2020), 'Spitzer Follow-up of Extremely Cold Brown Dwarfs Discovered by the Backyard Worlds: Planet 9 Citizen Science Project', **899**(2), 123.

Meisner, A. M., Schneider, A. C., Burgasser, A. J., Marocco, F., Line, M. R., Faherty, J. K., Kirkpatrick, J. D., Caselden, D., Kuchner, M. J., Gelino, C. R., Gagné, J., Theissen, C., Gerasimov, R., Aganze, C., Hsu, C.-c., Wisniewski, J. P., Casewell, S. L., Bardalez Gagliuffi, D. C., Logsdon, S. E., Eisenhardt, P. R. M., Allers, K., Debes, J. H., Allen, M. B., Stevnbak Andersen, N., Goodman, S., Gramaize, L., Martin, D. W., Sainio, A., Cushing, M. C. & Backyard Worlds: Planet 9 Collaboration (2021), 'New Candidate Extreme T Subdwarfs from the Backyard Worlds: Planet 9 Citizen Science Project', **915**(2), 120.

Metchev, S. A., Heinze, A., Apai, D., Flateau, D., Radigan, J., Burgasser, A., Marley, M. S., Artigau, É., Plavchan, P. & Goldman, B. (2015), 'Weather on Other Worlds. II. Survey Results: Spots are Ubiquitous on L and T Dwarfs', **799**(2), 154.

Metchev, S. A. & Hillenbrand, L. A. (2009), 'The Palomar/Keck Adaptive Optics Survey of Young Solar Analogs: Evidence for a Universal Companion Mass Function', **181**(1), 62–109.

Metchev, S. A., Kirkpatrick, J. D., Berriman, G. B. & Looper, D. (2008), 'A Cross-Match of 2MASS and SDSS: Newly Found L and T Dwarfs and an Estimate of the Space Density of T Dwarfs', **676**(2), 1281–1306.

Metchev, S., Heinze, A., Apai, D., Flateau, D., Radigan, J., Burgasser, A., Marley, M., Artigau, É., Plavchan, P. & Goldman, B. (2016*a*), Low-gravity L Dwarfs Are Likely More Variable, *in* J. H. Kastner, B. Stelzer & S. A. Metchev, eds, 'Young Stars & Planets Near the Sun', Vol. 314, pp. 121–123.

Metchev, S., Heinze, A., Apai, D., Flateau, D., Radigan, J., Burgasser, A., Marley, M., Artigau, É., Plavchan, P. & Goldman, B. (2016*b*), Low-gravity L Dwarfs Are Likely More Variable, *in* J. H. Kastner, B. Stelzer & S. A. Metchev, eds, 'Young Stars & Planets Near the Sun', Vol. 314 of *IAU Symposium*, pp. 121–123.

Miller, G. E. & Scalo, J. M. (1979), 'The Initial Mass Function and Stellar Birthrate in the Solar Neighborhood', **41**, 513.

Miret-Roig, N., Bouy, H., Raymond, S. N., Tamura, M., Bertin, E., Barrado, D., Olivares, J., Galli, P. A. B., Cuillandre, J.-C., Sarro, L. M., Berihuete, A. & Huélamo, N. (2021), 'A rich population of free-floating planets in the Upper Scorpius young stellar association', *Nature Astronomy* .

Miret-Roig, N., Bouy, H., Raymond, S. N., Tamura, M., Bertin, E., Barrado, D., Olivares, J., Galli, P. A. B., Cuillandre, J.-C., Sarro, L. M., Berihuete, A. & Huélamo, N. (2022), 'A rich population of free-floating planets in the Upper Scorpius young stellar association', *Nature Astronomy* **6**, 89–97.

Mohanty, S. & Basri, G. (2003), 'Rotation and Activity in Mid-M to L Field Dwarfs', **583**(1), 451–472.

Mohanty, S., Basri, G., Shu, F., Allard, F. & Chabrier, G. (2002), 'Activity in Very Cool Stars: Magnetic Dissipation in Late M and L Dwarf Atmospheres', **571**(1), 469–486.

Morell, O., Kallander, D. & Butcher, H. R. (1992), 'The age of the galaxy from thorium in G dwarfs, a re-analysis.', **259**, 543–548.

Morley, C. V., Fortney, J. J., Marley, M. S., Visscher, C., Saumon, D. & Leggett, S. K. (2012), 'Neglected Clouds in T and Y Dwarf Atmospheres', **756**(2), 172.

Mužić, K., Schödel, R., Scholz, A. e., Geers, V. C., Jayawardhana, R., Ascenso, J. & Cieza, L. A. (2017), 'The low-mass content of the massive young star cluster RCW 38', **471**(3), 3699–3712.

Myeong, G. C., Evans, N. W., Belokurov, V., Sanders, J. L. & Koposov, S. E. (2018), 'The Sausage Globular Clusters', **863**(2), L28.

Myeong, G. C., Vasiliev, E., Iorio, G., Evans, N. W. & Belokurov, V. (2019), 'Evidence for two early accretion events that built the Milky Way stellar halo', **488**(1), 1235–1247.

Nakajima, T., Oppenheimer, B. R., Kulkarni, S. R., Golimowski, D. A., Matthews, K. & Durrance, S. T. (1995), 'Discovery of a cool brown dwarf', **378**(6556), 463–465.

Nelson, L. A., Rappaport, S. & Chiang, E. (1993), 'On the Li and Be Tests for Brown Dwarfs', **413**, 364.

Ng, Y. K. & Bertelli, G. (1998), 'Revised ages for stars in the solar neighbourhood', **329**, 943–950.

Nichols, J. D., Burleigh, M. R., Casewell, S. L., Cowley, S. W. H., Wynn, G. A., Clarke, J. T. & West, A. A. (2012), 'Origin of Electron Cyclotron Maser Induced Radio Emissions at Ultracool Dwarfs: Magnetosphere-Ionosphere Coupling Currents', **760**(1), 59.

Nordström, B., Mayor, M., Andersen, J., Holmberg, J., Pont, F., Jørgensen, B. R., Olsen, E. H., Udry, S. & Mowlavi, N. (2004), 'The Geneva-Copenhagen survey of the Solar neighbourhood. Ages, metallicities, and kinematic properties of ∼14 000 F and G dwarfs', **418**, 989–1019.

Parsons, S. G., Gänsicke, B. T., Marsh, T. R., Ashley, R. P., Breedt, E., Burleigh, M. R., Copperwheat, C. M., Dhillon, V. S., Green, M. J., Hermes, J. J., Irawati, P., Kerry, P., Littlefair, S. P., Rebassa-Mansergas, A., Sahman, D. I., Schreiber, M. R. & Zorotovic, M. (2018), 'The scatter of the M dwarf mass-radius relationship', **481**(1), 1083–1096.

Pasquet-Itam, J. & Pasquet, J. (2018), 'Deep learning approach for classifying, detecting and predicting photometric redshifts of quasars in the Sloan Digital Sky Survey stripe 82', **611**, A97.

Pastorelli, G., Marigo, P., Girardi, L., Aringer, B., Chen, Y., Rubele, S., Trabucchi, M., Bladh, S., Boyer, M. L., Bressan, A., Dalcanton, J. J., Groenewegen, M. A. T., Lebzelter, T., Mowlavi, N., Chubb, K. L., Cioni, M.-R. L., de Grijs, R., Ivanov, V. D., Nanni, A., van Loon, J. T. & Zaggia, S. (2020), 'Constraining the thermally pulsing asymptotic giant branch phase with resolved stellar populations in the Large Magellanic Cloud', **498**(3), 3283–3301.

Pastorelli, G., Marigo, P., Girardi, L., Chen, Y., Rubele, S., Trabucchi, M., Aringer, B., Bladh, S., Bressan, A., Montalbán, J., Boyer, M. L., Dalcanton, J. J., Eriksson, K., Groenewegen, M. A. T., Höfner, S., Lebzelter, T., Nanni, A., Rosenfield, P., Wood, P. R. & Cioni, M.-R. L. (2019), 'Constraining the thermally pulsing asymptotic giant branch phase with resolved stellar populations in the Small Magellanic Cloud', **485**(4), 5666–5692.

Paszke, A., Gross, S., Massa, F., Lerer, A., Bradbury, J., Chanan, G., Killeen, T., Lin, Z., Gimelshein, N., Antiga, L., Desmaison, A., Köpf, A., Yang, E., DeVito, Z., Raison, M., Tejani, A., Chilamkurthy, S., Steiner, B., Fang, L., Bai, J. & Chintala, S. (2019), 'PyTorch: An Imperative Style, High-Performance Deep Learning Library', *arXiv e-prints* p. arXiv:1912.01703.

Pecaut, M. J. & Mamajek, E. E. (2013), 'Intrinsic Colors, Temperatures, and Bolometric Corrections of Pre-main-sequence Stars', **208**(1), 9.

Peng, N., Zhang, Y., Zhao, Y. & Wu, X.-b. (2012), 'Selecting quasar candidates using a support vector machine classification system', **425**(4), 2599–2609.

Phan-Bao, N., Bessell, M. S., Nguyen-Thanh, D., Martín, E. L., Ho, P. T. P., Lee, C. F. & Parsons, H. (2017), 'Detection of lithium in nearby young late-M dwarfs', **600**, A19.

Phillips, M. W., Tremblin, P., Baraffe, I., Chabrier, G., Allard, N. F., Spiegelman, F., Goyal, J. M., Drummond, B. & Hébrard, E. (2020), 'A new set of atmosphere and evolution models for cool T-Y brown dwarfs and giant exoplanets', **637**, A38.

Pinfield, D. J., Burningham, B., Tamura, M., Leggett, S. K., Lodieu, N., Lucas, P. W., Mortlock, D. J., Warren, S. J., Homeier, D., Ishii, M., Deacon, N. R., McMahon, R. G., Hewett, P. C., Osori, M. R. Z., Martin, E. L., Jones, H. R. A., Venemans, B. P., Day-Jones, A. C., Dobbie, P. D., Folkes, S. L., Dye, S., Allard, F., Baraffe, I., Barrado Y Navascués, D., Casewell, S. L., Chiu, K., Chabrier, G., Clarke, F., Hodgkin, S. T., Magazzù, A., McCaughrean, M. J., Nakajima, T., Pavlenko, Y. & Tinney, C. G. (2008), 'Fifteen new T dwarfs discovered in the UKIDSS Large Area Survey', **390**(1), 304–322.

Pinfield, D. J., Gomes, J., Day-Jones, A. C., Leggett, S. K., Gromadzki, M., Burningham, B., Ruiz, M. T., Kurtev, R., Cattermole, T., Cardoso, C., Lodieu, N., Faherty, J., Littlefair, S., Smart, R., Irwin, M., Clarke, J. R. A., Smith, L., Lucas, P. W., Gálvez-Ortiz, M. C., Jenkins, J. S., Jones, H. R. A., Rebolo, R., Béjar, V. J. S. & Gauza, B. (2014), 'A deep WISE search for very late type objects and the discovery of two halo/thick-disc T dwarfs: WISE 0013+0634 and WISE 0833+0052', **437**(2), 1009–1026.

Portillo, S. K. N., Parejko, J. K., Vergara, J. R. & Connolly, A. J. (2020), 'Dimensionality Reduction of SDSS Spectra with Variational Autoencoders', **160**(1), 45.

Quinn, P. J., Hernquist, L. & Fullagar, D. P. (1993), 'Heating of Galactic Disks by Mergers', **403**, 74.

Quintana, E. V., Barclay, T., Raymond, S. N., Rowe, J. F., Bolmont, E., Caldwell, D. A., Howell, S. B., Kane, S. R., Huber, D., Crepp, J. R., Lissauer, J. J., Ciardi, D. R., Coughlin, J. L., Everett, M. E., Henze, C. E., Horch, E., Isaacson, H., Ford, E. B., Adams, F. C., Still, M., Hunter, R. C., Quarles, B. & Selsis, F. (2014), 'An Earth-Sized Planet in the Habitable Zone of a Cool Star', *Science* **344**(6181), 277–280.

Radigan, J., Jayawardhana, R., Lafrenière, D., Dupuy, T. J., Liu, M. C. & Scholz, A. (2013), 'Discovery of a Visual T-dwarf Triple System and Binarity at the L/T Transition', **778**(1), 36.

Radigan, J., Lafrenière, D., Jayawardhana, R. & Artigau, E. (2014), 'Strong Brightness Variations Signal Cloudy-to-clear Transition of Brown Dwarfs', **793**(2), 75.

Raghavan, D., McAlister, H. A., Henry, T. J., Latham, D. W., Marcy, G. W., Mason, B. D., Gies, D. R., White, R. J. & ten Brummelaar, T. A. (2010), 'A Survey of Stellar Families: Multiplicity of Solar-type Stars', **190**(1), 1–42.

Rebolo, R., Zapatero Osorio, M. R. & Martín, E. L. (1995), 'Discovery of a brown dwarf in the Pleiades star cluster', **377**(6545), 129–131.

Reid, I. N., Burgasser, A. J., Cruz, K. L., Kirkpatrick, J. D. & Gizis, J. E. (2001), 'Near-Infrared Spectral Classification of Late M and L Dwarfs', **121**(3), 1710–1721.

Reid, I. N., Cruz, K. L., Burgasser, A. J. & Liu, M. C. (2008), 'L-Dwarf Binaries in the 20-Parsec Sample', **135**(2), 580–587.

Reid, I. N., Cruz, K. L., Laurie, S. P., Liebert, J., Dahn, C. C., Harris, H. C., Guetter, H. H., Stone, R. C., Canzian, B., Luginbuhl, C. B., Levine, S. E., Monet, A. K. B. & Monet, D. G. (2003), 'Meeting the Cool Neighbors. IV. 2MASS 1835+32, a Newly Discovered M8.5 Dwarf within 6 Parsecs of the Sun', **125**(1), 354–358.

Reid, I. N. & Gizis, J. E. (1997), 'Low-Mass Binaries and the Stellar Luminosity Function', **113**, 2246.

Reid, I. N., Gizis, J. E. & Hawley, S. L. (2002), 'The Palomar/MSU Nearby Star Spectroscopic Survey. IV. The Luminosity Function in the Solar Neighborhood and M Dwarf Kinematics', **124**(5), 2721–2738.

Reid, I. N., Gizis, J. E., Kirkpatrick, J. D. & Koerner, D. W. (2001), 'A Search for L Dwarf Binary Systems', **121**(1), 489–502.

Reid, I. N. & Hawley, S. L. (2005), *New light on dark stars : red dwarfs, low-mass stars, brown dwarfs*.

Reid, I. N., Kirkpatrick, J. D., Liebert, J., Burrows, A., Gizis, J. E., Burgasser, A., Dahn, C. C., Monet, D., Cutri, R. & Beichman, C. A. (1999), 'L Dwarfs and the Substellar Mass Function', **521**(2), 613–629.

Reid, I. N. et al. (1999), 'L Dwarfs and the Substellar Mass Function', **521**(2), 613–629.

Reid, N. & Majewski, S. R. (1993), 'Star Counts Redivivus. I. A New Look at the Galaxy at Faint Magnitudes', **409**, 635.

Reiners, A. & Basri, G. (2009), 'A Volume-Limited Sample of 63 M7-M9.5 Dwarfs. I. Space Motion, Kinematic Age, and Lithium', **705**(2), 1416–1424.

Reiners, A. & Mohanty, S. (2012), 'Radius-dependent Angular Momentum Evolution in Low-mass Stars. I', **746**(1), 43.

Retterer, J. M. (1980), 'The binding-energy distribution of the binaries in a star cluster. I - Time-independent, homogeneous cluster models', **85**, 249–264.

Reylé, C. (2018), 'New ultra-cool and brown dwarf candidates in Gaia DR2', **619**, L8.

Reylé, C., Delorme, P., Willott, C. J., Albert, L., Delfosse, X., Forveille, T., Artigau, E., Malo, L., Hill, G. J. & Doyon, R. (2010), 'The ultracool-field dwarf luminosity-function and space density from the Canada-France Brown Dwarf Survey', **522**, A112.

Reylé, C., Jardine, K., Fouqué, P., Caballero, J. A., Smart, R. L. & Sozzetti, A. (2021), 'The 10 parsec sample in the Gaia era', *arXiv e-prints* p. arXiv:2104.14972.

Ribas, I. (2006), 'Masses and Radii of Low-Mass Stars: Theory Versus Observations', **304**(1-4), 89–92.

Riello, M., De Angeli, F., Evans, D. W., Montegriffo, P., Carrasco, J. M., Busso, G., Palaversa, L., Burgess, P. W., Diener, C., Davidson, M., Rowell, N., Fabricius, C., Jordi, C., Bellazzini, M., Pancino, E., Harrison, D. L., Cacciari, C., van Leeuwen, F., Hambly, N. C., Hodgkin, S. T., Osborne, P. J., Altavilla, G., Barstow, M. A., Brown, A. G. A., Castellani, M., Cowell, S., De Luise, F., Gilmore, G., Giuffrida, G., Hidalgo, S., Holland, G., Marinoni, S., Pagani, C., Piersimoni, A. M., Pulone, L., Ragaini, S., Rainer, M., Richards, P. J., Sanna, N., Walton, N. A., Weiler, M. & Yoldas, A. (2021), 'Gaia Early Data Release 3. Photometric content and validation', **649**, A3.

Rilinger, A. M., Espaillat, C. C. & Macías, E. (2019), 'Modeling the Protoplanetary Disks of Two Brown Dwarfs in the Taurus Molecular Cloud', *arXiv e-prints* p. arXiv:1905.05829.

Rimoldini, L., Dubath, P., Süveges, M., López, M., Sarro, L. M., Blomme, J., De Ridder, J., Cuypers, J., Guy, L., Mowlavi, N., Lecoeur-Taïbi, I., Beck, M., Jan, A., Nienartowicz, K., Ordóñez-Blanco, D., Lebzelter, T. & Eyer, L. (2012), 'Automated classification of Hipparcos unsolved variables', **427**(4), 2917–2937.

Rocha-Pinto, H. J., Scalo, J., Maciel, W. J. & Flynn, C. (2000), 'An Intermittent Star Formation History in a "Normal" Disk Galaxy: The Milky Way', **531**(2), L115–L118.

Roweis, S. T. & Saul, L. K. (2000), 'Nonlinear Dimensionality Reduction by Locally Linear Embedding', *Science* **290**(5500), 2323–2326.

Rutledge, R. E., Basri, G., Martín, E. L. & Bildsten, L. (2000*a*), 'Chandra Detection of an X-Ray Flare from the Brown Dwarf LP 944-20', **538**(2), L141–L144.

Rutledge, R. E., Basri, G., Martín, E. L. & Bildsten, L. (2000*b*), 'Chandra Detection of an X-Ray Flare from the Brown Dwarf LP 944-20', **538**(2), L141–L144.

Ryan, R. E., J., Hathi, N. P., Cohen, S. H. & Windhorst, R. A. (2005), 'Constraining the Distribution of L and T Dwarfs in the Galaxy', **631**(2), L159–L162.

Ryan, R. E., J. & Reid, I. N. (2016), 'The Surface Densities of Disk Brown Dwarfs in JWST Surveys', **151**(4), 92.

Ryan, Russell E., J., Thorman, P. A., Schmidt, S. J., Cohen, S. H., Hathi, N. P., Holwerda, B. W., Lunine, J. I., Pirzkal, N., Windhorst, R. A. & Young, E. (2017), 'The Effect of Atmospheric Cooling on Vertical Velocity Dispersion and Density Distribution of Brown Dwarfs', **847**(1), 53.

Salpeter, E. E. (1955), 'The Luminosity Function and Stellar Evolution.', **121**, 161.

Sandage, A., Lubin, L. M. & VandenBerg, D. A. (2003), 'The Age of the Oldest Stars in the Local Galactic Disk from Hipparcos Parallaxes of G and K Subgiants', **115**(812), 1187–1206.

Saumon, D., Hubbard, W. B., Burrows, A., Guillot, T., Lunine, J. I. & Chabrier, G. (1996), 'A Theory of Extrasolar Giant Planets', **460**, 993.

Saumon, D. & Marley, M. S. (2008), 'The Evolution of L and T Dwarfs in Color-Magnitude Diagrams', **689**(2), 1327–1344.

Saumon, D., Marley, M. S., Abel, M., Frommhold, L. & Freedman, R. S. (2012), 'New H_2 Collision-induced Absorption and NH_3 Opacity and the Spectra of the Coolest Brown Dwarfs', **750**(1), 74.

Saumon, D., Marley, M. S., Cushing, M. C., Leggett, S. K., Roellig, T. L., Lodders, K. & Freedman, R. S. (2006), 'Ammonia as a Tracer of Chemical Equilibrium in the T7.5 Dwarf Gliese 570D', **647**(1), 552–557.

Schiavon, R. P., Barbuy, B. & Singh, P. D. (1997*a*), 'The FeH Wing-Ford Band in Spectra of M Stars', **484**(1), 499–510.

Schiavon, R. P., Barbuy, B. & Singh, P. D. (1997*b*), 'The FeH Wing-Ford Band in Spectra of M Stars', **484**(1), 499–510.

Schlesinger, K. J., Johnson, J. A., Rockosi, C. M., Lee, Y. S., Beers, T. C., Harding, P., Allende Prieto, C., Bird, J. C., Schönrich, R., Yanny, B., Schneider, D. P., Weaver, B. A. & Brinkmann, J. (2014), 'The Vertical Metallicity Gradient of the Milky Way Disk: Transitions in [α/Fe] Populations', **791**(2), 112.

Schmidt, M. (1968), 'Space Distribution and Luminosity Functions of Quasi-Stellar Radio Sources', **151**, 393.

Schmidt, S. J., Hawley, S. L., West, A. A., Bochanski, J. J., Davenport, J. R. A., Ge, J. & Schneider, D. P. (2015*a*), 'BOSS Ultracool Dwarfs. I. Colors and Magnetic Activity of M and L Dwarfs', **149**(5), 158.

Schmidt, S. J., Hawley, S. L., West, A. A., Bochanski, J. J., Davenport, J. R. A., Ge, J. & Schneider, D. P. (2015*b*), 'BOSS Ultracool Dwarfs. I. Colors and Magnetic Activity of M and L Dwarfs', **149**(5), 158.

Schneider, A. C., Burgasser, A. J., Gerasimov, R., Marocco, F., Gagné, J., Goodman, S., Beaulieu, P., Pendrill, W., Rothermich, A., Sainio, A., Kuchner, M. J., Caselden, D., Meisner, A. M., Faherty, J. K., Mamajek, E. E., Hsu, C.-C., Greco, J. J., Cushing, M. C., Kirkpatrick, J. D., Bardalez-Gagliuffi, D., Logsdon, S. E., Allers, K., Debes, J. H. & Backyard Worlds: Planet 9 Collaboration (2020), 'WISEA J041451.67-585456.7 and WISEA J181006.18-101000.5: The First Extreme T-type Subdwarfs?', **898**(1), 77.

Schneider, A. C., Cushing, M. C., Kirkpatrick, J. D., Mace, G. N., Gelino, C. R., Faherty, J. K., Fajardo-Acosta, S. & Sheppard, S. S. (2014), 'Discovery of the Young L Dwarf WISE J174102.78-464225.5', **147**(2), 34.

Schönrich, R. & Binney, J. (2009), 'Chemical evolution with radial mixing', **396**(1), 203–222.

Showman, A. P. (2016), 'Astrophysics: Illuminating brown dwarfs', **533**(7603), 330–331.

Showman, A. P., Tan, X. & Zhang, X. (2018), 'Atmospheric Circulation of Brown Dwarfs and Jupiter and Saturn-like Planets: Zonal Jets, Long-term Variability, and QBO-type Oscillations', *arXiv e-prints* p. arXiv:1807.08433.

Skrutskie, M. F., Cutri, R. M., Stiening, R., Weinberg, M. D., Schneider, S., Carpenter, J. M., Beichman, C., Capps, R., Chester, T., Elias, J., Huchra, J., Liebert, J., Lonsdale, C., Monet,

D. G., Price, S., Seitzer, P., Jarrett, T., Kirkpatrick, J. D., Gizis, J. E., Howard, E., Evans, T., Fowler, J., Fullmer, L., Hurt, R., Light, R., Kopan, E. L., Marsh, K. A., McCallon, H. L., Tam, R., Van Dyk, S. & Wheelock, S. (2006), 'The Two Micron All Sky Survey (2MASS)', **131**(2), 1163–1183.

Skrzypek, N., Warren, S. J. & Faherty, J. K. (2016), 'Photometric brown-dwarf classification. II. A homogeneous sample of 1361 L and T dwarfs brighter than J = 17.5 with accurate spectral types', **589**, A49.

Skrzypek, N., Warren, S. J., Faherty, J. K., Mortlock, D. J., Burgasser, A. J. & Hewett, P. C. (2015), 'Photometric brown-dwarf classification. I. A method to identify and accurately classify large samples of brown dwarfs without spectroscopy', **574**, A78.

Smart, R. L., Marocco, F., Caballero, J. A., Jones, H. R. A., Barrado, D., Beamín, J. C., Pinfield, D. J. & Sarro, L. M. (2017), 'The Gaia ultracool dwarf sample - I. Known L and T dwarfs and the first Gaia data release', **469**(1), 401–415.

Smart, R. L., Marocco, F., Sarro, L. M., Barrado, D., Beamín, J. C., Caballero, J. A. & Jones, H. R. A. (2019), 'The Gaia ultracool dwarf sample - II. Structure at the end of the main sequence', **485**(3), 4423–4440.

Sofue, Y. (2017), 'Rotation and mass in the Milky Way and spiral galaxies', **69**(1), R1.

Spitzer, Lyman, J. & Schwarzschild, M. (1951), 'The Possible Influence of Interstellar Clouds on Stellar Velocities.', **114**, 385.

Spitzer, Lyman, J. & Schwarzschild, M. (1953), 'The Possible Influence of Interstellar Clouds on Stellar Velocities. II.', **118**, 106.

Steele, P. R., Burleigh, M. R., Dobbie, P. D., Jameson, R. F., Barstow, M. A. & Satterthwaite, R. P. (2011), 'White dwarfs in the UKIRT Infrared Deep Sky Survey Large Area Survey: the substellar companion fraction', **416**(4), 2768–2791.

Stephens, D. C. & Leggett, S. K. (2004), 'JHK Magnitudes for L and T Dwarfs and Infrared Photometric Systems', **116**(815), 9–21.

Strauss, M. A., Knapp, G. R., Lupton, R. H., Gunn, J. E., Ivezic, Z., Carr, M., Fan, X., Vogeley, M. S. & SDSS Collaboration (1999), The Sloan Digital Sky Survey, *in* M. D. Bicay, R. M. Cutri & B. F. Madore, eds, 'Astrophysics with Infrared Surveys: A Prelude to SIRTF', Vol. 177 of *Astronomical Society of the Pacific Conference Series*, p. 390.

Tan, X. & Showman, A. P. (2017), 'Effects of Latent Heating on Atmospheres of Brown Dwarfs and Directly Imaged Planets', **835**(2), 186.

Tan, X. & Showman, A. P. (2019), 'Atmospheric Variability Driven by Radiative Cloud Feedback in Brown Dwarfs and Directly Imaged Extrasolar Giant Planets', **874**(2), 111.

Tan, X. & Showman, A. P. (2021), 'Atmospheric circulation of brown dwarfs and directly imaged exoplanets driven by cloud radiative feedback: global and equatorial dynamics', **502**(2), 2198–2219.

Tang, J., Bressan, A., Rosenfield, P., Slemer, A., Marigo, P., Girardi, L. & Bianchi, L. (2014), 'New PARSEC evolutionary tracks of massive stars at low metallicity: testing canonical stellar evolution in nearby star-forming dwarf galaxies', **445**(4), 4287–4305.

Tannock, M. E., Metchev, S., Heinze, A., Miles-Páez, P. A., Gagné, J., Burgasser, A., Marley, M. S., Apai, D., Suárez, G. & Plavchan, P. (2021), 'Weather on Other Worlds. V. The Three Most Rapidly Rotating Ultra-cool Dwarfs', **161**(5), 224.

Taylor, M. B. (2005), TOPCAT & STIL: Starlink Table/VOTable Processing Software, *in* P. Shopbell, M. Britton & R. Ebert, eds, 'Astronomical Data Analysis Software and Systems XIV', Vol. 347 of *Astronomical Society of the Pacific Conference Series*, p. 29.

Tenenbaum, J. B., de Silva, V. & Langford, J. C. (2000), 'A Global Geometric Framework for Nonlinear Dimensionality Reduction', *Science* **290**(5500), 2319–2323.

Torres, G. (2013), 'Fundamental properties of lower main-sequence stars', *Astronomische Nachrichten* **334**(1-2), 4.

Tremblin, P., Amundsen, D. S., Chabrier, G., Baraffe, I., Drummond, B., Hinkley, S., Mourier, P. & Venot, O. (2016), 'Cloudless Atmospheres for L/T Dwarfs and Extrasolar Giant Planets', **817**, L19.

Tremblin, P., Amundsen, D. S., Mourier, P., Baraffe, I., Chabrier, G., Drummond, B., Homeier, D. & Venot, O. (2015), 'Fingering convection and cloudless models for cool brown dwarf atmospheres', *The Astrophysical Journal* **804**(1), L17.
URL: *https://doi.org/10.1088*

Tremblin, P., Chabrier, G., Baraffe, I., Liu, M. C., Magnier, E. A., Lagage, P. O., Alves de Oliveira, C., Burgasser, A. J., Amundsen, D. S. & Drummond, B. (2017), 'Cloudless Atmospheres for Young Low-gravity Substellar Objects', **850**(1), 46.

Tremblin, P., Padioleau, T., Phillips, M. W., Chabrier, G., Baraffe, I., Fromang, S., Audit, E., Bloch, H., Burgasser, A. J., Drummond, B., González, M., Kestener, P., Kokh, S., Lagage, P. O. & Stauffert, M. (2019), 'Thermo-compositional Diabatic Convection in the Atmospheres of Brown Dwarfs and in Earth's Atmosphere and Oceans', **876**(2), 144.

Tsuji, T. & Nakajima, T. (2014), 'Near-infrared spectroscopy of M dwarfs. I. CO molecule as an abundance indicator of carbon', **66**(5), 98.

Tsuji, T., Nakajima, T. & Takeda, Y. (2015), 'Near-infrared spectroscopy of M dwarfs. II. H_2O molecule as an abundance indicator of oxygen', **67**(2), 26.

Tsuji, T., Ohnaka, K. & Aoki, W. (1996), 'Dust formation in stellar photospheres: a case of very low mass stars and a possible resolution on the effective temperature scale of M dwarfs.', **305**, L1.

Tsuji, T., Ohnaka, K. & Aoki, W. (1999), 'Warm Dust in the Cool Brown Dwarf Gliese 229B and Spectroscopic Diagnosis of Dusty Photospheres', **520**(2), L119–L122.

van der Kruit, P. C. (1988), 'The three-dimensional distribution of light and mass in disks of spiral galaxies.', **192**, 117–127.

van der Maaten, L. & Hinton, G. (2008), 'Visualizing high-dimensional data using t-sne'.

Vedantham, H. K., Callingham, J. R., Shimwell, T. W., Dupuy, T., Best, W. M. J., Liu, M. C., Zhang, Z., De, K., Lamy, L., Zarka, P., Rottgering, H. J. A. & Shulevski, A. (2020), 'Direct radio discovery of a cold brown dwarf', *arXiv e-prints* p. arXiv:2010.01915.

Villalobos, Á. & Helmi, A. (2008), 'Simulations of minor mergers - I. General properties of thick discs', **391**(4), 1806–1827.

Visscher, C. & Moses, J. I. (2011), 'Quenching of carbon monoxide and methane in the atmospheres of cool brown dwarfs and hot jupiters', *The Astrophysical Journal* **738**(1), 72.
URL: *https://doi.org/10.1088*

Vos, J., Allers, K., Apai, D., Biller, B., Burgasser, A. J., Faherty, J., Gagne, J., Helling, C., Morley, C., Radigan, J., Showman, A., Tan, X. & Tremblin, P. (2019), 'The L/T Transition', **51**(3), 253.

Ward-Duong, K., Patience, J., De Rosa, R. J., Bulger, J., Rajan, A., Goodwin, S. P., Parker, R. J., McCarthy, D. W. & Kulesa, C. (2015), 'The M-dwarfs in Multiples (MINMS) survey - I. Stellar multiplicity among low-mass stars within 15 pc', **449**(3), 2618–2637.

Warren, S. J., Ahmed, S. & Laithwaite, R. C. (2021), 'The local vertical density distribution of ultracool dwarfs M7 to L2.5 and their luminosity function', *The Open Journal of Astrophysics* **4**(1), 4.

Warren, S. J., Hambly, N. C., Dye, S., Almaini, O., Cross, N. J. G., Edge, A. C., Foucaud, S., Hewett, P. C., Hodgkin, S. T., Irwin, M. J., Jameson, R. F., Lawrence, A., Lucas, P. W., Adamson, A. J., Bandyopadhyay, R. M., Bryant, J., Collins, R. S., Davis, C. J., Dunlop, J. S., Emerson, J. P., Evans, D. W., Gonzales-Solares, E. A., Hirst, P., Jarvis, M. J., Kendall, T. R., Kerr, T. H., Leggett, S. K., Lewis, J. R., Mann, R. G., McLure, R. J., McMahon, R. G., Mortlock, D. J., Rawlings, M. G., Read, M. A., Riello, M., Simpson, C., Smith, D. J. B., Sutorius, E. T. W., Targett, T. A. & Varricatt, W. P. (2007), 'The United Kingdom Infrared Telescope Infrared Deep Sky Survey First Data Release', **375**(1), 213–226.

West, A. A., Morgan, D. P., Bochanski, J. J., Andersen, J. M., Bell, K. J., Kowalski, A. F., Davenport, J. R. A., Hawley, S. L., Schmidt, S. J. & Bernat, D. (2011), The Sloan Digital Sky

Survey Data Release 7 M Dwarf Spectroscopic Catalog, *in* C. Johns-Krull, M. K. Browning & A. A. West, eds, '16th Cambridge Workshop on Cool Stars, Stellar Systems, and the Sun', Vol. 448 of *Astronomical Society of the Pacific Conference Series*, p. 1407.

Whitworth, A., Bate, M. R., Nordlund, Å., Reipurth, B. & Zinnecker, H. (2007), The Formation of Brown Dwarfs: Theory, *in* B. Reipurth, D. Jewitt & K. Keil, eds, 'Protostars and Planets V', p. 459.

Wielen, R. (1977), 'The Diffusion of Stellar Orbits Derived from the Observed Age-Dependence of the Velocity Dispersion', **60**(2), 263–275.

Wing, R. F. & Ford, W. Kent, J. (1969), 'The Infrared Spectrum of the Cool Dwarf Wolf 359', **81**(482), 527–529.

Winters, J. G., Henry, T. J., Jao, W.-C., Subasavage, J. P., Chatelain, J. P., Slatten, K., Riedel, A. R., Silverstein, M. L. & Payne, M. J. (2019*a*), 'The Solar Neighborhood. XLV. The Stellar Multiplicity Rate of M Dwarfs Within 25 pc', **157**(6), 216.

Winters, J. G., Henry, T. J., Jao, W.-C., Subasavage, J. P., Chatelain, J. P., Slatten, K., Riedel, A. R., Silverstein, M. L. & Payne, M. J. (2019*b*), 'The Solar Neighborhood. XLV. The Stellar Multiplicity Rate of M Dwarfs Within 25 pc', **157**(6), 216.

Woitke, P. & Helling, C. (2004), 'Dust in brown dwarfs. III. Formation and structure of quasi-static cloud layers', **414**, 335–350.

Wright, E. L., Eisenhardt, P. R. M., Mainzer, A. K., Ressler, M. E., Cutri, R. M., Jarrett, T., Kirkpatrick, J. D., Padgett, D., McMillan, R. S., Skrutskie, M., Stanford, S. A., Cohen, M., Walker, R. G., Mather, J. C., Leisawitz, D., Gautier, Thomas N., I., McLean, I., Benford, D., Lonsdale, C. J., Blain, A., Mendez, B., Irace, W. R., Duval, V., Liu, F., Royer, D., Heinrichsen, I., Howard, J., Shannon, M., Kendall, M., Walsh, A. L., Larsen, M., Cardon, J. G., Schick, S., Schwalm, M., Abid, M., Fabinsky, B., Naes, L. & Tsai, C.-W. (2010), 'The Wide-field Infrared Survey Explorer (WISE): Mission Description and Initial On-orbit Performance', **140**(6), 1868–1881.

Zapatero Osorio, M. R., Martín, E. L., Bouy, H., Tata, R., Deshpande, R. & Wainscoat, R. J. (2006), 'Spectroscopic Rotational Velocities of Brown Dwarfs', **647**(2), 1405–1412.

Zhang, X. & Showman, A. P. (2014), 'Atmospheric Circulation of Brown Dwarfs: Jets, Vortices, and Time Variability', **788**(1), L6.

Zhang, Z. H., Burgasser, A. J., Gálvez-Ortiz, M. C., Lodieu, N., Zapatero Osorio, M. R., Pinfield, D. J. & Allard, F. (2019), 'Primeval very low-mass stars and brown dwarfs - VI. Population properties of metal-poor degenerate brown dwarfs', **486**(1), 1260–1282.

Zhang, Z. H., Galvez-Ortiz, M. C., Pinfield, D. J., Burgasser, A. J., Lodieu, N., Jones, H. R. A., Martín, E. L., Burningham, B., Homeier, D., Allard, F., Zapatero Osorio, M. R., Smith, L. C.,

Smart, R. L., López Martí, B., Marocco, F. & Rebolo, R. (2018), 'Primeval very low-mass stars and brown dwarfs - IV. New L subdwarfs, Gaia astrometry, population properties, and a blue brown dwarf binary', **480**(4), 5447–5474.

Zhang, Z. H., Homeier, D., Pinfield, D. J., Lodieu, N., Jones, H. R. A., Allard, F. & Pavlenko, Y. V. (2017), 'Primeval very low-mass stars and brown dwarfs - II. The most metal-poor substellar object', **468**(1), 261–271.

Zhao, S., Song, J. & Ermon, S. (2017), 'InfoVAE: Information Maximizing Variational Autoencoders', *arXiv e-prints* p. arXiv:1706.02262.

Zhou, Y., Apai, D., Metchev, S., Lew, B. W. P., Schneider, G., Marley, M. S., Karalidi, T., Manjavacas, E., Bedin, L. R., Cowan, N. B., Miles-Páez, P. A., Lowrance, P. J., Radigan, J. & Burgasser, A. J. (2018), 'Cloud Atlas: Rotational Modulations in the L/T Transition Brown Dwarf Companion HN Peg B', **155**(3), 132.